Investigating the role of fibroblast growth factor 23 in the pathogenesis of uraemic cardiomyopathy

by

JONATHAN PHILIP LAW

A thesis submitted to the University of Birmingham for the degree of
DOCTOR OF PHILOSOPHY

Institute of Cardiovascular Sciences
College of Medical and Dental Sciences
University of Birmingham
June 2023

UNIVERSITY OF
BIRMINGHAM

University of Birmingham Research Archive

e-theses repository

This unpublished thesis/dissertation is copyright of the author and/or third parties. The intellectual property rights of the author or third parties in respect of this work are as defined by The Copyright Designs and Patents Act 1988 or as modified by any successor legislation.

Any use made of information contained in this thesis/dissertation must be in accordance with that legislation and must be properly acknowledged. Further distribution or reproduction in any format is prohibited without the permission of the copyright holder.

Abstract

Uraemic cardiomyopathy, or CKD-associated cardiomyopathy, describes the clinical syndrome of myocardial hypertrophy and fibrosis, systolic and diastolic left ventricular failure found in chronic kidney disease, resulting in increased cardiovascular mortality attributable to heart failure and sudden cardiac death from cardiac arrhythmia. Circulating hormone fibroblast growth factor 23 (FGF23) is significantly elevated in chronic kidney disease and has previously been associated with cardiac remodelling and mechanoelectrical dysfunction. The work described in this thesis examines the hypothesis that FGF23 is a major player in the pathogenesis of uraemic cardiomyopathy by activating cardiac fibroblasts and disrupting cardiac ionic handling.

In this study, chronic activation of human cardiac fibroblasts led to an irreversible myofibroblast phenotype. FGF23 did not cause activation of human cardiac fibroblasts *in vitro*. Acute FGF23 treatment of *ex vivo* perfused murine hearts demonstrated shortening of left ventricular action potential and calcium transient duration by optical mapping, and increased incidence of cardiac arrhythmias. Moderate levels of FGF23 elevation in young adult mice caused arrhythmias without affecting cardiac ventricular morphology or mechanical function. These findings suggest that FGF23 causes increased cardiac arrhythmic phenomena through impaired cardiac ionic handling, which precedes clinically detectable hypertrophy and fibrosis.

To Sophie, Ellie, and Dan

Acknowledgements

I would first like to thank my primary supervisors Dr Davor Pavlovic and Professor Charles Ferro for their belief in my ability, mentorship, incredible wisdom, and continual guidance. In addition, this project would not have been possible without Professor Jonathan Townend, whose valuable help and advice was instrumental towards the successful grant application to the British Heart Foundation. Together, they continue to motivate me through their infectious enthusiasm for research.

Special thanks go to Caitlin Hall, Syeeda Nashitha Kabir, Dr Chris O'Shea, and Dr Winnie Chua, firstly for their friendship, but also their expert guidance and training to master the highly technical aspects of this laboratory study. I also owe a debt of gratitude to Dr Anna Price, Dr Luke Pickup who have been close friends and collaborators throughout.

Thank you also to members of the Cardiac Diseases theme, past and present, for welcoming me with open arms, with special mention to Dr Amar Azad, Max Cumberland, Dr Jasmeet Reyat, Dr Sophie Broadway-Stringer, Dr Molly O'Reilly, Dr Daniel Johnson, Dr Dannie Fobian, Professor Paulus Kirchhof and Professor Larissa Fabritz.

Last, but not least, I would like to thank my amazing parents Joshua and Claren, my beautiful wife Liying, and my cheeky daughters Ellie and Sophie for their unconditional love and support.

Funding

The work contained within this thesis was made possible through generous funding from a British Heart Foundation Clinical Research Training Fellowship (FS/19/16/34169), British Heart Foundation Accelerator Grant Fund, and University of Birmingham Research Development Fund.

Scientific outputs during registration period

Publications relating to thesis

Law JP, Pickup L, Pavlovic D, Townend JN, Ferro CJ. Hypertension and cardiomyopathy associated with chronic kidney disease: epidemiology, pathogenesis and treatment considerations. J Hum Hypertens. 2022.

Chua W, **Law JP**, Cardoso VR, Purmah Y, Neculau G, Jawad-UI-Qamar M, Russell K, Turner A, Tull SP, Nehaj F, Brady P, Kastner P, Ziegler A, Gkoutos GV, Pavlovic D, Ferro CJ, Kirchhof P, Fabritz L. Quantification of fibroblast growth factor 23 and N-terminal pro-B-type natriuretic peptide to identify patients with atrial fibrillation using a high-throughput platform: A validation study. PLoS Med. 2021 Feb 3;18(2):e13003405.

Law JP, Price AM, Pickup L, Radhakrishnan A, Weston C, Jones AM, McGettrick HM, Chua W, Steeds RP, Fabritz L, Kirchhof P, Pavlovic D, Townend JN, Ferro CJ. The Clinical Potential of Targeting Fibroblast Growth Factor-23 and αKlotho in the Treatment of Uraemic Cardiomyopathy. J Am Heart Assoc. 2020 Mar 26;9(7):e016041.

Pickup LC, **Law JP**, Townend JN, Ferro CJ. Sudden cardiac death in chronic renal disease: aetiology and risk reduction strategies. Nephrol Dial Transplant. 2019 Nov 20;36(8):1386-88.

Other publications

Radhakrishnan A, Pickup LC, Price AM, **Law JP**, McGee KC, Fabritz L, Senior R, Steeds RP, Ferro CJ, Townend JN. Coronary microvascular dysfunction is associated with degree of anaemia in end-stage renal disease. BMC Cardiovasc Disord. 2021 Apr 26;21(1):211.

Loutradis C, Pickup L, **Law JP**, Dasgupta I, Townend JN, Cockwell P, Sharif A, Sarafidis P, Ferro CJ. Acute kidney injury is more common in men than women after accounting for socioeconomic status, ethnicity, alcohol intake and smoking history. Biol Sex Differ. 2021 Apr 8;12(1):30.

Price AM, Moody WE, Stoll VM, Vijapurapu R, Hayer MK, Biasiolli L, Weston CJ, Webster R, Wesolowski R, McGee KC, Liu B, Baig S, Pickup LC, Radhakrishnan A, **Law JP**, Edwards NC, Steeds RP, Ferro CJ, Townend JN. Cardiovascular Effects of Unilateral Nephrectomy in Living Kidney Donors at 5 Years. Hypertension. 2021 Apr;77(4):1273-1284.

Law JP, Borrows R, McNulty D, Sharif A, Ferro CJ. Early renal function trajectories, cytomegalovirus serostatus and long-term graft outcomes in kidney transplant recipients. BMC Nephrol. 2021 Mar 20;22(1):102.

Pickup LC, **Law JP**, Radhakrishnan A, Price AM, Steeds RP, Smith T, Townend JN, Ferro CJ. Changes in left ventricular structure and function associated with renal transplantation; a systematic review and meta-analysis. ESC Heart Fail. 2021 Mar 15.

Pickup L, Loutradis C, **Law JP**, Arnold JJ, Dasgupta I, Sarafidis P, Townend JN, Cockwell P, Ferro CJ. The effect of admission and pre-admission serum creatinine at baseline to assess incidence and outcomes of acute kidney injury in acute medical admissions. Nephrol Dial Transplant. 2021 Jan 17;gfaa333.

Pickup L, **Law JP**, Townend JN, Ferro CJ. Cardiorenal medicine: an emerging new specialty or a need for closer collaboration? Br J Cardio. 2020 Sept;27(3):77-8.

Price AM, Greenhall GHB, Moody WE, Steeds RP, Mark PB, Edwards NC, Hayer MK, Pickup LC, Radhakrishnan A, **Law JP**, Banerjee D, Campbell T, Tomson CRV, Cockcroft JR, Shrestha B, Wilkinson IB, Tomlinson LA, Ferro CJ, Townend JN. Changes in blood pressure and arterial haemodynamics following living kidney donation (The EARNEST Study – UK). Clin J Am Soc Nephrol. 2020 Sept;15(9):1330-1339.

Radhakrishan A, Price AM, Pickup LC, **Law JP**, McGee KC, Fabritz L, Senior R, Steeds RP, Ferro CJ, Townend JN. Coronary flow velocity reserve and inflammatory markers in living kidney donors. Int J Cardiol. 2020 Dec 1;320:141-147.

Law JP, Pickup LC, Townend JN, Ferro CJ. Anticoagulant strategies for the patient with chronic kidney disease. Clin Med (Lond). 2020 Mar;20(2):151-5.

Radhakrishnan A, Pickup LC, Price AM, **Law JP**, Edwards NC, Steeds RP, Ferro CJ, Townend JT. Coronary microvascular dysfunction: a key step in the development of uraemic cardiomyopathy? Heart. 2019 Sep;105(17):1302-1309.

Manuscripts undergoing peer review

Hall C*, **Law JP***, Reyat JS, Cumberland MJ, Huang S, Vo NTN, Raniga K, Weston CJ, O'Shea C, Townend JN, Gehmlich K, Ferro CJ, Denning C, Pavlovic D. Chronic activation of human cardiac fibroblasts *in vitro* attenuates the reversibility of the myofibroblast phenotype. Under review at Scientific Reports.

* shared first authorship

Invited oral presentations

British Heart Foundation Accelerator Award Symposium, Birmingham, United Kingdom 2022

Institute of Cardiovascular Sciences Away Day, Birmingham, United Kingdom 2021

Institute of Cardiovascular Sciences Imaging & Technology Theme Meeting, Birmingham, United Kingdom

Published abstracts

Law JP, Kabir SN, O'Shea C, Gallagher L, Morgan J, Chua W, Townend JN, Ferro CJ, Pavlovic D. Fibroblast growth factor 23 shortens left ventricular action potential duration and increases arrhythmogenicity. *Journal of Molecular and Cellular Cardiology 2022;173(Suppl).*

Hall C, **Law JP**, Reyat JS, Cumberland M, Weston C, Townend JN, Ferro CJ, Gehmlich K, Denning C, Pavlovic D. Long term activation of human cardiac fibroblasts in 2D culture is irreversible. *Journal of Molecular and Cellular Cardiology 2022;173(Suppl).*

Hall C, **Law JP**, Reyat JS, Fabritz L, Kirchhof, Gehmlich K, Weston C, Townend JN, Ferro CJ, Denning C, Pavlovic D. Investigating the potential for reversal of myofibroblast activation in human cardiac fibroblasts in 2D culture. *EP Europace 2021;23(Suppl 3).*

Radhakrishnan A, Pickup LC, Price AM, **Law JP**, McGee KC, Fabritz L, Senior R, Steeds RP, Ferro CJ, Townend JN. Anaemia and coronary microvascular dysfunction in end-stage renal disease. *European Heart Journal – Cardiovascular Imaging 2021;22(Suppl 1).*

Price A, Moody W, Stoll V, Vijapurapu R, Hayer M, Biasiolli L, Weston CJ, Webster R, Wesolowski R, McGee K, Edwards N, Liu B, Baig S, Pickup L, Radhakrishnan A, **Law J**, Steeds R, Ferro C, Townend J. Cardiovascular effects of living kidney donation: a five year longitudinal study. *Heart 2020;106(Suppl 2).*

Radhakrishnan A, Pickup LC, Price AM, **Law J**, Fabritz L, Steeds R, Ferro C, Townend. Coronary flow reserve is reduced in asymptomatic living kidney donors – results of the chronic renal impairment in Birmingham coronary flow reserve (CRIB-FLOW) study. *Heart 2020;106(Suppl 2).*

Price A, Moody W, Stoll V, Vijapurapu R, Hayer M, Biasiolli L, Weston CJ, Webster R, Wesolowski R, McGee K, Kaur A, Pickup L, Radhakrishnan A, **Law JP**, Steeds R, Ferro C, Townend J. Cardiovascular effects of unilateral nephrectomy in living kidney donors at five years. *Nephrology Dialysis and Transplantation 2020;35(Suppl 3).*

Price A, Stoll V, Vijapurapu R, McGee K, Wesolowski R, Hayer M, Moody W, Edwards N, Liu B, Kaur A, Pickup L, Radhakrishnan A, **Law JP**, Steeds R, Ferro C, Townend J. Myocardial tissue characterisation in living kidney donors 5 years after nephrectomy. *Nephrology Dialysis and Transplantation 2020;35(Suppl 3).*

Law JP, Borrows R, McNulty D, Sharif A, Ferro CJ. Early renal function trajectories, cytomegalovirus serostatus and long-term graft outcomes in kidney transplant recipients: A Bayesian analysis study. *Nephrology Dialysis and Transplantation 2020;35(Suppl 3).*

Chua W, **Law JP**, Purmah Y, Neculau G, Mahmood H, Russell K, Turner A, Tull SP, Cardoso VR, Ul-Qamar MJ, Nehaj F, Brady P, Kastner P, Ziegler A, Gkoutos GV, Pavlovic D, Ferro CJ, Kirchhof P, Fabritz L. Validation of a data-driven biomarker model for atrial fibrillation in an unselected community-based patient cohort presenting acutely to hospital. *European Journal of Arrhythmia & Electrophysiology 2019;5(Suppl 1).*

Price AM, Pickup LC, Radhakrishnan A, **Law JP**, Hayer MK, Moody WE, Edwards NC, Ferro CJ, Townend JN. Nocturnal dipping and blood pressure variability in living kidney donors five years after nephrectomy. *Journal of Human Hypertension 2019;33(Suppl 1).*

Price AM, **Law JP**, Hayer MK, Pickup LC, Radhakrishnan A, Moody WE, Edwards NC, Ferro CJ, Townend JN. Medium term haemodynamic and blood pressure effects of living kidney donation. *Journal of Human Hypertension 2019;33(Suppl 1).*

Table of Contents

Chapter 1. Introduction 1

1.1. Extent of personal contribution 2

1.2. Chronic kidney disease 3

1.2.1. Definition and classification of CKD 3

1.2.2. Determination of GFR 6

1.3. Uraemic cardiomyopathy 6

1.3.1. Clinical phenotype of cardiomyopathy in CKD 6

1.3.1.1. Increased left ventricular mass and hypertrophy 7

1.3.1.2. Diastolic and systolic left ventricular dysfunction 9

1.3.1.3. Myocardial fibrosis 10

1.3.2. Drivers of uraemic cardiomyopathy in CKD 12

1.3.2.1. Increased afterload 13

1.3.2.2. Increased preload 15

1.3.2.3. Intrinsic factors 16

1.4. Fibroblast growth factor-23 and αKlotho 17

1.4.1. Biology of FGF23 and αKlotho 17

1.4.2. FGF23 and αKlotho in CKD 19

1.4.3. Cardiovascular effects of FGF23 and αKlotho 20

1.4.3.1. Left ventricular mass and hypertrophy 20

1.4.3.2. Myocardial fibrosis 21

1.4.3.3. Cardiac arrhythmias 22

1.5. Treatment of uraemic cardiomyopathy 23

1.5.1. Hypertension 23

1.5.1.1. Intensive blood pressure lowering 24

1.5.1.2. Antihypertensives, cardiac structure and function 24

1.5.2. Renal replacement therapy 27
1.5.2.1. Intensive dialysis 27
1.5.2.2. Renal transplantation 28
1.5.3. Management of CKD-MBD 29
1.5.3.1. Reducing serum phosphate 29
1.5.3.2. Vitamin D replacement 30
1.5.3.3. Targeting parathyroid hormone 31
1.5.3.4. Directly targeting FGF23 31
1.5.3.5. Targeting αKlotho 33
1.6. Thesis hypotheses and aims 36
Chapter 2. Experimental Methods 37
2.1. Extent of personal contribution 38
2.2. Human cardiac fibroblast cell culture 39
2.2.1. Primary human cardiac fibroblast culture 39
2.2.2. hiPSC-cFb culture 40
2.2.3. Human cardiac fibroblast culture on standard polystyrene and low stiffness surfaces 43
2.2.4. Treatment of human cardiac fibroblasts with fibroblast growth factor-23 or transforming growth factor-β 44
2.3. mRNA expression by real-time polymerase chain reaction 44
2.3.1. RNA extraction and cDNA conversion 44
2.3.2. Real-time PCR, mRNA expression by comparative $2^{-\Delta\Delta CT}$ method 45
2.4. Protein expression by western blot 46
2.4.1. Protein extraction 46
2.4.1.1. Cardiac fibroblast sample preparation 46
2.4.1.2. Mouse cardiac chamber preparation 47

2.4.2. SDS-PAGE protein gel electrophoresis 47
2.4.3. Transfer and immunoblotting 48
2.4.4. Image analysis 50
2.5. CyQUANT® NF cell proliferation assay 50
2.6. Immunofluorescence microscopy 51
2.7. Animal experimental protocols 52
2.7.1. Ethical statement and study approval 52
2.7.2. Animal models of acute and chronic cardiac FGF23 exposure 52
2.7.2.1. Acute model: *ex vivo* FGF23 administration 52
2.7.2.2. Chronic model: *in vivo* FGF23 administration 53
2.7.3. *Ex vivo* optical mapping buffer solutions and reagents 53
2.7.3.1. Modified Krebs-Henseleit Buffer 53
2.7.3.2. Blebbistatin 54
2.7.3.3. Recombinant mouse FGF23 54
2.7.3.4. Di-4-ANEPPS 55
2.7.3.5. Rhod-2-AM 55
2.7.3.6. Rh-237 55
2.7.4. Mouse cardiac extraction 56
2.7.4.1. Anaesthesia 56
2.7.4.2. Cardiac isolation and cannulation 57
2.7.5. Langendorff perfusion and optical mapping 59
2.7.5.1. Langendorff perfusion 59
2.7.5.2. Ex vivo optical mapping 60
2.7.5.3. Ex vivo left ventricular pacing 63
2.7.6. Optical mapping data analysis using ElectroMap 64
2.7.7. Quantification of *ex vivo* arrhythmia burden 65

2.7.8. *In vivo* echocardiography 66
2.7.9. Plasma separation and FGF23 quantification 69
2.7.9.1. Plasma separation 69
2.7.9.2. Plasma FGF23 quantification 69
2.7.10. Cardiac weights and tibial length measurements 70
2.8. Statistical analysis 71
Chapter 3. Chronic human cardiac fibroblast activation *in vitro* attenuates myofibroblast phenotype reversibility 72
3.1. Extent of personal contribution 73
3.2. Introduction 74
3.3. Methods 76
3.4. Results 78
3.4.1. Long-term culture of human cardiac fibroblasts on stiff substrates leads to non-reversible myofibroblast transition 78
3.4.2. A combination of mechanical and biochemical inputs has no effect on myofibroblast activation 87
3.4.3. hiPSC derived cardiac fibroblasts are responsive to TGF-β stimulation and inhibition 93
3.5. Discussion 105
3.5.1. Proliferative capacity of human cardiac fibroblasts 106
3.5.2. Reversal of myofibroblast phenotype through TGF-β inhibition 108
3.5.3. Terminally differentiated cardiac myofibroblasts cannot be de-activated 110
3.5.4. The role of mechanical stiffness and myofibroblast activation 112
3.6. Conclusion and future direction 113
Chapter 4. Human cardiac fibroblasts activation status following fibroblast growth factor 23 treatment 114

4.1. Extent of personal contribution 115
4.2. Introduction 116
4.2.1. Fibroblast growth factor-23 and myocardial fibrosis in CKD-associated cardiomyopathy 117
4.3. Methods 118
4.4. Results 119
4.4.1. Fibroblast growth factor receptor expression 119
4.4.2. Human cardiac fibroblast activation 126
4.4.3. hiPSC-derived cardiac fibroblast studies 134
4.5. Discussion 138
4.5.1. Culture Surface Stiffness on Activation Status 139
4.5.2. αKlotho 140
4.5.3. Constituents of Commercial Fibroblast Media, and Other Factors 140
Chapter 5. Quantifying the effects of acutely elevated fibroblast growth factor 23 on murine ventricular electrophysiology 143
5.1. Extent of personal Contribution 144
5.2. Introduction 145
5.2.1. The cardiac conduction system 145
5.2.2. The ventricular action potential 146
5.2.3. Effective refractory period 148
5.2.4. Cardiac excitation-contraction coupling 148
5.2.5. Regulation of calcium release and re-entry into the sarcoplasmic reticulum by SERCA2a and RyR2 151
5.3. Methods 153
5.4. Results 154
5.4.1. Action potential duration 154

5.4.2. Action potential duration heterogeneity 158
5.4.3. Conduction Velocity 162
5.4.4. Triangulation 164
5.4.5. Time to peak of action potential depolarisation 166
5.4.6. Diastolic interval 168
5.4.7. Ventricular arrhythmia burden 170
5.5. Discussion 172
5.5.1. FGF23 alters action potential duration and increases arrhythmogenic burden 172
5.5.2. FGF23 increases action potential heterogeneity and reduces conduction velocity 174
Chapter 6. Exploring murine ventricular calcium ionic handling following acute fibroblast growth factor 23 treatment 176
6.1. Extent of personal contribution 177
6.2. Introduction 178
6.3. Results 179
6.3.1. Effect of FGF23 on action potential duration and heterogeneity 179
6.3.2. Effect of FGF23 on action potential conduction velocity, time to peak depolarisation and diastolic interval 184
6.3.3. FGF23 effects on ventricular calcium transient duration and amplitude 188
6.3.4. Time to peak of calcium transient and calcium transient decay following FGF23 treatment 194
6.3.5. Ventricular arrhythmia burden and effective refractory period 198
6.4. Discussion 200
6.4.1. FGF23, ventricular APD shortening and increased arrhythmogenicity 200

6.4.2. Differences between single, and dual calcium-voltage loaded experiments 200
6.4.3. FGF23 and ventricular calcium handling 202
Chapter 7. Consequences of chronically raised fibroblast growth factor 23 on murine cardiac morphology and electrophysiology 205
7.1. Extent of personal contribution 206
7.2. Introduction 207
7.3. Results 208
7.3.1. Plasma FGF23 quantification 208
7.3.2. Body and tissue weight 210
7.3.3. Echocardiogram parameters – LV mass and function 212
7.3.4. Optical mapping and arrhythmias 214
7.3.5. Immunoblotting of cardiac lysates 220
7.4. Discussion 224
Chapter 8. Conclusions 229
8.1. Thesis outcomes 230
8.2. General Limitations 232
8.2.1. Cellular studies 232
8.2.1.1. Limitations of single cell-type studies and cellular isolation .. 232
8.2.1.2. Mechano-electrically static culture conditions 233
8.2.1.3. αKlotho 234
8.2.1.4. Western blots 234
8.2.2. Murine studies 234
8.2.2.1. Murine versus human cardiac physiology 234
8.2.2.2. Cardiac isolation and tissue ischaemia 235
8.2.2.3. Duration of exposure and circulating concentration of FGF23 in the chronic murine model 235

8.2.3. Optical mapping limitations 236
8.2.3.1. Blebbistatin 236
8.2.3.2. Limited depth of penetration 237
8.3. Future Work 237
8.3.1. In vitro experiments 237
8.3.2. Optical mapping experiments and analysis 238
8.3.2.1. Phase mapping 238
8.3.2.2. Further characterisation of cardiac ionic handling 239
8.3.2.3. High circulating concentration, chronic FGF23 excess model 240
References 242

Table of figures

Figure 1-1. Definition of CKD..... 4

Figure 1-2. Evolution of CKD classification..... 5

Figure 1-3 . Fibroblast growth factor 23 (FGF23) signal transduction and signaling pathways 18

Figure 1-4. Summary figure of potential therapeutic options targeting fibroblast growth factor 23 (FGF23) and the kidney-parathyroid-heart axis in patients with chronic kidney disease. 35

Figure 2-1. Derivation of hiPSC-cFbs. 41

Figure 2-2. Phase contrast microscopy and immunofluorescence staining of day 18 hiPSC-cFbs. 42

Figure 2-3. Anaesthetic and cardiac isolation setup 56

Figure 2-4. Isolated mouse heart within the thoracic cavity. 58

Figure 2-5. Langendorff system and optical mapping setup 59

Figure 2-6. Langendorff perfused heart placed within a water jacketed bowl... 60

Figure 2-7. Schematic of optical mapping method 62

Figure 2-8. Summary of echocardiographic parameters used to assess left ventricular 67

Figure 3-1. Activation status and proliferation of human cardiac fibroblasts on 3 GPa, 25 and 2 kPa culture plates. 80

Figure 3-2. Activation status and proliferation of human cardiac fibroblasts on 3 GPa culture plates. 83

Figure 3-3. Immunofluorescence staining of α-SMA in HCFs. 85

Figure 3-4. Representative images for secondary antibody only negative controls in HCFs. 86
Figure 3-5. Activation status and proliferation of human cardiac fibroblasts on 25 kPa culture plates. 89
Figure 3-6. Activation status and proliferation of human cardiac fibroblasts on 2 kPa culture plates. 91
Figure 3-7. Schematic of experimental process for human induced pluripotent stem cell derived cardiac fibroblasts (hiPSC-cFbs). 94
Figure 3-8. Immunofluorescence staining of α-SMA in quiescent and activated human induced pluripotent stem cell derived cardiac fibroblasts (hiPSC-cFbs). 95
Figure 3-9. Activation status of quiescent human induced pluripotent stem cell induced cardiac fibroblasts (hiPSC-cFBs) cultured on stiff substrates over 7 days. 98
Figure 3-10. Representative immunofluorescence images for Figure 3-9. 99
Figure 3-11. Activation status of quiescent and activated human induced pluripotent stem cell derived cardiac fibroblasts (hiPSC-cFbs) in response to TGF-β and SD208. 102
Figure 3-12. Analysis of proliferation of quiescent and activated human induced pluripotent stem cell induced cardiac fibroblasts (hiPSC-cFBs). 104
Figure 4-1. Human cardiac fibroblast (HCF) fibroblast growth factor receptor (FGFR) gene expression by RT-PCR. 121
Figure 4-2. Effect of culture plate stiffness on human cardiac fibroblast (HCF) fibroblast growth factor receptor (FGFR) gene expression by RT-PCR. 122

Figure 4-3. Effect of FGF23 and TGFβ treatment on HCF fibroblast growth factor receptor (FGFR) gene expression by RT-PCR..... 123
Figure 4-4. Effect of culture plate stiffness on human cardiac fibroblast (HCF) markers of activation by RT-PCR. 127
Figure 4-5. Effect of FGF23 and TGF-β treatment on HCF activation markers by RT-PCR. 128
Figure 4-6. Effect of FGF23 and TGF-β treatment on HCF activation markers by western blotting. 131
Figure 4-7. α-SMA Expression in Cultured Primary HCF by Immunofluorescence. 133
Figure 4-8. Human induced pluripotent stem cell derived cardiac fibroblast (iPSC-cFb) fibroblast growth factor receptor (FGFR) gene expression by RT-PCR. 135
Figure 4-9. Human induced pluripotent stem cell derived cardiac fibroblast (hiPSC-cFb) fibroblast growth factor receptor (FGFR) gene expression following FGF23 exposure. 136
Figure 4-10. Effect of FGF23 and TGF-β on human induced pluripotent stem cell derived cardiac fibroblast (hiPSC-cFb) activation. 137
Figure 5-1. Ventricular action potential in human and mouse. 147
Figure 5-2. Schematic of calcium transport and excitation-contraction coupling in ventricular myocytes. 150
Figure 5-3. Effect of FGF23 on murine left ventricular action potential duration by optical mapping. 155
Figure 5-4. Effect of FGF23 on murine left ventricular action potential duration heterogeneity by optical mapping. 159

Figure 5-5. Effect of FGF23 on murine left ventricular conduction velocity by optical mapping. 163
Figure 5-6. Effect of FGF23 on murine left ventricular action potential triangulation by optical mapping. 165
Figure 5-7. Effect of FGF23 on murine left ventricular time to peak of action potential depolarisation by optical mapping. 167
Figure 5-8. Effect of FGF23 on murine left ventricular diastolic interval by optical mapping. 169
Figure 5-9. Ventricular arrhythmia burden in *ex vivo* murine hearts in response to acute FGF23 treatment. 171
Figure 6-1. Effect of FGF23 on murine left ventricular action potential duration by optical mapping. 180
Figure 6-2. Effect of FGF23 on murine left ventricular action potential duration heterogeneity by optical mapping. 182
Figure 6-3. Effect of FGF23 on murine left ventricular conduction velocity by optical mapping. 185
Figure 6-4. Effect of FGF23 on murine left ventricular time to peak of action potential depolarisation by optical mapping. 186
Figure 6-5. Effect of FGF23 on murine left ventricular diastolic interval by optical mapping. 187
Figure 6-6. Effect of FGF23 on murine left ventricular calcium transient duration and amplitude by optical mapping. 190
Figure 6-7. Effect of FGF23 on murine left ventricular calcium transient duration heterogeneity by optical mapping. 192

Figure 6-8. Effect of FGF23 on murine left ventricular time to peak of calcium transient by optical mapping. 195
Figure 6-9. Effect of FGF23 on murine left ventricular calcium transient decay coefficient tau by optical mapping. 196
Figure 6-10. Effect of FGF23 on murine left ventricular calcium transient decay heterogeneity by optical mapping. 197
Figure 6-11. Ventricular arrhythmia burden and effective refractory period of *ex vivo* murine hearts in response to acute FGF23 treatment. 199
Figure 7-1. Plasma c-terminal FGF23 quantification by sandwich ELISA. 209
Figure 7-2. Body and tissue weights. 211
Figure 7-3. In vivo echocardiogram. 213
Figure 7-4. Left ventricle optical mapping. 216
Figure 7-5. Correlation of left ventricle electrophysiological parameter with plasma FGF23 level. 218
Figure 7-6. Ventricular arrhythmia burden and effective refractory period of *ex vivo* murine hearts in response to chronic systemic FGF23 treatment. 219
Figure 7-7. Western blot of collagen 1 and troponin T in murine left ventricular lysates. 221
Figure 7-8. Western blot of collagen 3 and heat shock protein 27 (HSP27) in murine left ventricular lysates. 223

Table of tables

Table 2-1. TaqMan™ Gene Expression Assays..... 46

Table 2-2. Primary antibodies used for immunoblotting 49

Table 2-3. Secondary antibodies used for western blot..... 49

Table 3-1. Experimental conditions and outcomes for HCFs and hiPSC-cFbs 77

Table 3-2. Myofibroblast Markers on Soft Culture Plates by RT-PCR and Western Blot. 88

Table 3-3. Summary of principle findings 106

Abbreviations

ADP	adenosine diphosphate
AF	atrial fibrillation
ANOVA	one-way analysis of variance
ANP	atrial natriuretic peptide
AP	action potential
APD	action potential duration
α-SMA	alpha-smooth muscle actin
ATP	adenosine triphosphate
BNP	brain natriuretic peptide
BSA	bovine serum albumin
$[Ca^{2+}]_i$	intracellular calcium
CaMKII	calcium-calmodulin dependent protein kinase II
CaT(D)	calcium transient (duration)
CI	confidence interval
CL	cycle length
CMR	cardiac magnetic resonance imaging
CKD	chronic kidney disease
CV	conduction velocity
DAD	delayed afterdepolarisation
DMSO	dimethyl sulfoxide
ECC	excitation-contraction coupling
ECG	electrocardiography

ECM	extracellular matrix
EF	ejection fraction
eGFR	estimated glomerular filtration rate
ERK	extracellular signal-regulated kinase
ERP	effective refractory period
FGF23	fibroblast growth factor 23
FGFR	fibroblast growth factor receptor
FGM3	fibroblast growth medium 3
FRS2α	fibroblast growth factor receptor substrate-2α
GAPDH	glyceraldehyde 3-phosphate dehydrogenase
HCF	human cardiac fibroblast
HD	haemodialysis
hiPSC-cFb	human induced pluripotent stem cell-derived cardiac fibroblast
I_{CaL}	inward Ca^{2+} current via L-type Ca^{2+} channels
IF	immunofluorescence
I_{K1}	inward rectifier K^+ current
I_{Kr}	rapid activating delayed outward rectifier K^+ current
I_{Ks}	slow activating delayed outward rectifier K^+ current
$I_{K,slow1}$	rapid activating, slowly inactivating K^+ current
$I_{K,slow2}$	slowly inactivating outward K^+ current
$I_{Na,early}$	early Na^+ current
$I_{Na,late}$	late Na^+ current
I_{SS}	non-inactivating outward K^+ current

$I_{to,f}$	transient outward K^+ current, fast
$I_{to,s}$	transient outward K^+ current, slow
KFRT	kidney failure with replacement therapy
KHB	Krebs-Henseleit buffer
KDIGO	Kidney Disease: Improving Global Outcomes
LA	left atrium
LTCC	L-type Ca^{2+} channel
LV	left ventricle
LVH	left ventricular hypertrophy
MAPK	mitogen-activated protein kinase
MHC	myosin heavy chain
mRNA	messenger ribonucleic acid
NCX	Na^+/Ca^{2+} exchanger
NFAT	nuclear factor of activated T cells
NKF-KDOQI	National Kidney Foundation Kidney Disease Outcomes Quality Initiative
NT-proBNP	B-type natriuretic peptide
PCR	polymerase chain reaction
PD	peritoneal dialysis
PBS	phosphate-buffered saline
PKA	protein kinase A
PLB	phospholamban
PLCγ	phospholipase Cγ
PTH	parathyroid hormone

PVDF	polyvinylidene fluoride
RA	right atrium
RAAS	renin-angiotensin-aldosterone system
RIPA	radioimmunoprecipitation assay
RRT	renal replacement therapy
RT-PCR	reverse transcriptase polymerase chain reaction
RV	right ventricular
RyR2	ryanodine receptor
SDS	sodium dodecyl-sulphate
SDS-PAGE	sodium dodecyl-sulphate polyacrylamide gel electrophoresis
SERCA2a	sarcoplasmic reticulum Ca^{2+}-ATPase
SNR	signal-to-noise ratio
SR	sarcoplasmic reticulum
TGF-β	transforming growth factor-beta
TTP	time to peak
WB	western blot
WT	wild type

CHAPTER 1. INTRODUCTION

1.1. EXTENT OF PERSONAL CONTRIBUTION

This chapter is based on the following published first author articles[1,2]:

Law JP, Pickup L, Pavlovic D, Townend JN, Ferro CJ. Hypertension and cardiomyopathy associated with chronic kidney disease: epidemiology, pathogenesis and treatment considerations. J Hum Hypertens. 2022 Sep 22. doi: 10.1038/s41371-022-00751-4. [Epub ahead of print] Review. PubMed PMID: 36138105.

Law JP, Price AM, Pickup L, Radhakrishnan A, Weston C, Jones AM, McGettrick HM, Chua W, Steeds RP, Fabritz L, Kirchhof P, Pavlovic D, Townend JN, Ferro CJ. The Clinical Potential of Targeting Fibroblast Growth Factor-23 and αKlotho in the Treatment of Uraemic Cardiomyopathy. J Am Heart Assoc. 2020 Mar 26;9(7):e016041. doi: 10.1161/JAHA.120.016041. Epub 2020 Mar 26. Review. PubMed PMID: 32212912

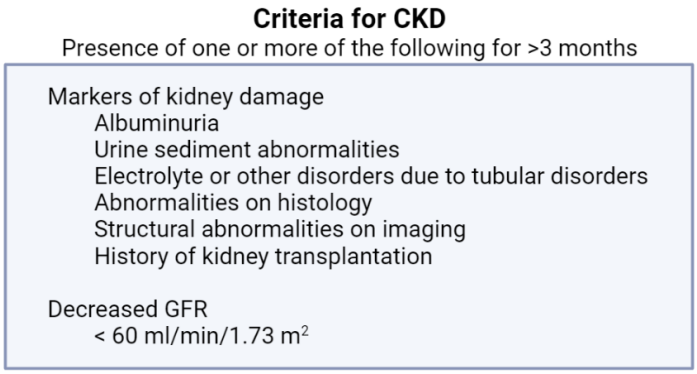
The first drafts of these manuscripts were written by me. I was responsible for all edits and revisions. All figures are original and created by me.

1.2. CHRONIC KIDNEY DISEASE

1.2.1. Definition and classification of CKD

Chronic kidney disease (CKD) encompasses a heterogenous group of disorders which adversely affect kidney structure or function. Its chronicity is defined by the presence of any markers of kidney damage or reduced glomerular filtration rate (GFR) for greater than three months (**Figure 1-1**). Prior to the 2002 Clinical Practice Guidelines for CKD published by the National Kidney Foundation Kidney Disease Outcomes Quality Initiative (NKF-KDOQI) [3], there was no universally accepted definition of CKD. With the NKF-KDOQI 2002 classification system (**Figure 1-2**) came a uniform system in which CKD could be defined and staged based on severity. Furthermore, this gave those caring for patients with or at risk of kidney disease better tools for early detection and intervention to delay or prevent the need for renal replacement therapy (RRT). Under the direction of Kidney Disease: Improving Global Outcomes (KDIGO), a meta-analysis consisting of 1,555,332 patients confirmed that both reducing glomerular filtration rate and increasing albuminuria were robustly associated with important clinical outcomes, including all-cause mortality, cardiovascular mortality, kidney failure with replacement therapy (KFRT; formerly known as end stage kidney disease), acute kidney injury and CKD progression [4]. Based on these findings, a revised CKD classification system was born and adopted in the most recent 2012 KDIGO CKD guidelines, adding albuminuria classification to every CKD stage, subdivision of stage 3 CKD into stages 3a and 3b, and a heatmap showing the implications to health and CKD (**Figure 1-2**) [5].

Figure 1-1. Definition of CKD



CKD, chronic kidney disease; GFR, glomerular filtration rate

Figure 1-2. Evolution of CKD classification

From the first NKF-KDOQI staging released in 2002, to the current 2012 KDIGO staging system, which includes not only albuminuria categories, but also a prognosis tool for estimating risk of CKD progression and mortality. Green indicates low risk in the absence of other markers of kidney damage; yellow implies moderately increased risk; orange is high risk; and red, very high risk. Figure has been adapted from National Kidney Foundation (2002) and KDIGO CKD Working Group (2013) [3,5].

NKF-KDOQI 2002 CKD Classification

Stage	Description	GFR (mL/min/1.73 m2)
1	Kidney damage with normal or increased GFR	≥ 90
2	Kidney damage with mildly reduced GFR	60-89
3	Moderately reduced GFR	30-59
4	Severely reduced GFR	15-29
5	Kidney failure	<15 (or on dialysis)

KDIGO 2012 CKD Classification
prognosis by GFR and albuminuria

GFR categories,descriptions and range (ml/min/1.73 m^2)				Albuminuria categories, descriptions and range (mg/g)		
				A1	A2	A3
				Normal to mildly increased	Moderately increased	Severely increased
				<30	30-300	>300
	G1	Normal or high	≥90			
	G2	Mild	60-89			
	G3a	Mild to moderate	45-59			
	G3b	Moderate to severe	30-44			
	G4	Severe	15-29			
	G5	Kidney failure	<15			

1.2.2. Determination of GFR

Glomerular filtration rate is the sum of filtration rates in all the nephrons in the kidney, and is widely accepted as the best measure of kidney function [6]. Estimation of GFR can be done through evaluating the serum concentration of an endogenous or exogenous marker substance which is renally excreted. Commonly, serum creatinine is measured by a standardised assay and used in combination with a GFR estimating equation such as the Modification of Diet in Renal Disease (MDRD) equation [7] – released in 1999 and revised in 2006 [8]. This has largely been replaced by the newer Chronic Kidney Disease Epidemiology Collaboration (CKD-EPI) equation [9]. CKD-EPI equation has been shown to give a more accurate estimation of GFR (or estimated GFR; eGFR); patients were less likely to be over-diagnosed with CKD; more likely to be correctly classified into the CKD stages, which led to a better predictor of risk of mortality and KFRT [10]. KDIGO now recommend the CKD-EPI creatinine equation to derive eGFR from serum creatinine [5]. In conditions where serum creatinine is in a non-steady state; factors affecting creatinine generation, secretion and elimination are present; or there is interference with the creatinine assay, an alternative such as serum cystatin C used in combination with a GFR estimating equation, or a clearance measurement may be necessary [5].

1.3. URAEMIC CARDIOMYOPATHY

1.3.1. Clinical phenotype of cardiomyopathy in CKD

The concept of uraemic cardiomyopathy, or CKD-associated cardiomyopathy, first appeared in the 1980s following reports of common abnormalities in cardiac

structure and function in patients with CKD and KFRT [11,12]. The key features described were:

- increased left ventricular (LV) mass and left ventricular hypertrophy (LVH)
- diastolic and systolic LV dysfunction
- profound myocardial fibrosis on histology [13-27]

Whilst these features have been predominantly identified in patients with KFRT, who are undoubtedly uraemic, those with mild to moderately reduced eGFR already exhibit structural and functional changes consistent with CKD-associated cardiomyopathy [18]. This is consistent with observational studies reporting a 20% higher risk of death and cardiovascular events in patients with eGFR between 45 to 59 ml/min/1.73 m^2 compared to those with eGFR greater than 60 ml/min/1.73 m^2 [28].

1.3.1.1. Increased left ventricular mass and hypertrophy

The connection between CKD and LVH was first described by several 19th century physicians. Pioneering British physician Richard Bright (1789-1858) depicted with meticulous detail first observations of LVH present on autopsies of patients with albuminuria [29]. Years later, his successor Sir Samuel Wilks (1824-1911) described pathological changes in the heart and arteries accompanying Bright's disease [30]. Further publications in the 1850s by Ludwig Traube (1818-56) and William Kirkes (1822-64) introduced the concept of arteriosclerosis and high intra-arterial pressure as a driver of LVH in renal disease, laying the foundation for our understanding of CKD-associated cardiomyopathy [31,32].

Recent imaging studies confirm that increased LV mass and LVH are common manifestations of CKD-associated cardiomyopathy. LVH is found in 48-84% of patients with pre-dialysis CKD [33-35], and in up to 90% of patients with KFRT receiving haemodialysis [21,36,37]. Similarly, LV mass is a continuous variable with a graded association with adverse cardiovascular outcomes and mortality [38-43]. In an analysis of 1,249 patients with predialysis CKD, LVH was associated with a mortality risk of 25 deaths per 1000 person-years [39]. In patients who have LVH at dialysis initiation, the risk of mortality was 1.75-fold greater than those without LVH at 6 years follow-up [37]. Conversely, LVH regression may improve outcomes in patients with KFRT [36].

LVH is associated with an increased risk of arrhythmia, which may explain, in part, the increased incidence of cardiovascular death in CKD [44]. A meta-analysis of 10 studies (27,141 patients) found that patients had 3.4-fold and 2.8-fold greater odds of developing sustained supraventricular tachycardia and ventricular arrhythmias, respectively, in the presence of LVH [45]. Other studies reported a 20% increase in the risk of atrial fibrillation (AF) for every standard deviation increase in LV mass [41]. The presence of LVH in hypertensive patients was a predictor for progression from paroxysmal to permanent AF [42], whilst blood pressure reductions of 7.3/1.8 mmHg resulted in regression of LV mass index with a corresponding 7-fold decline in the prevalence of paroxysmal AF after a mean follow-up of 24 months [46].

Increased LV mass and LVH are common manifestations of CKD-associated cardiomyopathy. Forty per cent of patients with an eGFR below 30 ml/min per 1.73 m2 have LVH on echocardiography [34], increasing to around 80% in KFRT

[21,37]. In patients with CKD/KFRT, LVH is strongly associated with death; diastolic and systolic heart failure; and cardiac arrhythmias [21,37]. However, LV mass is a continuous variable, with a graded relationship with adverse cardiovascular outcomes [38,40,47-49]. It is also important to emphasise that cardiac structural changes occur early in the course of CKD, with a linear association between worsening renal function and a higher prevalence of LVH [29,30]. While elevated blood pressure is an important determinant of LV mass [50], evidence from both animal and human studies supports the presence of mechanisms that are independent of pressure overload and hypertension in driving cardiac hypertrophy in CKD/KFRT [51-55].

1.3.1.2. Diastolic and systolic left ventricular dysfunction

Diastolic dysfunction characterised by slow LV relaxation and increased LV stiffness [56]. It is highly prevalent in patients with CKD [57] with studies reporting an incidence of 71% in CKD stages 2-4 [33] and up to 85-90% in KFRT [58-60]. Excess myocardial deposition of collagen affects cardiac muscle viscoelasticity, leading to increased ventricular stiffness, impaired myocardial relaxation and diastolic recoil [61]. Diastolic dysfunction is strongly association with increased LV mass and LVH [62], as well as myocardial fibrosis [24,63], and is associated with increased mortality [59,63]. Indeed, the American Society of Echocardiography and the European Association of Cardiovascular Imaging considers LVH as an indicator of diastolic dysfunction [64]. Furthermore, the presence of diastolic dysfunction is considered to be a major cause for the frequent presentation of HD patients with pulmonary oedema or intradialytic hypotension with only minor changes in fluid status [62,63]. Overt LV systolic dysfunction, as manifest by a reduced left ventricular

ejection fraction [65], is relatively uncommon in pre-dialysis CKD, with a reported prevalence of 8% and no association with eGFR [19,33]. However, several studies have shown changes in LV deformation in early stages of CKD indicating the presence of sub-normal LV systolic function [66-68]. In KFRT, LV systolic dysfunction is very common with a reported prevalence 10-30 times greater than in the general population [69-72].

The presence of LVH has also been associated with the risk of development of systolic dysfunction in hypertensive subjects [73-75]. The 2013 American College of Cardiology Foundation/American Heart Association Guideline for the Management of Heart Failure recognised hypertension and LVH as stage A and B heart failure. The guideline emphasised the progressive nature of heart failure, and the importance of long-term treatment of elevated blood pressure to prevent symptomatic heart failure [76].

1.3.1.3. Myocardial fibrosis

It has been suggested that myocardial fibrosis may be the unifying pathophysiological process underlying CKD-associated cardiomyopathy [77]. In the 1990s, a post-mortem study found that myocardial fibrosis was present in 91% of CKD/KFRT patients without significant flow-limiting coronary lesions. The severity of fibrosis was related to the length of time on dialysis, but independent of hypertension, blood pressure, diabetes or anaemia [13]. However, given a plethora of drivers of cardiac fibrosis, as demonstrated by numerous preclinical and clinical studies, we cannot discount the contributing roles of these diseases on the activation of cardiac fibroblasts [78]. Over a decade later, Aoki et al. performed endocardial biopsies in 40 KFRT patients with reduced LV ejection

fraction without coronary artery disease [14]. The predominant pathologic findings were extensive fibrosis and cardiomyocyte hypertrophy similar to that seen in the dilated phase of hypertrophic cardiomyopathy, a condition associated with extremely high morbidity and mortality [79,80].

A post-mortem study of LV tissue from patients with KFRT found reduced capillary density, increased cardiomyocyte cross-sectional area and expansion of interstitial matrix. The apparent myocyte-capillary mismatch brought about by the reduction in capillary supply within a hypertrophied myocardium increases the oxygen diffusion distance, thereby exposing the heart to the risk of ischaemic injury and subsequent cardiac dysfunction [81]. Recent advances in imaging technology have enabled the indirect assessment of coronary microvascular dysfunction (CMD). Coronary flow reserve (CFR) is the most widely used surrogate marker, and has been successfully utilised to indirectly measure CMD in conditions such as hypertrophic cardiomyopathy and heart failure with preserved ejection fraction, both of which are characterised by LVH and myocardial fibrosis, similar to CKD-associated cardiomyopathy [82,83]. Although data are limited, imaging studies utilising positron emission tomography, angiography and echocardiography have reported a prevalence of 24-90% in CKD patients with a graded relationship with eGFR [84]. In a retrospective study of CKD patients, which included those on dialysis, reduced CFR below 1.5 was associated with 2.1-fold increased risk of cardiovascular mortality independent of risk factors and LV function [85]. The mortality risk remained elevated in a later analysis of the dialysis-dependent cohort [86].

Studying myocardial fibrosis in CKD/KFRT has been challenging given that myocardial biopsies are ethically difficult to justify [87,88]. Contrast-enhanced cardiac magnetic resonance (CMR) imaging has been used for the assessment of myocardial fibrosis in conditions such as myocardial infarction [89], dilated [90] and hypertrophic cardiomyopathies [91]. Patients with KFRT demonstrate midwall patterns of late gadolinium enhancement consistent with replacement myocardial fibrosis not associated with large vessel coronary artery disease [19]. Non-contrast myocardial native T1 relaxation time, or T1 mapping, has emerged as a viable alternative for the assessment of myocardial fibrosis in CKD/KFRT [23]. In cardiac tissues, T1 relaxation time outside regions of scarring has been shown to correlate with histologically measured interstitial fibrosis severity in a number of disease states [92]. In patients with KFRT, native T1 times are higher than age- and sex-matched controls, and correlate with increased LV mass [16,17]. In parallel with the changes to LV mass and function, native T1 times have been shown to be increased in early CKD[15] and increase with worsening CKD stages [93]**.** The contribution of myocardial water content to the increased T1 times remains contentious and to date, T1 times have not been validated with diffuse interstitial fibrosis in CKD-associated cardiomyopathy.

1.3.2. Drivers of uraemic cardiomyopathy in CKD

The pathogenesis of uraemic cardiomyopathy is likely to be multifactorial but can broadly be divided into three categories:

- increased afterload [94]
- increased preload [95]

- intrinsic factors not directly related to afterload or preload [96]

Although these categories are considered separately, it is important to note that there is considerable overlap between them [23,24,84,97,98]. Factors within these categories may indeed interact and exert their effects synergistically.

1.3.2.1. Increased afterload

Afterload is defined as the force opposing myocardial fibre shortening during systole and is dependent arterial blood pressure and vascular tone [99]. Raised intra-arterial or aortic pressure induces cardiac hypertrophy through chronic haemodynamic stress on the myocardium. In vitro experimental models of cardiomyocyte and non-myocyte stretch resulted in cell hypertrophy and hyperplasia, induction of protein synthesis and increased expression of prohypertrophic proto-oncogenes such as *fos*, *jun*, *myc*, *Ha-ras*, and genes encoding atrial natriuretic factor and β-myosin heavy chain [100-102]. This was recapitulated in murine and porcine studies of hypertension and volume overload where transcription of prohypertrophic genes, and development of LVH were observed [103-107].

Arterial stiffening occurs from the early stages of CKD and increases with the progression to KFRT [108-110]. The extent of arterial stiffness can be reliably estimated by non-invasive measurement of carotid-femoral pulse wave velocity (PWV), which can confer prognostic value in CKD patients independent of traditional risk factors [111,112].

Arterial stiffness is both a cause and result of systolic hypertension, although extricating the bidirectional relationship can be challenging [113,114]. Studies have

demonstrated increased arterial stiffness as a consequence of increased distending vascular wall stress and remodelling from hypertension itself, so called pressure-dependent increases in PWV [115-117]. Other studies show that increased arterial stiffness, more specifically higher PWV, predicts future development of hypertension [118-121], possibly as a result of inherent pressure-independent vasculopathy. In patients with KFRT, PWV is independently associated with nonfatal stroke and myocardial infarction [110] and with cardiovascular and all-cause mortality [110,122,123]. Of those patients who died, it was found that the persistence of increased PWV despite a reduction in blood pressure by haemodialytic and pharmacological strategies (angiotensin converting enzyme inhibitor; ACEi) was a significant independent risk factor. This is in contrast to the surviving patients where a similar fall in blood pressure was mirrored by a reduction in PWV [123].

In addition to elevated blood pressure, there are several other postulated pathophysiological drivers of increased arterial stiffness in CKD such as activation of the renin-angiotensin-aldosterone system (RAAS), build-up of uraemic toxins, disordered bone and mineral metabolism (CKD-MBD), accumulation of advanced glycation end-products, chronic inflammation and oxidative stress which adversely affect endothelial function and calcific remodelling of the vessel wall [113,124]. The reduced vessel compliance is manifested by hypertension and wide pulse pressure, and disruptions to end-organ perfusion, resulting in myocardial fibrosis, increased LV mass/LVH and diastolic dysfunction bearing the hallmarks of CKD-associated cardiomyopathy [125].

1.3.2.2. Increased preload

Cardiac preload is the degree of ventricular myocyte stretch at the end of diastole [99]. Intravascular volume expansion/hypervolaemia, secondary to salt and water loading, is a frequent occurrence in CKD/KRFT and a determinant of LV mass and mortality [126,127]. Indeed, volume expansion is a major contributor to the hypertension observed in patients with CKD/KRFT [127,128]. Reduced GFR, activation of the RAAS as well as superimposed cardiovascular disease all contribute to sodium and water retention in these patients [129-131].

As haemoglobin concentrations fall, complex haemodynamic compensatory mechanisms are activated to increase cardiac output and blood flow to compensate for tissue hypoxia[132]. These include a reduction in afterload secondary to reduced systemic vascular resistance, an increase in preload secondary to increased venous return, and increased LV function as a consequence of increased sympathetic tone [133,134]. Treatment of anaemia in CKD with erythropoietin stimulating agents (ESAs) reduces stroke volume and cardiac output as a consequence of both reduced venous return and increased peripheral resistance [135-138]. These functional changes are paralleled by structural changes in the LV, with partial reduction of LVH [136,137]. It should also be noted that treatment with ESAs increases blood pressure by direct vasomotor effects [139-141].

The use of arteriovenous fistulas for haemodialysis is preferrable to vascular catheters due to improved dialysis quality and reduced infection rates [142-144]. However, the creation of a shunt between a high pressure arterial vasculature and a low resistance venous system increases cardiac output through the shunting itself, activation of the sympathetic nervous system, neurohormonal

changes, and increased venous return [143]. Chronically increased preload and cardiac output lead to LVH and right ventricular remodelling, which in turn is associated with an 3.9-fold increased risk of death [145]. Several studies of fistulas being tied off after successful kidney transplantation show some evidence of LVH regression [146,147]. However, although creation of an arteriovenous fistula decreases systemic blood pressure, ligation increases systolic blood pressure by an average of 5 mmHg [148]. The decision to proceed with fistula ligation should therefore balance, on an individualised basis, the benefits of cardiac remodelling regression against the potential adverse effect on blood pressure control.

1.3.2.3. Intrinsic factors

In addition to the haemodynamic factors already discussed, several other factors that become dysregulated in patients with CKD are involved in the pathogenesis of CKD-associated cardiomyopathy. These include activation of RAAS, sympathetic nervous system overactivity, increased transforming growth factor-beta (TGFß) signalling, insulin resistance, uraemic toxins (e.g. indoxyl sulfate, p-cresyl sulfate), increase in cardiotonic steroids, oxidative stress and factors associated with CKD-MBD namely hyperparathyroidism, vitamin D deficiency, increased circulating fibroblast growth factor-23 (FGF23), decreased αKlotho expression and hyperphosphataemia [2,24,149,150].

1.4. FIBROBLAST GROWTH FACTOR-23 AND αKLOTHO

1.4.1. Biology of FGF23 and αKlotho

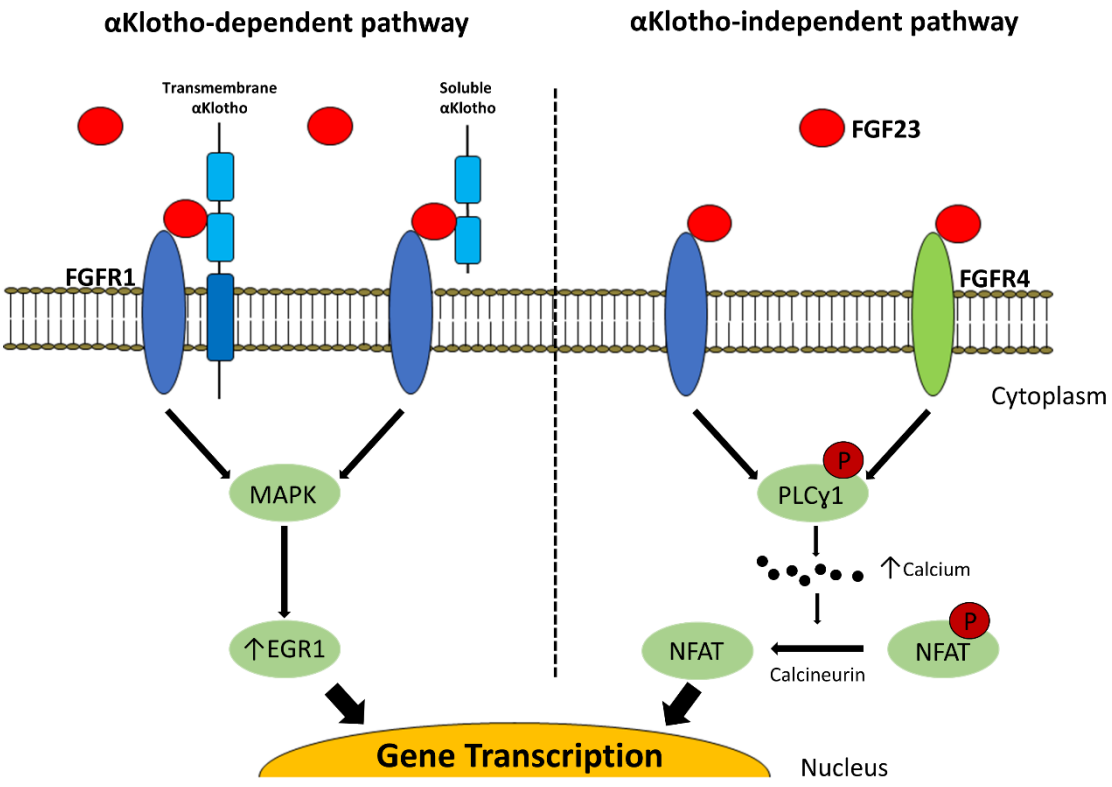
The hormone fibroblast growth factor-23 (FGF23), first discovered in 2000, is a circulating growth factor secreted by osteocytes whose main physiological role is to increase urinary phosphate excretion [151,152]. The four mammalian FGF receptors (FGFR1-4) are membrane-bound receptor tyrosine kinases [153,154]. FGFR1 is suggested to be the primary FGF23 receptor in target organs – the kidneys and parathyroid glands [155-158]. Crystallography studies clearly demonstrate that the presence of αKlotho is required for the efficient binding of FGF23 to FGFR1 [159]. αKlotho is a cell-surface protein, mainly expressed in the kidneys and parathyroid glands [160-162]. In addition to the membrane-associated full-length protein, the ectodomain of αKlotho can exist in a soluble form [163-166]. In the presence of membrane-bound αKlotho or soluble αKlotho, FGF23 can activate Fibroblast Growth Factor Receptor Substrate-2(FRS2α)/Ras/Mitogen Activated Protein Kinase(MAPK) signalling (**Figure 1-3**) [159,167,168]. Soluble αKlotho, therefore, may act as a circulating FGF23 co-receptor in cells that do not express αKlotho. Such a mechanism has been reported in osteoblasts [169]. However, its role in the heart is yet to be fully characterised as neither cardiomyocytes nor cardiac fibroblasts express αKlotho [152]. It is possible that FGF23 might act on these cells with circulating αKlotho as a cofactor. Treatment of cardiac myofibroblasts with full-length αKlotho resulted in upregulated proliferation and ERK phosphorylation, which was suppressed by FGFR1 antagonism [170]. This suggests the presence of FGFR1 in cardiac myofibroblasts

for which soluble Klotho acts as a circulating co-receptor, although the authors do not comment on endogenous FGFR1/FGF23 expression.

FGF23 can also exert cellular effects via αKlotho-independent mechanisms [171]. FGF23 has been shown to stimulate Phospholipase Cγ (PLCγ) / calcineurin / Nuclear Factor of Activated T-cells (NFAT) via FGFR4 in cells that lack αKlotho (**Figure 1-3**) [171-174]. Such increases in PLCγ / calcineurin / NFAT signalling appear to be important in pathological, as opposed to physiological, cardiac hypertrophy [175,176]. Clearly further mechanistic studies are warranted to delineate mechanisms that can be targeted therapeutically in patients with elevated FGF23 levels.

Figure 1-3 . Fibroblast growth factor 23 (FGF23) signal transduction and signaling pathways

Figure adapted from Law et al. (2020) [2]



1.4.2. FGF23 and αKlotho in CKD

One of the first clinically detectable signs of CKD is an elevation in serum FGF23, probably in response to increased extracellular phosphate although the details of the stimulus and its detection are still unclear, with levels rising steeply as kidney function worsens [151,177]. Indeed, elevations are observed as early as eGFR 75 ml/min/1.73 m^2, long before increased concentrations in PTH or phosphate are observed [177]. Circulating FGF23 levels are two to five-fold above the normal range in early/intermediate CKD, but can reach levels of 1000-fold above normal in KFRT [177-179]. Increased FGF23 levels are also found in heart failure [180-185] and AF [186-190], and are associated with all-cause and cardiovascular mortality in patients with and without CKD [184,185,191-196]. Ongoing research therefore explores FGF23 as both a potential biomarker [197] and a causative factor for cardiac mechanoelectrical dysfunction. However, effective quantification of circulating FGF23 is not currently standardised. Several FGF23 assay kits utilise differing detection techniques, epitope binding regions, analytical ranges and measurement units, making direct comparisons challenging [198].

The kidney is the principle source of circulating soluble αKlotho [166,199]. Its levels are downregulated in the presence of vitamin D deficiency [200,201], albuminuria [202], inflammation [203], RAAS overactivity [204,205], FGF23 excess [206], and with the progression of CKD [207]. αKlotho levels start to decline in CKD stage 2 and precede the elevation of FGF23, PTH and serum phosphate [208].

In its secreted, circulating form, soluble αKlotho exerts a broad array of biological functions as evidenced in studies of αKlotho-deficient mice which manifested an ageing phenotype of phosphate imbalance, osteoporosis/osteopenia [209], vascular

calcification, growth retardation, emphysema [210] and premature death [160], cardiac hypertrophy and fibrosis [211-213]. In addition, αKlotho has a role in blood pressure homeostasis. In a study of 2,774 subjects, higher αKlotho was associated with a lower risk of incident hypertension [214]. Low levels of circulating αKlotho are associated with increased cardiovascular events and mortality in patients with CKD/KFRT [215-218]. Preclinical studies have shed light on the potential underlying mechanisms, including αKlotho inhibition of inflammation-associated renal sodium retention [219,220] and endothelial dysfunction through reduced oxidative stress and increased nitric oxide availability[221-223] in murine and in vitro studies.

It is, therefore, conceivable that some of the adverse physiological effects that have been attributed to increased FGF23 may be either due to, or compounded by, lower αKlotho. These mechanistic complexities require further investigation and need to be considered when developing FGF23/αKlotho-directed therapies.

1.4.3. Cardiovascular effects of FGF23 and αKlotho

1.4.3.1. Left ventricular mass and hypertrophy

The heart has been shown to respond to FGF23, increasing LV mass independently of blood pressure, promoting cardiac fibrosis and reducing LV systolic function in animal models [171,172,174,224,225]. Elevations of cardiac FGFR4 and enhanced PLCγ/calcineurin/NFAT signalling have been observed in both animal models of CKD and in patients with CKD/KFRT [172,226-228]. Several studies have shown that repetitive administration of FGF23 in wild-type mice, either intravenous or intraperitoneal, induced cardiac hypertrophy within 5 days [171,224,225]. The signalling actions of FGF23 on the heart are still not fully

characterised. However, several independent experimental approaches demonstrate the involvement of the αKlotho-independent FGFR4-PLCγ/calcineurin/NFAT signalling pathway in cardiomyocytes [171,172,174]. Although often considered in isolation, there are significant overlaps and crosstalk between RAAS and FGF23 pathways. For example, FGF23 activates RAAS through suppression of ACE2 [229], which downregulates vasodilatory angiotensin-(1-7), and upregulates plasma/cardiac Angiotensin II and aldosterone [230-232]. In turn, aldosterone stimulates FGF23 transcription in osteoblasts in vitro, an effect reversed by mineralocorticoid receptor blockade [233]. More recently, Böckmann et al. showed that FGF23 stimulated expression of RAAS genes and hypertrophic growth in cultured neonatal rat ventricular myocytes [234]. Independent studies demonstrate that αKlotho may be cardioprotective and that subnormal levels as found in CKD may be required for FGF23 to induce LVH [211,235-237].

Whilst many of the studies indicate that elevation of FGF23 and reduction in αKlotho are involved in the development of LVH, recent studies by Leifheit-Nestler and Slavic have not recapitulated these findings [238,239]. Chronic FGF23 overexpression (via myocardial gene transfer), or genetic ablation of FGF23 or Klotho on the background of transverse aortic constriction did not affect cardiac function or morphology [238,239].

1.4.3.2. Myocardial fibrosis

Fibroblasts produce the extracellular matrix in the heart and act as regulators of the cardiac interstitium [240,241]. In the injured myocardium, inflammation and mechanical stress promote activation of fibroblasts to myofibroblasts, leading to

maladaptive deposition of extensively cross-linked extracellular matrix, which drives increased stiffness and impaired mechanoelectrical coupling of cardiomyocytes. This loss of cardiomyocyte coupling not only leads to attenuated cardiac function, but also provides a substrate for arrhythmias [242-245]. Whilst recent studies have shown that FGF23 can activate cardiac fibroblasts, neither the underlying mechanism [246,247] nor its role in the development of cardiac fibrosis are fully defined [246,248]. As cardiac fibroblasts do not express αKlotho [171,199,227,228], the alternative pathway of αKlotho-independent FGF23 signalling through FGFR4-PLCγ/calcineurin/NFAT is likely to play a role. Further evidence of this was presented in a small study which found increased FGF23 and FGFR4 expression in atrial tissues of patients with AF compared to those in sinus rhythm. In addition, they exhibited greater collagen fraction, collagen 1 and α-Smooth Muslce Actin (αSMA) expression by immunohistochemistry [189].

1.4.3.3. Cardiac arrhythmias

Patients with CKD/KFRT are at increased risk of a wide spectrum of cardiac arrhythmias, including supraventricular tachycardias, particularly AF, and potentially lethal ventricular arrhythmias [249-251]. All three components of CKD-associated cardiomyopathy (increased LV mass/LVH; diastolic and systolic dysfunction; and especially myocardial fibrosis) are associated with arrhythmogenesis [250,252]. While emerging evidence from implantable loop recorder studies is beginning to implicate bradyarrhythmias as the major cause of SCD in KFRT, rather than the previously assumed tachyarrhythmias, the precise causes of SCD in KFRT are the subject of investigation [251]. αKlotho has been found in sinoatrial node pacemaker cells in mice [253] and αKlotho-deficient

animals exhibit sinoatrial node dysfunction, and higher rates of bradyarrhythmias and SCD [253].

FGF23 distrupts intracellular calcium cycling within the cardiomyocyte, which is an important risk factor for arrhythmogenesis [254-256]. Administration of FGF23 to rat ventricular cardiomyocytes caused calmodulin-dependent protein kinase II-dependent abberant intracellular calcium resulting in *in vitro* and *in vivo* arrhythmogenicity [257]. Administration of recombinant αKlotho or a pan-FGFR blocker prevented contractile dysfunction and reduced pro-arrhythmogenic activity [257].

Large observational studies in patients with CKD or AF, and in the general population have found an association between elevated FGF23 and increased risk of developing AF [186,190,194,258-262]. High FGF23 and low αKlotho levels are associated with periods of AF in patients with paroxysmal or persistent AF [188]. Increased expression of FGF23, FGFR4 mRNA and FGFR4 protein in the right atrial appendages of patients with AF has been reported and positively correlate with atrial collagen fraction. Collectively these data/studies suggest that FGF23/FGFR4 may play a role in promoting AF through atrial fibrosis [263].

1.5. TREATMENT OF URAEMIC CARDIOMYOPATHY

1.5.1. Hypertension

Hypertension is a significant global problem and remains one of the most important preventable causes of mortality worldwide [264,265], with the prevalence expected to rise to 1.56 billion by 2025 [264]. Affecting 67-92% of patients with CKD,

hypertension is also the most common comorbidity with increasing prevalence and severity as kidney function progresses [266]. Its pathogenesis and that of CKD are tightly intertwined, with hypertension being both a complication of and driver of kidney disease progression [267-269].

1.5.1.1. Intensive blood pressure lowering

Prior to publication of the SPRINT trial results [270], most societies and guidelines recommend lowering blood pressure to below 140/90 mmHg [271-275] with some suggesting higher thresholds for the elderly [271,272,275] and lower thresholds for those at higher high risk including patients with diabetic mellitus and patients with CKD [271,272,275]. The SPRINT investigators reported a 25% lower risk of major cardiovascular events such as myocardial infarction, heart failure and stroke and 27% lower risk of all-cause mortality when treating to a target systolic blood pressure of less than 120 mmHg compared to the standard target of 140 mmHg. Intensive treatment of hypertension in those with CKD, which formed 28% of the SPRINT cohort, was associated with improved cardiovascular outcomes and all-cause mortality, with no adverse effects on kidney function or increased risk of dialysis [270]. The recently published Kidney Disease Improving Global Outcomes (KDIGO) 2021 guideline on the management of blood pressure in CKD also recommends an intensive systolic blood pressure target of 120 mmHg or less in patients with CKD (excluding those with a functioning kidney transplant) [276].

1.5.1.2. Antihypertensives, cardiac structure and function

In the general population, regression of LVH is associated with a significant improvement in cardiovascular events [277]. Several landmark trials have confirmed

that LV regression in response to treatment with antihypertensive medication is associated with significant reduction in cardiovascular events [278-281]. All classes of anti-hypertensive medications have been shown to regress LVH [282-285]. Meta-analyses have shown that ACE-inhibitors, angiotensin receptor blockers (ARBs) and calcium channel blockers are more effective than beta-blockers at regressing LVH [286,287].

Factors associated with persistent LVH and lack of regression of LVH with antihypertensive treatment include older age, higher body mass index, sub-optimal blood pressure control, duration of hypertension and crucially, the presence of CKD [282,288,289]. This, together with the fewer and much smaller studies available make the literature in patients with CKD/KRFT less clear. Most, but not all [290,291] studies of ACEi/ARB compared with placebo or standard treatment in both patients with CKD [292] or on dialysis [53,293-295] have shown no significant reduction in LVM. The same is true for studies comparing ACEi/ARB with a CCB [296-298] or beta-blocker[299,300] which have shown no difference between agents. Several novel therapies with potential benefit to patients with CKD-associated cardiomyopathy have recently been trialled.

A meta-analysis of sacubitril/valsartan, the first in a new class of angiotensin receptor neprilysin inhibitors (ARNI), in patients with CKD and heart failure with reduced ejection fraction (HFrEF) versus a RAAS-blocker found that ARNIs significantly reduced blood pressure and N-terminal pro-brain natriuretic peptide (NT-proBNP), and was mildly renoprotective [301]. As previously discussed, patients with CKD can present with diastolic dysfunction only, or heart failure with preserved ejection fraction (HFpEF). The efficacy of ARNIs in HFpEF is less

convincing. PARAGON-HF reported no significant change in heart failure hospitalisations and cardiovascular death when compared to valsartan alone [302]. In the PARALLAX trial, ARNI did not increase functional- or symptom-based scores despite a 16% reduction in NT-proBNP versus RAAS inhibition/placebo [303].

Sodium-glucose co-transporter-2 (SGLT2) inhibitors are a recent class of oral antidiabetic agents. They decrease sodium-reabsorption, exhibiting a mild natriuretic and diuretic effect [304,305]. A recent meta-analysis of large RCTs clearly demonstrated a 23% reduction in CV morbidity and mortality, especially heart failure hospitalizations in patients with diabetes mellitus [306]. Similar results are emerging in patients with CKD and with heart failure without diabetes [307,308]. It should be noted that SGLT2-inhibitors also significantly lower systolic and diastolic blood pressure by 3-5/1-2 mmHg [305], through their diuretic and natriuretic actions, as well as reported reductions in sympathetic activity, arterial stiffness and vascular resistance [304,305]. A significant correlation between blood pressure reduction and regression of LVH with SGLT2-inhibitor use has been reported [309]. SGLT2-inhibitors might therefore be useful agents to improve CKD-associated cardiomyopathy acting via both blood pressure reduction and blood pressure independent mechanisms.

Mineralocorticoid receptor antagonists (MRA) have consistently shown beneficial effects on left ventricular dilation, cardiac function, fibrosis or collagen content in preclinical studies [310-312] and also regress LVH in clinical trials [284]. MRA have consistently been shown to improve outcomes in patients with HFrEF–and potentially in patients with HFpEF [313]. Whether the lowering of LV mass in CKD

patients is independent on the blood pressure lowering effect of MRAs is unclear [314,315]. Recently two large placebo-controlled studies with the non-steroidal MRA finerenone have shown significant reductions in cardiovascular events and mortality in patients with diabetic nephropathy with little effect on blood pressure [316-318]. Consistent with the effect of blood pressure on stroke risk [319,320] the incidence of stroke did not vary between groups [313]. The lower incidence of hyperkalaemia versus steroidal MRAs (spironolactone and eplerenone) makes finerenone an attractive option for the treatment of CKD-associated cardiomyopathy [313].

1.5.2. Renal replacement therapy

1.5.2.1. Intensive dialysis

Studies have shown that longer, frequent 'intensive' dialysis regimens are associated with reductions in LV mass, lower prevalence of LVH and reduced hospitalisations [321-324]. However, it is not clear if the reductions in LV mass are a direct consequence of the dialysis treatment - clearance of uraemic toxins, better phosphate and haemoglobin control; or improved blood pressure control [325-327]. An intriguing, but small, study of 54 incident haemodialysis patients found that lowering dialysate temperature by an average of 1 ˚C significantly reduced LV mass (treatment difference between groups 15.6, 95%CI 1.9-29.4 g) measured by CMR over a 12 month period with no differences in blood pressure between groups [328]. However, 10 of the 54 patients had their 12-month CMR results imputed. This study finding requires confirmation in larger trials.

The previously discussed effects of intensive dialysis on reduction of hypertension and improvement in LV mass are encouraging, however it is still

unclear as to whether this leads to better patient survival. A recent meta-analysis encompassing 70,506 patients found that intensive dialysis was associated with reduced mortality when compared to conventional dialysis, but the overall quality of the evidence was low [329]. Whilst intensive dialysis has clear health and quality of life benefits, it needs to be considered in conjunction with the potential risks of increased patient and caregiver burden, infection, loss of residual kidney function and vascular access complications [330].

1.5.2.2. Renal transplantation

The gold-standard for the treatment of KFRT is kidney transplantation [331]. The associated improvement in GFR reduces cardiovascular risk below that of those on waiting lists [332]. However, cardiovascular risk still remains higher than healthy individuals of the same age and sex with transplant recipients displaying a three-fold increased risk [333]. The restoration of kidney function associated with kidney transplantation improves many factors thought to cause CKD-associated cardiomyopathy. As a result it is generally assumed that kidney transplantation reduces LV mass, and improves diastolic and systolic function, and potentially reverses myocardial fibrosis [334,335]. Indeed, review articles continue to state that CKD-associated cardiomyopathy is reversed by kidney transplantation. However, these articles frequently either do not cite any references [24], cite small, uncontrolled studies using either echocardiography [336] or radionucleotide ventriculography-gated blood pool scans [334,337], or refer to other review articles [338].

A recent systematic review and meta-analysis has indeed confirmed that many echocardiographic studies reported significant reductions in LV mass after kidney

transplantation [339]. However, this study highlighted key problems in the available literature. Few studies were blinded or had a control group thus were prone to bias; meta-analysis of the four studies containing a control group did not find any association between transplantation and LV mass. Echocardiography is unreliable for LV mass determination in dialysis patients [340]; few studies used CMR which is more reproducible in KFRT patients [23]. Indeed, none of the three CMR studies included in the review found a significant change in LV mass.

Intriguingly, a small study in 44 kidney transplant recipients found a significant reduction in native T1 time at 6 months after transplantation with no reduction in LV mass [341]. A smaller study found no difference in global T1 times 6 weeks after transplantation suggesting changes may continue to progress over time [342]. Larger, controlled studies utilising CMR are required to further investigate this fundamental question.

1.5.3. Management of CKD-MBD

CKD–mineral and bone disorder (CKD–MBD) encompasses the progressive deterioration in the homeostasis of calcium, phosphate due to disruption in circulating hormones FGF23 and its co-receptor αKlotho, PTH and vitamin D. Treatment specifically targeting these factors are discussed below and summarised in Figure 1-4 at the end of this section.

1.5.3.1. Reducing serum phosphate

Studies in healthy subjects have shown that circulating FGF23 levels are associated with dietary phosphate intake levels [343,344], and can be further increased by acute phosphate loading [345]. This can be reduced, in the short-term,

by aggressive reduction of dietary phosphate absorption [344,346-349] and restriction [350]. Overall, in relatively short-term studies, non-calcium based phosphate binders lower FGF23 in patients with CKD/KFRT whereas calcium-based binders do not [351-355]. Calcium is thought to be a secondary stimulus for FGF23 synthesis [356,357]. However, lowering intestinal phosphate absorption with dietary change, phosphate binders, nicotinamide [358], tenapanor [359-361] or combination therapy[362] produces only modest falls in FGF23 that do not appear to be sustained in the long term [353,362]. Whether this is due to increased total intestinal phosphate absorption by active phosphate transport [363-365], high pill burden or intolerability of the medications is unknown.

1.5.3.2. Vitamin D replacement

There is strong experimental data supporting vitamin D as a potential treatment for FGF23-mediated CKD-associated cardiomyopathy. Calcitriol, the synthetic analogue of vitamin D_3, blocks FGF23-induced activation of FGFR4 and cardiomyocyte growth [228]. Increases in FGF23 expression, FGFR4-induced calcineurin/NFAT signalling and LVH in 5/6 nephrectomised rats are reduced by calcitriol [228]. Vitamin D also increases αKlotho expression [366,367]. Observational studies demonstrate a survival advantage of vitamin D therapy in patients with CKD/KFRT despite raising calcium and phosphate levels [368,369]. However, in a randomised, placebo-controlled study in patients with CKD stages 4-5, paricalcitol (activated vitamin D_2 analogue) treatment did not reduce LV mass [370]. Taken together, these data suggest combining vitamin D receptor activation with FGF23/FGFR4 signalling blockade could have beneficial synergistic actions on CKD-associated cardiomyopathy.

1.5.3.3. Targeting parathyroid hormone

In patients on dialysis, the clinically available allosteric modulators (calcimimetics) of the calcium-sensing receptor, cinacalcet and etelcalcetide, are used to treat hyperparathyroidism and consistently lower circulating FGF23 [371-375]. In secondary analyses of the large and well-designed Evaluation of Cinacalcet HCl Therapy to Lower Cardiovascular Events (EVOLVE) trial, a greater than 30% reduction in FGF23 in patients randomised to cinacalcet was associated with a reduction in cardiovascular mortality, SCD and admissions for heart failure. The findings were amplified in those with a greater than 50% reduction in FGF23 [184]. However, it should be noted that calcimimetics appear to have a consistent blood pressure lowering effect in experimental models of uraemia and patients with CKD and KFRT [371,374,376-378].

In CKD patients not requiring dialysis, randomised-controlled trials of cinacalcet have reported significant reductions in FGF23, but also poor suppression of PTH as well as high rates of hypocalcaemia and hyperphosphataemia [379,380]. These actions are thought to negate many of the clinical benefits of calcimimetics and these agents are not licensed for use in patients with non-end stage CKD. Nevertheless, cinacalcet remains a promising therapeutic option for the treatment of CKD-associated cardiomyopathy in KFRT.

1.5.3.4. Directly targeting FGF23

The mechanism(s) regulating FGF23 synthesis are poorly understood and no “phosphate-sensor” has yet been found in mammals [381,382]. Animal data has recently suggested that sodium-phosphate co-transporter PiT2 found in bone might regulate phosphate-dependent regulation of FGF23 synthesis and that

targeting PiT2 could potentially reduce FGF23 synthesis [382]. The development of novel small molecules against PiT2 or the yet to be characterised PiT2-FGF23 pathway would give a proof of principle approach in animals for blocking FGF23 synthesis.

Indiscriminate FGF23 neutralisation with monoclonal antibodies has been shown to worsen hyperphosphataemia, and increase vascular calcification and mortality in rat models of CKD [383,384]. Use of anti-FGF23 monoclonal antibodies such as burosumab, currently approved for the treatment of x-linked hypophosphataemia, causes severe side effects in patients with CKD by decreasing phosphaturia [385]. Analogous to the use of calcimimetics, total blockade of FGF23 may theoretically be of benefit in KFRT. From a clinical therapeutic and drug development perspective, the ideal target would be the FGFR responsible for the adverse cardiac effects of FGF23 and not FGFR1, which is critical for maintaining normal phosphate levels. Indiscriminate blockade of FGFRs, whilst shown to be effective at preventing the development of [386], and reversing LVH in rodents [171], results in cardiac toxicity, hyperphosphataemia and ectopic calcium deposition [387]. Targeting cardiac FGFR4, especially its αKlotho-independent activation of downstream signalling pathways, represents an exciting possibility. Indeed, FGFR4-blocking antibodies have been shown to inhibit FGF23-induced hypertrophy of isolated rat cardiomyocytes *in vitro*, and attenuated LVH in a 5/6 nephrectomy rat model of CKD [172]. Currently, very little is known about the specific FGFRs mediating the actions of FGF23 in non-myocyte cardiac cells including fibroblasts, or whether blocking FGFR4 prevents or reverses cardiac fibrosis [247]. Several anti-FGF small-molecule tyrosine kinase inhibitors and related

compounds, monoclonal antibodies and FGFR-analogues currently in development are mainly for use in oncology [388]. Development of these agents specifically for the treatment of CKD-associated cardiomyopathy is, therefore, a real possibility.

1.5.3.5. Targeting αKlotho

In murine studies, administration of αKlotho protein has been shown to be effective in protecting against progression of CKD [389-392]. Intravenous administration of a transgene-encoding soluble αKlotho reduces LVH in αKlotho-deficient mice [213]. αKlotho supplementation in uraemic and diabetic mice also attenuates cardiac remodelling, fibrosis and LVH, through protection from inflammation[393] and oxidative stress[393], angiotensin II-dependent myocardial TGF-beta1 expression [394], hyperphosphataemia [391], acute kidney injury [391], uraemic toxin [237], and through induction of myocardia FGF21[395]. In another study, αKlotho improved cardiac function and reduced hypertrophy and fibrosis in a mouse model of hypertension, whilst decreasing FGF23 expression [394].

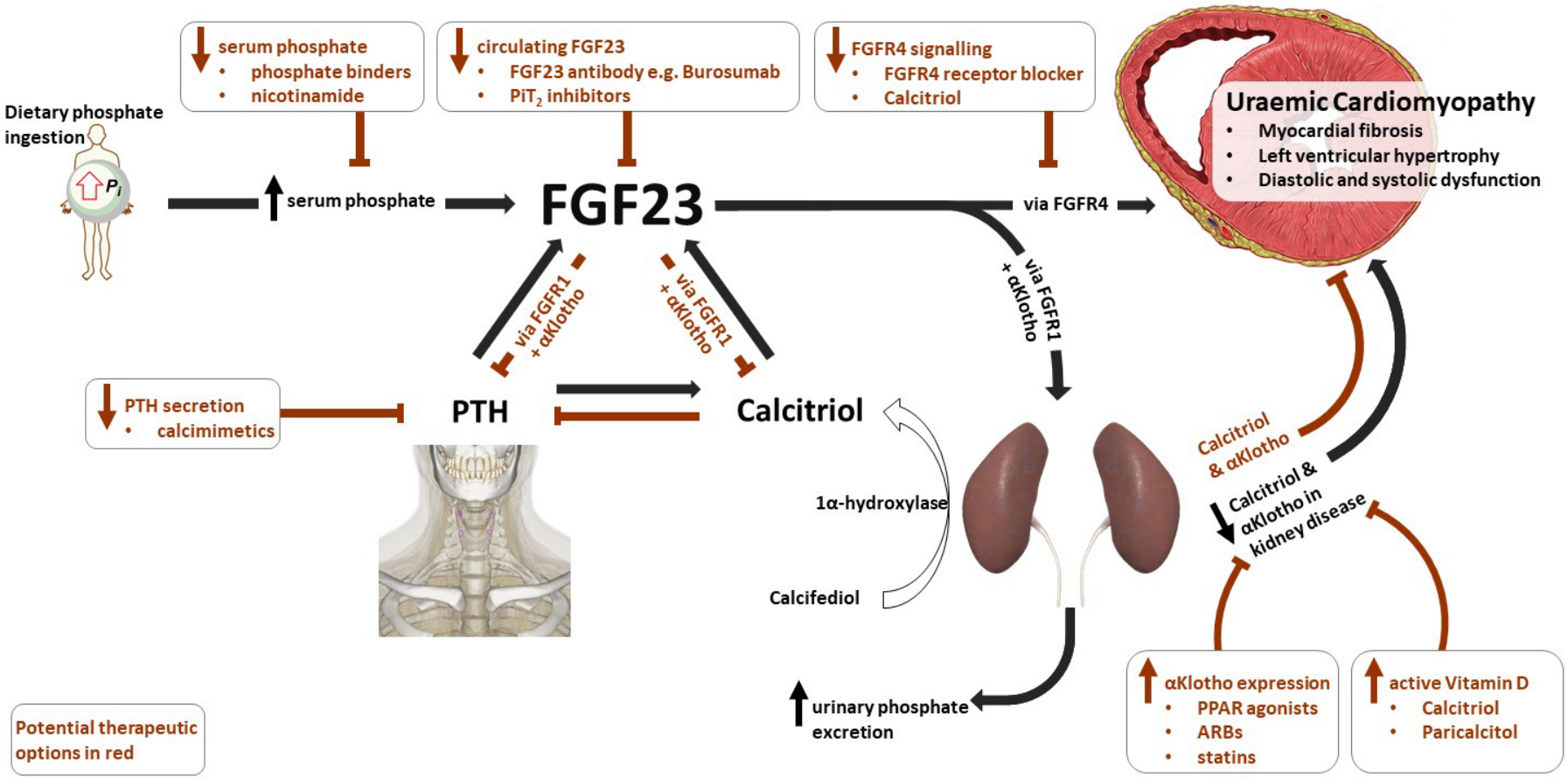
However, it remains unclear whether αKlotho, either as an endogenous circulating factor or through exogenous supplementation, is cardioprotective in the absence of increased FGF23. Its efficacy in larger mammals is also untested. Elevated FGF23 and decreased circulating αKlotho, are observed in both ageing and in CKD [211,213,392] leading to speculation that both CKD and the age-related decline in this and other physiological functions are caused in part by increased FGF23 and decreased αKlotho [152]. If true, this would assume soluble αKlotho acts as an inhibitor of αKlotho-independent actions of FGF23. Potential mechanisms include

inhibiting FGF23/FGFR4 signalling by either binding first to FGFR4 or via an initial interaction with FGF23 (decoy receptor). An alternative mechanism involves FGF23 and FGFR4 forming a complex in the presence of soluble αKlotho but activating FRS2αRas/MAPK rather than PLCγ/calcineurin/NFAT signalling [152]. The recently discovered co-crystal structure of αKlotho:FGF23:FGFR1 in a 1:1:1 relationship has provided new insight into this dynamic interplay of factors and may reveal new therapeutic options [159]. Therefore, development of αKlotho-mimetics, through the development of protein-protein inhibitors provides another potential therapeutic option.

To date, small molecule αKlotho modulators have been identified from a high-throughput screen of 150,000 compounds with those showing most promise being αKlotho transcription activators. Furthermore, extracellular signal-regulated kinase phosphorylation in FGFR-transfected cells increased, demonstrating an effect on FGF23 signalling [396]. Although clearly at an early stage of exploration, the identification of new small molecules demonstrates the potential of drugs acting *via* αKlotho. Trials of such agents to prevent progression of CKD and CKD-associated cardiomyopathy are expected to start in the next couple of years and remain promising therapeutic options.

Figure 1-4. Summary figure of potential therapeutic options targeting fibroblast growth factor 23 (FGF23) and the kidney-parathyroid-heart axis in patients with chronic kidney disease.

Figure adapted from Law et al. (2020) [2]



1.6. THESIS HYPOTHESES AND AIMS

- Cardiac fibrosis is driven by activation of cardiac fibroblasts into myofibroblasts, which are characterised by αSMA expression and increased collagen excretion. I hypothesise that this process is reversible through inhibition of known pro-fibrotic pathways such as TGF-β, and through modulation of extra-cellular matrix stiffness. My aim is to determine the potential for reversal of chronically activated human cardiac myofibroblasts back to a quiescent fibroblast phenotype *in vitro*, through the use of TGF-β inhibitors and soft tissue culture substrates.
- It is unclear whether the fibrosis observed in CKD-associated cardiomyopathy is directly attributable to elevated circulating FGF23 levels. I hypothesise that elevated circulating FGF23 levels can cause cardiac fibrosis through activation of cardiac fibroblasts. My aims are to determine whether human cardiac fibroblasts express receptors to FGF23, and to investigate if human cardiac fibroblasts are susceptible to activation by FGF23.
- CKD is associated with increased atrial and ventricular arrhythmias. I hypothesise that elevated FGF23 levels can directly affect cardiac electrical physiology resulting in pro-arrhythmic phenomena. Using murine models of acute and chronic FGF23 excess, I aim to determine the effect of acute FGF23 elevations on murine left ventricular electrophysiology; and characterise the effect of chronic FGF23 elevation on murine cardiac left ventricular structure, function and electrophysiology.

CHAPTER 2. EXPERIMENTAL METHODS

2.1. EXTENT OF PERSONAL CONTRIBUTION

The following chapter details the experimental methods used within this thesis. All methodology and analysis were performed by the author of this thesis unless specifically indicated below. The work and contributions of other researchers at the University of Birmingham are attributed as follows:

Max Cumberland supplied the differentiated human induced pluripotent stem cell-derived cardiac fibroblasts (Chapter 2.2.2). Caitlin Hall performed the CyQUANT NF Proliferation Assay (Chapter 2.5) and immunofluorescence work (Chapter 2.6). Animal technicians at Biomedical Sciences Unit administered the intraperitoneal FGF23 injections and performed the saphenous vein venepuncture (Chapter 2.7.2.2). Sophie Broadway-Stringer conducted the *in vivo* murine echocardiography (Chapter 2.7.8).

2.2. HUMAN CARDIAC FIBROBLAST CELL CULTURE

Two human cardiac fibroblasts cell lines were utilised - primary human cardiac fibroblasts (HCF) and human induced pluripotent stem cell-derived cardiac fibroblasts (hiPSC-cFb). Cell cultures were kept in a humidified 5% CO_2 incubator set at 37 °C. All cell culture work was performed within a Class II HEPA filtered laminar flow tissue culture hood sterilised with 70% alcohol. All culture materials, bottles and gloved hands were sprayed with 70% ethanol before use within the culture hood. Sterile serological pipettes, pipette tips and reagents were used throughout. Routine cell observation and microscopy was performed using an EVOS® XL digital microscope (Thermo Fisher Scientific, AME3300).

2.2.1. Primary human cardiac fibroblast culture

Primary ventricular HCFs isolated from explanted hearts were obtained from PromoCell GmbH (C-12375). The two donors, aged 60 and 63, were both diabetic with cardiomyopathy. HCFs were received cryopreserved at passage 2. Following thawing, HCF were cultured in a 25 cm^2 cell culture flask (Corning®, CLS430639) using Fibroblast Growth Medium 3 (FGM3; PromoCell, C-23025) with 1% penicillin-streptomycin (Gibco™, 15140122). Upon reaching 90% confluence, the culture was passaged into 75 cm^2 cell culture flasks (Corning®, CLS430641). Subsequent passages and expansion of culture was performed upon reaching 80-90% confluence and discarded after 9 passages. To allow for the larger subcultures, 150 cm^2 cell culture flasks (Corning®, CLS430825) were also used. Culture media was changed every 48 hours unless otherwise specified.

The procedure for HCF cell passaging was as follows: Cells in culture flasks were examined under microscope to confirm 90% confluence. Medium was removed from the cell culture flask by aspiration before washing with 10 mL Dulbecco's Phosphate Buffered Saline (DPBS; Sigma-Aldrich, D8662) to remove dead cell debris and residual media. 6 mL TrypLE™ Express 1X (Gibco™, 12605010) was then added to the cells after which the flask was returned to the CO_2 incubator for 3 to 5 minutes until cells appeared visually rounded under microscope. The flask may be tapped several times on its side to aid detachment of cells. 10 mL pre-warmed FGM3 was added to dilute the dissociation solution. The cells were gently resuspended, transferred into a 15 mL conical tube (Corning®, CLS430791) and centrifuged for 4 minutes at 1000 x g to pellet the cells. The supernatant was removed without disturbing the cell pellet, followed by resuspension of the pellet in 10 mL FGM3. The cell number was quantified using a Countess™ II cell counter (Invitrogen™, AMQAX1000) and inoculated at the desired seeding density – typically 3,500 to 12,000 cells per cm^2 – into a new culture flask.

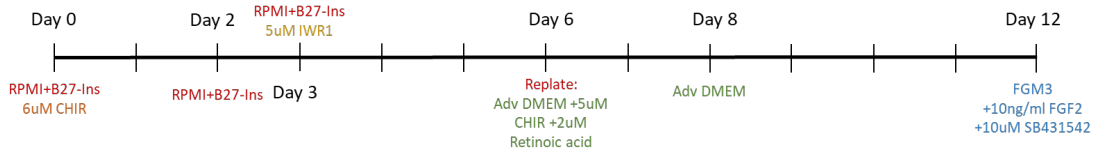
2.2.2. hiPSC-cFb culture

hiPSC-cFbs were derived using the hiPSC Kolfc2 line from a healthy Caucasian male using an established protocol[397] (**Figure 2-1**) as follows: Day 0 hiPSC were cultured in RPMI $^{+}$B27 $^{-}$Insulin with 6 µM CHIR99021 (Tocris Bioscience, 4424) for two days. Day 2 hiPSCs were seeded at 30,000 cells/cm^2 in Essential 8 medium (Lifetech, A1517001) on Matrigel® (Corning®, 356231). 5 µM IWR1 (Sigma, I0161) was added at day 3. At day 6, hiPSC were replated at 20,000 cells/cm^2 in Advanced DMEM with 5 µM CHIR99021 and 2 µM retinoic acid. On

day 8, culture media was changed to Advanced DMEM. At day 12, a further media change was performed using FGM3 in the presence of 10 μM SB431542 (Selleck Chemicals, S1067) and 10 ng/ml fibroblast growth factor 2 (FGF2) (Peprotech, 100-18B).

Figure 2-1. Derivation of hiPSC-cFbs.

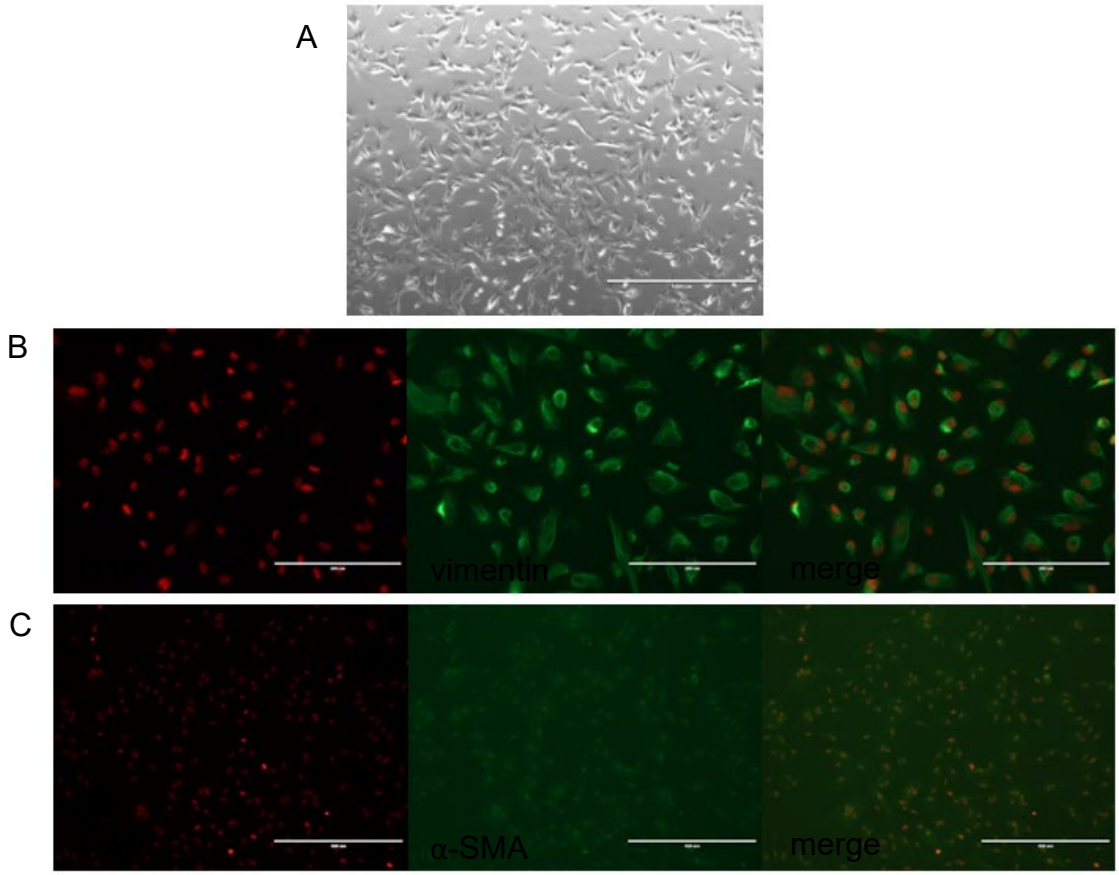
Protocol uses CHIR99021, IWR-1, retinoic acid, and fibroblast growth factor 2.



At day 18, a vimentin and α-SMA immunofluorescence stain was conducted (**Figure 2-2**). A positive vimentin and negative α-SMA stain confirmed successful generation of quiescent iPSC-cFbs (**Figure 2-2 B, C**). iPSC-cFbs were maintained in FGM3 supplemented with SB431542 and FGF2 and cultured on Matrigel® for up to 10 passages (split ratio 1:10).

Figure 2-2. Phase contrast microscopy and immunofluorescence staining of day 18 hiPSC-cFbs.

A – Brightfield microscopy; scale bar = 1 μm. **B** – vimentin (green), DAPI (red) immunofluorescence stain; scale bar = 200 μm. **C** – α-SMA (green), DAPI (red) immunofluorescence stain; scale bar = 400 μm. Images provided by Max Cumberland (Institute of Cardiovascular Sciences, University of Birmingham).



2.2.3. Human cardiac fibroblast culture on standard polystyrene and low stiffness surfaces

Human cardiac fibroblasts at passage number 5 to 9 were seeded at 7,500 cells per cm^2 onto the 6-well flat-bottom tissue culture plates of varying elastic modulus (*E)* – Costar® $E \approx 3$ GPa tissue culture-treated (Corning®, CLS3516), Softwell® $E = 25$ kPa (Matrigen, SW6-EC-25), Softwell® $E = 2$ kPa (Matrigen, SW6-EC-2). Matrigen Softwell® culture plates achieve a lower elastic modulus compared to standard polypropylene plates using bisacrylamide-crosslinked polyacrylamide hydrogels. The available cell surface area of 9.5 cm^2 is maintained across the Costar® and Softwell® products. Each well was coated with 1 mL (10 µg/mL) fibronectin from bovine plasma (Sigma-Aldrich, F1141) for at least 45 minutes at room temperature to aid adhesion of cardiac fibroblasts. Fibronectin is produced by cardiac fibroblasts and is a principle component of the cardiac ECM [398,399]. Residual fibronectin solution was aspirated before the addition of cardiac fibroblasts and media.

Human cardiac fibroblasts were typically seeded at a density of 7,500 cells per cm^2 and cell pellets collected after 1 day or 4 days. To collect the cell pellets for subsequent protein and mRNA analyses, the following protocol was used: Old media was aspirated from each well and discarded, followed by the addition of 750 µL TrypLE™ Express 1X (Gibco™, 12605010). After 5 minutes incubation, or when cells appear visually detached, 750 uL FGM3 was used to dilute the dissociation solution. The resulting cell suspension was transferred into a 1.5 mL microcentrifuge tube (Eppendorf®, T9661) and centrifuged for 5 minutes at 15,000 x g. The supernatant was discarded. The cell pellet was resuspended in

200 µL DPBS (Sigma-Aldrich, D8662) and centrifuged for a further 5 minutes at 15,000 x g. The supernatant was discarded leaving a dry cell pellet. The cell pellet was stored at -80 °C if not immediately utilised for RNA or protein extraction.

2.2.4. Treatment of human cardiac fibroblasts with fibroblast growth factor-23 or transforming growth factor-β

Human cardiac fibroblasts were cultured in the presence of recombinant human fibroblast growth factor-23 (rhFGF23; Sigma-Aldrich, SRP3039) at 50 ng/mL, and transforming growth factor-β (TGF-β; R&D Systems, 240-B) at 10 ng/mL. Untreated HCFs were used as control. Human cardiac fibroblasts were treated for one and four days before cell pellets were collected for mRNA and protein analysis as described above.

2.3. mRNA EXPRESSION BY REAL-TIME POLYMERASE CHAIN REACTION

2.3.1. RNA extraction and cDNA conversion

RNA extraction was performed using the RNeasy Mini Kit (Qiagen, 74106). Cardiac fibroblasts were lysed in Buffer RLT containing guanidine-thiocyanate-containing buffer and homogenised by vortexing. Ethanol was then added to the cell homogenate to promote selective binding of RNA to the RNeasy Mini spin column membrane. The membrane-bound RNA was washed once in Buffer RW1, and twice in Buffer RPE, before being eluted in 30 µL RNase-free water. The quantity and purity of RNA eluted was determined with a NanoDrop™ Spectrophotometer (Thermo Scientific; ND-2000). Single-stranded cDNA was synthesised from RNA using the High-Capacity cDNA Reverse Transcription Kit

(Applied Biosystems™, 4368814) according to manufacturer protocols. In brief, a 2X reverse transcription master mix containing buffer, dNTP mix, random primers, reverse transcriptase, and nuclease-free water was added to the RNA samples. Up to 2 µg of RNA was entered into each cDNA conversion reaction. Reverse transcription was performed in a Labcycler thermal cycler (SensoQuest, 011-103) using the following profile: 25 °C for 10 minutes, 37 °C for 120 minutes, 85 °C for 5 minutes, and kept at 4 °C until sample was ready for collection.

2.3.2. Real-time PCR, mRNA expression by comparative $2^{-\Delta\Delta CT}$ method

Real-time PCR was performed using TaqMan™ gene expression chemistry and Applied Biosystems 7500 Fast 96-well (HCF) or QuantStudio 5 384-well (iPSC-cFb) real-time polymerase chain reaction (PCR) systems. In summary, cDNA combined with TaqMan™ Fast Advanced Master Mix (Applied Biosystems™, 4444557) and Taqman™ Gene Expression Assay (Applied Biosystems, 4331182; see **Table 2-1** for details of specific Taqman™ Gene Expression Assays used) was loaded in technical triplicate onto a 96-well or 384-well PCR plate and run in Fast mode. Gene expression by comparative $2^{-\Delta\Delta CT}$ was calculated from C_T values exported from the PCR machine into Excel 365 (Microsoft, version 2207) and Prism 9 (GraphPad, version 9.4.1). Glyceraldehyde 3-phosphate dehydrogenase (GAPDH) was used as an endogenous housekeeping gene and inter-plate calibrator. Samples with GAPDH C_T values greater than two standard deviations from the mean C_T of the dataset were removed from analysis. mRNA transcripts were deemed not expressed where C_T values exceeded 40 cycles in >50% of technical replicates.

Table 2-1. TaqMan™ Gene Expression Assays

Gene	Protein	Assay ID
ACTA2	α-Smooth muscle actin	Hs00426835_g1
COL1A1	Type 1 collagen	Hs00164004_m1
COL3A1	Type 3 collagen	Hs00943809_m1
FGFR1	Fibroblast growth factor receptor 1	Hs00241111_m1
FGFR2	Fibroblast growth factor receptor 2	Hs01552926_m1
FGFR3	Fibroblast growth factor receptor 3	Hs00179829_m1
FGFR4	Fibroblast growth factor receptor 4	Hs01106908_m1
GAPDH	Glyceraldehyde 3-phosphate dehydrogenase	Hs02786624_g1

2.4. PROTEIN EXPRESSION BY WESTERN BLOT

2.4.1. Protein extraction

2.4.1.1. Cardiac fibroblast sample preparation

Frozen cardiac fibroblasts pellets were thawed at room temperature, then re-suspended in 50 µL RIPA buffer (Sigma-Aldrich, R0278) with 1% Halt™ Protease and Phosphatase Inhibitor Cocktail 100X (Thermo Scientific™, 78441). The cell suspension was vortexed for 15 seconds before incubation over ice for 30 minutes, followed by centrifugation at 14,000 x g for 10 minutes at 22 °C to remove any sediment. The supernatant was transferred into a new 1.5 mL microcentrifuge tube (Eppendorf®, T9661). Protein quantification was performed using the DC™ modified Lowry protein assay (Bio-Rad, 5000116); the absorbance at 750 nm was read using a Gemini™ microplate reader (Molecular Devices). Using the results of the protein assay, samples were diluted in 2X

sample loading buffer (containing 100 mM Tris pH 6.8, 4% SDS, 0.2% bromophenol blue, 20% glycerol, and 5% β-mercaptoethanol) to achieve a final protein concentration of 2 µg/µL, then stored at -20 °C until required.

2.4.1.2. Mouse cardiac chamber preparation

Weights of the heart chambers were recorded. Atria were placed into 0.5 mL soft tissue homogenising CK14 tubes (Bertin Technology, P000933-LYSK0-A) and ventricles into 2 mL CK14 tubes (Bertin Technology, P000912-LYSK0-A). RIPA homogenisation buffer (Sigma-Aldrich, R0278) containing 1% Halt™ Protease and Phosphatase Inhibitor Cocktail 100X (Thermo Scientific™, 78441) was added to the tubes at a ratio of 10 µL homogenisation buffer per milligram of tissue. Cardiac tissue was mechanically homogenised using a Precellys 24 homogeniser (Bertin Technology, P002391-P24T0-A.0) set at 5000 rpm speed, 2 x 15 second cycles. Homogenates were transferred into a new 2 mL microcentrifuge tube (Eppendorf, T3045). Protein quantification and dilution in 2X sample loading buffer to 2 µg/µL was performed as above and stored at -80 °C until required.

2.4.2. SDS-PAGE protein gel electrophoresis

Mini-PROTEAN® TGX™ 4-15% gels (Bio-Rad, 4561086) were immersed in running buffer (containing 25 mM Tris, 192 mM glycine, 0.1% SDS; Bio-Rad, 1610734 / 1610416) within a Mini-PROTEAN® Tetra Vertical Electrophoresis Cells (Bio-Rad, 1658004). Each sample was heated at 95 °C for 5 minutes, then vortexed for uniformity before 30 (for HCF studies) – 50 µg (for LV lysates) of protein was loaded onto the gel. 8 µL Precision Plus Protein™ Dual-Colour

Standard (Bio-Rad, 1610374) was run alongside the samples to aid identification of target protein by molecular weight. Using a PowerPac™ Basic Power Supply (Bio-Rad, 1645050), 50V was applied across the gels for 5 minutes to allow the sample to stack in the individual wells, followed by an increase to 100-150 V until the sample buffer line approached the bottom of the gel.

2.4.3. Transfer and immunoblotting

In preparation for immunoblotting, protein was transferred from the gel to PVDF membrane using methanol-activated Trans-Blot® Turbo™ Mini PVDF Transfer Packs (Bio-Rad, 1704156) and Trans-Blot® Turbo™ Transfer System (Bio-Rad, 1704150) set at 2.5 A, 25 V over 10 minutes. The membrane was stained with 0.1% Ponceau S solution (Sigma-Aldrich, P7170-1L) to ensure satisfactory transfer before de-staining in Tris-buffered saline with 0.1% Tween 20 (TBS-T; containing 25mM Tris, 192 mM glycine, 0.1% w/v Tween 20; Bio-Rad, 1610734/1710781).

The membranes were submerged in TBS-T with 5% skimmed powdered milk (Marvel) and left at room temperature for 1 – 2 hours to block unoccupied binding sites and reduce nonspecific antibody binding. The membranes were probed overnight at 4 °C with primary monoclonal IgG antibodies (**Table 2-2**) diluted in TBS-T with 1% skimmed milk, followed by washing at room temperature for an hour in TBS-T (washing solution was changed every 10 minutes) to remove unbound antibody.

Table 2-2. Primary antibodies used for immunoblotting

Target Protein	Company, Catalogue #	Species	Dilution
Fibroblast growth factor receptor 1	CST, D8E4	Rabbit	1:1,000
Fibroblast growth factor receptor 2	CST, D4L2V	Rabbit	1:1,000
Fibroblast growth factor receptor 3	Santa Cruz, sc-390423	Mouse	1:100
Fibroblast growth factor receptor 4	Santa Cruz, sc-136988	Mouse	1:100
Glyceraldehyde 3-phosphate dehydrogenase	CST, D16H11	Rabbit	1:10,000
α-smooth muscle actin	CST, D4K9N	Rabbit	1:1,000
Collagen 1	Abcam, ab34710	Rabbit	1:1,000
Collagen 3	Abcam, ab7778	Rabbit	1:5000
Troponin T	Sigma, SAB4200717	Mouse	1:1000
Heat shock protein 27	CST, 2442	Rabbit	1:500

The membranes were further incubated for two hours at room temperature in Li-Cor IRDye® secondary dye-conjugated IgG antibodies (**Table 2-3**) diluted in TBS-T with 1% skimmed milk. Membranes were washed with TBS-T at room temperature for 15 minutes (washing solution changed every 5 minutes) to remove unbound antibody.

Table 2-3. Secondary antibodies used for western blot

Target Species	Company, Catalogue #	Host Species	Dilution
Rabbit	Li-Cor, 800CW 926-32211	Goat	1:10,000
Mouse	Li-Cor, 680RD 926-68070	Goat	1:10,000

Membranes which required re-probing were stripped using Restore™ PLUS Western Blot Stripping Buffer (Thermo Scientific; #46430) before undergoing the immunoblotting procedure again. Membranes were re-probed a maximum of two times and were incubated with one antibody at a time. No dual staining was performed.

2.4.4. Image analysis

Visualisation of the membranes was performed using the Odyssey® Fc imaging system (Li-Cor). Band detection was in the 700nm channel for the ladder and 680RD IRDye®, and 800nm for the 800CW IRDye® secondary antibody. Quantification of band fluorescence intensity was performed using Li-Cor Image Studio™ Lite Version 5.2 with no post-capture image data manipulation. GAPDH was used as the loading control; the band intensity of the protein of interest (POI) was normalised to the GAPDH loading control and presented as a ratio – POI/GAPDH – to account for protein loading errors and protein concentration variations.

2.5. CYQUANT® NF CELL PROLIFERATION ASSAY

The CyQUANT® NF proliferation assay (Invitrogen™, C35006) was performed by Caitlin Hall as per manufacturer's protocol. The 96-well assay measures cellular DNA content bound to a proprietary fluorescent CyQUANT® dye. Cardiac fibroblasts were seeded into 96-well plates at 7,500 cells per cm^2 (HCF) or 15,000 cells per cm^2 (hiPSC-cFb) in the presence or absence of 10 ng/mL TGF-β, 30 nM SD208 or 10 μM SB431542. Cells were then left for 3 – 4 hours to adhere at 37

°C and 5% CO2. Growth medium was removed by gentle aspiration, followed by the addition of 1X CyQUANT® dye binding solution. After a 60-minute incubation at 37 °C, a stable fluorescence endpoint was reached. The fluorescence was measured using a Molecular Devices FlexStation® 3 microplate reader (excitation: 485 nm; emission 530 nm). Proliferation was assessed at baseline and 48-hour timepoints. A percentage change was from baseline was calculated.

2.6. IMMUNOFLUORESCENCE MICROSCOPY

Immunofluorescence staining and microscopy was performed by Caitlin Hall. Adherent cardiac fibroblasts were fixed with 4% paraformaldehyde at room temperature for 10 minutes. Cells were then permeabilised with 0.1% Triton™X-100 for 5 minutes at room temperature and then blocked with 5% bovine serum albumin (BSA) for 1 hr at room temperature. Cells were then incubated with primary antibodies overnight at 4 °C (abcam®, ab45939 anti-vimentin 0.25 µg/mL and Sigma-Aldrich, A2547 anti-α-SMA 1:750 [HCF] or 1:500 [hiPSC-cFb]). The cells were blocked for a second time with 5% BSA for 30 minutes at room temperature followed by secondary antibody incubation (abcam®, Alexa Fluor® 488, ab150077 1:1000 or Thermofisher Scientific, Alexa Fluor® 647, A21235 1:1000) for 90 minutes at room temperature. Cells were then incubated with 1:1000 DAPI for 30 minutes before mounting with Hydromount™. Cells were visualised using the Zeiss LSM780 confocal laser scanning microscope equipped with a C-Apochromat 40x/1.20 W objective. Images were acquired using the Zen Black software (version 3.0).

2.7. ANIMAL EXPERIMENTAL PROTOCOLS

2.7.1. Ethical statement and study approval

All animal procedures/procedures were performed according to the UK Animals (Scientific Procedures) Act 1986. The programme of scientific procedures was approved by the Home Office Project (Project License PFDAAF77F and PP1649524) and underwent Animal Welfare Ethical Review Board review at the University of Birmingham.

2.7.2. Animal models of acute and chronic cardiac FGF23 exposure

Experiments were conducted in female adult mice (9 to 15 weeks old) bred on the CD1 background. Mice were housed with sex-matched littermates (2 – 4 mice per cage) in individually ventilated cages under standard conditions: 12-hour light/dark cycle, 22 °C and 55% relative humidity. Food and water were available ad libitum. Health status of the mice (body weight, grooming, bearing) were monitored daily by animal technicians at the University of Birmingham.

Recombinant mouse FGF23 (rmFGF23; R&D Systems, 2629-FG/CF) was administered according to pre-specified protocols – summarised below – to investigate the effects of acute and chronic FGF23 exposure on the murine ventricle.

2.7.2.1. Acute model: *ex vivo* FGF23 administration

Following cardiac extraction under terminal anaesthesia (Chapter 2.7.4) and Langendorff perfusion (Chapter 2.7.5) of the isolated mouse heart with Krebs-Henseleit buffer (KHB), the perfusate was switched to a KHB containing 10 ng/mL

mrFGF23, or vehicle control. The concentration chosen is equivalent to that found in the circulation of mice with chronic kidney disease states [400-404]. The heart was perfused for up to 30 minutes in the treated KHB, during which optical mapping of the left ventricles would take place at timepoints zero, 10 minutes, and 30 minutes. Untreated KHB was then perfused for a 20-minute washout period after which final optical mapping recordings were taken. Data from these experiments are presented in Chapter 5 (single, voltage loaded) and Chapter 6 (dual calcium-voltage loaded).

2.7.2.2. Chronic model: *in vivo* FGF23 administration

Female CD1 mice received seven daily intraperitoneal (IP) injections of 3.12 µg rmFGF23 in 200 µL PBS, or vehicle (PBS) alone. This dose would ensure that a 40 g mouse would receive no less than the 80 µg/kg/day dose used in prior literature[171,225,405]. Saphenous vein venepuncture for plasma c-terminal FGF23 quantification (Chapter 2.7.9.1) were performed on day 4. *In vivo* echocardiography (Chapter 2.7.8), followed by cardiac isolation under terminal anaesthesia (Chapter 2.7.4) and ventricular optical mapping (Chapter 2.7.5.2) were performed on day 8. Cardiac tissue was kept for heart weight measurements (2.7.10) and protein expression studies (Chapter 2.4.1.2). Data from these experiments are presented in Chapter 7

2.7.3. *Ex vivo* optical mapping buffer solutions and reagents

2.7.3.1. Modified Krebs-Henseleit Buffer

A modified KHB was used for all mouse ventricular optical mapping experiments containing the following in millimolar dissolved in ultrapure water: NaCl 114; KCl

4; $CaCl_2$ 1.8; $NaHCO_3$ 24; $MgSO_4 \cdot 7H_2O$ 1; NaH_2PO_4 1.5; Glucose 11; $C_3H_3NaO_3$ 1. The solution was filtered using 0.22 µM and stored at 4 °C in a sterile container until needed. Prior to use, KHB was equilibrated with 95% O_2/5% CO_2 medical gas resulting in a pH of 7.4 and delivered to the mouse heart at 37 °C.

2.7.3.2. Blebbistatin

(±)-Blebbistatin (Cayman Chemical, 13186) inhibits electrical and mechanical coupling through myosin inhibition. It was added to KHB to achieve complete cessation of cardiac muscle contraction. This effectively minimises motion artefacts during optical mapping. It was received as a dry powder and reconstituted with sterile dimethyl sulfoxide to a concentration of 50 mg/mL before storage at 4 °C. For every 100 mL of KHB, 7 µL of blebbistatin stock was added to achieve a final concentration of 12 µM.

2.7.3.3. Recombinant mouse FGF23

As described previously, rmFGF23 (R&D Systems, 2629-FG/CF) was used to produce an acute and chronic model of cardiac FGF23 excess. It was supplied as a dry powder. For the acute experiments, it was reconstituted with sterile PBS with 0.1% BSA with a stock concentration of 0.1 mg/mL. For every 100 mL of KHB required, 10 µL of rmFGF23 stock was added. For the chronic experiments, rmFGF23 was reconstituted with sterile PBS to produce 200 µL aliquots containing 3.12 µg ready to be injected intraperitoneally. Sterile PBS was used as the vehicle control. Aliquots were stored at -20 or -80 °C if not immediately utilised.

2.7.3.4. Di-4-ANEPPS

The voltage-sensitive dye Di-4-ANEPPS (Biotum, 61010) was used for the experimental data presented in Chapter 5. It was supplied as a dry powder, reconstituted with DMSO to make 5 mg/ml aliquots, and stored at -20 °C. 125 µg Di-4-ANEPPS dissolved in 1 mL of 37 °C KHB was perfused over 5 minutes into the Langendorff-perfused heart at the beginning of each optical mapping experiment.

2.7.3.5. Rhod-2-AM

Rhod-2-AM is an intracellular Ca^{2+} dye (Stratech, 21060-AAT) used in combination with Rh-237 for the experimental data presented in Chapter 6 to simultaneously acquire calcium and voltage data. The dry powder was combined with DMSO to make a 1 mg/mL solution. 100 µL aliquots were stored at -20 °C. Thirty minutes before loading into the heart, an aliquot was mixed with an equal volume of 20% Pluronic® F-127 in DMSO (Sigma-Aldrich, P2443) to ease solubilisation. The dye was then mixed with 1 mL 37 °C KHB and slowly infused over 1-2 minutes through the perfusion line of the Langendorff system.

2.7.3.6. Rh-237

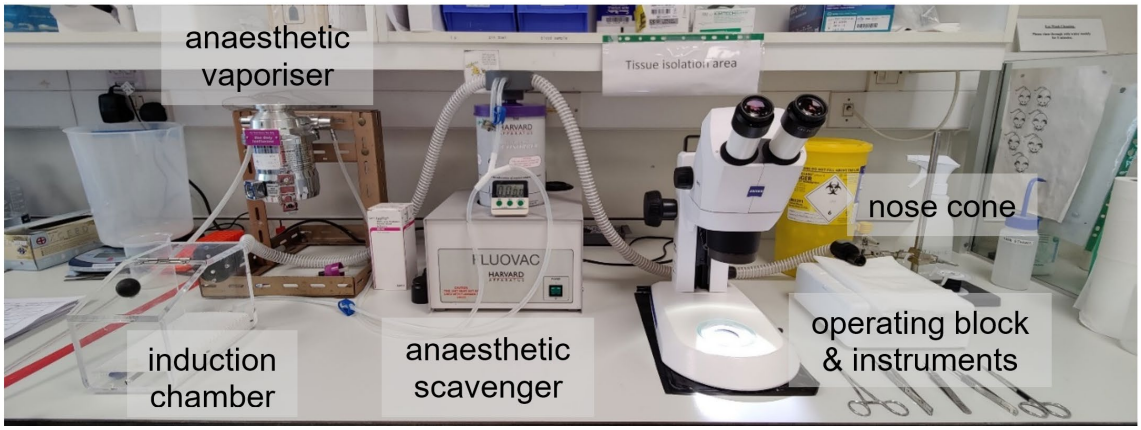
As previously described, the voltage-sensitive dye Rh-237 (Invitrogen, S1109) was used in conjunction with Rhod-2-AM. Supplied in dry powder form, it was reconstituted with DMSO at a concentration of 1.25 mg/mL. It was stored at 4 °C in 70 µL aliquots. The aliquot was dissolved in 1 mL of 37 °C KHB and infused into the heart over 1-2 minutes through the perfusion line of the Langendorff system.

2.7.4. Mouse cardiac extraction

2.7.4.1. Anaesthesia

Mouse hearts were extracted under deep terminal anaesthesia (**Figure 2-3**). After weighing, each mouse was placed into an anaesthetic induction chamber flooded with 4% isoflurane in pure oxygen at 2 L/min. The mouse was removed from the anaesthetic chamber and transferred onto a polystyrene operating block once breathing rate was significantly slowed, but regular, reduction in muscle tone, and loss of the righting reflex. Anaesthesia was maintained via a nose cone. An active gas scavenging system (Fluovac and Fluosorber, Harvard Apparatus) was used to reduce operator exposure to anaesthetic vapours. The mouse was secured in the supine position with the limbs taped down. Adequate anaesthetic depth was confirmed by absence of withdrawal reflexes to painful stimulation via a firm toe and tail pinch. Heparin (100 IU in 0.1 mL) was injected intraperitoneally using a 28g needle to reduce thrombus formation.

Figure 2-3. Anaesthetic and cardiac isolation setup

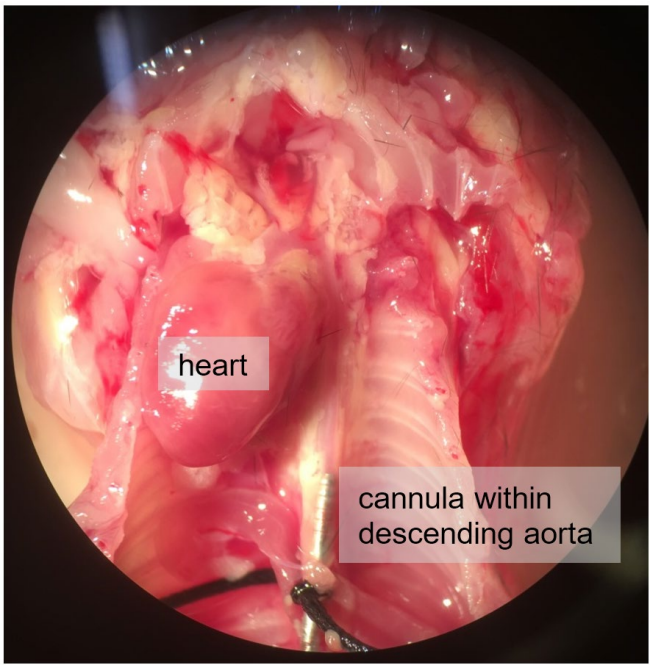


2.7.4.2. Cardiac isolation and cannulation

The chest was disinfected with 70% ethanol spray and opened in a clamshell fashion to expose the thoracic cavity. The base of the cervical spine was severed ensuring death by cervical dislocation and exsanguination, followed by a further incision through the dorsal rib cage and thoracic spine at the level of the diaphragm to release the thoracic chest with the heart in situ. Any excess or adherent tissue, for example skin, muscle, or fat, was simultaneously removed. The isolated heart/thoracic cavity was submerged in ice-cold heparinised KHB (100 IU heparin in 30 mL buffer) for 10 seconds to encourage cardioplegia, before transferring to siliconised petri dish. The lungs were excised, and the descending aorta cannulated and secured with a suture (**Figure 2-4**). A 2.5 mL syringe containing ice-cold heparinised KHB was used to flush the heart via retrograde perfusion. Clearing of blood from the coronary circulation was confirmed by blanching of the cardiac tissue.

Figure 2-4. Isolated mouse heart within the thoracic cavity.

The lungs have been removed. Tip of the cannula is placed within the descending aorta and secured with a suture.

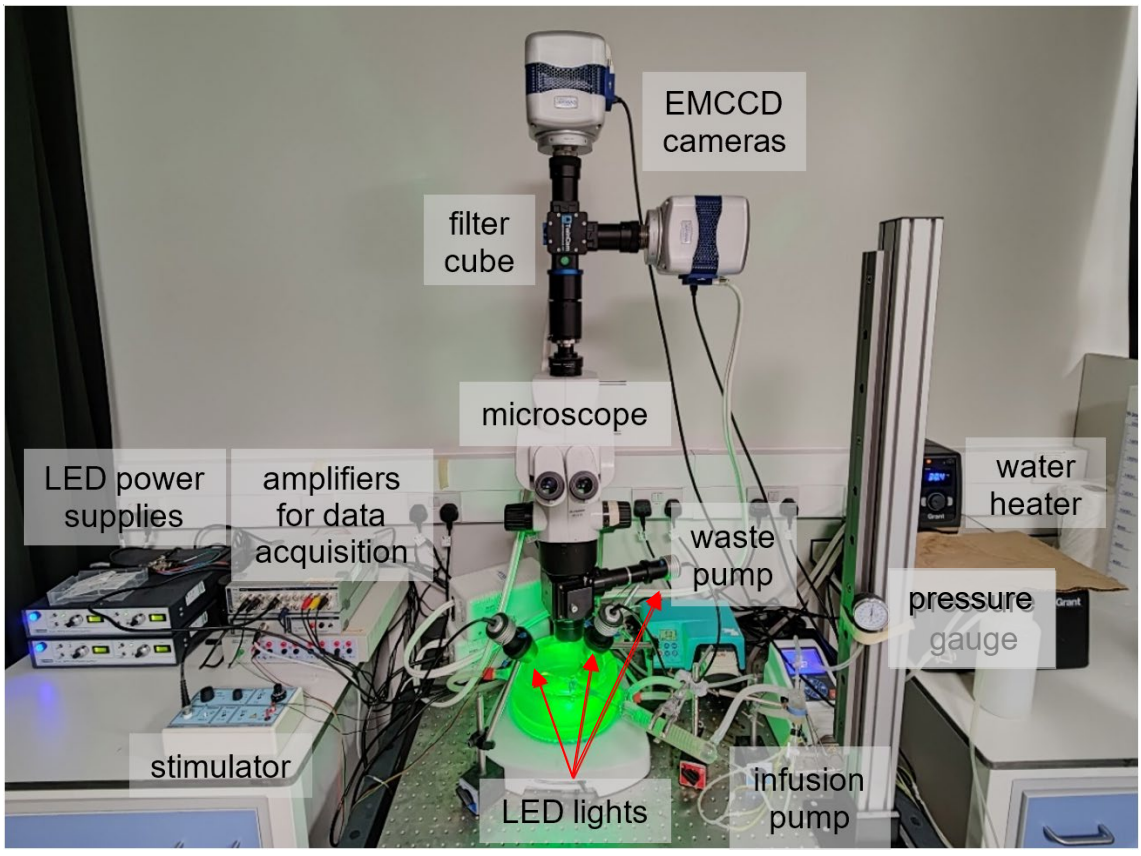


2.7.5. Langendorff perfusion and optical mapping

2.7.5.1. Langendorff perfusion

The cannulated heart was transferred to a Langendorff system (**Figure 2-5**) and perfused with 37 °C KHB continuously bubbled with 95% O_2/5% CO_2. The KHB contained 12 µM blebbistatin to stop cardiac muscle contraction by inhibiting the electrical and mechanical coupling of cardiomyocytes. A bubble trap was used in the perfusion circuit and the flow rate was controlled by peristaltic pumps adjusted to maintain a perfusion pressure of 80-90 mmHg. The perfusate could be switched between treatment (FGF23) and control KHB with minimal interruption in heart perfusion. Used perfusates were removed by peristaltic pumps and discarded such that no KHB was recirculated.

Figure 2-5. **Langendorff system and optical mapping setup**

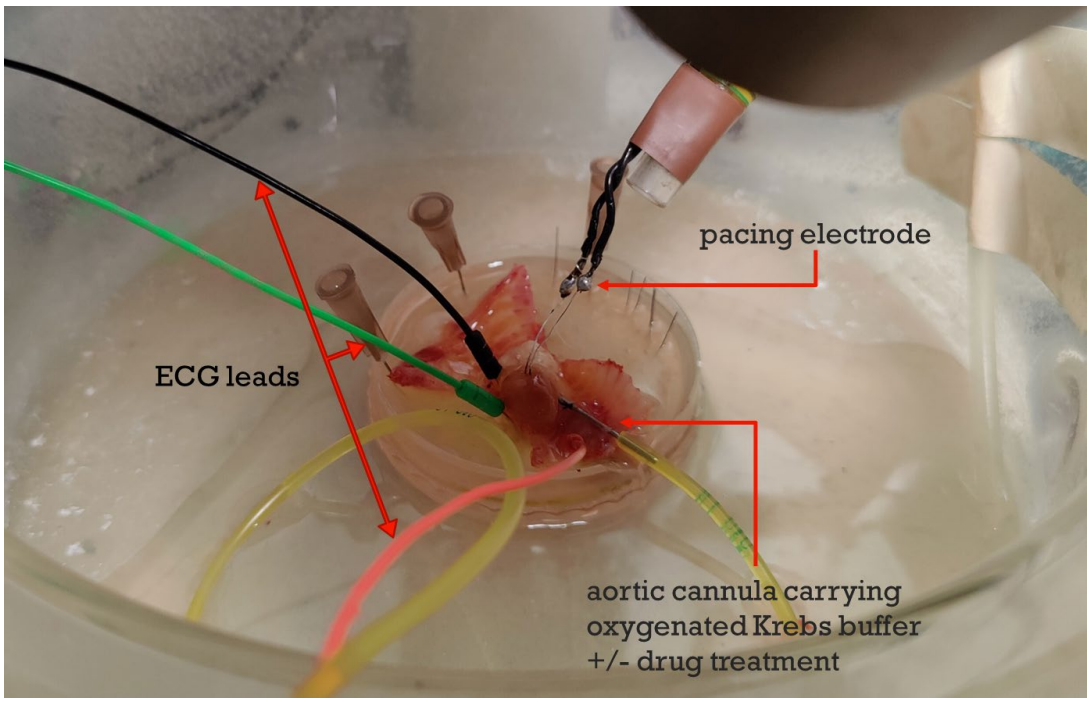


2.7.5.2. Ex vivo optical mapping

Bipolar electrocardiography (ECG) leads were inserted into the silicone base as shown in **Figure 2-6** to provide real-time monitoring of cardiac electrical activity using ADInstruments LabChart version 8. The heart was then loaded with sodium and/or calcium-sensitive fluorescent dyes as described in Chapter 2.7.3.4-6. Pacing electrodes placed at the base of the left ventricle were set to deliver a 2 ms long impulse at a holding cardiac cycle length of 120 ms, or 500 bpm. Cycle length (CL) is the time between impulses. Specific regarding cardiac pacing setup and protocols are discussed in a later section (Chapter 2.7.5.3).

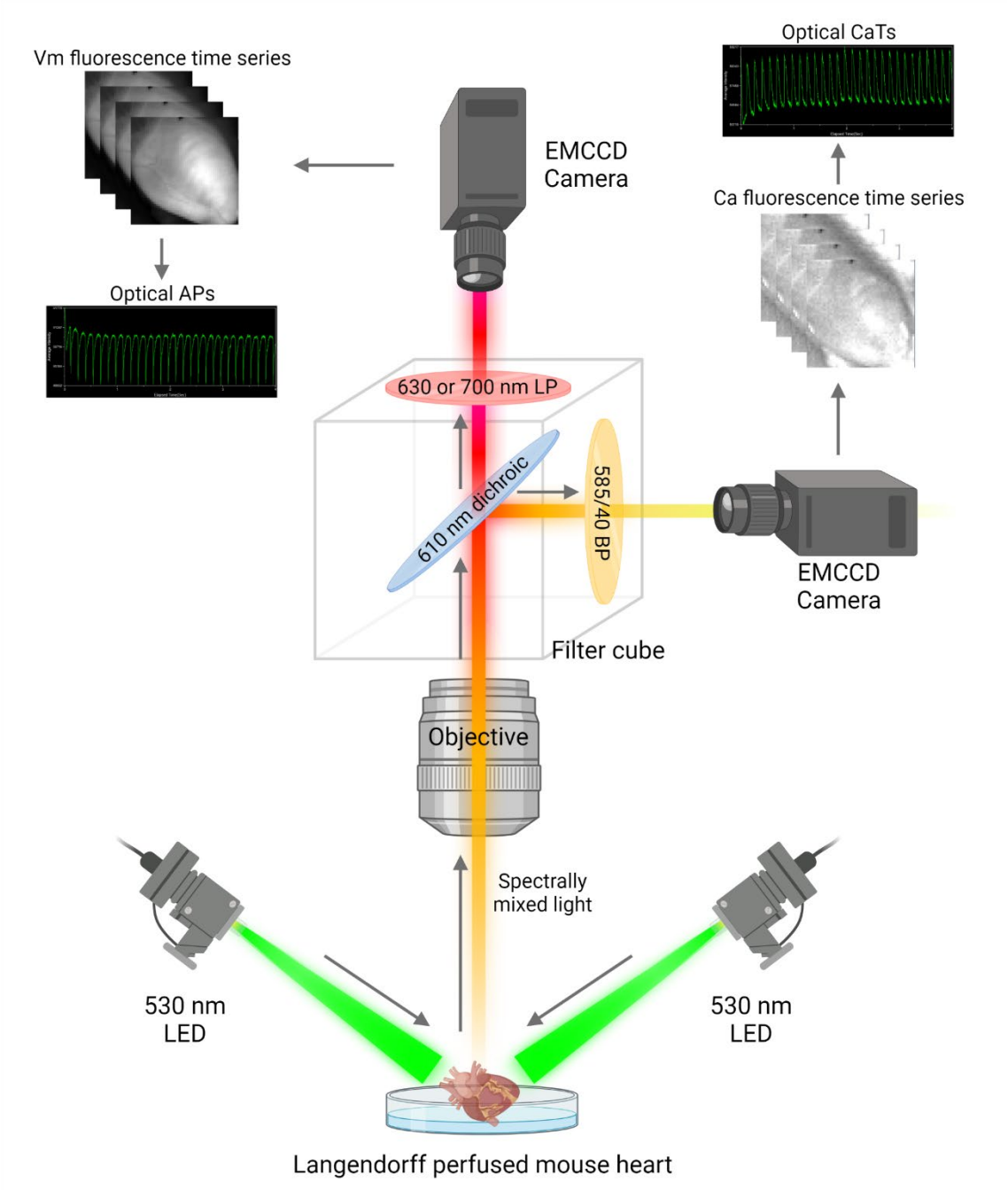
Figure 2-6. Langendorff perfused heart placed within a water jacketed bowl.

Krebs-Henseleit buffer at 37 °C continuously perfuses the heart via the aortic cannula. Electrocardiography leads provide real-time monitoring of cardiac electrical activity. Pacing electrodes are placed at the base of the heart allowing control of the heart rate.



After a 10-minute equilibration period, three LEDS emitting 530 ± 20 nm light were directed towards the left ventricle and used for illumination. The following filter set combinations were used to collect the fluorescent emissions depending on the fluorescent dyes used: Voltage-only mapping – 630 nm longpass for Di-4-ANEPPS; Simultaneous voltage and calcium (dual) mapping – 610 nm dichroic in combination with a 700 nm longpass for Rh-237, and 585/40 nm bandpass for Rhod-2 AM (**Figure 2-7**).

Figure 2-7. Schematic of optical mapping method



AP, action potential; BP, bandpass; Ca, calcium; CaT, calcium transient; EMCCD, electron multiplying charge-coupled device; LED, light emitting diode; LP, longpass; Vm, voltage.

The filtered fluorescent emission was captured by Photometrics Evolve 512Delta electron multiplying charge-coupled device cameras with a single pixel area of 16 μm^2 at 613.5 frames/s (≈1.6 ms exposure time) with 5 x 5 pixel binning to optimise signal-to-noise ratio and allow higher frame rates. Camera & LED control, image acquisition and export were all performed using MetaMorph (Molecular Devices). This allowed optical AP and CaT to be monitored during experiments (**Figure 2-7**) for motion artifacts, poor dye loading, or missed stimulus captures. Up to 36,000 images per recording were collected as a time series and exported in uncompressed Tagged Image File Format (TIFF) image stack with a resolution of 51 by 51 pixels. The maximum continuous recording time per time point was less than 60 seconds to minimise phototoxicity and photobleaching effects.

2.7.5.3. Ex vivo left ventricular pacing

Pacing electrodes were placed at the base of the left ventricles as previously described (Chapter 2.7.5.2). Pacing stimuli were generated using a Digitimer DS2A-Mk.II constant voltage isolated stimulator. The pacing threshold voltage was determined as the diastolic threshold of the preparation (typical 50 – 150 mV) and the left ventricle was paced at twice the threshold voltage. Pacing was controlled by Spike2 software (Cambridge Electronic Design Ltd.). As described previously, the baseline pacing CL was set at 120 ms, or 500 bpm. Pulse width was set at 2 ms.

Two custom pacing programmes were created using Spike 2 software for use during optical mapping recordings. A dynamic protocol was used to examine the restitution characteristics of the left ventricle in the presence or absence of FGF23. The protocol began with a 100-beat train at 150 ms CL. The CL was

then reduced by 10 ms every 20 beats, until a CL of 50 ms. There was a 2 s pause between each CL. A second 'S1-S2' protocol was used to investigate the effective refractory period. This consisted of a 20 beat S1 pacing train at 100 ms CLs, followed by an S2 extra-stimulus at 100 ms interval. The S1-S2 interval was progressively shortened by 5 ms decrements until a 40 ms interval was reached, after which the S1-S2 interval was shortened in 2 ms decrements until a 28 ms interval was reached. The protocol was halted when an arrythmia was induced, or at the point at which the first S2 extra-stimulus loses capture (i.e. the effective refractory period [ERP]), whichever occurs first. ERP determination was performed in LabChart (ADInstruments).

2.7.6. Optical mapping data analysis using ElectroMap

Optical mapping data was collected as a time series of images in the TIFF stack image format. Before analysis, these underwent lossless conversion to a MATLAB data file (.MAT) using a custom MATLAB script provided by Chris O'Shea to enable more efficient processing of the large data files. All optical mapping data were analysed using ElectroMap, an open-source software provided and developed by Chris O'Shea [406,407]. A custom region of interest was used to identify the left ventricular area for analysis. Images were processed using a Gaussian spatial filter – 3 x 3 pixel, standard deviation=1.5 – to reduce the noise floor and improve signal-to-noise ratio (SNR). A top-hat filter (100 ms length) was applied to normalise non-physiological baseline variability. Optical APs were inverted for analysis purposes. To account for adaption in cardiac electrical handling to changes in pacing CLs, the final 15 beats were ensemble averaged to improve signal-to-noise ratio.

The following analysis parameters were used [406]: 1. Action potential duration (APD)/calcium transient duration (CaTD) were defined as the time from maximum upstroke velocity (dF/dt_{max}) to 30, 50 and 80% repolarisation (APD_{30}, APD_{50} and APD_{80}) and decay ($CaTD_{30}$, $CaTD_{50}$ and $CaTD_{80}$), respectively; 2. Heterogeneity in ventricular repolarisation and calcium transient decay at 30, 50 and 80% was calculated as $\frac{X^{95}-X^{5}}{X^{50}}$, where X^{95} and X^{5} represent the 95th and 5th percentiles of the intraventricular APD and CaTD distribution within the region of interest, the median being X^{50}; 3. APD triangulation was represented as $APD_{80/30}$; 4. Conduction velocity (CV) was analysed using the multi-vector method, taking the mean of all local conduction vectors calculated across the region of interest; 5. APD and CaTD amplitude was measured from baseline to peak deflection; 6. Diastolic interval (DI) was calculated from APD_{90} to the following activation time; 7. Time to peak was defined as time from 10% to 90% rise; 8. Calcium exponential decay constant τ was calculated by exponential curve fitting between 30% and 90% from the peak.

2.7.7. Quantification of *ex vivo* arrhythmia burden

Bipolar ECGs collected during optical mapping experiments were analysed using ADInstruments LabChart. Incidence and type of ventricular arrhythmia were quantified. An arbitrary arrhythmia score based on the relative severity of ventricular arrhythmia was calculated for each mouse heart – for example, in increasing severity: sinus arrhythmia, premature ventricular beats, second degree heart block, non-sustained VT, third degree heart block and sustained VT.

2.7.8. *In vivo* echocardiography

In vivo murine echocardiography was performed by Sophie Broadway-Stringer on mice at day 8 of the chronic FGF23 protocol as described in Chapter 2.7.2.2. Transthoracic echocardiography was performed on a FUJIFILM Visualsonics Vevo® 2100 Imaging System with a MS 550D (40 MHz) transducer. Mice were placed in a supine position on a heated platform and sedated with 1-2% isoflurane. The chest was prepared with depilatory cream (Nair), shaved, and rinsed with water prior to imaging. Heart rate, core temperature and breathing rate were continuously monitored. Paws were secured to electrode pads to measure ECG. Eye lubrication was applied to prevent drying. Left ventricular geometry and systolic function were obtained from 2D parasternal long axis and short axis views in combination with M-mode echocardiography. Diastolic function was approximated from colour and pulsed doppler measurements of mitral flow velocities in an apical four-chamber view (**Figure 2-8**). Measurements from five cardiac cycles were averaged.

Figure 2-8. Summary of echocardiographic parameters used to assess left ventricular

A - systolic function, **B** - diastolic function, and **C** – corrected left ventricular mass (LVM). **D** - M-mode echocardiography of the left ventricle with interventricular septum thickness (IVS), left ventricle internal diameter (LVID) and left ventricular posterior wall (LVPW) measurements in both systole (s) and diastole (d). **E** – Doppler of blood flow velocity across mitral valve. Early (MV E) and late ventricular velocity (MV A); isovolumetric contraction (IVCT) and relaxation times (IVRT); and aortic ejection time (AET) are labelled.

Sophie Broadway-Stringer graciously supplied the example echocardiogram images.

A Ejection fraction (EF, %) $EF = 100 \times \left(\frac{LVvol;d - LVvol;s}{LVvol;d}\right)$

Fractional shortening (FS, %) $FS = 100 \times \left(\frac{LVID;d - LVID;s}{LVID;d}\right)$

Stroke volume (SV, μL) $SV = LVvol;d - LVvol;s$

where $LV\ end\ diastolic\ volume\ (LVvol;d) = \left(\frac{7.0}{2.4 + LVID;d}\right) \times LVID;d^3$

$LV\ end\ systolic\ volume\ (LVvol;s) = \left(\frac{7.0}{2.4 + LVID;s}\right) \times LVID;s^3$

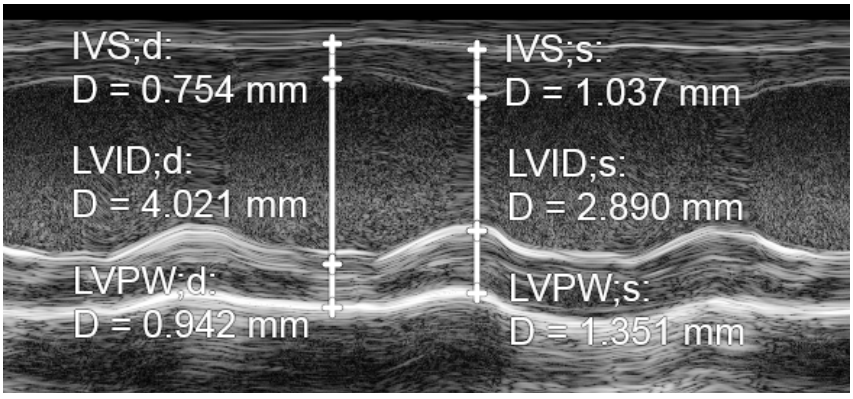
Cardiac output (CO, μL/min) $CO = SV \times heart\ rate$

B Myocardial performance index (MPI) $MPI = \frac{IVCT + IVRT}{AET}$

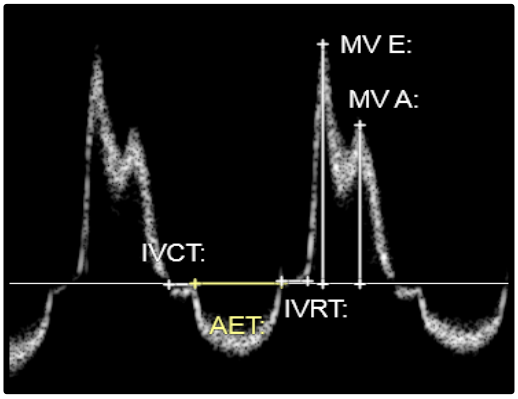
Mitra E/A ratio $E\ /\ A = \frac{MV\ E}{MV\ A}$

C LV mass $0.8 \times \{1.053 \times [(LVID;d + LVPW;d + IVS;d)^3 - LVID;d^3]\}$

D



E



2.7.9. Plasma separation and FGF23 quantification

2.7.9.1. Plasma separation

Animal technicians at the Biomedical Sciences Unit performed saphenous vein venepuncture on day 4 of the chronic FGF23 protocol as described in Chapter 2.7.2.2. Venepuncture occurred when at least 4 hours had elapsed following the intraperitoneal FGF23 injections. Venous blood was collected in EDTA-treated tubes and transferred to the laboratory within 60 minutes where it underwent centrifugation for 10 minutes at 2,000 x g in a refrigerated (4 °C) centrifuge. The separated plasma was placed into clean 200 µL Eppendorf tubes in 30 µL aliquots and stored at -80 °C until required.

2.7.9.2. Plasma FGF23 quantification

Plasma c-terminal FGF23 quantification was performed using the Immutopics mouse FGF-23 (C-Term) sandwich enzyme-linked immunosorbent assay kit (Quidel, 60-6300) according to manufacturer protocols.

Murine plasma samples collected as previously described (Chapter 2.7.7.1) were thawed on ice. Each sample was diluted between 1:2 and 1:10 to reduce the probability of a “hook effect” and assayed in duplicate. 25 µL of sample, control and FGF23 standards were pipetted into a streptavidin-coated 96-well plate provided in the kit, followed by 50 µL purified goat polyclonal antibody solution containing equal parts biotinylated anti-FGF23 antibody and horse radish peroxidase (HRP)-conjugated anti-FGF23 antibody. The plate was covered in foil and incubated at room temperature for 3 hours on a horizontal rotator set at 180-200 rpm. This allowed the FGF23 contained in the sample to be bound by the

capture antibodies, and for the biotinylated antibody to bind to the streptavidin-coated well forming a ‘sandwich’ complex. Wells were then thoroughly washed to remove unbound antibody before the addition of 100 µL tetramethylbenzidine-hydrogen peroxide chromogenic substrate and protected from light. Following an incubation period of 30 minutes at room temperature on a horizontal rotator, the absorbance at 620 nm was read in a Gemini™ spectrophotometric microplate reader (Molecular Devices). 50 µL stop solution containing 1 M sulfuric acid was added to each well before a second read at 450 nm. Absorbances were read and corrected against a reagent blank, and the mean corrected absorbance was calculated for each pair of duplicate assays. The mouse plasma FGF23 concentration was determined from the standard curve generated by plotting the absorbances against their respective FGF23 standards provided in the kit.

2.7.10. Cardiac weights and tibial length measurements

Mice undergoing the chronic FGF23 protocol (Chapter 2.7.2.2) had cardiac weight and tibial length measurements taken following the optical mapping experiment. The heart was excised from the thoracic cavity, stripped of any fat, and blotted dry. After weighing, the heart was divided into the following constituent parts - left atrium, right atrium, left ventricle, right ventricle, septum – blotted dry and re-weighed. Tissue was then immediately stored at -80 °C for later use in protein expression studies detailed in Chapter 2.4.

Both legs were severed above the knee joint. Skin, bone, and muscle were stripped mechanically to reveal expose the tibia. The tibia length was determined

using a micrometre calliper from the most proximal to the most distal end of the tibia. An average of both tibias was taken.

The cardiac weight was divided by total body weight and tibia length to produce heart weight to body weight (HW/BW) and heart weight to tibial length (HW/TL) ratios, respectively. Cardiac chamber weights were also normalised to body weight and tibial length.

2.8. STATISTICAL ANALYSIS

Optical mapping and echocardiograph analyses were done in a blinded fashion. All data are presented as mean ± standard error of the mean (SEM) for parametric variables, or median (interquartile range [IQR]) for non-parametric variables. Normality was assessed by Kolmogorov-Smirnov test and quantile-quantile polts. Biomarkers such as FGF23 tend to be non-parametrically distributed. Further statistical analyses using log-normal FGF23 were conducted. Statistical analysis was performed using unpaired Student's t test when comparing two groups. One-way Analysis of Variance (ANOVA) with Tukey post-hoc analysis when comparing two or more groups to the control mean, and two-way ANOVA with Sidak post-hoc analysis when two variables were being tested.

Nested analyses were performed where multiple observations, that is, technical replicates, were taken per biological replicate. For example, nested one-way ANOVA were performed for IF experiments detailed in Chapter 2.6, where the average fluorescence across three fields of views (images), or six wells (technical replicates) were taken per condition. GraphPad Prism 9.4.1 was used for statistical testing where significance as taken as $p<0.05$.

CHAPTER 3. CHRONIC HUMAN CARDIAC FIBROBLAST ACTIVATION *IN VITRO* ATTENUATES MYOFIBROBLAST PHENOTYPE REVERSIBILITY

3.1. EXTENT OF PERSONAL CONTRIBUTION

A manuscript containing data within this chapter is current being prepared for submission. I conducted the western blot and real-time polymerase chain reaction experiments. Caitlin Hall performed the CyQUANT NF Proliferation Assay and immunofluorescence work. We share first authorship of the submitted manuscript. Max Cumberland provided the differentiated human induced pluripotent stem cell-derived cardiac fibroblasts. Davor Pavlovic and Chris Denning share senior authorship.

3.2. INTRODUCTION

Cardiac fibrosis, both diffuse and focal, underlies multiple forms of cardiovascular disease (CVD) and is strongly associated with an increased risk of death [408-410]. A study by Gulati et al. found that patients with midwall fibrosis, linked to dilated cardiomyopathy, had increased risk of cardiovascular death and transplantation, sudden cardiac death and heart failure death [409]. Diabetes has also been linked to increased cardiac fibrosis and has been found to have increased incidence of hospitalisation for heart failure in these patients [411]. Furthermore, fibrosis has been linked to an increased susceptibility to arrhythmia and ventricular tachycardia [412]. There is, understandably, great interest in the development of effective therapeutic strategies which target reversal of cardiac fibrosis and have the potential to reduce morbidity and mortality [413-415].

Cardiac fibroblasts comprise roughly 30-60% of the total myocardial cell population providing both an essential structural support and a communication network coupled by gap junctions [416,417]. Fibroblasts support normal cardiac structure and electromechanical function through homeostasis of the extracellular matrix (ECM) and cross-talk with other cardiac cell types [418]. Mechanical stress, inflammation, hormonal stimulus, or ischaemia lead to activation of cardiac fibroblasts and excessive deposition of ECM, with an increase in collagen cross linking. This cardiac fibrosis leads to remodelling of the myocardium adversely affecting function, initially in diastole, and conduction [419,420].

Pathological cardiac remodelling is associated with activation and differentiation of fibroblasts into myofibroblasts [421]. Myofibroblasts are characterised as having a spindle shape, expression of contractile protein α-smooth muscle actin (α-

SMA), secretion of ECM components such as collagens and a change in proliferation rates [422,423]. Transition of fibroblasts into myofibroblasts occurs following immediate or sustained injury, which is mediated through several processes, including increased mechanical stress and secretion of cytokines, such as transforming growth factor-beta (TGF-β). Several studies have demonstrated that TGF-β activates cardiac fibroblasts [424-426], and contributes to *in vitro* and *in vivo* murine cardiac fibrosis and hypertrophy [427,428]. Further studies utilising models of TGF-β inhibition or knockdown have shown an attenuated fibrotic response. However, perhaps unsurprisingly, due to the complexity and widespread involvement of the TGF-β signalling pathway, increased mortality in murine models has also been observed suggesting this might not be a successful target for therapeutic use [429,430].

Healthy human myocardium is described as having a Young's modulus of ~10-30 kPa. Diseased or damaged myocardium is much stiffer, at more than 100 kPa, often due to the presence of fibrosis [78,431-433]. Recent studies have shown that use of stiff substrates (>50 kPa), which mimic the elastic modulus of a fibrotic myocardium, leads to activation of cardiac fibroblasts and transition into myofibroblasts [434,435]. Studies utilising murine cardiac fibroblasts demonstrate that this transition begins within days of isolation and culture, even in the absence of TGF-β [436,437]. It has therefore been suggested that the use of softer substrates, which more closely resemble the elastic modulus of healthy myocardium may prevent and possibly reverse activation of cardiac fibroblasts when maintained in 2D culture [431,436]. Whether chronically activated human myofibroblasts can be transformed back to the quiescent cardiac fibroblast phenotype is unclear.

Given the central role of the myofibroblast in fibrosis, this study investigates the potential for reversal of activated human cardiac myofibroblasts back to quiescent fibroblasts, as a means to reduce the fibrotic burden of the heart.

3.3. METHODS

The experimental methods used in this study are summarised below and in **Table 3-1.** Experimental conditions and outcomes for HCFs and hiPSC-cFbs. Protocols of each experimental technique have been detailed in Chapter 2, Experimental Methods.

Human cardiac fibroblasts (HCF) obtained from the ventricles of explanted hearts taken at the time of cardiac transplantation were purchased from PromoCell GmbH (C-12375). These cells were used to model chronically activated myofibroblasts as found in chronic heart failure and kidney failure with replacement therapy. After receipt from the supplier, HCFs were cultured using Fibroblast Growth Medium 3 (PromoCell®, C-23025) for up to 10 passages (split ratio 1:10) in T75 tissue culture flasks in a humidified incubator at 37 °C and 5% CO2. HCFs were then cultured on Corning stiff polystyrene culture plates (Young's modulus [*E*] = 3 GPa) before subculture on soft (*E* = 2 kPa and 25 kPa) hydrogel culture plates (Matrigen Softwell, SW6-EC-2/SW6-EC-25). To promote efficient adhesion of HCFs, all cultureware were coated with 10 µg/mL fibronectin (Sigma-Aldrich, F1141).

In separate experiments, human induced pluripotent stem cell derived cardiac fibroblasts (hiPSC-cFbs) were cultured on Matrigel ® coated Corning polystyrene culture plates using Fibroblast Growth Medium 3 (FGM3) in the presence of 10

μM SB431542 (Selleck Chemicals, S1067) and 10 ng/ml Fibroblast Growth Factor 2 (FGF2) (Peprotech, 100-18B). iPSC-cFbs were maintained for up to 10 passages (split ratio 1:10).

The following drugs were added to the respective culture media as summarised in Table 1: 10 ng/mL recombinant human TGF-β1 protein expressed from a CHO cell line (R&D Systems, 240-B) [438], 30 nM TGF-β receptor 1 inhibitor SD208 (Tocris, 3269) [439], 10 μM TGF-β receptor inhibitor SB431542 [397].

Table 3-1. Experimental conditions and outcomes for HCFs and hiPSC-cFbs

Cell	Substrate	Treatment	Treatment Duration	Outcome
HCF	3 GPa 25 kPa 2 kPa	Vehicle control 10 ng/ml TGF-β 30 nM SD208	2-4 days	Proliferation by CyQUANT Activation by RT-PCR (*ACTA2*, *COL1A1*); IF (α-SMA); and Western Blot (α-SMA, Collagen 1)
hiPSC-cFb	3 GPa	Vehicle control 10 ng/ml TGF-β 30 nM SD208 10 μM SB431542	2-4 days	Proliferation by CyQUANT Activation by RT-PCR (*ACTA2*, *COL1A1*, *COL3A1*); IF (α-SMA);

α-SMA, alpha-smooth muscle actin; E, elastic modulus; HCF, human cardiac fibroblast; IF, immunofluorescence; hiPSC-cFb, human induced pluripotent stem cell-derived cardiac fibroblast; TGF-β, transforming growth factor-beta; RT-PCR, real-time reverse transcriptase polymerase chain reaction.

Data are presented as mean ± standard error of the mean. Differences between group means were examined using nested one-way analysis of variance

(ANOVA) or Student's t test and were considered statistically significant when $P < 0.05$. Subgroups for the nested analysis were replicates done on different days with different passage numbers. Statistical analysis was conducted using GraphPad Prism 9.

3.4. RESULTS

3.4.1. Long-term culture of human cardiac fibroblasts on stiff substrates leads to non-reversible myofibroblast transition

Myocardium stiffness has been associated with activation of cardiac fibroblasts to myofibroblasts [78]. Culture of primary healthy murine cardiac fibroblasts on stiff plastic plates is thought to induce myofibroblast activation [440]. HCFs were obtained from the explanted hearts of patients undergoing cardiac transplantation and cultured in a 2D monolayer on "stiff" polystyrene plates (E = 3 GPa) for up to 10 passages to chronically activate HCFs. HCFs were then subcultured onto softer substrates (E = 25 or 2 kPa) - for 2 days for immunofluorescence and proliferation experiments and 4 days for qPCR and western blotting - to examine whether this might reverse or reduce the activation state of HCFs. α-SMA and collagen 1 were utilised as markers of fibroblast activation and transition into myofibroblasts. Vimentin was used as a marker for cardiac fibroblasts.

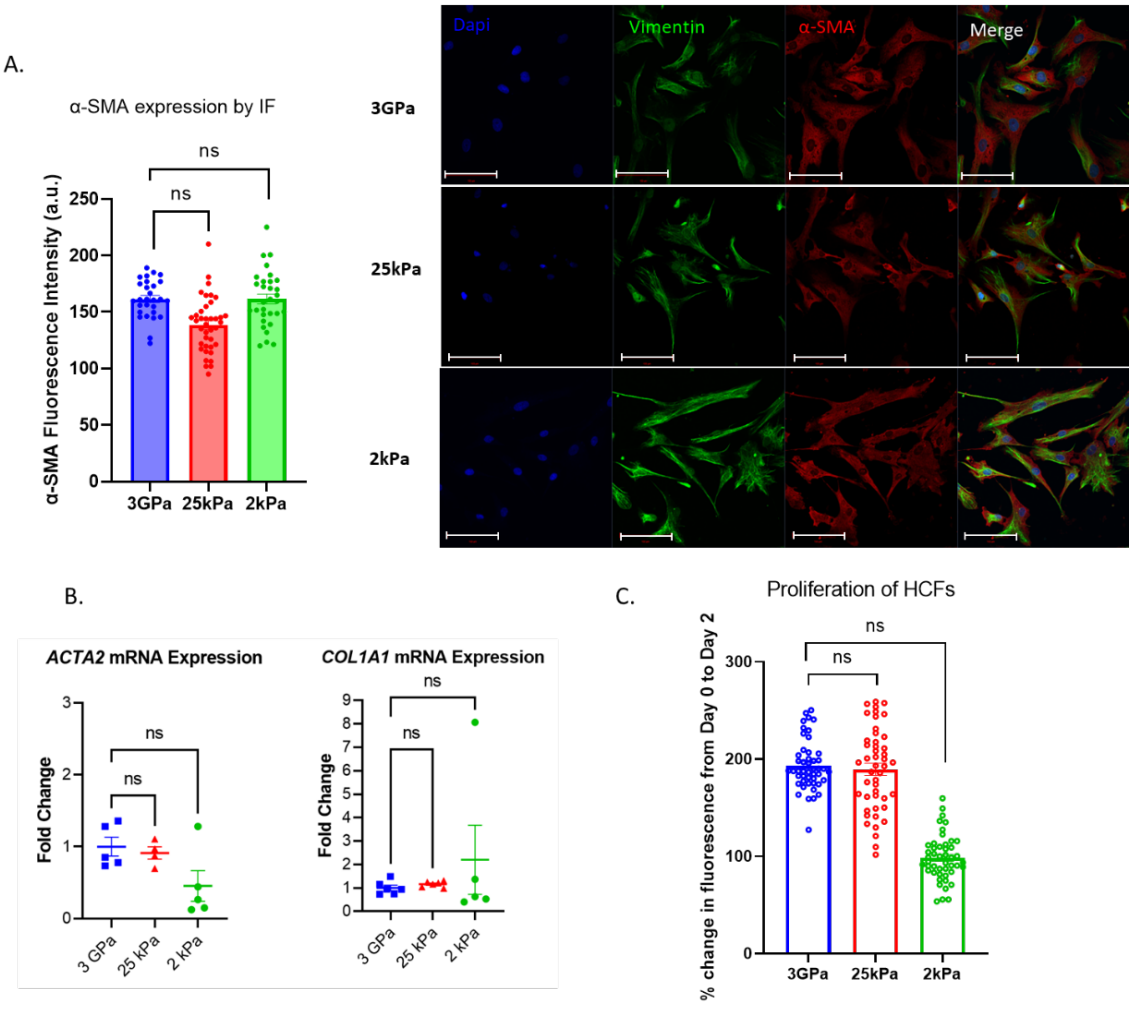
As expected, α-SMA was detected by immunofluorescence (IF) staining in HCF cultured on 3 GPa polystyrene plates (mean intensity 159±3.7 arbitrary units [a.u.]) (**Figure 3-1 A**). Subsequent culture on 25 kPa or 2 kPa soft substrates did not result in any significant reduction in α-SMA expression by IF (**Figure 3-1 A**, mean intensity 138±3.7 a.u, 161±4 a.u respectively, $p > 0.1$). These findings were

supported by RT-PCR analysis of *ACTA2* and *COL1A1* mRNA transcripts, which showed comparable levels of expression between HCFs cultured on the stiff and soft substrates (**Figure 3-1 B**). When proliferation was assessed over a 48-hour period, no significant difference was seen between HCFs grown on 3 GPa (**Figure 3-1 C**, mean % change 193.7±4.8) and 25 kPa (**Figure 3-1 C**, mean % change 193.2±7.4, p = >0.9). A non-significant reduction in proliferation of cells grown on 2 kPa (mean % change 97.9±5.5) when compared with 3 GPa (mean % change 193.7±4.8) was observed (**Figure 3-1 C**, p = >0.1).

These data suggest that chronically activated HCFs cannot be de-activated when subsequently cultured on softer substrates (25 kPa or 2 kPa) that more closely reflect the stiffness of a healthy human myocardium.

Figure 3-1. Activation status and proliferation of human cardiac fibroblasts on 3 GPa, 25 and 2 kPa culture plates.

A – Vimentin and α-SMA expression by immunofluorescence after two days in culture. Nuclei (DAPI in blue), vimentin (green), α-SMA (red) Scale bar = 100 µm. **B** – α-SMA (*ACTA2*) and Collagen 1 (*COL1A1*) expression by RT-PCR following 4 days in culture. **C** – Proliferation was assessed over 48 hours and evaluated as a percentage change in fluorescence from baseline (day 0). Data presented as mean ± S.E.M. N = 3 experiments, 3 images per condition (A), 4-6 (B); 4 plates, 47 wells/biological replicates per plate (C). Nested one-way ANOVA compared with control (3GPa cells). Subgroups for nested analyses were replicates from different days and passages. Statistical significance was defined as $p < 0.05$.



TGF-β is a well-established inducer of the myofibroblast phenotype. Studies have shown that use of a TGF-β receptor inhibitor, such as SD208, can prevent activation [429]. Having established that the HCFs were activated at baseline (**Figure 3-1**), the possibility of further activation using TGF-β and reversal of this activation using TGF-β receptor inhibition was investigated.

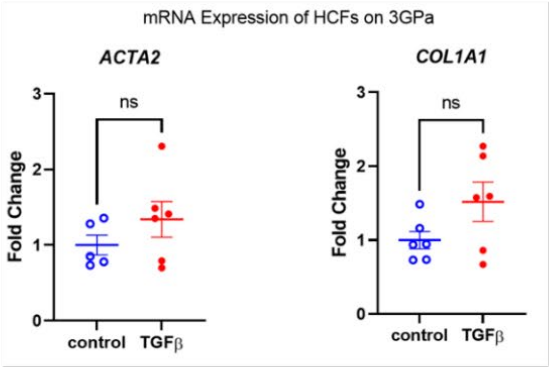
HCFs treated with TGF-β for 4 days demonstrated no significant increase in α-SMA and Collagen 1 expression at mRNA (**Figure 3-2 A**, $ACTA2_{TGF\text{-}\beta}$ mean fold change 1.3±0.2 , p = >0.5; $COL1A1_{TGF\text{-}\beta}$ mean fold change1.5±0.3, p = >0.1) or protein levels (**Figure 3-2 B**, α-SMA/$GAPDH_{control}$ 106.2±15.2, α-SMA/$GAPDH_{TGF\text{-}\beta}$ 128.1±12.8, p = >0.3; Collagen 1/$GAPDH_{control}$ 99.9±7.5, Collagen 1/$GAPDH_{TGF\text{-}\beta}$ 96.7±6.3, p = > 0.7) compared to vehicle control, when cultured on 3 GPa plastic. Neither the use of TGF-β (mean % change 179±7.6) nor its receptor inhibitor SD208 (mean % change 181±6.5) had any detectable effect on proliferation (**Figure 3-2 C**, p = >0.5). HCFs displayed ~70% positive staining for α-SMA when assessed by immunofluorescence staining (**Figure 3-3**). There was also no significant effect on α-SMA expression by IF following treatment with TGF-β (mean intensity 159.2 ±4) or SD208 (mean intensity 149.9±4.4) (**Figure 3-2 D & E**, p = >0.9). Surprisingly, α-SMA staining showed a diffuse staining pattern rather than the expected fibre-like pattern (**Figure 3-1 A**, **Figure 3-2 E**, **Figure 3-5 E** and **Figure 3-6 E)**. Secondary antibody-only controls show that this was not due to non-specific binding or background fluorescence staining (**Figure 3-4**).

These results indicate that long-term culture of diseased HCFs on stiff substrates leads to persistent myofibroblast transition and renders them unresponsive to TGF-β stimulation or indeed TGF-β inhibition, using SD208. Our results therefore imply that once chronically activated, human cardiac myofibroblasts cannot transition back to quiescent fibroblasts.

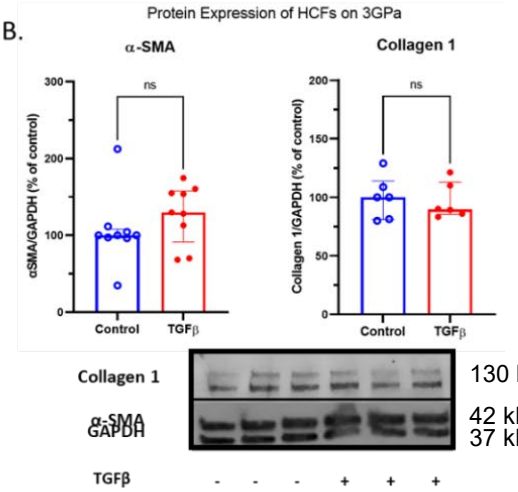
Figure 3-2. Activation status and proliferation of human cardiac fibroblasts on 3 GPa culture plates.

Cells were grown in the presence and absence of 10 ng/ml TGF-β and/or 30 nM SD208 for four days. **A** – Activation of HCF as measured by RT-PCR for *ACTA2* and *COL1A1*. **B** – Activation status of HCF measured by western blotting for α-SMA and collagen 1 protein. **C** – Proliferation over 48 hours was evaluated as a percentage change from baseline (day 0) in fluorescence by CyQUANT assay. **D** – Quantification of α-SMA protein expression by immunofluorescence. **E** – Representative immunofluorescence images for panel D. Scale bar = 100 μm. Data presented as mean ± S.E.M. N = 5 (A), 6-9 (B); 4 plates, 6+ wells per plate (C), 3 experiments, 3 images per condition (D). t-test (A, B) and nested one-way ANOVA (C, D) compared with undrugged control. Significance was defined by $p < 0.05$.

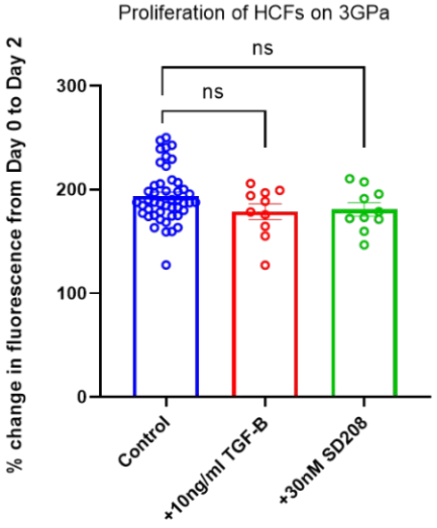
A.


mRNA Expression of HCFs on 3GPa
ACTA2
COL1A1
Fold Change
ns
control
TGFβ

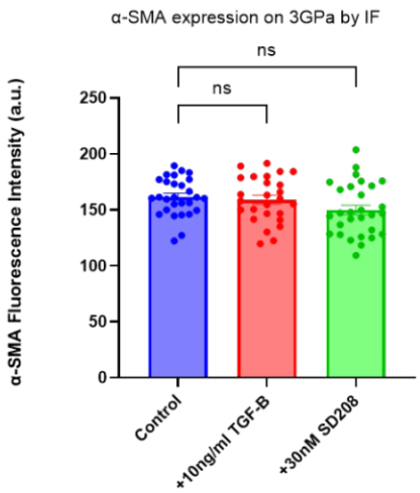
B.


Protein Expression of HCFs on 3GPa
α-SMA
Collagen 1
αSMA/GAPDH (% of control)
Collagen 1/GAPDH (% of control)
ns
Control
TGFβ
Collagen 1
α-SMA
GAPDH
130 kDa
42 kDa
37 kDa
TGFβ

C.


Proliferation of HCFs on 3GPa
% change in fluorescence from Day 0 to Day 2
ns
Control
+10ng/ml TGF-B
+30nM SD208

D.


α-SMA expression on 3GPa by IF
α-SMA Fluorescence Intensity (a.u.)
ns
Control
+10ng/ml TGF-B
+30nM SD208

E.

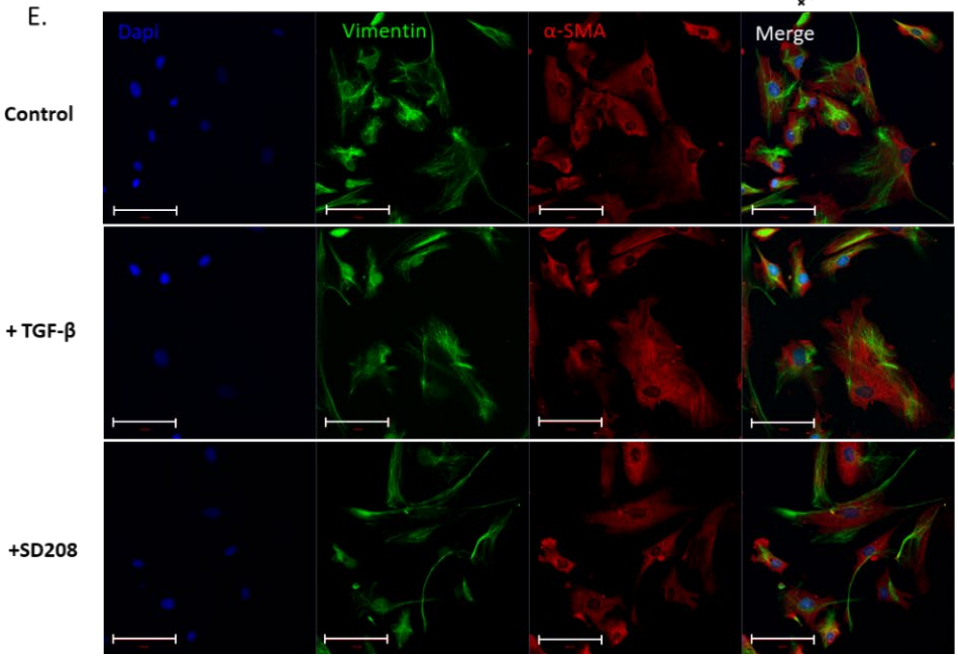

Dapi
Vimentin
α-SMA
Merge
Control
+ TGF-β
+SD208

Figure 3-3. Immunofluorescence staining of α-SMA in HCFs.

Cells were grown in the presence of TGF-B, SD208 for 48 hours. Data presented as percentage of cells displaying positive α-SMA expression. No significant difference was seen in α-SMA expression in any of the drugged conditions (p = > 0.9). Data presented as mean ± S.E.M. N = 3 plates, 18 wells, nested one-way ANOVA compared with control.

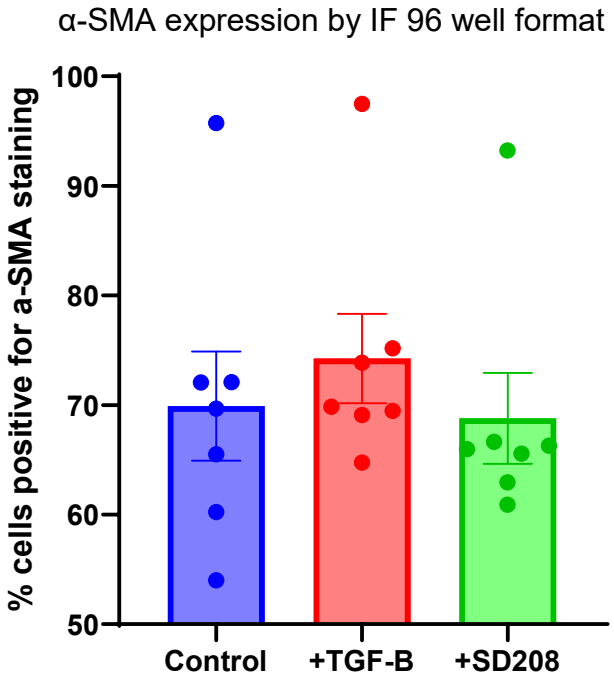
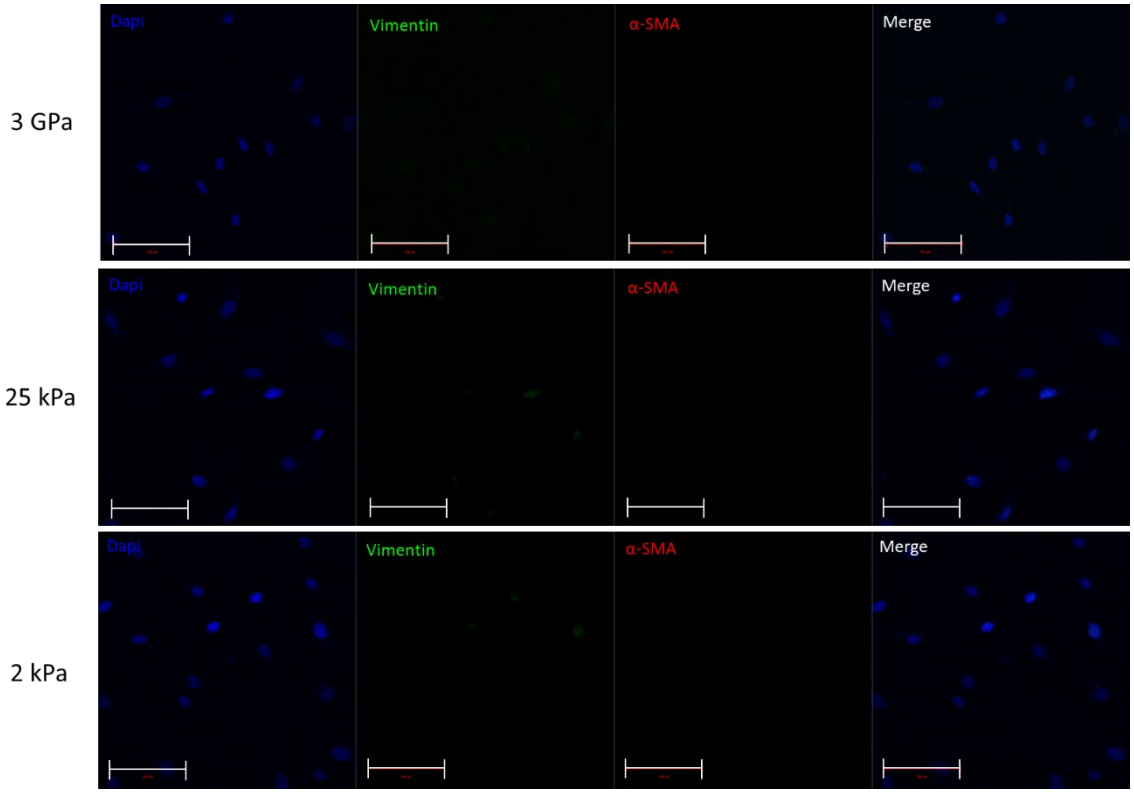


Figure 3-4. Representative images for secondary antibody only negative controls in HCFs.

Cells were grown on stiff 3 GPa plastic, soft 25 or 2 kPa substrates for 48 hours. No non-specific background staining is observed for Alexa fluor® 488 (vimentin) or Alexa fluor® 647 (α-SMA). Scale bar is 100 μm.



3.4.2. A combination of mechanical and biochemical inputs has no effect on myofibroblast activation

In an independent set of experiments, we investigated whether a combination of culture on soft substrates and TGF-β receptor inhibition could reverse fibroblast activation. Myofibroblasts generated from long-term culture (over 2 weeks) on 3 GPa substrates were subcultured onto the soft 25 and 2 kPa plates in combination with TGF-β addition and/or TGF-β receptor inhibition (SD208).

Culture on 25 kPa, in the presence of TGF-β (mean % change 221±12) or SD208 (mean % change 191±11) demonstrated no significant effect on proliferation (**Figure 3-5 C**, p = >0.9), nor expression of α-SMA as assessed by immunofluorescence (**Figure 3-5 D & E**; TGF-β treated mean intensity 146.7±3.5; SD208 treated mean intensity 140.7±3.1, p = >0.5). As demonstrated in Figure 4, mRNA and protein expression of α-SMA or Collagen 1 were also unaffected by addition of TGF-β (**Figure 3-5 A & B**, summarised in **Table 3-2**).

Culture on 2 kPa in the presence of TGF-β (mean % change 56±13) or SD208 (mean % change 39±11), similarly yielded no significant differences in proliferation (**Figure 3-6 C**, p = >0.5), nor expression of α-SMA (**Figure 3-6 D & E** TGF-β treated mean intensity 170±5.7; SD208 treated mean intensity 172±3.9, p = >0.5). Expression of α-SMA and Collagen 1 were also unaffected at the mRNA transcript or protein level (**Figure 3-6 A & B**, summarised in **Table 3-2**).

These data further demonstrate that chronically activated HCFs do not respond to TGF-β treatment and cannot transition back to quiescent state when cultured on soft substrates in the presence or absence of TGF-β inhibitor.

Table 3-2. Myofibroblast Markers on Soft Culture Plates by RT-PCR and Western Blot.

Data presented as mean ± S.E.M. *t*-test of TGF-β treated cells versus vehicle control. Western blot data presented as a ratio of protein of interest (POI) and GAPDH as a loading control.

RT-PCR	Gene of Interest	TGF-β Mean Fold Change versus Control	P
25 kPa	*ACTA2*	1.2 ± 0.6	0.9
	COL1A1	1.0 ± 0.1	0.9
2 kPa	*ACTA2*	0.4 ± 0.2	0.6
	COL1A1	0.5 ± 0.1	0.8

Western Blot	Protein of Interest	Control (POI/GAPDH)	TGF-B (POI/GAPDH)	P
25 kPa	α-SMA	107.2 ± 6.8	168.7 ± 26.5	0.2
	Collagen 1	101.3 5.5	97.8 7.1	0.7
2 kPa	α-SMA	96.6 ± 3.5	130.2 ± 29.4	0.3
	Collagen 1	142.2 ± 52.8	135.9 ± 53.8	0.9

Figure 3-5. Activation status and proliferation of human cardiac fibroblasts on 25 kPa culture plates.

Cells were grown in the presence and absence of TGF-β and/or SD208 for 4 days. **A** – Activation of HCF as measured by RT-PCR for ACTA2 and COL1A1. **B** – Activation status of HCF as determined by western blotting of α-SMA and collagen 1 protein. **C** – Proliferation over 48 hours was evaluated as a percentage change in fluorescence from baseline (day 0) by CyQUANT assay. **D** – α-SMA expression by immunofluorescence. **E** – Representative immunofluorescence images for panel D. Scale bar = 100 μm. Data presented as mean ± S.E.M. N = 6 (A), 6-12 (B); 4 plates, 6+ wells per plate (C), 3 experiments, 3 images per condition (D). t-test (A, B) and nested one-way ANOVA (C, D) compared with undrugged control. Significance was defined as $p < 0.05$.

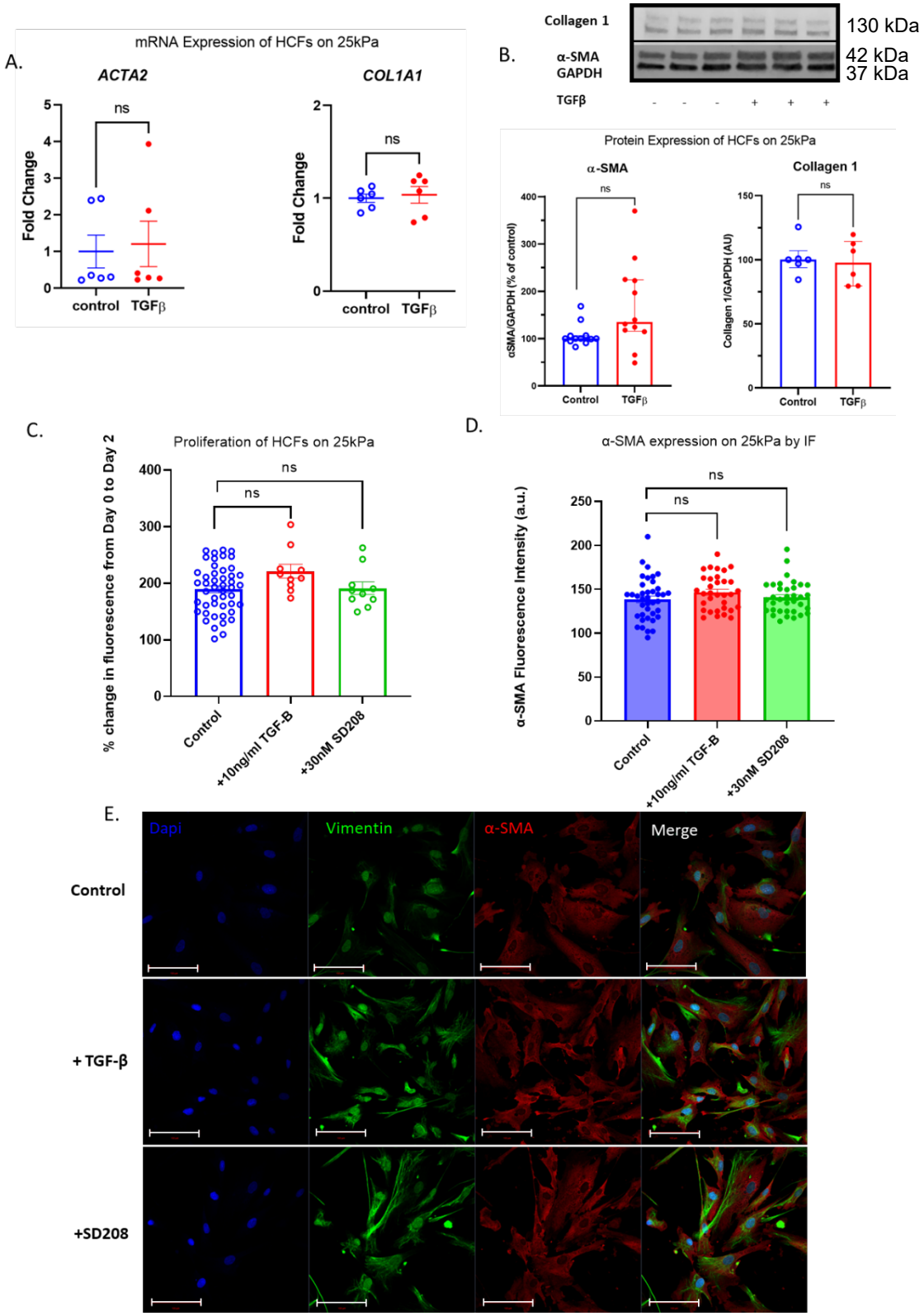
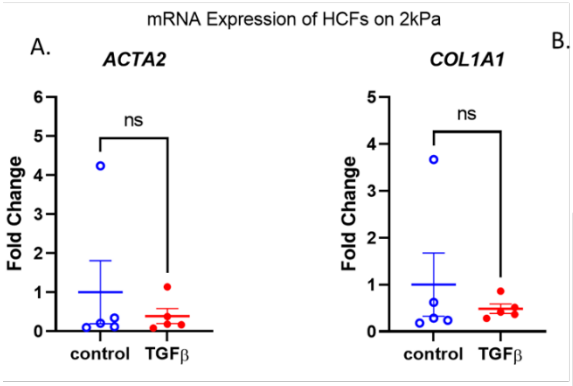
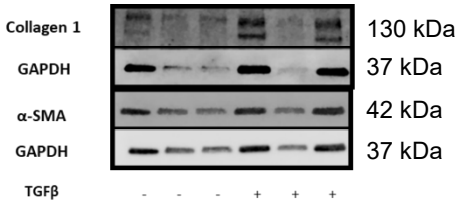
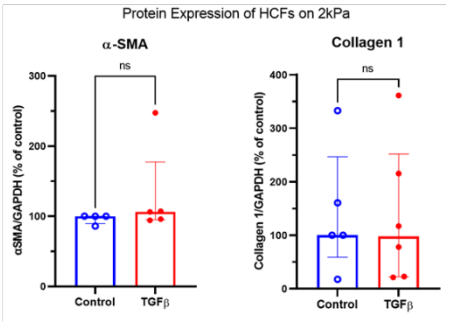

A.
mRNA Expression of HCFs on 25kPa
ACTA2
COL1A1
Fold Change
ns
control
TGFβ
B.
Collagen 1
α-SMA
GAPDH
130 kDa
42 kDa
37 kDa
TGFβ
Protein Expression of HCFs on 25kPa
α-SMA
Collagen 1
αSMA/GAPDH (% of control)
Collagen 1/GAPDH (AU)
Control
TGFβ
C.
Proliferation of HCFs on 25kPa
% change in fluorescence from Day 0 to Day 2
Control
+10ng/ml TGF-B
+30nM SD208
D.
α-SMA expression on 25kPa by IF
α-SMA Fluorescence Intensity (a.u.)
E.
Dapi
Vimentin
α-SMA
Merge
Control
+ TGF-β
+SD208

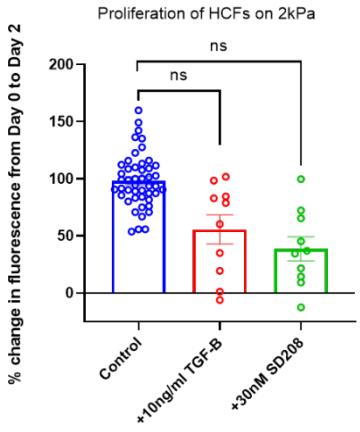
Figure 3-6. Activation status and proliferation of human cardiac fibroblasts on 2 kPa culture plates.

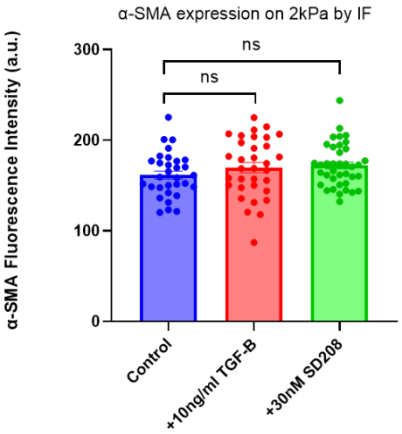
Cells were grown in the presence and absence of TGF-β and/or SD208 for four days. **A** – Activation of HCF as detected by RT-PCR for ACTA2 and COL1A1. **B** – Activation status of HCF as determined by western blotting for α-SMA and collagen 1 protein. **C** – Proliferation over 48 hours was evaluated as a percentage change in fluorescence from baseline (day 0) by CyQUANT assay. **D** – α-SMA expression by immunofluorescence. **E** – Representative immunofluorescence images for panel D. Scale bar = 100 μm. Data presented as mean ± S.E.M. N = 5 (A), 4-5 (B); 4 plates, 6+ wells per plate (C), 3 experiments, 3 images per condition (D). t-test (A, B) and nested one-way ANOVA (C, D) compared with undrugged control. Significance was defined as $p < 0.05$.

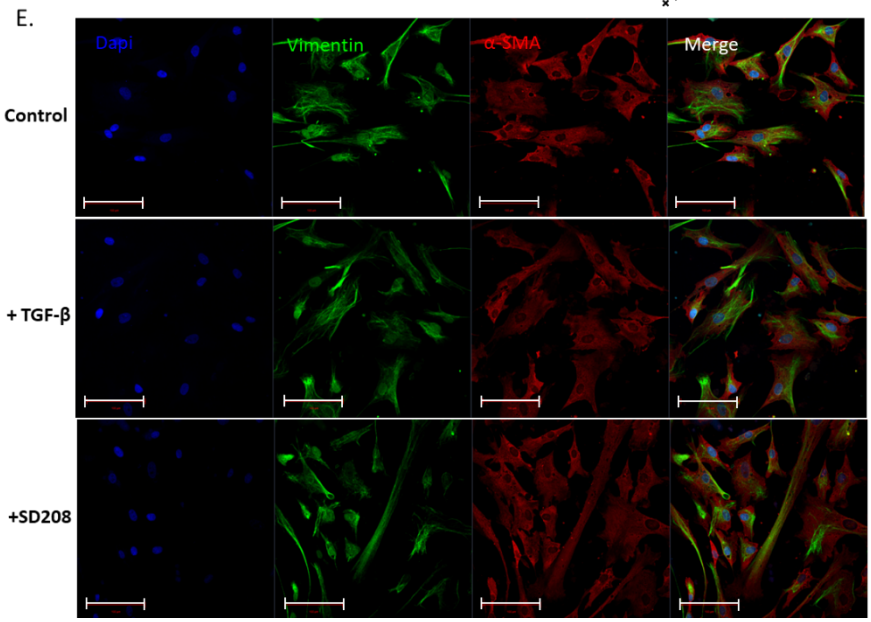

mRNA Expression of HCFs on 2kPa
A.
ACTA2
COL1A1
Fold Change
ns
control
TGFβ


B.
Collagen 1
GAPDH
α-SMA
GAPDH
TGFβ
130 kDa
37 kDa
42 kDa
37 kDa


Protein Expression of HCFs on 2kPa
α-SMA
Collagen 1
αSMA/GAPDH (% of control)
Collagen 1/GAPDH (% of control)
ns
Control
TGFβ


C.
Proliferation of HCFs on 2kPa
% change in fluorescence from Day 0 to Day 2
ns
Control
+10ng/ml TGF-B
+30nM SD208


D.
α-SMA expression on 2kPa by IF
α-SMA Fluorescence Intensity (a.u.)
ns
Control
+10ng/ml TGF-B
+30nM SD208


E.
Dapi
Vimentin
α-SMA
Merge
Control
+ TGF-β
+SD208

3.4.3. hiPSC derived cardiac fibroblasts are responsive to TGF-β stimulation and inhibition

To further investigate whether chronic activation of HCFs is reversible, separate experiments using hiPSC-cFbs were performed (see **Figure 3-7** for protocol schematic). Human iPSC-cFbs were cultured on 3 GPa substrates in the presence of TGF-β receptor inhibitor SB431542 to generate a quiescent cardiac fibroblast. hiPSC-cFbs were cultured in the absence of SB431542 to generate an activated fibroblast (myofibroblast) phenotype. Quiescent cells showed a significant increase in α-SMA expression when exposed to TGF-β (13.26%±2.1 versus 44.41%±1.5, p = <0.001) (**Figure 3-8 A**). Of note is that after two days of culture on stiff surfaces in the absence of TGF-β a two-fold increase in the number of quiescent cells positively expressing α-SMA was observed (**Figure 3-8 A**, 13.26%±2.1 vs 25.42%±1.6, p = 0.07), indicating that culture on stiff substrates alone induces α-SMA expression.

As expected, exposure to TGF-β, or subsequently to inhibitors SD208 and SB431542, did not significantly modify α-SMA expression in activated hiPSC-cFbs when compared to the control (**Figure 3-8 B**, p = >0.5). This mirrors our observation with the activated HCFs; culture on stiff substrates (3 GPa) activates cardiac fibroblasts and makes them unresponsive to TGF-β stimulation and inhibition. Surprisingly, culture of hiPSC-cFbs over 2 weeks in the absence of SB431542 supressed the number of α-SMA positive cells that display fibre-like staining pattern (**Figure 3-8 B**).

Figure 3-7. Schematic of experimental process for human induced pluripotent stem cell derived cardiac fibroblasts (hiPSC-cFbs).

Cells were grown for 2 weeks in the presence or absence of 10 μM SB431542 to generate quiescent and activated fibroblasts, respectively. hiPSC-cFbs were subjected to further treatments of 10 ng/ml TGF-β, 30 nM SD208 or 10 μM SB431542 for 2-4 days.

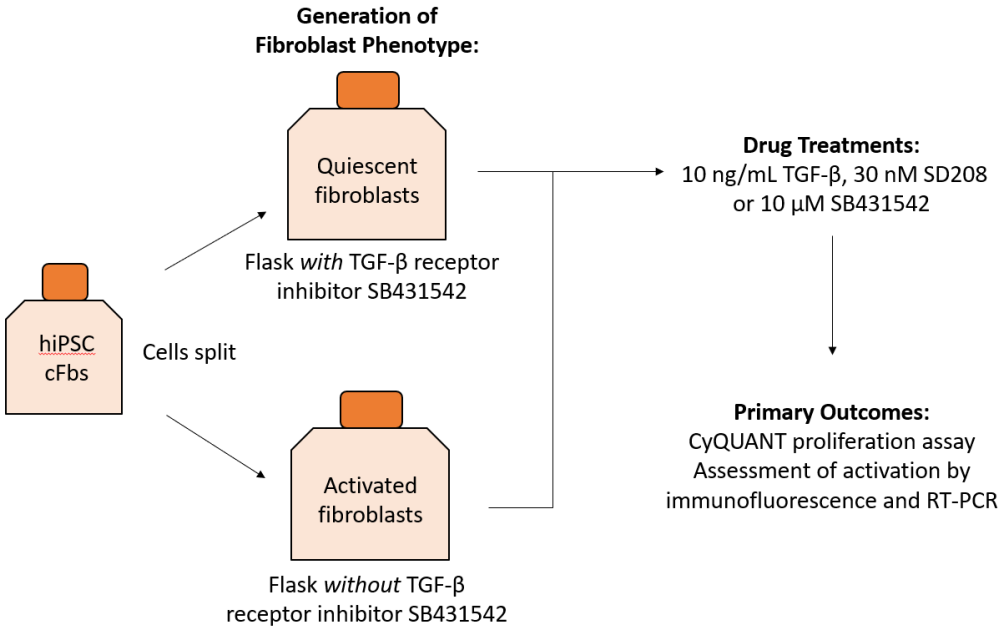
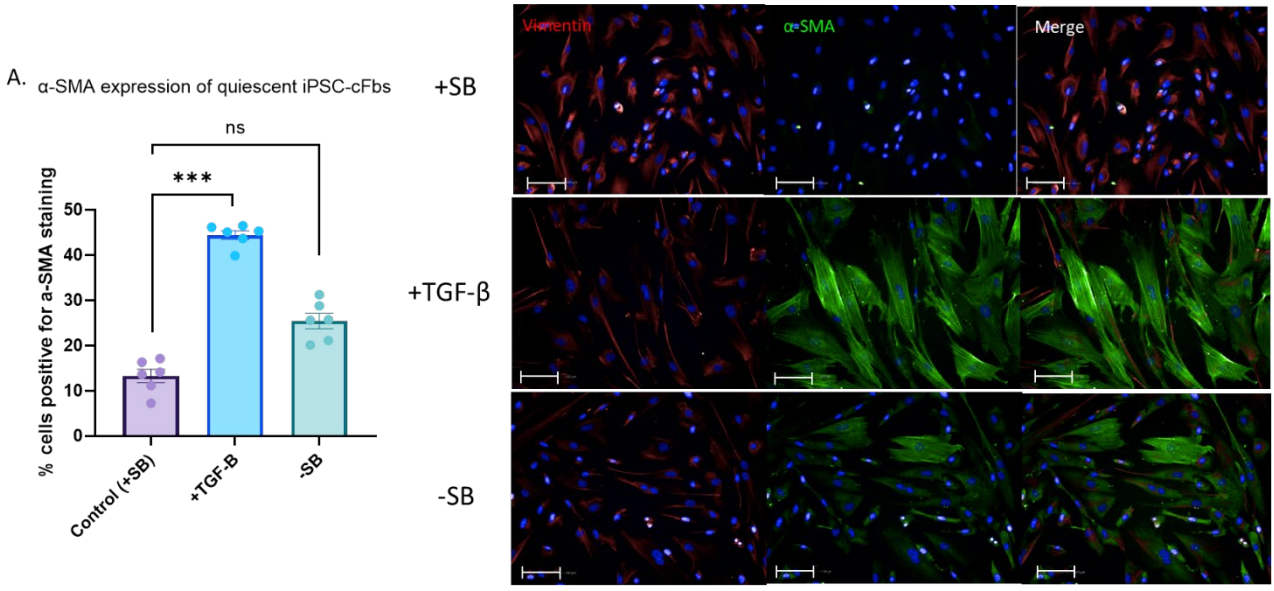


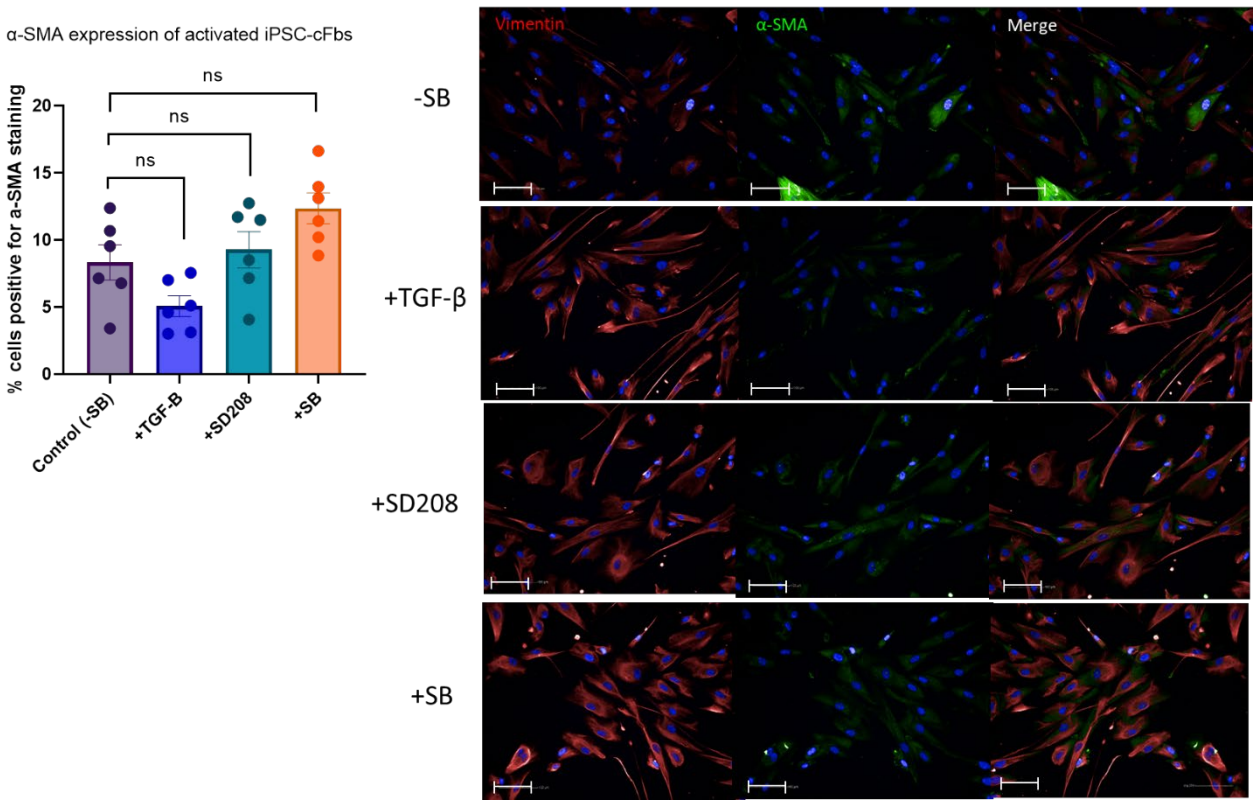
Figure 3-8. Immunofluorescence staining of α-SMA in quiescent and activated human induced pluripotent stem cell derived cardiac fibroblasts (hiPSC-cFbs).

A - Quiescent hiPSC-cFbs generated through culture for two weeks in the presence of SB435142 were treated with TGF-β. The effect of withdrawal of SB435142 (SB) was assessed. **B** - Activated hiPSC-cFbs generated through culture for two weeks in the absence of SB435142 were also treated with TGF-β. In addition, the effect of TGF-β receptor inhibition with SD208, and SB435142 (SB) re-introduction was assessed. Data presented as percentage of cells displaying α-SMA expression by immunofluorescence. Scale bar 100 μm. Data presented as mean ± S.E.M. N = 3 plates, 18 wells, nested one-way ANOVA, Tukey post-hoc versus control.

A.


α-SMA expression of quiescent iPSC-cFbs
ns
***
% cells positive for a-SMA staining
50
40
30
20
10
0
Control (+SB)
+TGF-B
-SB
+SB
+TGF-β
-SB
Vimentin
α-SMA
Merge

B.


α-SMA expression of activated iPSC-cFbs
ns
ns
ns
% cells positive for a-SMA staining
20
15
10
5
0
Control (-SB)
+TGF-B
+SD208
+SB
-SB
+TGF-β
+SD208
+SB
Vimentin
α-SMA
Merge

To investigate this phenomenon further, we explored the effect of culture on stiff 3 GPa substrates and the addition of TGF-β on the activation state of quiescent hiPSC-cFbs over time. A qualitative assessment of α-SMA expression was conducted over the period of 1 week using immunofluorescence. hiPSC-cFbs were cultured in the absence of a TGF-β receptor inhibitor.

α-SMA fibres began to appear at the 24-hour mark (**Figure 3-9** and **Figure 3-10**) both in the absence and presence of TGF-β. In the presence of TGF-β, an increased proportion of cells stained with α-SMA up to 96 hours (50-80% of cells, **Figure 3-9** and **Figure 3-10**). Culture on 3 GPa alone also resulted in an increase in α-SMA fibrous staining, but to a lesser degree than with TGF-β at each of the time points investigated (5-20% of cells, **Figure 3-9** and **Figure 3-10**). In both conditions, the percentage of cells expressing α-SMA began to decrease between 96 hours and 1 week (168 hours). This is in line with our previous observations (**Figure 3-8 B**) where a loss of fibrous staining was seen in activated hiPSC-cFbs following long term (over two weeks) culture on stiff substrates in the absence of a TGF-β receptor inhibitor.

This data confirms that hiPSC-cFbs are activated by culture on 3 GPa substrates alone, independent of TGF-β, albeit to a lesser extent. This data also shows that activation by hard substrates begins within 24 hours, with a peak at around 96 hours of culture.

Figure 3-9. Activation status of quiescent human induced pluripotent stem cell induced cardiac fibroblasts (hiPSC-cFBs) cultured on stiff substrates over 7 days.

α-SMA staining in quiescent hiPSC-cFbs was assessed over a 7-day period following culture on 3 GPa substrates, and in the presence of TGF-β. The percentage of cells in a field of view staining positive for α-SMA fibres was recorded. Representative images shown in Figure 3-10. Data presented as minimum to maximum *N* = 3 wells, 3 images per well.

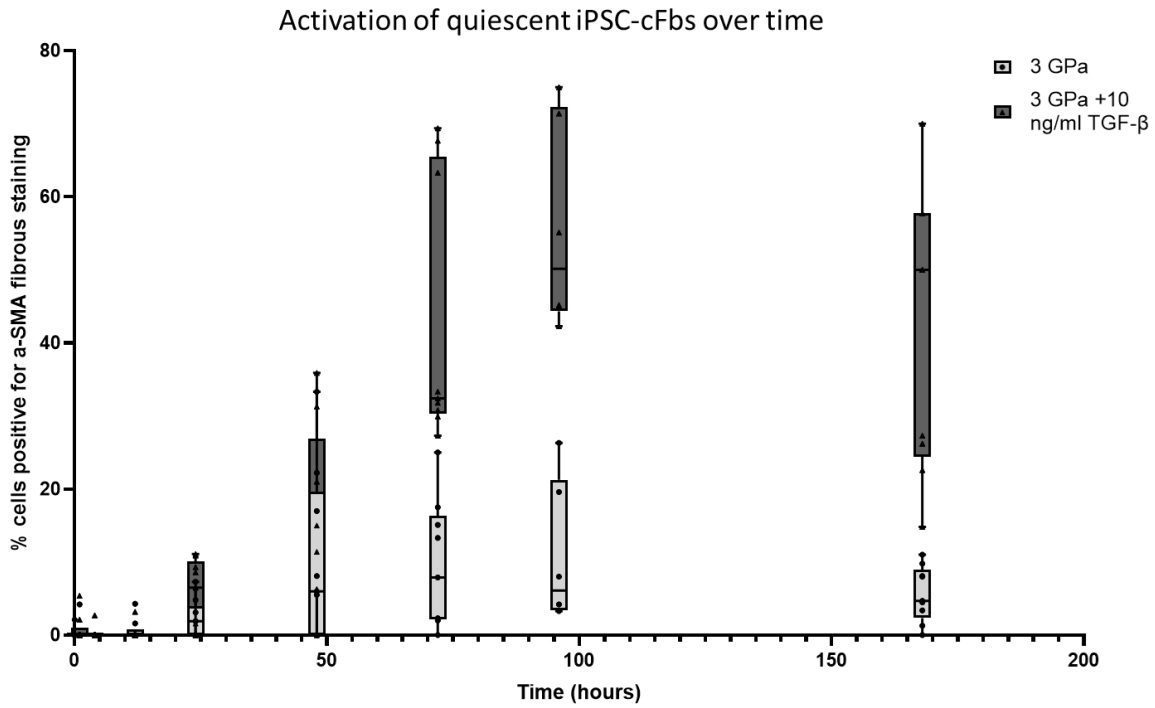
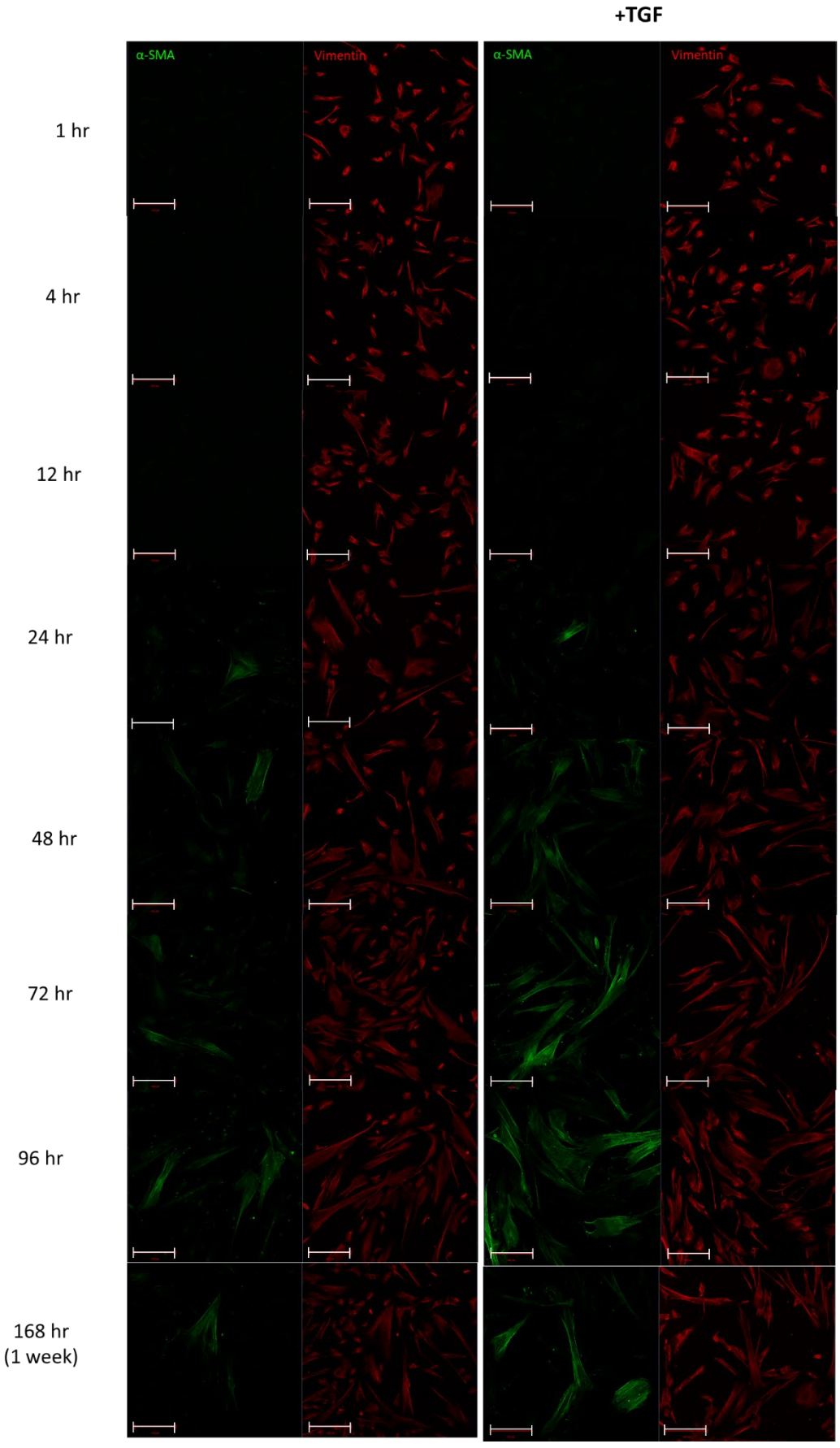


Figure 3-10. Representative immunofluorescence images for Figure 3-9.

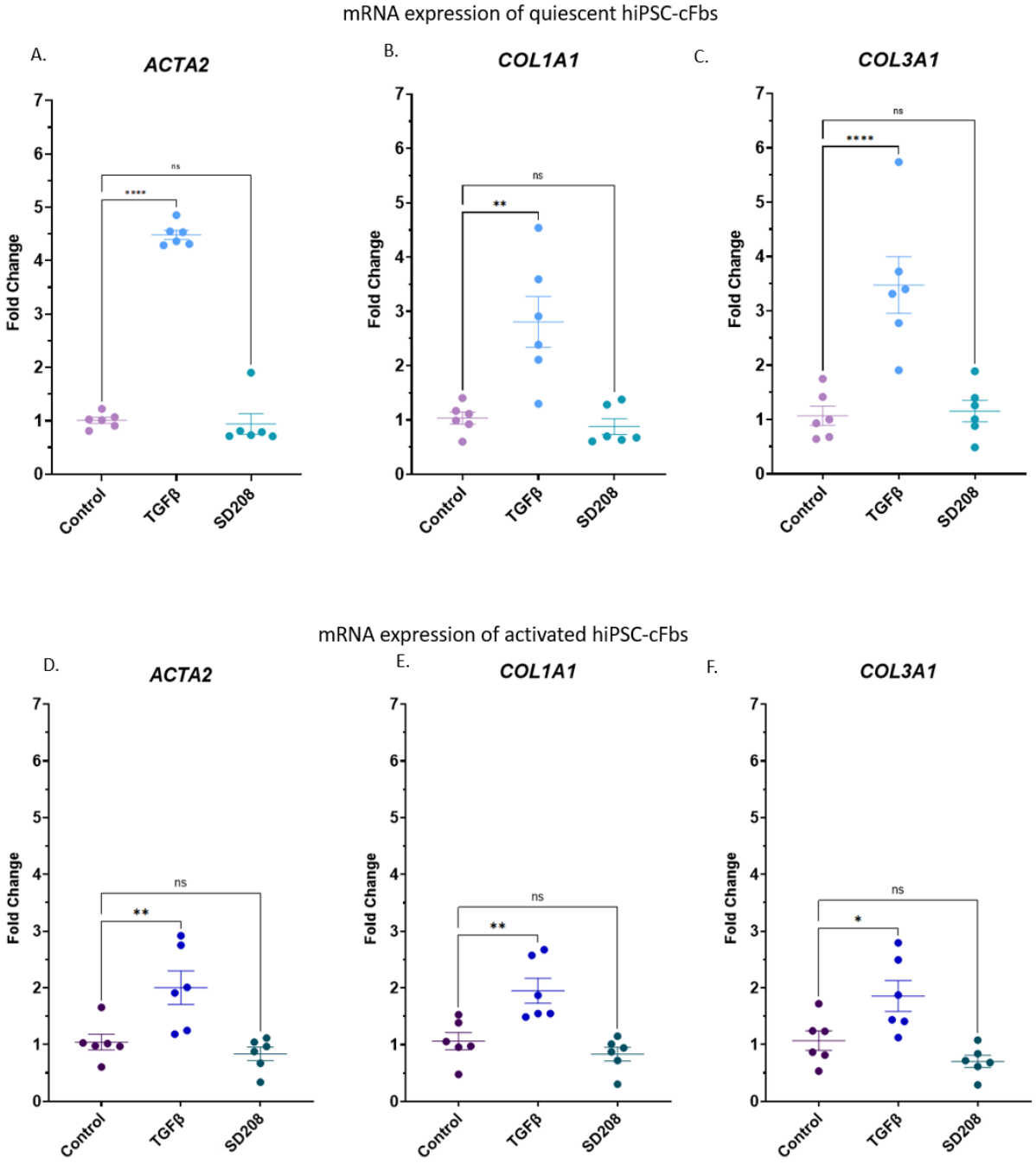
α-SMA staining in hiPSC-cFbs over a 1-week period in the presence and absence of 10 ng/mL TGF-β. On the left are cells grown without TGF-β and on the right are cells grown with 10 ng/mL TGF-β. α-SMA in green and vimentin, as a marker for cardiac fibroblasts, is in red. Scale bar is 200 μm.


+TGF
α-SMA
Vimentin
α-SMA
Vimentin
1 hr
4 hr
12 hr
24 hr
48 hr
72 hr
96 hr
168 hr
(1 week)

Characterisation of mRNA expression changes of hiPSC-cFbs in response to TGF-β by RT-PCR demonstrated that quiescent hiPSC-cFbs displayed a robust increase in α-SMA (mean fold change = 4.485, p <0.0001), collagen 1 (mean fold change = 2.806, p = <0.01) and collagen 3 (mean fold change = 3.477, p <0.0001) versus vehicle treated hiPSC-cFbs (**Figure 3-11**). Activated hiPSC-cFbs also had an observable but attenuated response to TGF-β (**Figure 3-11 D**, p = <0.01), leading to a comparatively smaller increase in α-SMA, collagen 1 and collagen 3 (**Figure 3-11 D, E and F**). SD208 treatment did not alter the expression of α-SMA, Collagen 1 or Collagen 3 in either the activated or quiescent hiPSC-cFbs (**Figure 3-11**).

Figure 3-11. Activation status of quiescent and activated human induced pluripotent stem cell derived cardiac fibroblasts (hiPSC-cFbs) in response to TGF-β and SD208.

Activation of quiescent and activated hiPSC-cFbs as determined by RT-PCR for *ACTA2*, *COL1A1* and *COL3A1* following four days in culture. Data presented as mean ± S.E.M. N = 6. * p < 0.05, ** p < 0.01, *** p < 0.001, one-way ANOVA compared with control.

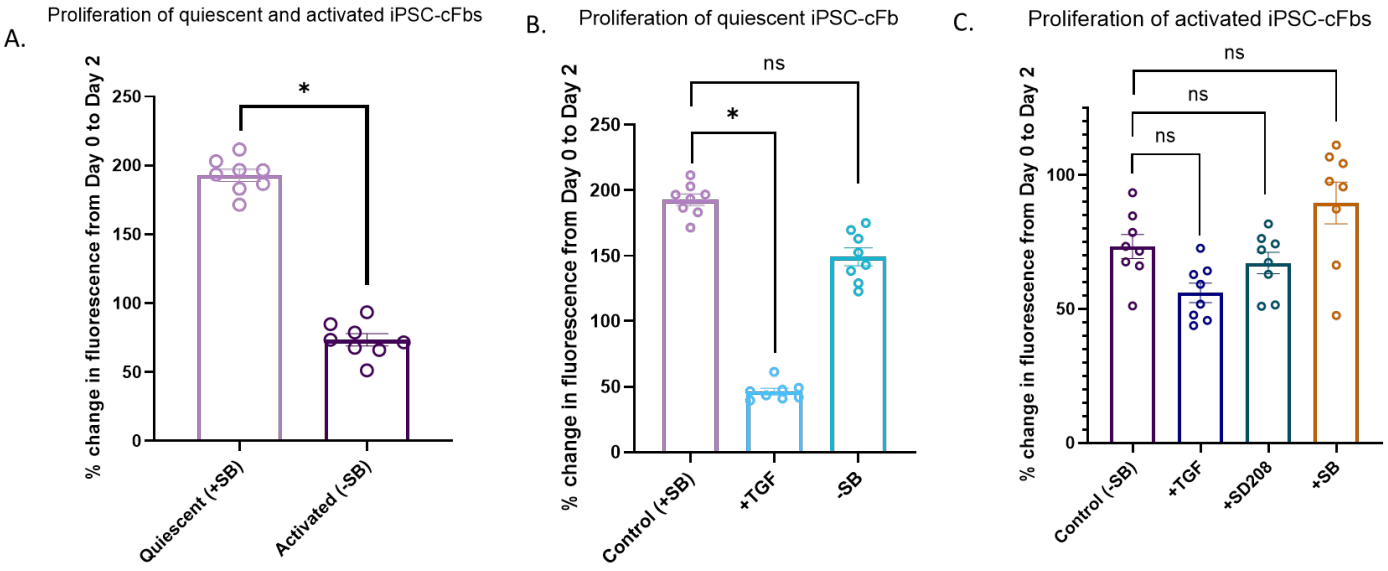


Proliferation of hiPSC-cFbs was also assessed. Activated hiPSC-cFbs show a significantly reduced proliferation rate when compared to their quiescent counterparts (**Figure 3-12 A**, mean % change 73.3±6.9 vs 192.8±9.3 respectively, p = <0.05). These data suggest that in hiPSC-cFbs, activation leads to a reduction in proliferation, rather than the expected increase in proliferation.

Quiescent hiPSC-cFbs demonstrated higher proliferation rates compared to the activated hiPSC-cFbs (**Figure 3-12 A**). A decrease in proliferative capacity was observed in response to TGF-β in quiescent hiPSC-cFbs (**Figure 3-12 B**, mean % change 192.8±9.3 vs 46.28±4.2, p = 0.01). The proliferative capacity of quiescent hiPSC-cFbs showed a small but non-significant decrease when SB431542 was removed from the culture media, (**Figure 3-12 B**, mean % change -SB 149.2±11.1 vs +SB 192.8±9.3, p = >0.1). Activated hiPSC-cFbs did not respond to either recombinant TGF-β or inhibition of the TGF-B signalling pathway by SB431542 or SD208 (**Figure 3-12 C**, p = >0.9).

Figure 3-12. Analysis of proliferation of quiescent and activated human induced pluripotent stem cell induced cardiac fibroblasts (hiPSC-cFBs).

Proliferation was assessed as a percentage change in fluorescence over 48 hours compared to at baseline. **A** – Proliferation of untreated quiescent and activated hiPSC-cFBs. **B** – Proliferation of quiescent hiPSC-cFBs in the presence of TGF-β (+TGF) and following withdrawal of SB431542 (-SB). **C** – Proliferation of activated hiPSC-cFBs in response to TGF-β (+TGF) and TGF-β receptor inhibitors SD208 (+SD208) and SB431542 (+SB). Data presented as mean ± S.E.M. N = 3 plates, 24 wells. * $p < 0.05$, nested one-way ANOVA compared with control.



3.5. DISCUSSION

There have been significant efforts to identify effective therapeutic approaches against long-established cardiac fibrosis targets. However, clinical trials of drugs which target the mineralocorticoid receptor, renin-angiotensin system, natriuretic peptide degradation, vascular tone, and others have yielded mixed results in reducing fibrosis-related outcomes in patients with heart failure with preserved and reduced ejection fraction and ischaemic heart disease despite encouraging preclinical data (Reviewed in [441]). Given the leading role of the myofibroblast in cardiac fibrosis, our study intended to investigate the potential for the reversal of activated human cardiac myofibroblasts to a more quiescent phenotype.

The principal findings of this study (**Table 3-3**) are that chronically activated primary human cardiac ventricular fibroblasts show a diminished response to activation by TGF-β and that neither culture on softer substrates, nor TGF-β receptor inhibition are able to reverse the observed myofibroblast phenotype. Our findings are confirmed in hiPSC-cFbs, indicating that chronic activation of human cardiac fibroblasts leads to a terminal differentiation into myofibroblasts. We further demonstrate that culture of hiPSC-cFbs on stiff surfaces results in activation within 24 hours, and intriguingly longer-term culture (>96 hours) results in the loss of fibrous α-SMA expression.

Table 3-3. Summary of principle findings

Cell Type	Pre-Treatment Conditions	Treatment Conditions	Outcomes	
			Proliferation	Myofibroblast Markers
HCFs from patients with diabetic cardiomyopathy	Long-term culture on stiff substrates (3 GPa, ≤ 10 passages)	Stiff substrate (3 GPa) ± TGF-β ±TGF-βRi	No change	No change
		Soft substrate (25 kPa, 2 kPa) ± TGF-β ±TGF-βRi	No change	No change
hiPSC-cFbs	Quiescent hiPSC-cFbs (2-week culture *with* TGF-βRi)	TGF-β	Reduced	Increased
		TGF-βRi	No change	No change
	Activated hiPSC-cFbs (2-week culture *without* TGF-βRi)	TGF-β	No change	No change
		TGF-βRi	No change	No change

hiPSC-cFbs, human induced pluripotent stem cell derived cardiac fibroblasts; TGF-β, transforming growth factor-beta; TGF-βRi, transforming growth factor-beta receptor inhibitor

3.5.1. Proliferative capacity of human cardiac fibroblasts

Conflicting data exists concerning the correlation between cardiac fibroblast activation and proliferation. Intriguingly, our data highlights significantly higher proliferation rates in quiescent hiPSC-cFbs compared to the activated hiPSC-cFbs. Accordingly, TGF-β treatment reduced the proliferative capacity in quiescent hiPSC-cFbs but did not alter proliferation of activated hiPSC-cFbs or fibroblasts isolated from a patient. Similarly, Hecker et al. also showed that human lung myofibroblasts, activated using TGF-β, exhibited less proliferation than quiescent fibroblasts as well as an attenuated proliferative response to serum [426]. When using freshly isolated mouse cardiac fibroblasts, Herum et al. observed no changes in proliferation rates when cultured on multiple different

substrates (3, 8, 10, and 50 kPa) as well as no changes when substrates were stiffened from 3 or 8 kPa to 30 kPa after 5 days of culture [435]. A further study using human cardiac fibroblasts found that although there was a higher density of vimentin positive cells in failing hearts, there was a significant decrease in the proliferative marker Ki-67 in the failing hearts when compared to the non-failing hearts. Myofibroblasts (α-SMA positive cells) from both groups showed similarly low levels of Ki-67 staining [429]. Other studies have implicated the renin-angiotensin-aldosterone system in the proliferation of cardiac fibroblasts [442,443]. Using freshly isolated rat cardiac fibroblasts, Olson et al. were able to attenuate myofibroblast differentiation and cardiac fibroblast proliferation by inhibiting mitogen-activated protein kinase mediated signalling with polyphenolresveratrol [444]. Whether the same affects would be observed *in vivo* remains to be studied.

Cardiac fibroblasts derive from mesenchymal cells with a variety of origins. These include, but are not limited to, the pro-epicardium, epicardium, and cardiac endothelium through epithelial- or endothelial- to mesenchymal transformation (EMT and EndMT, respectively). Although cardiac fibroblasts show a decreased proliferative capacity once having undergone myofibroblast differentiation, cellular cues may instigate enhanced EMT/EndMT to maintain or increase cardiac fibroblast numbers within the heart [445,446]. The exact processes underpinning this require further investigation, where targeted attenuation of these mechanisms could present an alternative avenue to decreasing the fibrotic burden of the heart.

3.5.2. Reversal of myofibroblast phenotype through TGF-β inhibition

Cardiac fibrosis, whilst generally thought of as a maladaptive and pathophysiological process, is essential to ensuring tissue integrity following acute injury. For example, fibrotic tissue replaces necrotic myocardium following myocardial infarction thus maintaining cardiac mechanical function and preventing myocardial rupture [424]. This replacement fibrosis leads to impaired systolic and diastolic function, and to arrhythmias, around its margins. In contrast, diffuse interstitial fibrosis appears to be a purely maladaptive response with adverse effects on both ventricular function and susceptibility to arrhythmia [447]. The key role of TGF-β in cardiac fibroblast activation and proliferation is well-studied. Clinical studies have consistently reported upregulated TGF-β expression in the myocardium of patients with heart failure [448-450]. The induction of fibrosis because of activation of myofibroblasts via small mothers against decapentaplegic (SMAD) and non-SMAD-mediated signalling pathways such as ERK, JNK and p38 has also been previously described [78,451,452].

A recent study by Nagaraju et al. similarly investigated the potential for reversal of cardiac fibroblast activation using TGF-β receptor inhibition. Using freshly isolated human cardiac fibroblasts from explanted hearts of transplant recipients, the authors found that incubation with the TGF-β receptor inhibitor SD208 resulted in loss of α-SMA and reduced expression of profibrotic genes [429]. To achieve this, a high concentration of SD208 (3 μM) was utilised. In contrast, we found no effect on the activation status (proliferation rate and α-SMA expression) of isolated human ventricular cardiac fibroblasts when SD208 was used at a

concentration of 30 nM (IC_{50} = 49 nM [453]), similar to that used in other cardiac fibroblast studies [439].

Inhibition of TGF-β or its signalling components has been shown to be an effective anti-fibrotic treatment in preclinical studies. Transgenic rodent studies have demonstrated that disruption of fibroblast-specific TGF-β receptor 1 produced cardiac-protective effects against fibrosis and diastolic dysfunction [438]. Further *in vivo* studies utilising neutralising monoclonal antibodies and small molecular inhibitors directed against TGF-β and TGF-β receptor 1, respectively, reported significant reductions in cardiac fibrosis in murine tissue [430,454,455]. However, anti-TGF-β therapies are associated with significant dose-limiting drug toxicity given the ubiquitous expression of TGF-β and its receptors in healthy tissue throughout the human body, which restricts the effectiveness of such treatments. Mitra et al. reported widespread dose-dependent complications associated with pan-TGF-β inhibition in both mouse and monkey models. These included vascular and cardiac valvular inflammation, systemic bleeding, bone dysplasia and increased mortality [456]. Studies employing targeted inhibition via small molecular inhibitors against TGF-β receptor 1 also reported similar cardiac and haemorrhagic complications [457,458]. Due to these challenges, there has yet to be an anti-TGF-β therapy that has successfully found the balance between achieving an adequate anti-fibrotic response whilst avoiding serious cardiovascular side effects, despite candidate drugs such as galunisertib showing initial promise in cancer trials [459,460].

3.5.3. Terminally differentiated cardiac myofibroblasts cannot be de-activated

The discrepancy between our reported findings of irreversibly activated myofibroblasts and that of Nagaraju et al. [429] may also be explained by differing cell culture approaches, specifically, the duration in culture and passage number prior to application of a de-activating agent or treatment. In their experiments, the authors utilised the isolated cardiac fibroblasts within four days of isolation without passaging, in contrast to our HCF and hiPSC-cFb cell lines, which were intentionally cultured long-term for up to 10 passages / 2-4 weeks before usage to produce a chronically activated myofibroblast phenotype. Taken together, our results suggest the presence of a 'threshold' after which fibroblasts become unresponsive to a de-activating treatment, which warrants further discussion.

Studies have supported the concept that the plasticity of myofibroblast phenotype is only conserved and demonstrable when using freshly isolated cells [431], or cells which have been cultured in 'activating' conditions for a short period of time [461]. Penke & Peters-Golden [462] challenged the idea of the fibroblast and myofibroblast being discrete, categorical phenotypes. Instead, they proposed the presence of an intermediate 'protomyofibroblast' stage, encompassing a continuum of cellular processes and fibroblast phenotypes, which bridge the differentiation of fibroblasts into myofibroblasts. In parallel, the potential for myofibroblast de-differentiation would also follow a similar principle and depend on where they lie on the continuum of phenotypes. Indeed, data from single cell RNA sequencing already provides evidence that there are several distinct subpopulations of

cardiac fibroblasts in healthy hearts [416,417], and at different stages of ischaemic injury in murine studies [463,464].

Our immunofluorescence data show that chronically activated HCFs and hiPSC-cFbs exhibited an unusual α-SMA staining pattern. Though these cells are unresponsive to TGF-β, and therefore assumed to be activated, they do not exhibit the "classic" actin fibres as found in our quiescent hiPSC-cFbs following TGF-β treatment. Instead, the activated cardiac fibroblasts displayed dispersed α-SMA staining within the cytoplasm (**Figure 3-1 A**, **Figure 3-2 E**, and **Figure 3-8 B**). Use of secondary antibody-only controls shows that this effect is not due to non-specific staining (**Figure 3-4**). The exact explanation for this is unclear, however we hypothesise that chronic culture in activating conditions may result in disassembly of actin fibres. This hypothesis may be supported by the decrease in α-SMA fibrous staining seen in Figures 8 and 9 from 96 hours to 1 week of activation by both hard substrates alone and in conjunction with TGF-β. The localisation of α-SMA within the cardiac fibroblast requires further investigation as a potential marker for late stage and/or irreversible activation status.

It is therefore conceivable that our cell culture approach, which bears resemblance to the persistent, longer duration of cardiac fibroblast activation at the latter stages of cardiac disease, resulted in irreversible terminal differentiation of myofibroblasts, a phenomenon that has been reported in other organ systems such as the lung [461,465].

3.5.4. The role of mechanical stiffness and myofibroblast activation

Our data show that human cardiac fibroblasts are activated by culture on stiff ~3 GPa substrates. Chronically activated cardiac fibroblasts failed to transition back to a quiescent phenotype by subsequent culture on softer culture substrates (2 and 25 kPa), suggesting a loss of feedback from the surrounding mechanical environment. Healthy myocardium has a typical elastic modulus of between 10 to 30 kPa [431,466,467], rising to over 100 kPa in diseased tissues [432,468]. Several other studies have indicated that prolonged culture on a hard plastic surface is sufficient to cause increased α-SMA expression in freshly isolated murine cardiac fibroblasts [443,467,469-471]. However, the cellular mechanisms that regulate the cardiac fibroblast phenotype and function in response to mechanical stimuli are complex. Studies have reported some success in de-activating human and porcine myofibroblasts through the use of soft hydrogels [431,472] and three-dimensional microfabricated tissues associated with reduced tissue tension [473]. Still, the reversal tended to be incomplete, and experiments utilised freshly isolated cells cultured for shorter periods [443,471], further supporting the concept of there being a range of protomyofibroblast states.

We also note that recommended culture of hiPSC-cFbs requires use of TGF-β receptor antagonist SB431542 at high concentrations (10 μM; IC_{50} 94 nM) to maintain quiescence [397,439]. It may be that use of soft substrates would allow the use of lower concentrations of TGF-β antagonism. In particular, the consequences of longer-term cardiac fibroblast culture in the presence of an

inhibitor, and whether the effects of mechanical stress of the substrate can be fully suppressed over prolonged periods remain unclear.

3.6. CONCLUSION AND FUTURE DIRECTION

The lack of efficacious treatments for the reversal of cardiac fibrosis is a product of the complex cellular pathways, which are common to extracellular matrix generation and turnover in both health and disease. The cardiac fibroblast is the principal cell type in the fibrotic process, and we show, using diseased patient-derived cardiac fibroblasts, that their activation into myofibroblasts under chronic disease conditions is a challenging phenotype to reverse *in vitro*. Our experiments using hiPSC-cFbs recapitulated these findings. Whether cardiac fibroblasts isolated from healthy human myocardium would yield similar findings presents an intriguing and important avenue for future investigation.

CHAPTER 4. HUMAN CARDIAC FIBROBLASTS ACTIVATION STATUS FOLLOWING FIBROBLAST GROWTH FACTOR 23 TREATMENT

4.1. EXTENT OF PERSONAL CONTRIBUTION

Max Cumberland provided the human induced pluripotent stem cell-derived cardiac fibroblasts. Caitlin Hall performed the immunofluorescence experiments. I performed all other experimental procedures. These experiments were conducted in parallel with those in Chapter 3.

4.2. INTRODUCTION

The cardiovascular risk experienced by patients with CKD is more pronounced [474], with a shift in morbidity and mortality from atherosclerotic complications to those due to heart failure, arrhythmias and sudden cardiac death [251,475]. In particular, atrial fibrillation (AF) is common and seen in 41% of patients requiring haemodialysis [251]. The pathophysiological basis for these events has been attributed to CKD-associated cardiomyopathy, a condition typically characterised by left ventricular hypertrophy (LVH), myocardial fibrosis and development of cardiac mechanical and electrical dysfunction [13,14,19]. Serum levels of FGF23 increase in response to rising serum phosphate levels as kidney function worsens, reaching levels two to five-fold normal ranges in earlier stages of CKD and increasing to over 1000-fold above normal in ESKD [177-179]. A growing body of evidence strongly suggests that the heart is responsive to FGF23-mediated effects. In animal studies, FGF23 has been shown to increase LV mass independently of blood pressure via αKlotho-independent activation of FGFR4 [171,172]. Furthermore, FGF23 disrupted intracellular calcium cycling within the cardiomyocyte resulting in *in vitro* and *in vivo* arrhythmogenicity[257]. In humans, large observational studies have found an association between elevated FGF23 and increased risk of developing AF and LVH [186-188]. In separate studies, we demonstrated the utility of FGF23 as a biomarker to identify patients with prevalent AF [190,259]. Others have reported increased expression of FGF23, FGFR4 mRNA by real-time PCR (qPCR) in the right atrial appendages of AF patients, which correlated with atrial collagen fraction by histology [263].

4.2.1. Fibroblast growth factor-23 and myocardial fibrosis in CKD-associated cardiomyopathy

Cardiac fibroblasts make up between 30-60% of all cells, by number, in the myocardium, and act as regulators of extracellular matrix in the heart [78,240,476]. Activation of cardiac fibroblasts in the injured myocardium promotes their differentiation to myofibroblasts, which in turn are characterised by altered cellular motility, acquisition of procontractile proteins such as α-smooth muscle actin (αSMA), and increased synthesis of extracellular matrix (ECM) and profibrotic proteins. The result is increased ECM stiffness and impaired mechano-electrical coupling with cardiomyocytes, providing a substrate for arrhythmias and attenuation of cardiac function[422]. Increased ECM stiffness itself can lead to further activation of fibroblasts and transition into myofibroblasts [431,435]. The stiffness, or Young's modulus, of healthy human myocardium has been reported to vary between 10 to 30 kPa in the literature, increasing by at least ten-fold in fibrotic tissue[78].

Histological studies have demonstrated severe interstitial fibrosis and myocardial disarray in KFRT patients on haemodialysis in the absence of flow-limiting coronary artery disease and independent of blood pressure, diabetes or anaemia [13,14]. Whilst two recent studies have shown that FGF23 can activate murine cardiac fibroblasts [246,477], the underlying mechanism has yet to be fully defined. There have also been no published studies examining whether human cardiac fibroblasts show the same response to FGF23 stimulation.

The main aims of this study are as follows:

1. Elucidate the role of FGF23 in human cardiac fibroblast activation to a myofibroblast phenotype, and
2. Assess whether human cardiac fibroblasts cultured as a 2D monolayer on surfaces with varying elastic moduli exhibit differential activation responses to FGF23.

4.3. METHODS

Detailed methodology has been discussed in Chapter 2. In brief, primary human cardiac fibroblasts obtained from PromoCell were cultured on 6-well flat-bottomed tissue culture plates of varying elastic modulus - standard 3 GPa polystyrene (Corning) and Softwell 25 & 2 kPa (Matrigen). Cells were discarded after 10 passages. Following growth in fibroblast growth medium 3, FGM3 in the presence or absence of 10 ng/mL TGF-β and 50 ng/mL FGF23 for up to 4 days, cardiac fibroblasts were detached using a dissociation solution. Cell pellets were collected for protein and mRNA analyses at the 1 day and 4 day timepoints to investigate FGFR expression and markers of fibroblast activation. Separate cell culture experiments were conducted for immunofluorescence staining of α-SMA. Fluorescent intensity was normalised to cell surface area. Finally, experiments were repeated in a hiPSC-derived cardiac fibroblast line. Cell pellets were collected for mRNA analyses of FGFR and markers of fibroblast activation by RT-PCR. In separate experiments, hiPSC-derived cardiac fibroblasts were cultured on standard 3 GPa 6-well polystyrene plates treated with 10 ng/mL TGF-β, 50 ng/mL FGF23 or control for up to 4 days. Cell pellets were collected for mRNA analyses by RT-PCR

4.4. RESULTS

4.4.1. Fibroblast growth factor receptor expression

All four fibroblast growth factors were present in primary human cardiac fibroblasts. FGFR1 being the dominantly expressed receptor (**Figure 4-1**). FGFR3 and FGFR4, which were expressed equally, with FGFR2 being the least abundantly expressed of the four receptors (**Figure 4-1**). Co-receptor Klotho was not expressed (dCT >40 in over 50% technical replicates). Receptor expression by dCT method should be interpreted with caution; instead, quantitative PCR can be used to quantify the abundance of a gene transcript.

Receptor expression was generally unchanged across the three culture substrates after one and four days in culture except for FGFR1 (**Figure 4-2**). Following 1 day in culture, FGFR1 expression was significantly greater on a 25 kPa substrate compared to cardiac fibroblasts which had been cultured for the same duration on 3 GPa (mean 2^{-ddCT}1.974 vs 3 GPa, p = 0.0321) and 2 kPa (mean 2^{-ddCT} 1.974 vs 2 kPa, p = 0.0424; **Figure 4-2 A**). However, these differences were not seen following 4 days in culture (p > 0.8; **Figure 4-2 B**).

Human cardiac fibroblasts were subjected to high-dose FGF23 and TGF-β to investigate the potential for these treatments to regulate FGFR expression. A four-day FGF23 and TGF-β treatment period did not alter FGFR gene expression in primary human cardiac fibroblasts cultured on standard 3 GPa polystyrene plates (p > 0.36; **Figure 4-3 A1, B1, C1, D1**). FGFR expression was similarly unchanged by FGF23 and TGF-β treatment when fibroblasts were cultured on

softer 25 kPa ($p > 0.29$; **Figure 4-3 A2, B2, C2, D2**) and 2 kPa plates ($p > 0.11$; **Figure 4-3 A3, B3, C3, D3**).

Figure 4-1. Human cardiac fibroblast (HCF) fibroblast growth factor receptor (FGFR) gene expression by RT-PCR.

FGFR1 to 4 gene expression in cultured primary HCFs normalised to housekeeping gene GAPDH. Data presented as mean ± S.E.M, N = 12.

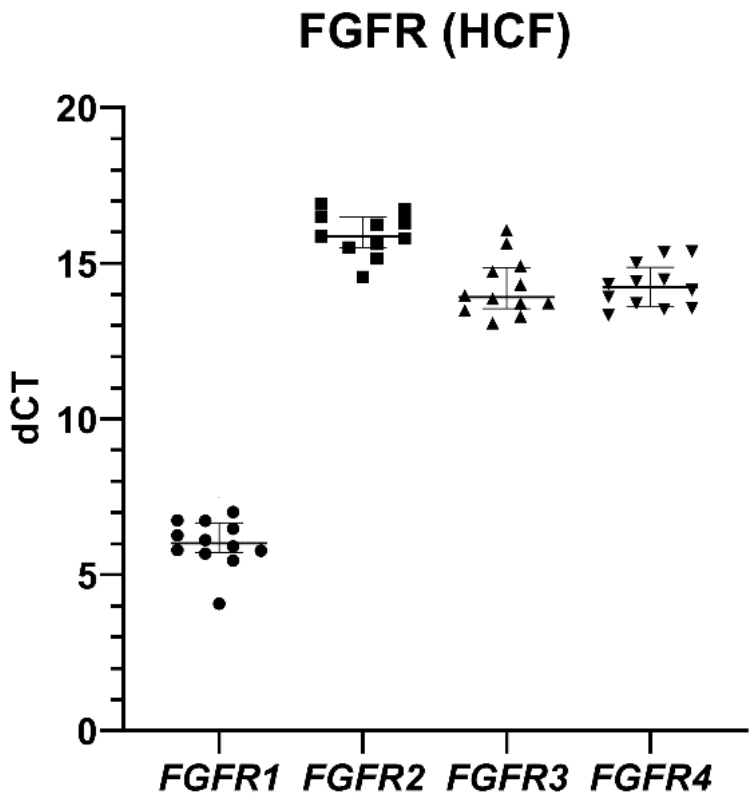


Figure 4-2. Effect of culture plate stiffness on human cardiac fibroblast (HCF) fibroblast growth factor receptor (FGFR) gene expression by RT-PCR.

FGFR gene expression in cultured primary HCF on stiff (3 GPa) and soft (25 kPa, 2 kPa) culture substrates. **A** – FGFR expression after 1 day in culture (N = 9-12). **B** – FGFR expression after 4 days in culture (N = 5-6). Data presented as mean ± S.E.M., one-way ANOVA with Tukey multiple comparisons test.

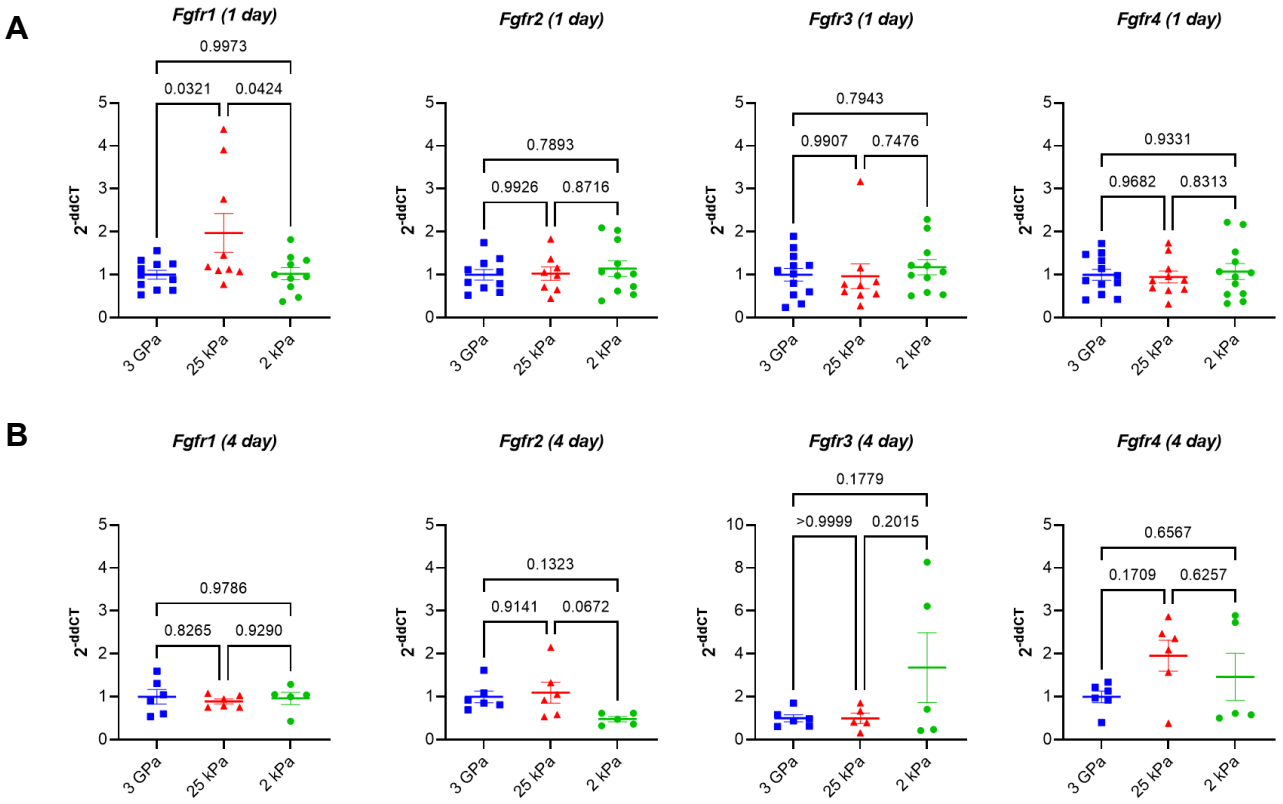
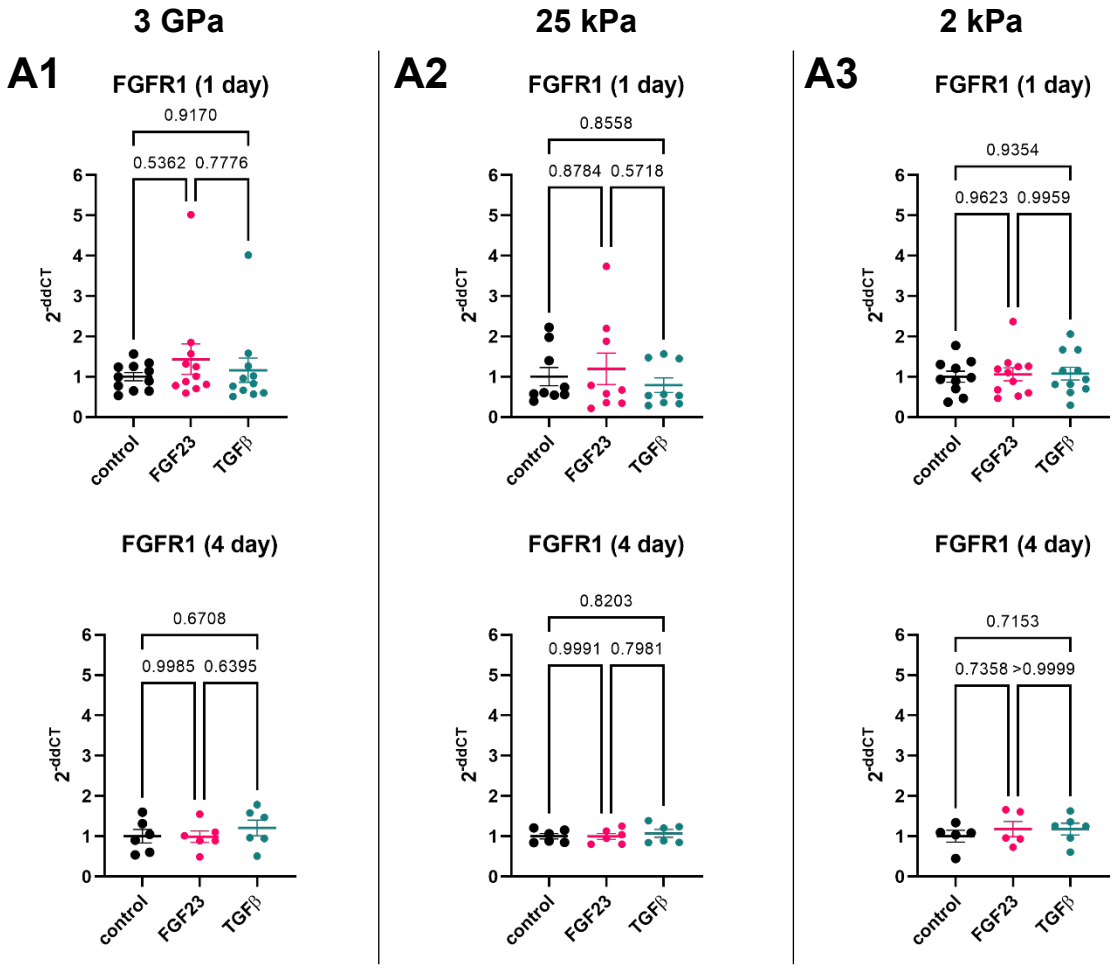
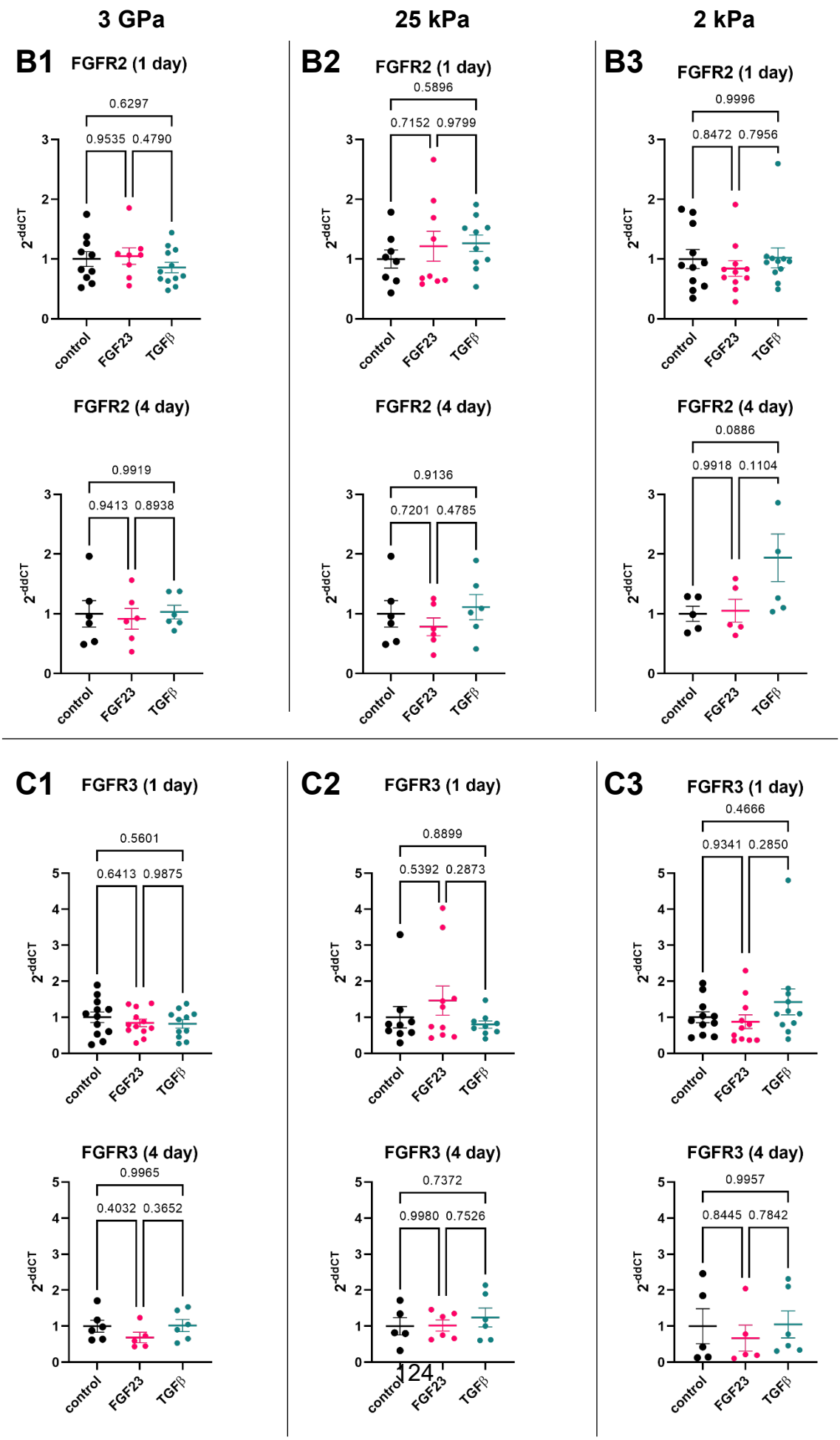
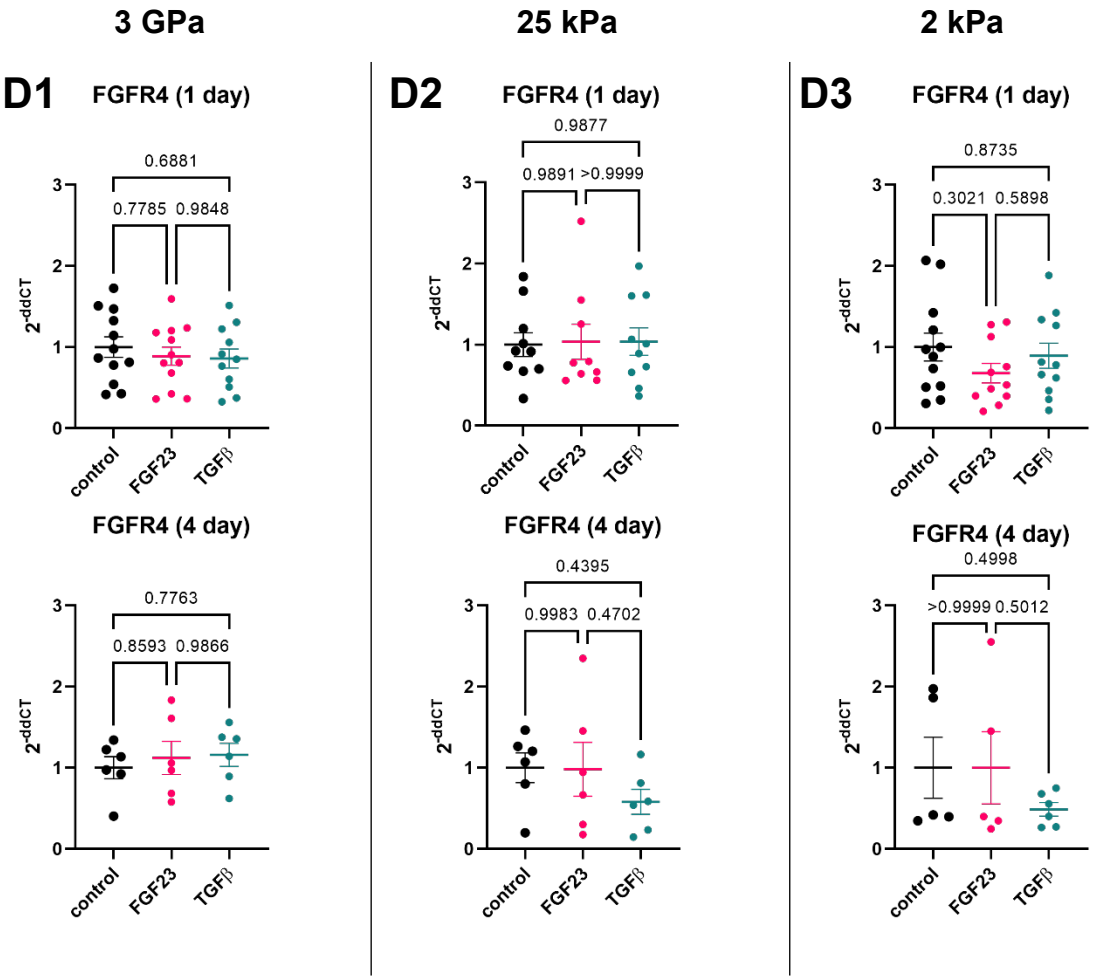


Figure 4-3. Effect of FGF23 and TGFβ treatment on HCF fibroblast growth factor receptor (FGFR) gene expression by RT-PCR.

HCFs were cultured for 1 and 4 days in the presence of 50 ng/mL FGF23, 10 ng/mL TGF-β, or vehicle control on stiff (3 GPa) and soft (25 kPa, 2 kPa) culture substrates. **A** – FGFR1 gene expression on 3 GPa (A1); 25 kPa (A2); and 2 kPa (A3). **B** – FGFR2 gene expression on 3 GPa (B1); 25 kPa (B2); and 2 kPa (B3). **C** – FGFR3 gene expression on 3 GPa (C1); 25 kPa (C2); and 2 kPa (C3). **D** – FGFR4 gene expression on 3 GPa (D1); 25 kPa (D2); and 2 kPa (D3). Data presented as mean ± S.E.M., one-way ANOVA with Tukey post-hoc.




3 GPa
25 kPa
2 kPa
B1
FGFR2 (1 day)
0.6297
0.9535 0.4790
B2
FGFR2 (1 day)
0.5896
0.7152 0.9799
B3
FGFR2 (1 day)
0.9996
0.8472 0.7956
FGFR2 (4 day)
0.9919
0.9413 0.8938
FGFR2 (4 day)
0.9136
0.7201 0.4785
FGFR2 (4 day)
0.0886
0.9918 0.1104
C1
FGFR3 (1 day)
0.5601
0.6413 0.9875
C2
FGFR3 (1 day)
0.8899
0.5392 0.2873
C3
FGFR3 (1 day)
0.4666
0.9341 0.2850
FGFR3 (4 day)
0.9965
0.4032 0.3652
FGFR3 (4 day)
0.7372
0.9980 0.7526
FGFR3 (4 day)
0.9957
0.8445 0.7842
2-ddCT
control
FGF23
TGFβ


3 GPa
25 kPa
2 kPa
D1
FGFR4 (1 day)
0.6881
0.7785
0.9848
FGFR4 (4 day)
0.7763
0.8593
0.9866
D2
FGFR4 (1 day)
0.9877
0.9891
>0.9999
FGFR4 (4 day)
0.4395
0.9983
0.4702
D3
FGFR4 (1 day)
0.8735
0.3021
0.5898
FGFR4 (4 day)
0.4998
>0.9999
0.5012
2-ddCT
control
FGF23
TGFβ

4.4.2. Human cardiac fibroblast activation

Activation of human cardiac fibroblasts was assessed by mRNA expression of myofibroblast marker *ACTA2*, which encodes the α-smooth muscle actin (α-SMA), and *COL1A1* encoding collagen type 1. There was a non-significant trend towards lower *ACTA2* expression on 2 kPa substrates versus stiff substrates ($p = 0.0742$ at 1 day; $p = 0.0750$ at 4 days versus 3 GPa; **Figure 4-4**). Expression of *ACTA2* was broadly similar between 25 kPa and 3 GPa ($p = 0.7772$ at 1 day; $p = 0.9255$ at 4 days; **Figure 4-4**). No significant differences in *COLA1A1* were seen at either time point in response to culture on substrates of varying stiffness ($p > 0.39$; **Figure 4-4**).

Human cardiac fibroblasts were then treated with high-dose FGF23 and TGF-β to investigate whether they became activated and acquired myofibroblast phenotype. Data shown in **Figure 4-5** indicates that FGF23 and TGF-β treatment for up to four days did not significantly alter mRNA expression of *ACTA2* and *COL1A1* at either 1 or 4 day timepoints in fibroblasts cultured on 3 GPa (**Figure 4-5 A**). Culture on softer 25 kPa (**Figure 4-5 B**) and 2 kPa (**Figure 4-5 C**) culture substrates did not alter the susceptibility of cardiac fibroblasts to activation by FGF23 or TGF-β.

Figure 4-4. Effect of culture plate stiffness on human cardiac fibroblast (HCF) markers of activation by RT-PCR.

α-Smooth muscle actin (ACTA2) and collagen 1 (COL1A1) gene expression in cultured HCFs maintained on stiff (3 GPa) and soft (25 kPa, 2 kPa) culture substrates. **A** – Expression after 1 day in culture (N = 10-11). **B** – Expression after 4 days in culture (N = 4-6). Data presented as mean ± S.E.M., one-way ANOVA with Tukey multiple comparisons test.

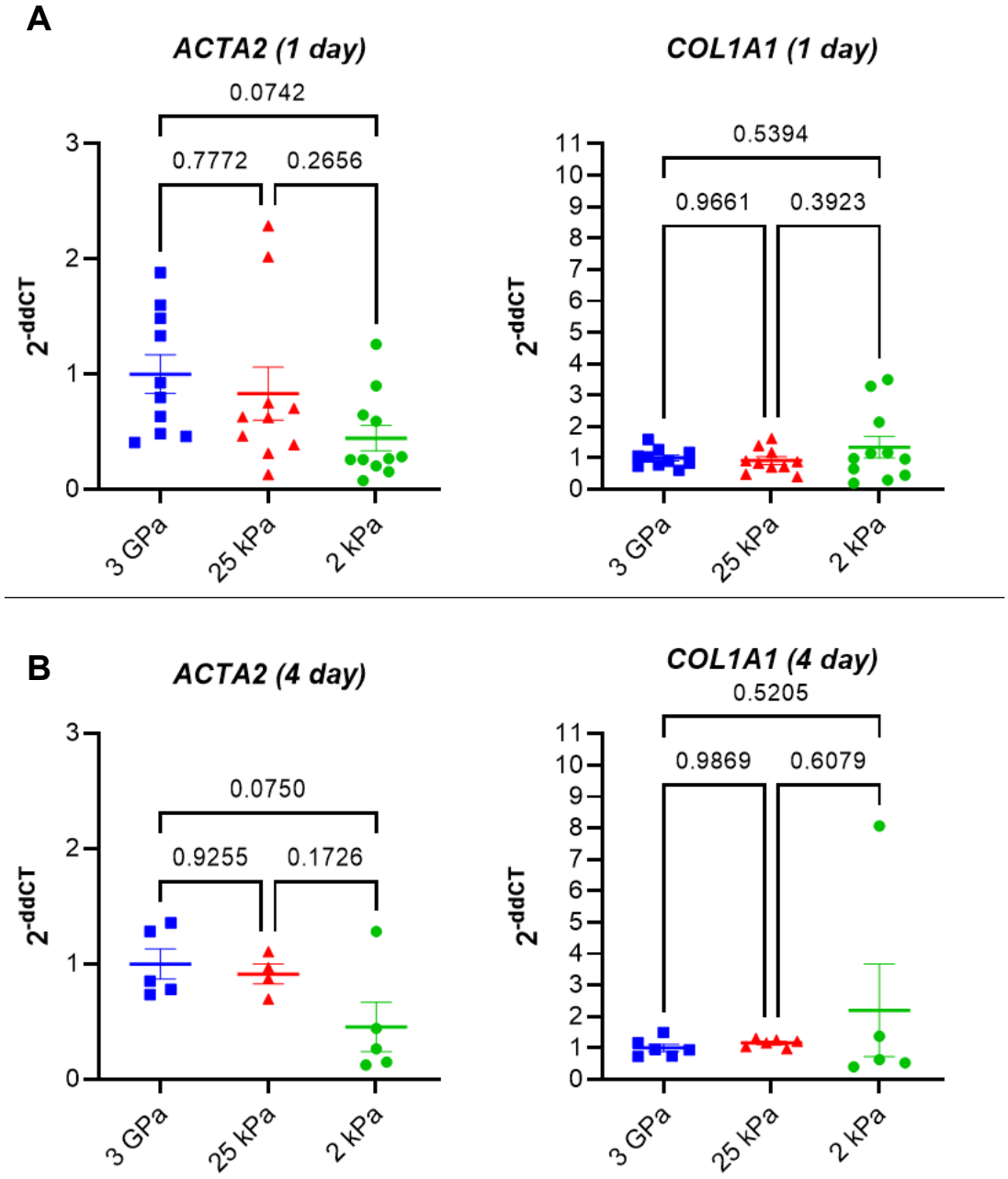
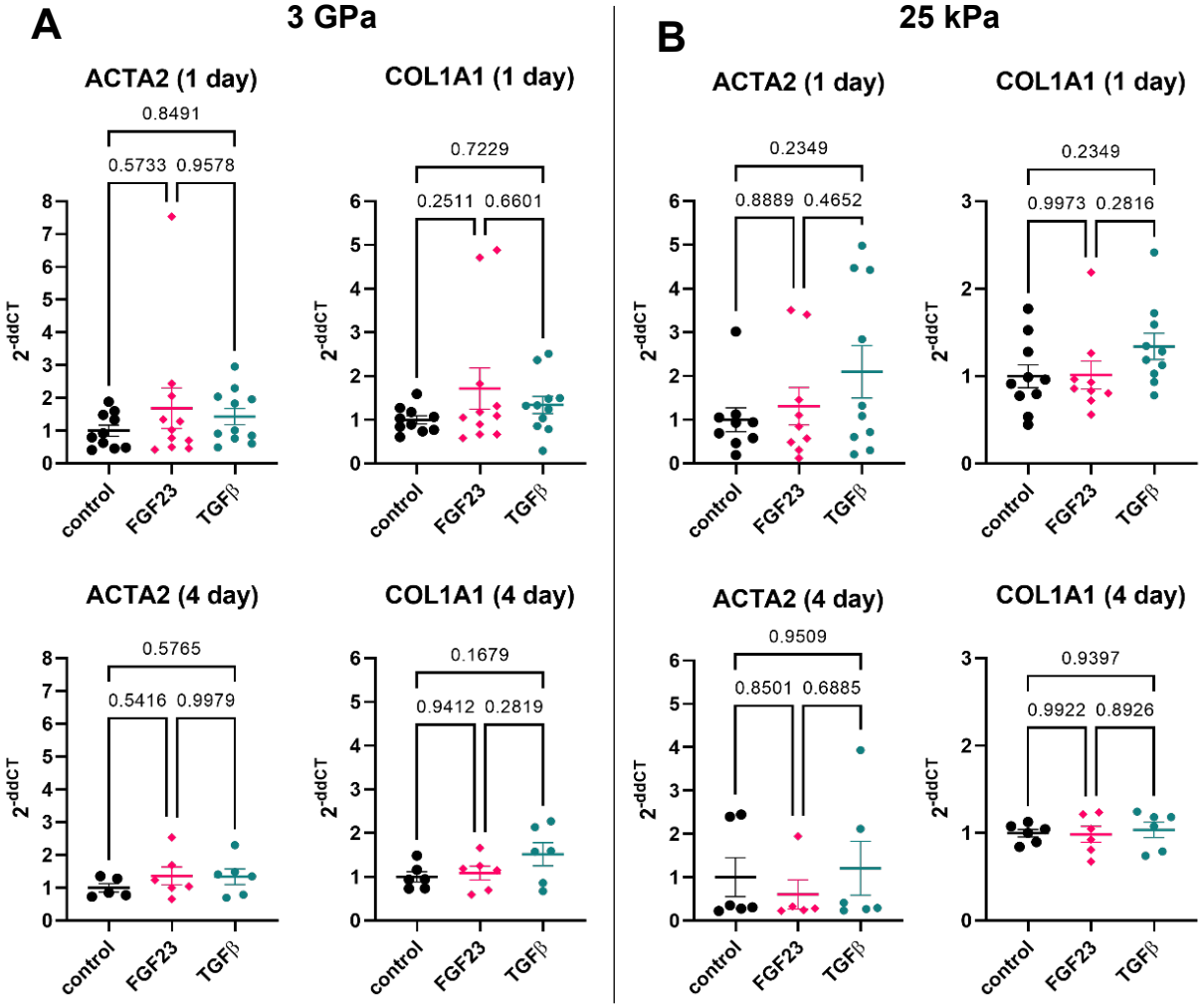
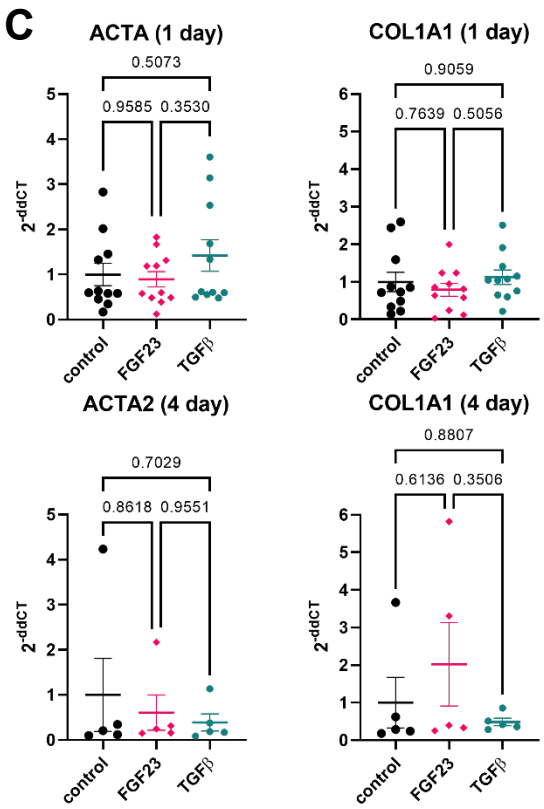


Figure 4-5. Effect of FGF23 and TGF-β treatment on HCF activation markers by RT-PCR.

HCFs were cultured for 1 and 4 days on culture plates with Young's modulus (*E*) of 3 GPa, 25 kPa & 2 kPa in the presence of 10 ng/mL TGFβ, 50 ng/mL FGF23, or vehicle control. *ACTA2* and *COL1A1* mRNA expression by RT-PCR. GAPDH was used as housekeeping gene. Relative expression of gene of interest in HCFs cultured on: **A** – 3 GPa (N = 5-11); **B** – 25 kPa (N = 5-10); and **C** – 2 kPa substrates (N = 5-11). Data presented as mean ± S.E.M., one-way ANOVA with Tukey post-hoc.



2 kPa

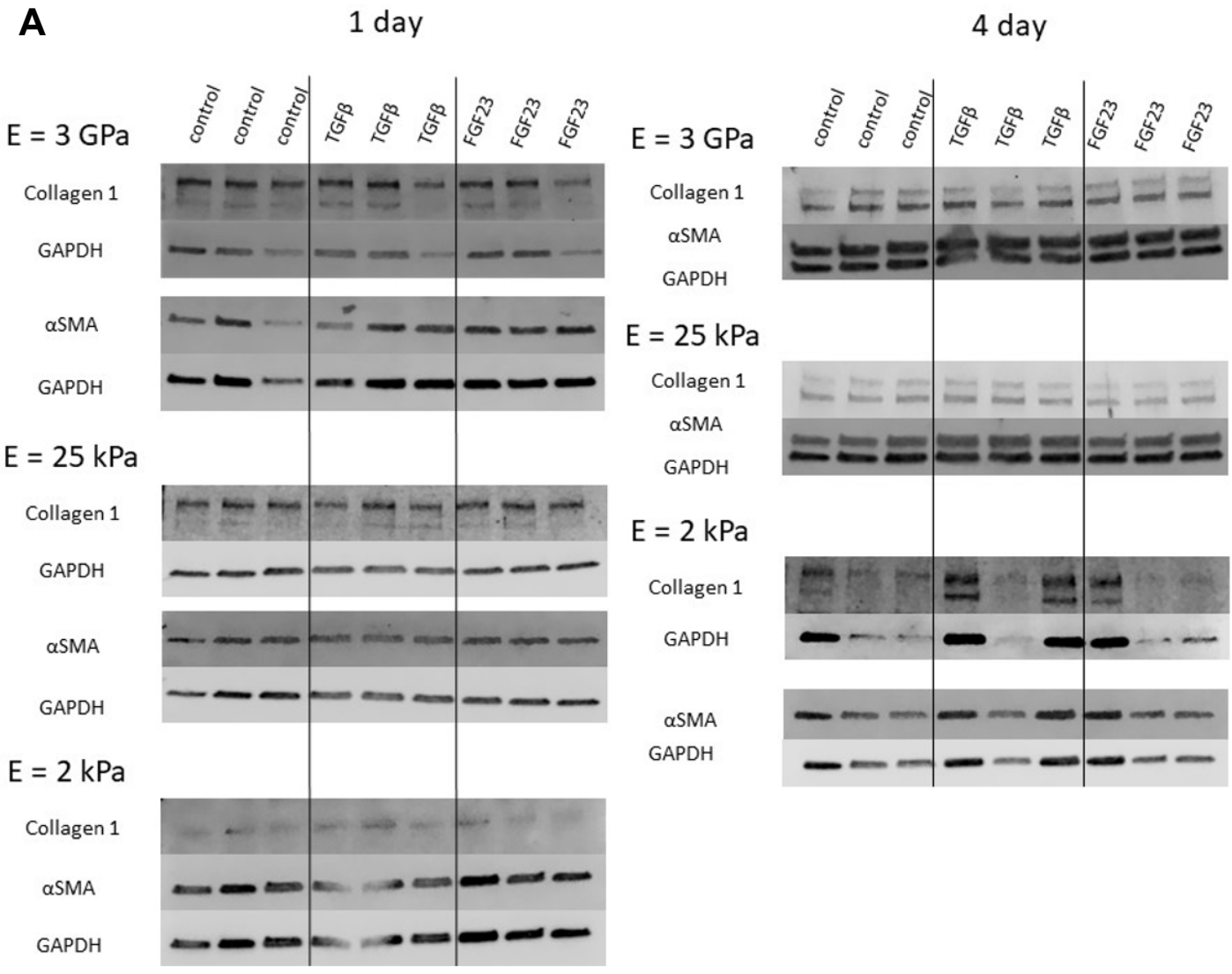

C
ACTA (1 day)
0.5073
0.9585
0.3530
2-ddCT
control
FGF23
TGFβ
COL1A1 (1 day)
0.9059
0.7639
0.5056
ACTA2 (4 day)
0.7029
0.8618
0.9551
COL1A1 (4 day)
0.8807
0.6136
0.3506

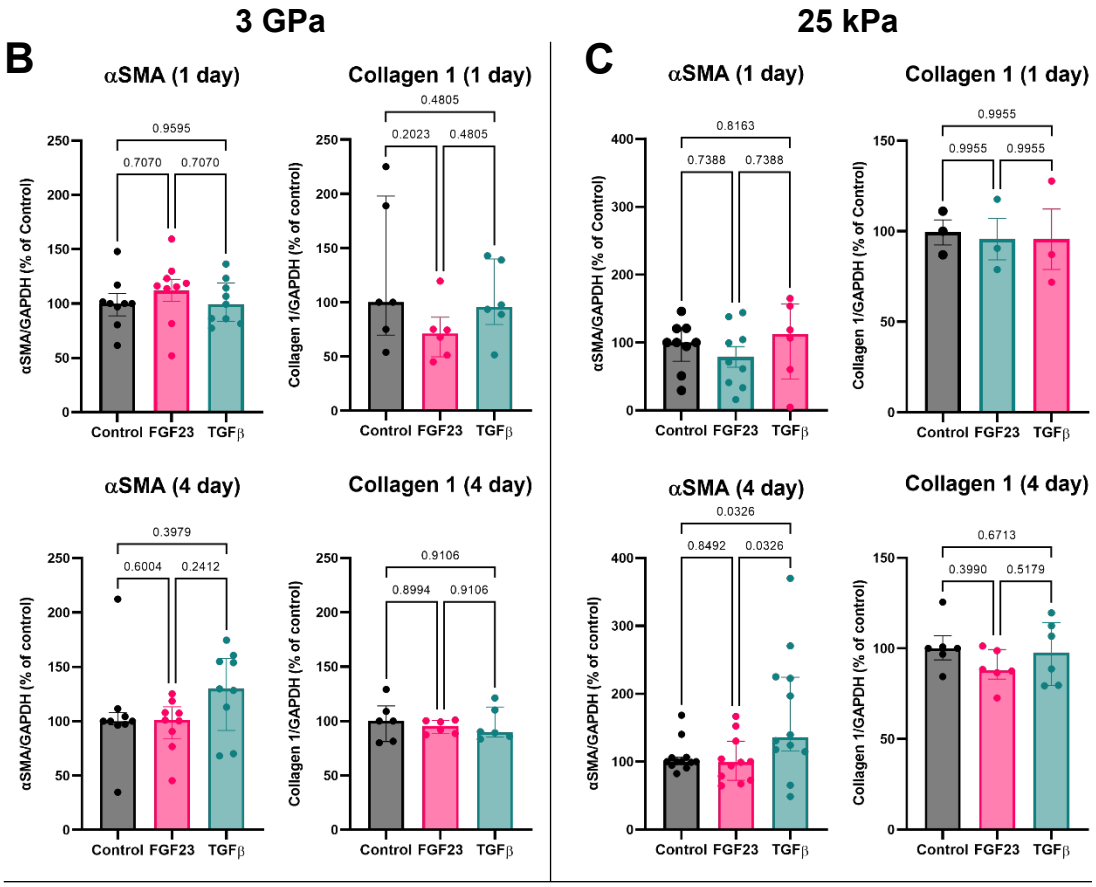
This data was confirmed by protein expression. Representative immunoblots are shown in **Figure 4-6** panel **A**; protein quantification in panel **B**. Collagen type 1 and α-SMA protein expression was largely unaltered by FGF23 and TGFβ treatment regardless of culture substrate stiffness, with the exception of α-SMA expression following a four day treatment with TGF-β when cultured on 3 GPa and 24 kPa substrates. Human cardiac fibroblasts showed a trends towards increased α-SMA expression on the 3 GPa when treated with TGF-β compared to control (121.9%, p = 0.3979; **Figure 4-6 B**). On the 25 kPa substrate, α-SMA expression was significantly increased, and to a similar degree compared with control and the FGF23-treated cells (~160%, p = 0.0326; **Figure 4-6 C**).

Finally, α-SMA expression was assessed by immunofluorescence (**Figure 4-7**). A trend towards increased α-SMA expression was observed in response to TGF-β treatment in fibroblasts cultured on 25 kPa, echoing the immunoblotting findings. However, this did not reach statistical significance (p = 0.0880, **Figure 4-7 B**). No other change in α-SMA or Collagen 1 was seen in response to FGF23 or TGF-β treatment on the 3 GPa and 25 kPa substrates (p > 0.33, **Figure 4-7 A & B**). Intriguingly, α-SMA expression appeared to be downregulated by TGF-β treatment (p < 0.0001 versus FGF23 and control fibroblasts (**Figure 4-7 C**).

Figure 4-6. Effect of FGF23 and TGF-β treatment on HCF activation markers by western blotting.

HCFs were cultured for 1 and 4 days on culture plates with Young's modulus (*E*) of 3 GPa, 25 kPa & 2 kPa in the presence of 10 ng/mL TGFβ, 50 ng/mL FGF23, or vehicle control. **A** – αSMA and collagen 1 protein expression by near-infrared immunoblotting. GAPDH was used as loading control. Quantification of protein of interest/GAPDH in HCFs cultured on: **B** – 3 GPa (N = 6-9); **C** – 25 kPa (N = 3-9); and **D** – 2 kPa substrates (N = 3-9). Data presented as mean ± S.E.M., one-way ANOVA with Tukey post-hoc.




3 GPa
25 kPa
B
C
αSMA (1 day)
Collagen 1 (1 day)
αSMA (4 day)
Collagen 1 (4 day)
αSMA/GAPDH (% of Control)
Collagen 1/GAPDH (% of control)
Control FGF23 TGFβ
0.9595
0.7070 0.7070
0.4805
0.2023 0.4805
0.3979
0.6004 0.2412
0.9106
0.8994 0.9106
0.8163
0.7388 0.7388
0.9955
0.9955 0.9955
0.0326
0.8492 0.0326
0.6713
0.3990 0.5179

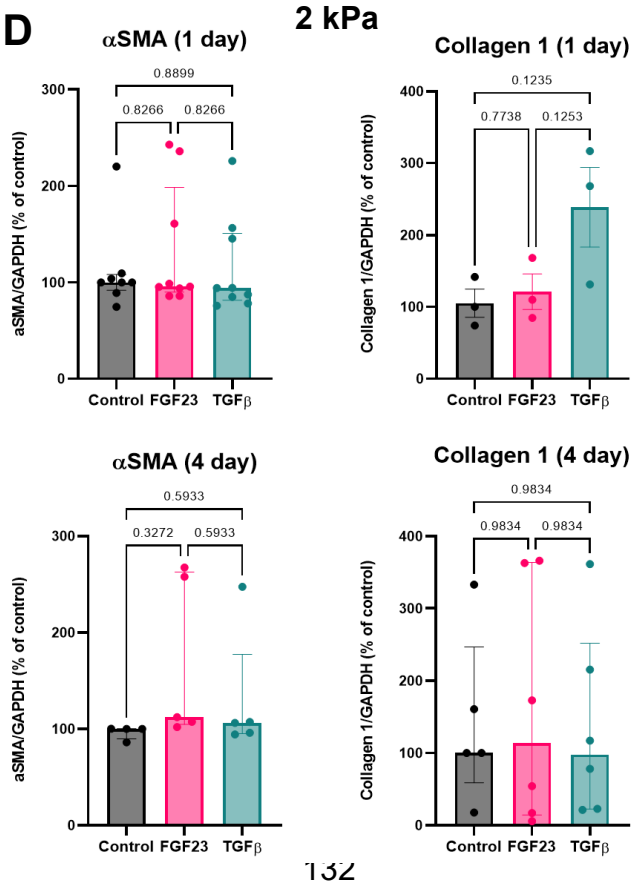
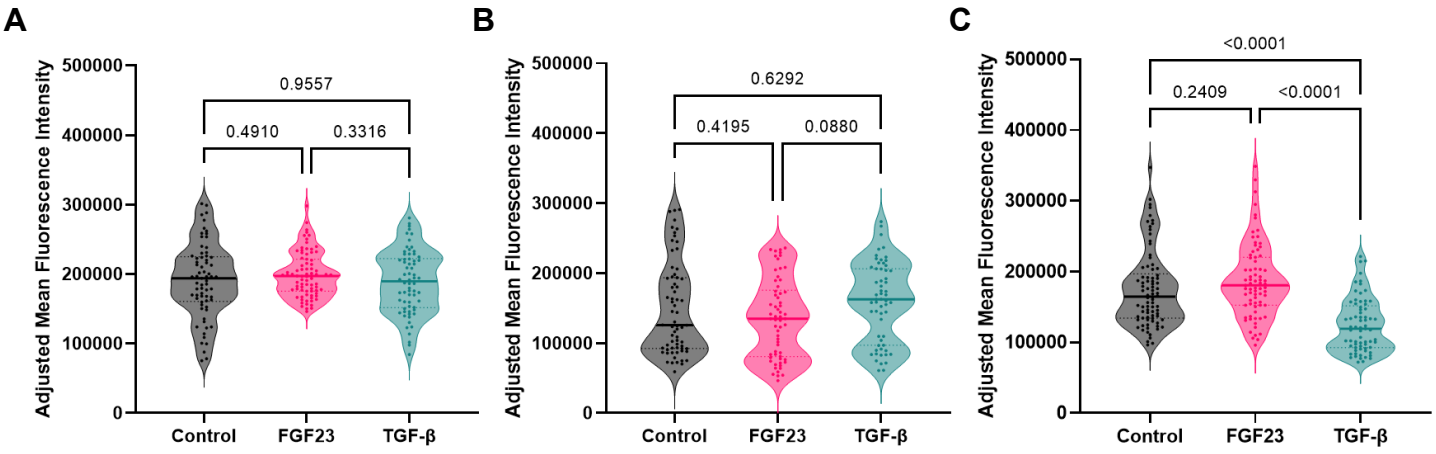

D
2 kPa
αSMA (1 day)
Collagen 1 (1 day)
αSMA (4 day)
Collagen 1 (4 day)
αSMA/GAPDH (% of control)
Collagen 1/GAPDH (% of control)
Control FGF23 TGFβ
0.8899
0.8266 0.8266
0.1235
0.7738 0.1253
0.5933
0.3272 0.5933
0.9834
0.9834 0.9834

Figure 4-7. α-SMA Expression in Cultured Primary HCF by Immunofluorescence.

α-SMA expression was assessed by confocal microscopy following culture on substrates of varying stiffness. HCFs were treated with vehicle control, 50 ng/mL FGF23 or 10 ng/mL TGF-β for 1 day. Fluorescent intensity was normalised to cell surface area. **A** – 3GPa substrate. **B** – 25 kPa substrate. **C** – 2 kPa substrate. Nested one-way ANOVA with Tukey multiple comparison test. (N = 5-11 technical, 3 biological replicates).



4.4.3. hiPSC-derived cardiac fibroblast studies

Separate experiments were conducted to further investigate the effects of FGF23 on fibroblast phenotype using a different fibroblast cell line. hiPSC-derived cardiac fibroblasts (hiPSC-cFb) were cultured on 6-well, hard 3 GPa tissue culture plates for a four-day period in the presence or absence of FGF23 and TGF-β.

Similar to that found in primary isolated human cardiac fibroblasts, FGFR1 was the dominantly expressed FGF receptor in hiPSC, whilst no differences in FGFR2, FGFR3 and FGFR4 mRNA were observed (**Figure 4-8**). FGFR mRNA expression did not change in response to 4 days treatment with 50 ng/mL FGF23 ($p > 0.3$, **Figure 4-9**).

hiPSC-cFb activation was assessed by mRNA expression of ACTA2, COL1A1 and COL3A1 (**Figure 4-10**). In these experiments, hiPSC-cFb displayed increased markers of activation in response to TGF-β treatment: ACTA2 (mean fold change = 3.964, $p < 0.0001$), COL1A1 (mean fold change = 2.476, $p = 0.0072$), and COL3A1 (mean fold change = 3.556, $p = 0.0004$) versus control fibroblasts. Like in the primary human cardiac fibroblasts, treatment with FGF23 did not result in activation of hiPSC-cFb ($p > 0.7$).

Figure 4-8. Human induced pluripotent stem cell derived cardiac fibroblast (iPSC-cFb) fibroblast growth factor receptor (FGFR) gene expression by RT-PCR.

FGFR1 to 4 gene expression in cultured human iPSC-cFb normalised to housekeeping gene GAPDH. Data presented as mean ± S.E.M., N = 11.

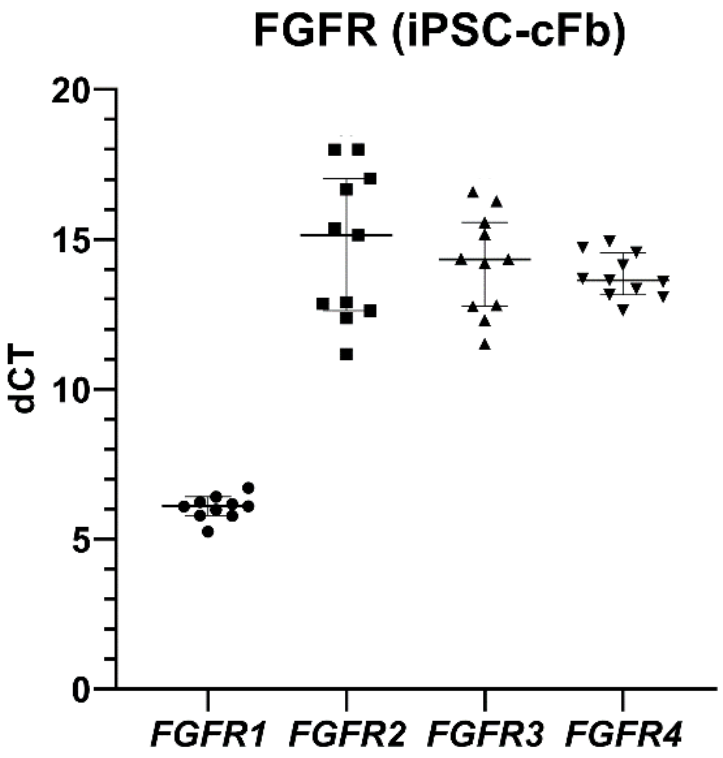


Figure 4-9. Human induced pluripotent stem cell derived cardiac fibroblast (hiPSC-cFb) fibroblast growth factor receptor (FGFR) gene expression following FGF23 exposure.

Human iPSC-cFb were treated with 50 ng/mL FGF23 for four days. FGFR gene expression was assessed by RT-PCR. Data presented as mean ± S.E.M.; unpaired t-test, N = 11.

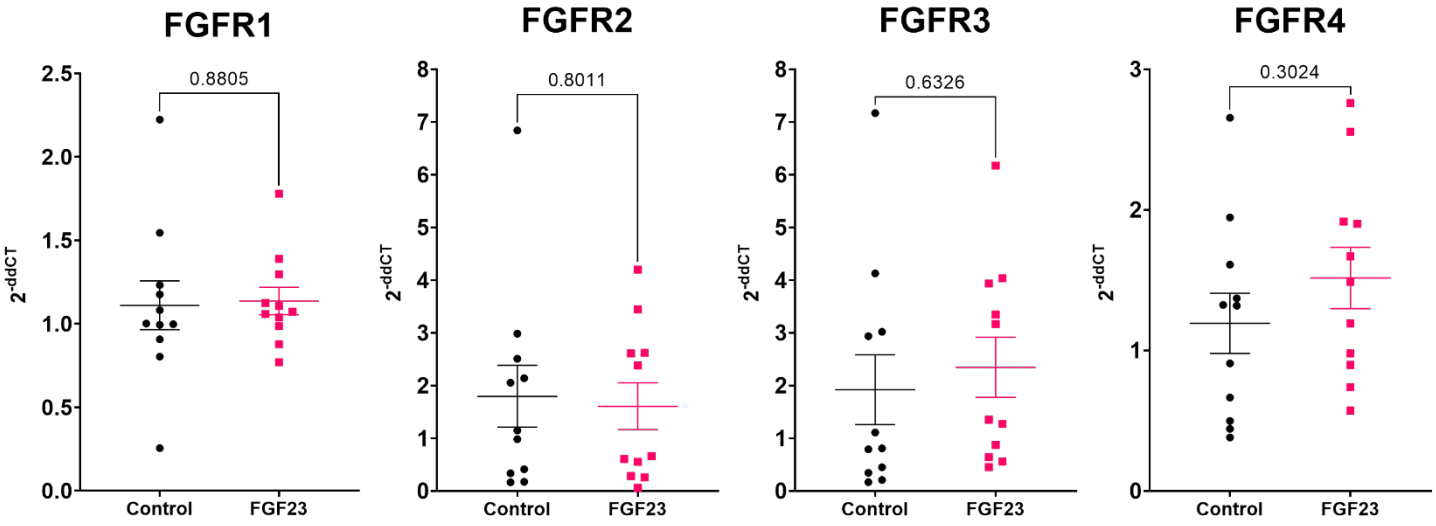
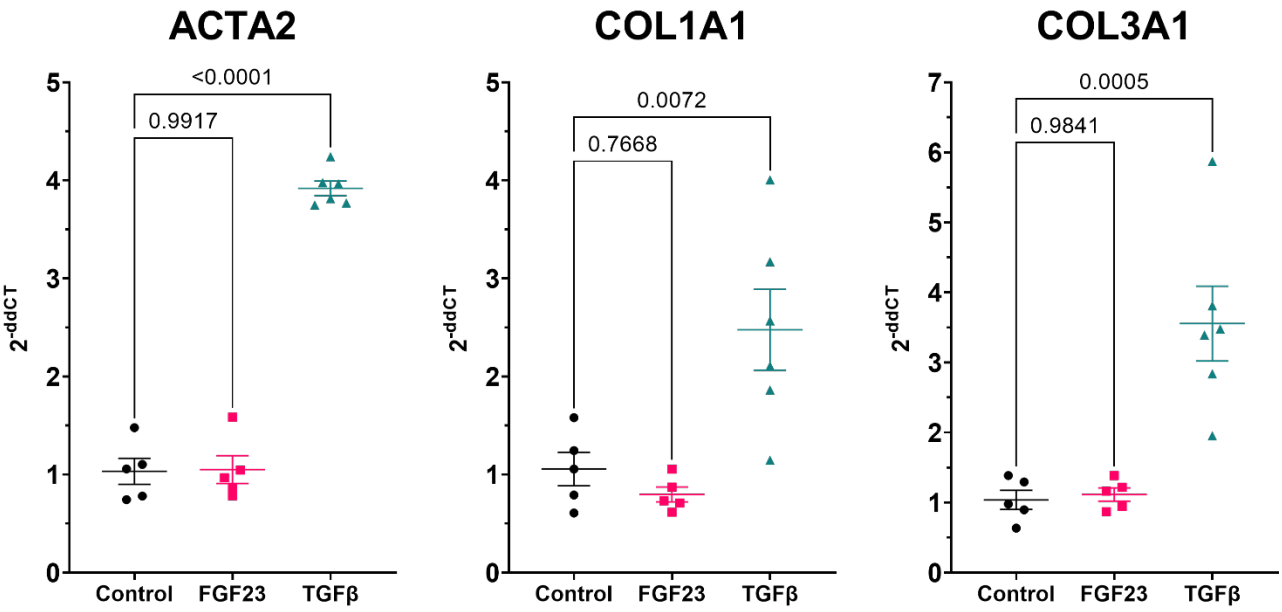


Figure 4-10. Effect of FGF23 and TGF-β on human induced pluripotent stem cell derived cardiac fibroblast (hiPSC-cFb) activation.

Human iPSC-cFbs were cultured for 4 days in the presence of 50 ng/mL FGF23, 10 ng/mL TGF-β, or vehicle control. Myofibroblast markers *ACTA2*, *COL1A1*, *COL3A1* mRNA expression by RT-PCR. Data presented as mean ± S.E.M., one-way ANOVA with Tukey post-hoc (N = 5-6).



4.5. DISCUSSION

CKD-associated cardiomyopathy is associated with heart failure and cardiac arrhythmias [62,251]. Histological studies have demonstrated that myocardial fibrosis is present in patients with ESKD [13,14]. Fibroblasts make up a large proportion of the resident cells of the heart, and act as key regulators of the cardiac interstitium [240]. Under stress, fibroblasts become activated, proliferate, and transition into myofibroblasts. Myofibroblasts express contractile proteins such as α-SMA, and deposit extracellular matrix including collagens as part of a (mal)adaptive response to injury, resulting in fibrosis and scar tissue formation [478,479]. This study seeks to examine the role of FGF23 in the development of CKD-associated cardiomyopathy through a profibrotic mechanism, as implicated by recently published studies using *murine* cells [480-482], and utilises *human* cardiac ventricular fibroblasts as the starting point of experimentation.

There are four known human fibroblast growth factor receptors which are differentially expressed in the human body. FGF23 has been shown to signal through both FGF receptors 1 and 4 in the heart, with FGF receptor 1 being the dominant isoform [248]. FGF receptor has been implicated in the development of cardiac hypertrophy in both in vitro and in vivo studies [171,172,224,225]. In this study, FGFR1 was the dominantly expressed receptor. Furthermore, its expression was significantly greater in HCFs cultured at 25kPa versus 3GPa and 2kPa for 1 day. There were, however, no differences seen between the three culture stiffnesses after 4 days in culture, indicating ECM stiffness may not play a role in longer term expression of FGFR1. Further, larger experiments are indicated as there are, to this date, no published data available for comparison. This study also found that

treatment with FGF23 did not alter FGF receptor expression of HCFs at 1 and 4 days in culture, irrespective of culture plate stiffness.

Neither FGF23 treatment, nor culture on stiff or soft culture plates altered HCF activation status by way of αSMA and Collagen 1 expression at mRNA and protein level. However, the data suggests that the primary cardiac fibroblasts have the potential to be activated by TGF-β; the activation state is evidenced by an increase in α-SMA protein expression without a change in collagen type 1 expression in primary cardiac fibroblasts, whereas genes encoding collagen type 1 and type 3 expression are also upregulated by TGF-β treatment in hiPSC-cFbs. Several potential explanations for the lack of effect of FGF23 and culture surface stiffness on HCF activation status have been postulated.

4.5.1. Culture Surface Stiffness on Activation Status

Previous studies demonstrated that fibroblasts grown on softer culture plates demonstrated lower collagen, α-SMA and fibronectin expression compared to when cultured on conventional polystyrene plates [483,484]. They used freshly isolated murine cells. In our study, we used human cells purchased from PromoCell, and the initial maintenance of HCFs prior to experimentation on softer culture plates was performed on Costar polystyrene plates with a typical Young's modulus of 3 GPa [485]. It is likely that HCFs were already activated by the stiff culture environment prior to this study, supported by data already presented in Chapter 3, blunting the effect of any further treatments with FGF23 and TGFβ. Routine culture of HCFs on soft culture flasks was not possible during this study due to costs.

There was a non-statistically significant trend towards lower αSMA mRNA expression in HCFs cultured on softer culture plates at both 1- and 4-day timepoints, indicating that it may be possible to reverse the activation state of HCFs by lowering the stiffness of its surrounding environment. This was also observed in α-SMA immunofluorescence data in Chapter 3.

4.5.2. αKlotho

αKlotho is an important co-receptor for high affinity binding of FGF23 to FGFR1, and determines the tissue specificity of FGF23 [155,160]. Membrane-bound αKlotho is not expressed in the heart, but it has been hypothesised that circulating αKlotho produced by the kidneys can act on distant tissues as a co-receptor to facilitate FGF23-FGFR1 binding in cell types such as cardiac fibroblasts and myocytes which do not natively express αKlotho [159]. In the current study protocol, there is neither native, nor circulating Klotho, preventing effective FGF23-FGFR1 binding. An alternate, αKlotho-independent pathway has been demonstrated by Faul [171], Grabner [172,174], Han [482] and colleagues via FGFR4, which was implicated in *in vitro* cardiomyocyte hypertrophy and *in vivo* murine cardiac hypertrophy. Although the HCFs in this study expressed FGFR4, the activation status of HCFs *in vitro* was not altered by FGF23.

4.5.3. Constituents of Commercial Fibroblast Media, and Other Factors

PromoCell-recommended FGM3 media was utilised for all HCF culture. Whilst the exact formulation is proprietary, fibroblast growth factor 2 is a present at 1 ng/mL as per the product datasheet. In the hiPSC-cFb experiments, the concentration of FGF2 was 10 ng/mL. FGF2 is part of the FGF superfamily, and

has potent anti-fibrotic response mediated by antagonism of TGF-β-dependent myofibroblast activation [486-490]. Its presence within FGM3 and its inclusion in the hiPSC-cFb maintenance medium could result in partial or complete blockade of TGFβ-mediated signalling. This may be beneficial for maintenance of cardiac fibroblasts in a quiescent state but interfere with experiments investigating their activation to other biomechanical stimuli. Whilst no published studies have studied the effect of FGF23 on human cardiac fibroblasts, a study by Hao et al. [246] found that adult mouse cardiac fibroblasts that had been cultured for four days in FGF23-treated media expressed higher levels of collagen 1 and collagen 3 protein and promoted fibroblast proliferation. A later study by Leifheit-Nestler et al. [477] recapitulated these findings in neonatal rat cardiac fibroblasts, and also found that FGF23 stimulated TGF-β receptor and Smad complexes. Crucially, both studies utilised FGF23 concentrations five to 10 times higher than in our study (Hao et al.: 50 ng/mL, Leifheit-Nestler et al.: 100 ng/mL), that is at the upper end of, and beyond, circulating levels found in patients with advanced kidney disease [491]. Furthermore, their murine cells were cultured in Dulbecco's modified Eagle's medium-based culture media that did not contain FGF2.

The FGF23 and TGF-β used, whilst both derived from human protein, were diluted in 0.1% bovine serum albumin to increase storage and *in vitro* stability, potentially reducing the biological activity of the proteins. However, this was not expected to completely blunt the biological effects of FGF23 and TGF-β.

Finally, a longer experiment duration, in the presence of other key resident cell types in the myocardium as part of a co-culture experiment or in an *in vivo* model of FGF23 excess, is needed to better recapitulate the consequences of

chronically elevated FGF23 circulating levels, as observed in CKD, on the human heart.

CHAPTER 5. QUANTIFYING THE EFFECTS OF ACUTELY ELEVATED FIBROBLAST GROWTH FACTOR 23 ON MURINE VENTRICULAR ELECTROPHYSIOLOGY

5.1. EXTENT OF PERSONAL CONTRIBUTION

All experiments were conducted by the author of this thesis.

5.2. INTRODUCTION

This chapter investigates the effect of acute, high-dose FGF23 exposure on ventricular electrophysiology using an *ex vivo* murine model. The mammalian cardiac conduction system and electrophysiological principles underpinning the ventricular action potential and excitation-contraction coupling are first reviewed.

5.2.1. The cardiac conduction system

The heart resides within the thoracic cavity of all mammalian creatures. Its key purpose is to maintain circulatory blood pressure through coordinated contraction of four hollow chambers, receiving deoxygenated, carbon-dioxide enriched blood from the systemic venous circulation via the inferior and superior vena cava into the right atrium (RA) and the right ventricle (RV). These chambers pump blood through the pulmonary artery into the lungs where it is oxygenated. The blood is received by the left atrium (LA) and the left ventricle (LV) where it is pumped through the aorta and into the systemic arterial system. The synchronous contraction is governed by the cardiac conduction system, which generates action potentials from the sinoatrial node located at the junction of the right atrium and super vena cava [492]. Cells within this region produce an impulse which propagates throughout the RA and LA, initiating atrial contraction and filling of the RV and LV. The impulse conducts towards the atrioventricular[493] (AV) node located at the base of the atrial septum within the triangle of Koch, where propagation to the ventricles is delayed to allow complete atrial depolarisation and contraction, and ventricular filling [493]. The AV node continues distally into the bundle of His before splitting into the left and right bundle branches, which are surrounded by a fibrous sheath providing isolation of the electrical conduction

system to adjacent, electrically active ventricular myocardial tissue. The impulse is finally delivered to the left and right ventricular myocardium via an extensive Purkinje fibre network which forms the terminal conduction system and makes contact with the ventricular myocardium [494].

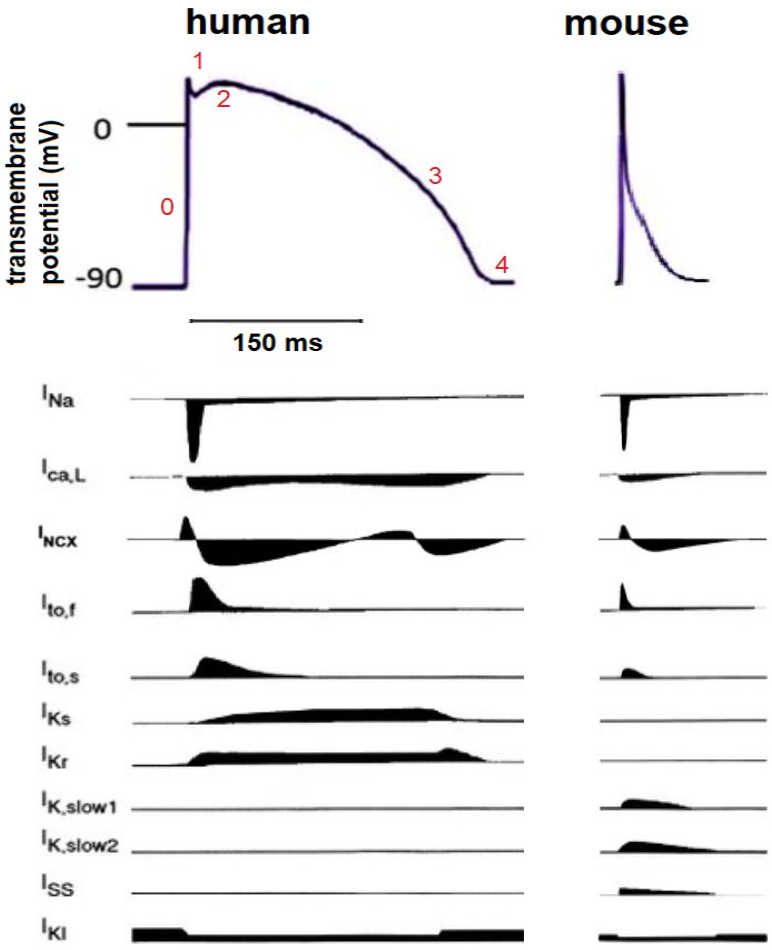
5.2.2. The ventricular action potential

There are five phases to a normal ventricular cardiomyocyte action potential (AP) (**Figure 5-1**). Electrical diastole (phase 4) is maintained by high outward K+ currents (I_{K1}) keeping the resting membrane potential at – 90 mV [495]. When an AP is propagated from neighbouring cells and results in depolarisation above a threshold voltage of – 70 mV, this triggers a rapid inward current of Na^+ ions (I_{Na} or $I_{Na,early}$) generating a large and fast depolarisation of the membrane potential (phase 0) [496]. In humans, this is followed by a fast repolarisation phase (phase 1) brought about by Ca^{2+}-dependent transient outward K^+ currents ($I_{to,f}$ and $I_{to,s}$), and an AP plateau (phase 2) due to an inward Ca^{2+} current (I_{CaL}), prolonging the action potential duration (APD). Repolarisation (phase 3) is primarily attributable to rapid and slow activating delayed outward rectifier K^+ currents (I_{Kr} and I_{Ks}).

In contrast, the murine AP has a less well-defined plateau phase due to smaller I_{CaL} and a faster repolarisation due to $I_{to,f}$, and $I_{to,s}$, and the additional repolarisation currents – slowly inactivating K^+ current ($I_{K,slow1}$, $I_{K,slow2}$) and non-inactivating outward K^+ current (I_{ss}), which are not present in humans [497]. I_{Kr} and I_{Ks} are present in murine hearts, but their function remains unclear [498]. Altogether, these differences produce a shorter, triangle-shaped murine ventricular APD [499].

Figure 5-1. Ventricular action potential in human and mouse.

Representative ventricular action potentials are shown with the five phases denoted by red numbers. Ionic currents contributing to human and murine ventricle action potential are shown below. Inward, depolarising currents project below axis; outward, repolarising currents project above axis. Figure adapted from [495,500,501].



5.2.3. Effective refractory period

A period exists during phases 0 to part of phase 3, when further electrical stimulus, for example from a propagated AP from a neighbouring cell, will not elicit a new AP. This is termed the effective refractory period (ERP) caused by inactivation of voltage-gated sodium channels which remain in a non-conducting closed state until the cell membrane repolarises. This serves as a protective mechanism, coordinating cardiac relaxation and contraction and preventing cardiac arrhythmia [502].

5.2.4. Cardiac excitation-contraction coupling

The process of excitation-contraction coupling (ECC) links the electrical activation of the cardiomyocyte membrane by an action potential to contraction and subsequently relaxation (**Figure 5-2**). Changes in intracellular Ca^{2+} ($[Ca^{2+}]_i$), subsequent binding and unbinding of Ca2+ to cardiac troponin causes a conformational change in the actin-myosin filament complex, ultimately resulting in shortening and lengthening, respectively, of the sarcomere.

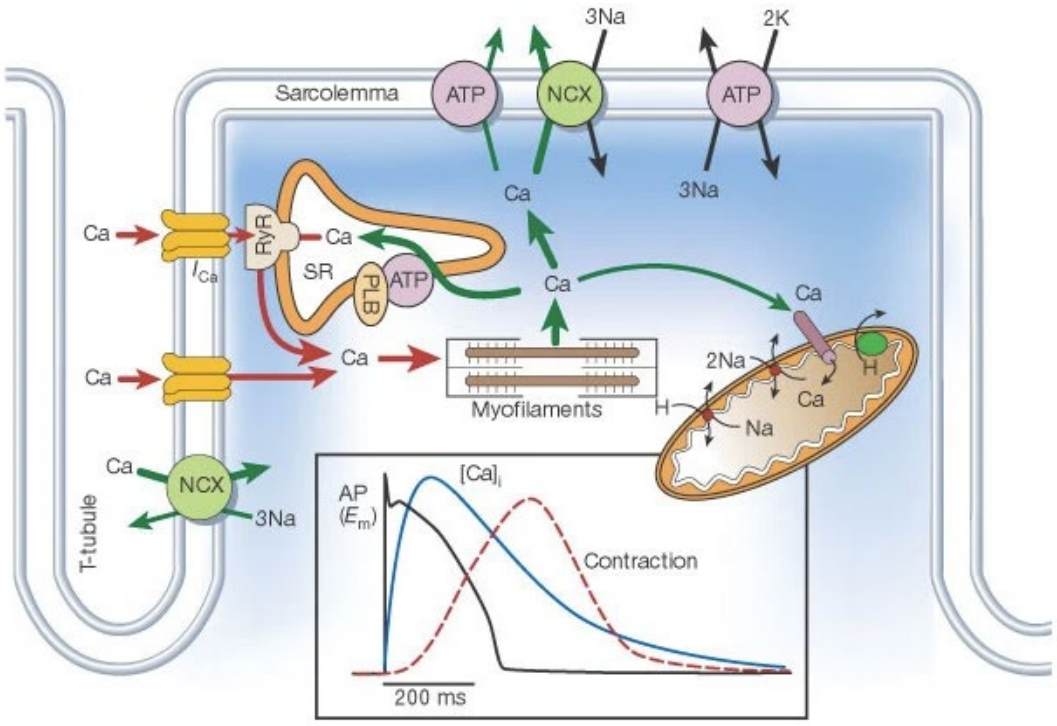
ECC begins with an AP from a neighbouring cell moving along the myocyte sarcolemma and down into the T-tubule. Depolarisation of the membrane by the AP opens voltage-sensitive L-type Ca^{2+} channels (LTCC) on the membrane a T-tubules, causing an influx of Ca^{2+} (I_{CaL}) into the cytoplasm corresponding to the action potential plateau in phase 2. This triggers further Ca^{2+} release from the sarcoplasmic reticulum (SR) through small clusters of juxtaposed ryanodine receptors (RyR2) in a process termed calcium-induced calcium release, resulting in a large rise in $[Ca^{2+}]_i$ [503]. Free calcium binds to troponin complex, which causes

tropomyosin to rotate around the actin thin filament, exposing the myosin binding site[504]. Adenosine triphosphate (ATP) hydrolysis occurs, releasing energy to allow myosin-actin cycling: myosin binds to actin, change its conformation and pull on actin to shorten the sarcomere. At the end of the cycle, a new ATP molecule binds to the myosin head, displacing adenosine diphosphate (ADP) and phosphate created from the hydrolysis of ATP, causing the release of actin, restoration of sarcomere length [505].

In the absence of sufficient $[Ca^{2+}]_i$, muscle contraction does not occur. This is the case during diastole and is essential for ventricular filling. Calcium is sequestered from the cytosol by several mechanisms at the end of phase 2. It is pumped back into the SR by SR Ca^{2+}-ATPase (SERCA2a); sarcolemmal Na^+/Ca^{2+} exchange (NCX) and Ca^{2+}-ATPase transports calcium out of the myocyte; and calcium is taken into the mitochondria through Ca^{2+} uniporters. Simultaneously, calcium release from the SR is terminated as RyR2 close and SR calcium is depleted. The resultant reduction in $[Ca^{2+}]_i$ allows calcium to dissociate from the myofilament troponin complex and the actin binding site to become inhibited from binding to myosin, resulting in muscle relaxation during diastole [506].

Figure 5-2. Schematic of calcium transport and excitation-contraction coupling in ventricular myocytes.

Temporal relationship between action potential, calcium transient and cellular contractile force shown in inset derived from rabbit ventricular cardiomyocyte. The sarcoplasmic reticulum (labelled SR, top left) and mitochondria (oval shape, bottom right) are shown on either side of the myofilaments. Figure from Bers (2022) [506]



5.2.5. Regulation of calcium release and re-entry into the sarcoplasmic reticulum by SERCA2a and RyR2

In humans, SERCA2a activity accounts for the removal of the majority of cytosolic calcium and is bound to a reversibly phosphorylated protein phospholamban (PLB), which regulates its activity. In its dephosphorylated sate, PLB inhibits SERCA2 activity. When PLB is phosphorylated by protein kinase A (PKA) at Ser16 through β-adrenergic stimulation or by calcium-calmodulin-dependent protein kinase II (CaMKII) at Thr17, PLB dissociates from SERCA2a, activating the SERCA2 pump [507,508]. Therefore, SERCA2 activity determines the rate of cardiac relaxation proportional to the rate of calcium re-uptake into the SR, and also the size of diastolic SR calcium store. In turn, this will influence the amount of calcium released from the SR during systole and consequently cardiac contractility.

As discussed above, calcium release from the SR is through RyR2. Its open probability can be increased through phosphorylation by PKA at Ser2809 [509], which results in dissociation from channel stabilising molecule calstabin2 (FKBP12.6); or by phosphorylation of CaMKII at Ser2809 and Ser2815 [509-511] by augmenting RyR2 sensitivity to calcium-dependent activation [512].

It is therefore conceivable that disorders in calcium handling such as in heart failure – either through RyR2 hyperphosphorylation, dysfunction and diastolic SR calcium leak from upregulation of CaMKII and PKA [513]; defective removal of cytoplasmic calcium either due to increased NCX expression [514] or reduced SR calcium uptake [515]; a combination of RyR2 calcium leak and SERCA2a inhibition caused by reactive oxygen species [516] [517]; and dyssynchronous ECC from

ultrastructural changes in the T tubule system [518] or remodelling of the LTCC-RyR2 dyad [519] – result in increased risk of arrhythmias [520], reduced SR calcium load and contractile dysfunction [521].

As previously discussed, there have been numerous clinical associations with FGF23 and atrial and ventricular arrhythmias [186,187,190,522]. Emerging evidence utilising whole cell patch clamp technique [254,257,523-525] and intracellular calcium imaging of isolated cardiomyocytes [254,257,524,525] or tissue strips [526] have implicated impaired cardiomyocyte calcium handling as a potential mechanism underpinning FGF23-induced arrhythmogenesis.

The primary aims of this chapter were to investigate the effect of acute FGF23 treatment on murine ventricular electrophysiology using a whole tissue, *ex vivo* 'beating heart' model. Specifically, action potential morphology and conduction through the left ventricle were examined using optical mapping. Using fluorescent dyes to study the electrical behaviour, optical mapping offers superior spatial-temporal resolution to traditional electrode/single-cell techniques [527]. The arrhythmia burden was also quantified by *ex vivo* bipolar ECG.

5.3. METHODS

Full experimental methodology can be found in Chapter 2.

Hearts were isolated via thoracotomy from wild-type CD1 female mice (9 to 15 weeks old) under terminal anaesthesia and immediately Langendorf-perfused in KHB solution containing Blebbistatin (12 μM). Voltage-sensitive dye Di-4-ANEPPS (125 μg) was then loaded over 5 minutes. Following a 10-minute stabilisation period, optical mapping recordings at baseline, 10 minutes, and 30 minutes into infusion with 10 ng/mL FGF23 or vehicle control KHB were taken. After a 20-minute KHB washout period, a final optical mapping recording was taken. During each timepoint, a dynamic pacing protocol was employed, starting at 150 ms cycle length, reducing by 10 ms every 20 beats, until a cycle length of 80 ms was reached. Simultaneous bipolar ECGs were recorded and analysed using LabChart version 8 (ADInstruments). Optical mapping recordings were saved using MetaMorph (Molecular Devices) and exported to ElectroMap for processing and analysis. The first 5 beats of each cycle length train were discarded, leaving 15 beats for analysis.

Two-way ANOVA with Sidak multiple comparisons test was employed to examine the effect of treatment on the electrophysiological parameter of interest across different cycle lengths.

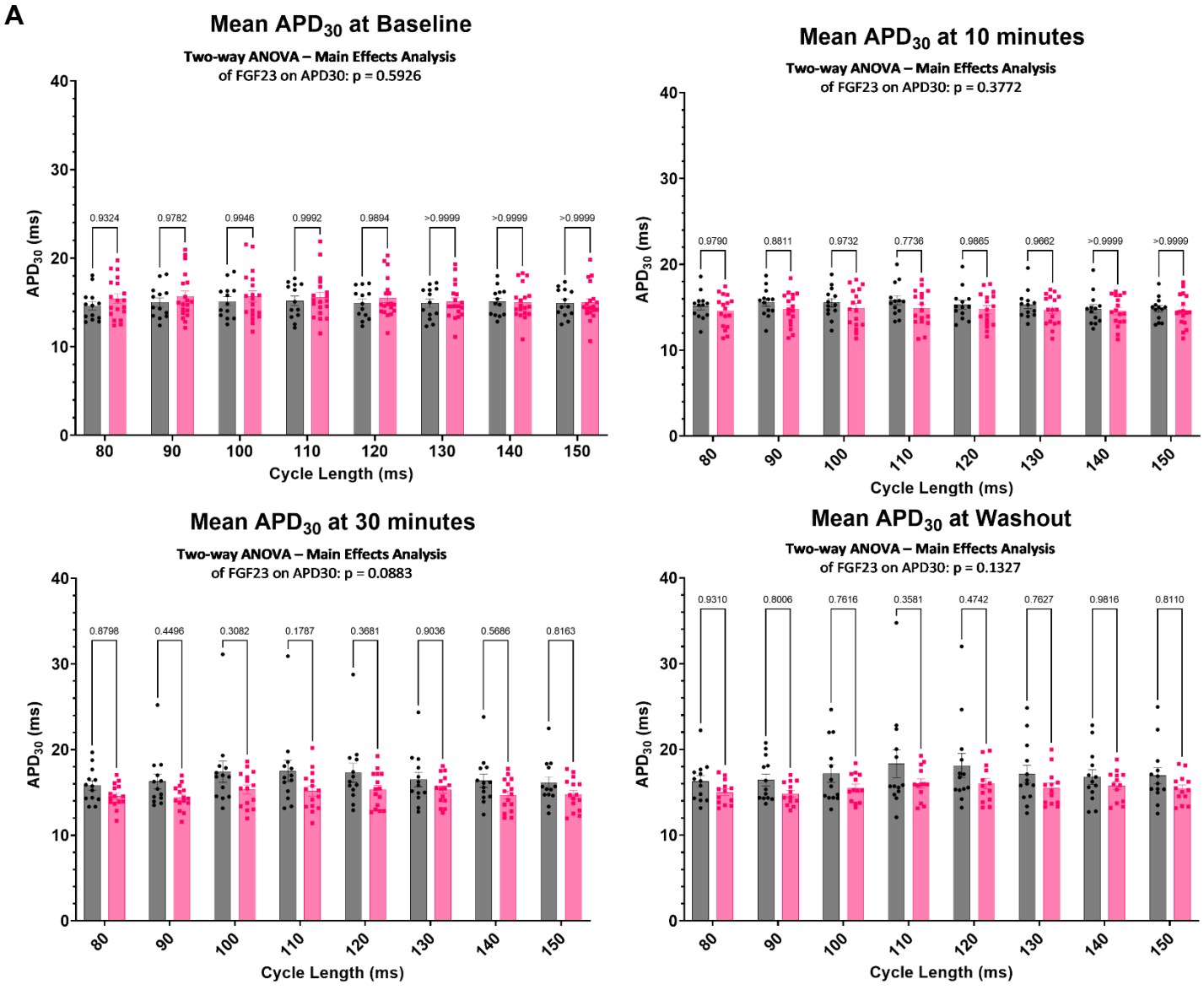
5.4. RESULTS

5.4.1. Action potential duration

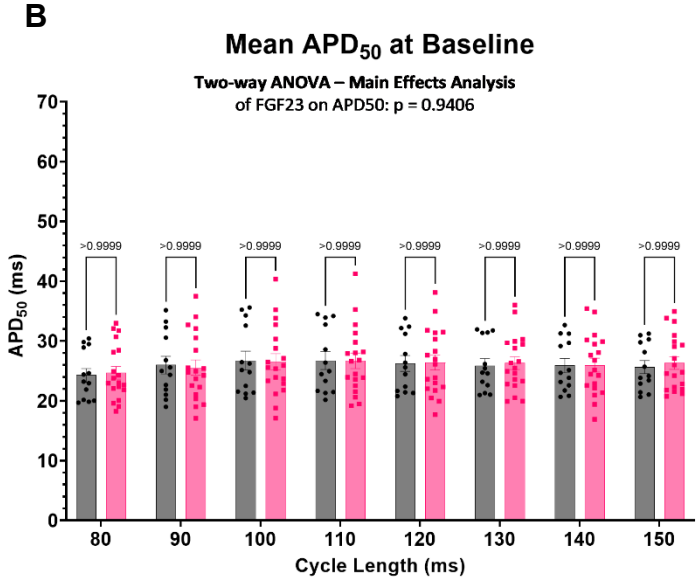
Left ventricular action potential duration was determined from the maximum upstroke velocity to at 30% (APD_{30}, **Figure 5-3 A**), 50% (APD_{50}, **Figure 5-3 B**) and 80% (APD_{80}, **Figure 5-3 C**) repolarisation. No difference in APD30 (simple main effects p = 0.5926), APD50 (simple main effects p = 0.9406) or APD80 (simple main effects p = 0.7855) between FGF23 (N = 13 hearts) and control (N = 13-18 hearts) groups were observed at the baseline. After 10 minutes of infusion with 10 ng/mL FGF23, there was non-statistically significant shortening of APD_{50} (mean reduction in APD_{50} = 3.18 ms [95%CI -0.62 to 7.0], p = 0.0975) and APD_{80} (mean reduction in APD_{80} = 5.02 ms [95%CI -0.34 to 10.37], p = 0.0651). At 30 minutes, shortening of left ventricular was seen at APD_{50} (mean reduction in APD_{50} = 5.43 ms [95%CI 0.56 to 10.30], p = 0.0303) and APD_{80} (mean reduction in APD_{80} = 7.29 ms [95%CI 0.99 to 13.59], p = 0.0250) versus vehicle infused hearts. There was a trend towards shortening of APD_{30} at 30 minutes, but this did not reach statistical significance (mean reduction in APD_{30} = 1.71 ms [95%CI -0.27 to 3.69], p = 0.0883). Following 20-minute washout in KHB, there were no statistically significant differences in APD30 (simple main effects p = 0.1327), APD50 (simple main effects p = 0.5926) or APD80 (simple main effects p = 0.1922) between the FGF23 and control groups. Cycle length had a significant effect on APD at all timepoints and is a well-described phenomenon [528]. Cycle length did not interact with the treatment variable. These data show that 10 ng/mL FGF23 infusion shortens ventricular action potential duration.

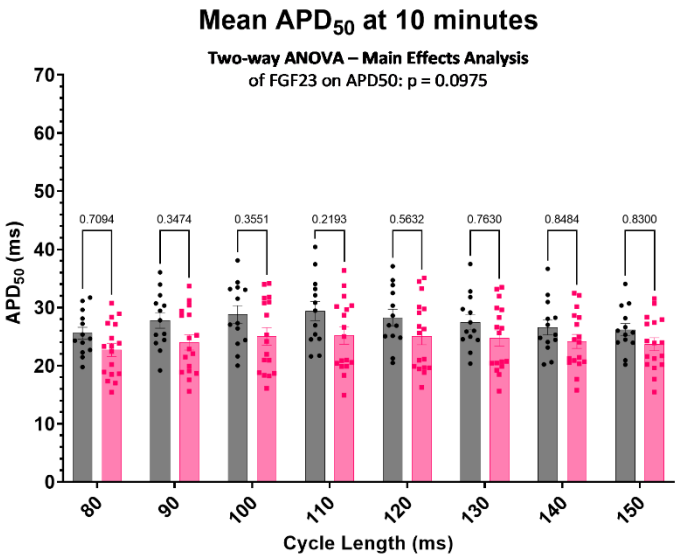
Figure 5-3. Effect of FGF23 on murine left ventricular action potential duration by optical mapping.

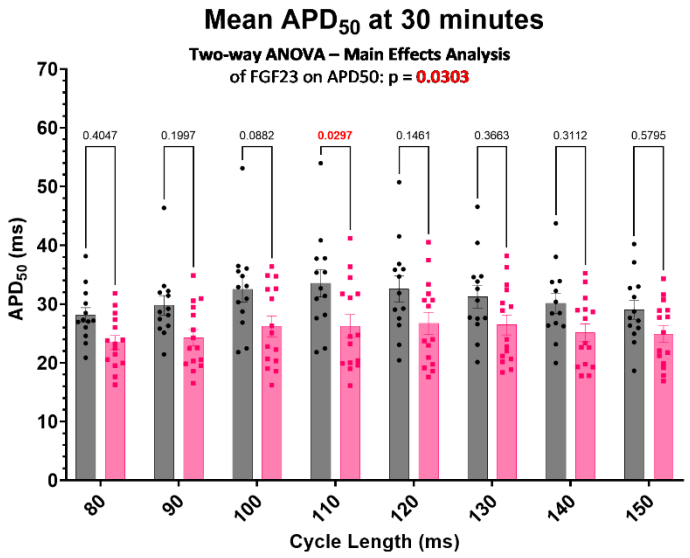
Action potential duration (APD) at **A** – 30% repolarisation; **B** – 50% repolarisation with representative APD maps at 110 ms cycle length; and **C** – 80% repolarisation with representative APD maps at 110 ms cycle length. Optical mapping recordings were taken at baseline, 10 & 30 minutes into treatment with 10 ng/mL FGF23 (**pink**) or vehicle control phosphate buffered saline (**grey**), and following a 20-minute washout period. Data presented as mean ± S.E.M. Two-way ANOVA (treatment x APD); P values shown for main effects analysis of FGF23 on APD, and Sidak multiple comparison tests (N = 13 – 15 hearts per group).

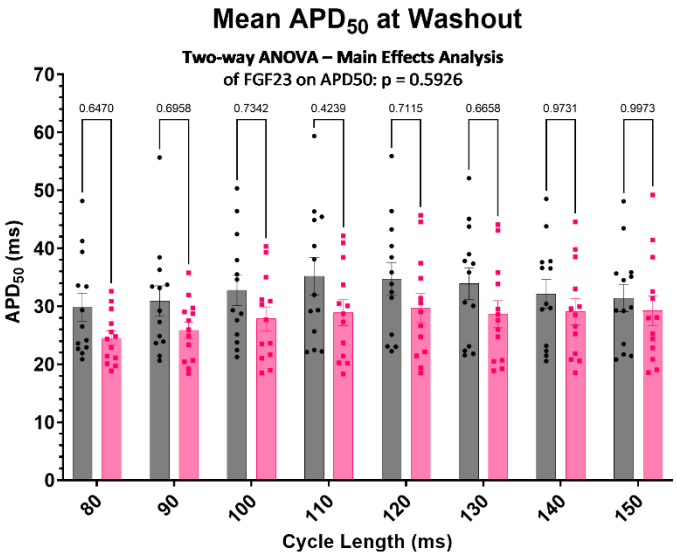


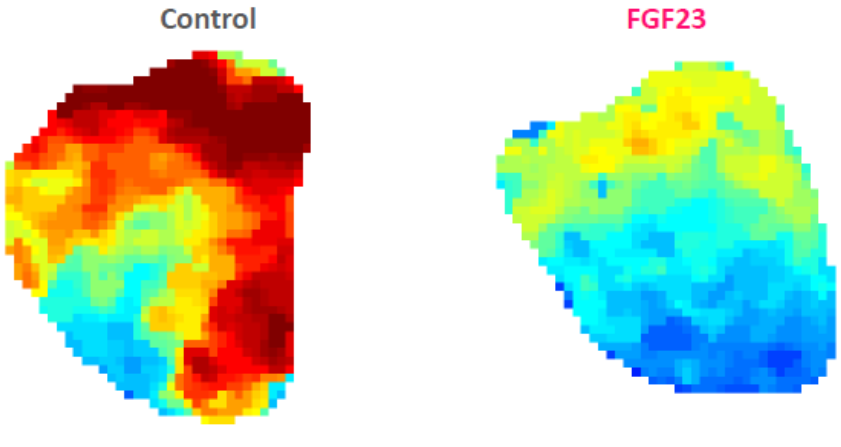
B


Mean APD50 at Baseline
Two-way ANOVA – Main Effects Analysis
of FGF23 on APD50: p = 0.9406
APD50 (ms)
Cycle Length (ms)
>0.9999

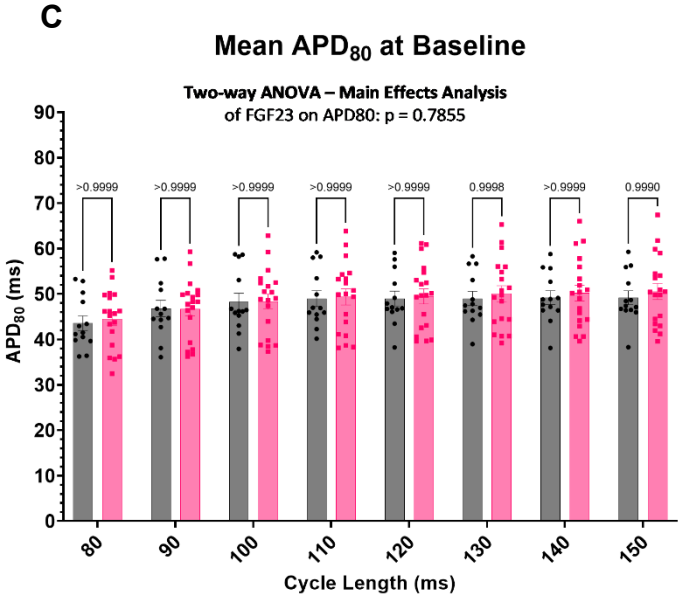

Mean APD50 at 10 minutes
Two-way ANOVA – Main Effects Analysis
of FGF23 on APD50: p = 0.0975
APD50 (ms)
Cycle Length (ms)
0.7094
0.3474
0.3551
0.2193
0.5632
0.7630
0.8484
0.8300

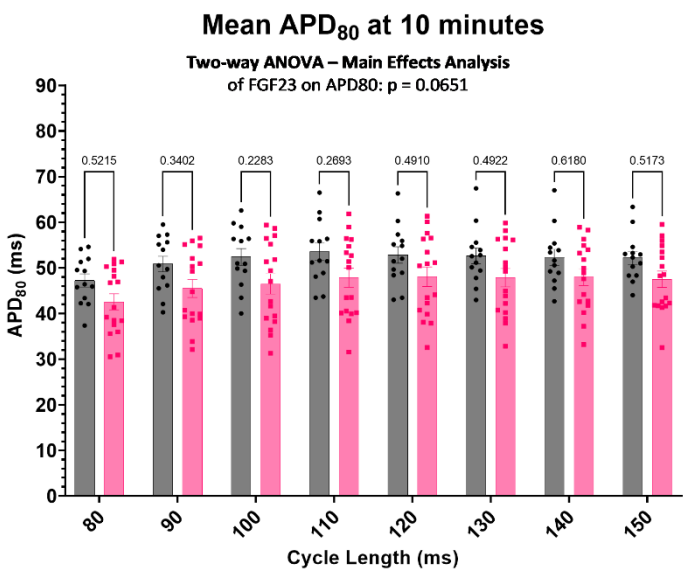

Mean APD50 at 30 minutes
Two-way ANOVA – Main Effects Analysis
of FGF23 on APD50: p = 0.0303
APD50 (ms)
Cycle Length (ms)
0.4047
0.1997
0.0882
0.0297
0.1461
0.3663
0.3112
0.5795

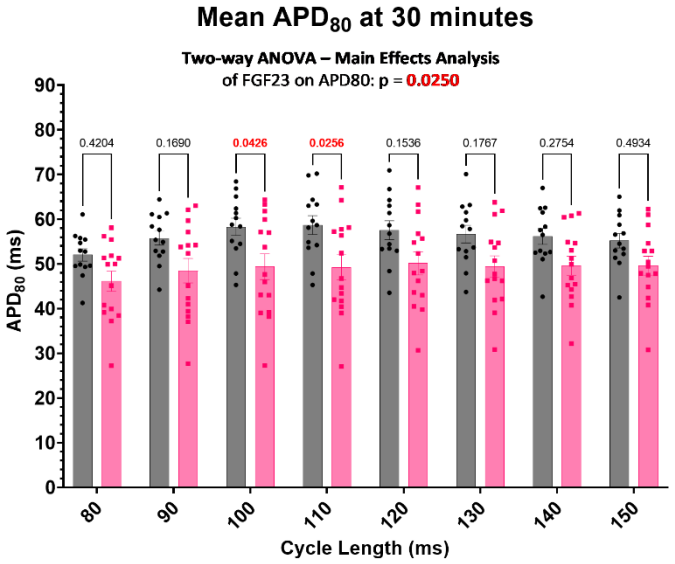

Mean APD50 at Washout
Two-way ANOVA – Main Effects Analysis
of FGF23 on APD50: p = 0.5926
APD50 (ms)
Cycle Length (ms)
0.6470
0.6958
0.7342
0.4239
0.7115
0.6658
0.9731
0.9973

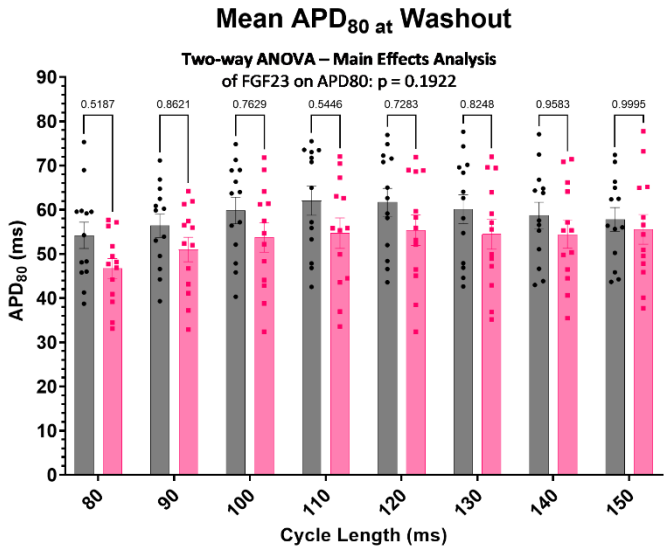

Control
FGF23
Duration (ms)

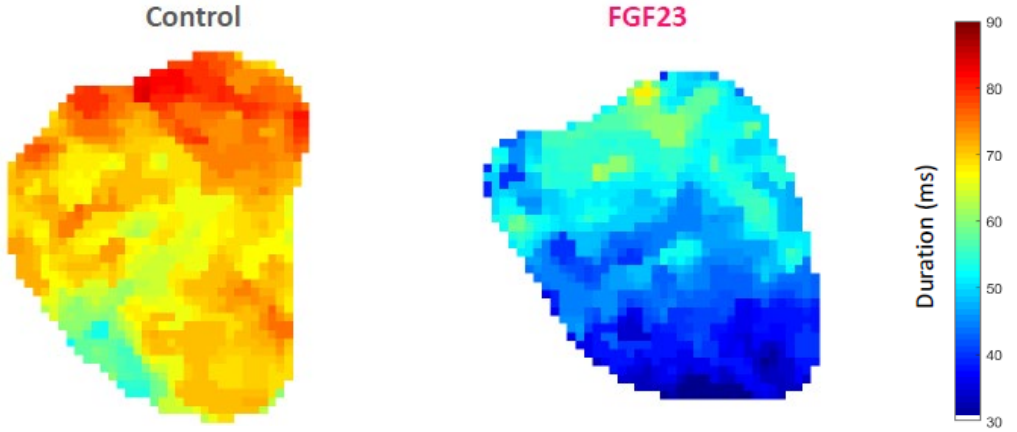
C


Mean APD80 at Baseline
Two-way ANOVA – Main Effects Analysis
of FGF23 on APD80: p = 0.7855
>0.9999
>0.9999
>0.9999
>0.9999
>0.9999
0.9998
>0.9999
0.9990
APD80 (ms)
Cycle Length (ms)


Mean APD80 at 10 minutes
Two-way ANOVA – Main Effects Analysis
of FGF23 on APD80: p = 0.0651
0.5215
0.3402
0.2283
0.2693
0.4910
0.4922
0.6180
0.5173
APD80 (ms)
Cycle Length (ms)


Mean APD80 at 30 minutes
Two-way ANOVA – Main Effects Analysis
of FGF23 on APD80: p = 0.0250
0.4204
0.1690
0.0426
0.0256
0.1536
0.1767
0.2754
0.4934
APD80 (ms)
Cycle Length (ms)


Mean APD80 at Washout
Two-way ANOVA – Main Effects Analysis
of FGF23 on APD80: p = 0.1922
0.5187
0.8621
0.7629
0.5446
0.7283
0.8248
0.9583
0.9995
APD80 (ms)
Cycle Length (ms)


Control
FGF23
Duration (ms)

5.4.2. Action potential duration heterogeneity

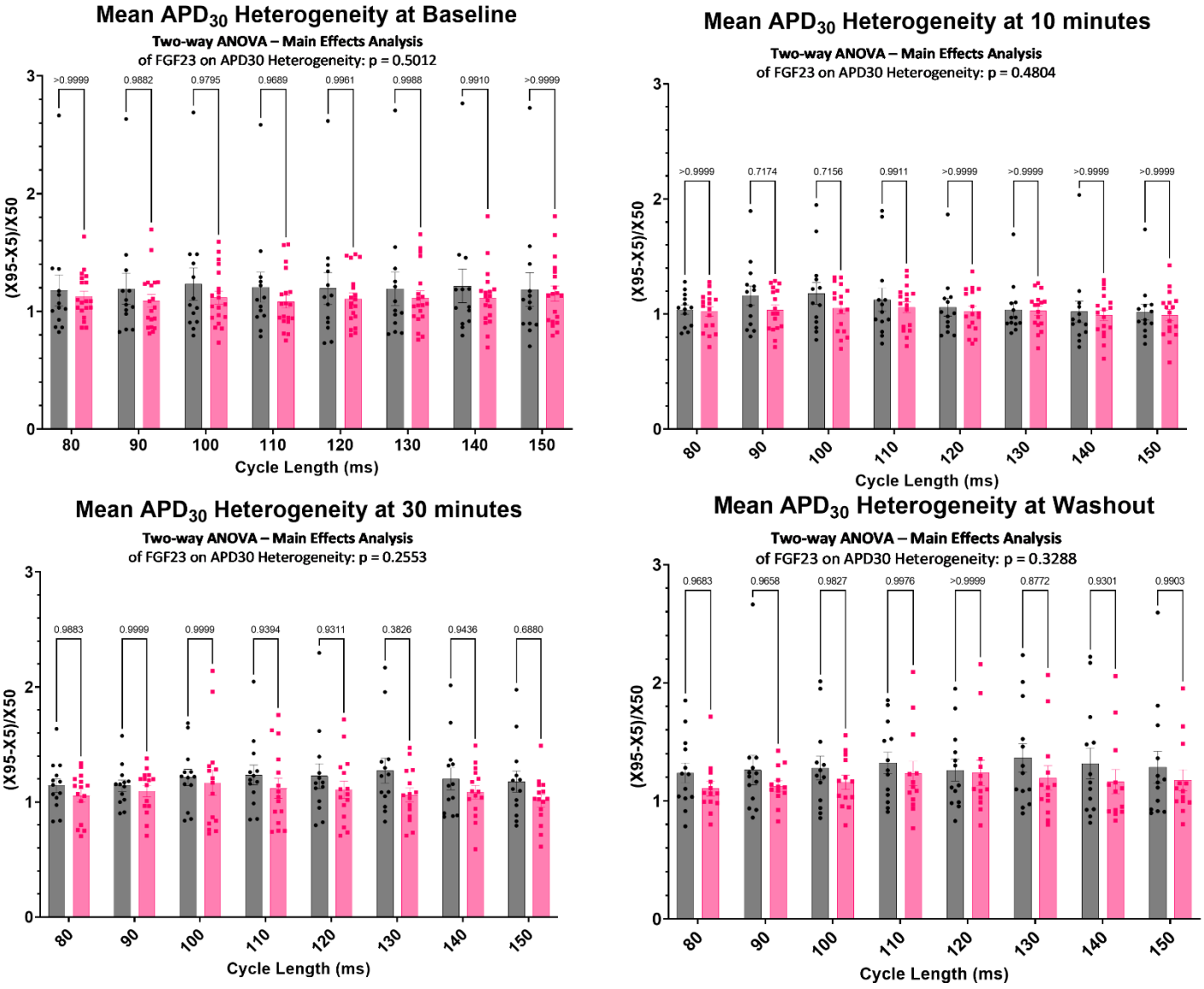
Action potential duration heterogeneity was defined as $\frac{X^{95}-X^{5}}{X^{50}}$ and describes the intraventricular distribution, or spatial dispersion, of APD within the area of interest, which in the present study was the anterior surface of the left ventricle. There is inherent spatial heterogeneity in the heart due to specialised electrical properties of various regions characterised by differential expression of ion channels and connexin proteins [529,530]. In the healthy ventricle, there is both transmural heterogeneity [531,532] and also regional differences between apical and basal cardiomyocytes [533]. Pathological increases in heterogeneity may increase the likelihood of re-entrant arrhythmias [534,535].

In this study, 10 ng/mL FGF23 treatment increased APD80 heterogeneity compared to control (**Figure 5-4 C**). At 10 minutes, there was a mean increase in heterogeneity of 0.09 (95%CI -0.04 to 0.22), although this did not reach statistical significance (p = 0.0243). At 30 minutes, there was a significant mean increase in heterogeneity of 0.15 (95%CI 0.02 to 0.27, p = 0.0243). The increase in heterogeneity as a result of FGF23 treatment was not seen after washout (simple main effects p = 0.3381). FGF23 treatment did not increase APD heterogeneity at 30% (**Figure 5-4 A**) or 50% (**Figure 5-4 B**) repolarisation.

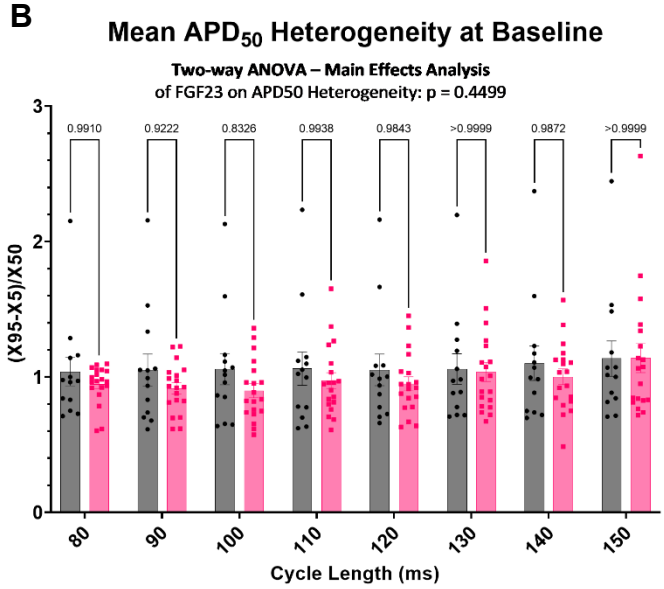
Figure 5-4. Effect of FGF23 on murine left ventricular action potential duration heterogeneity by optical mapping.

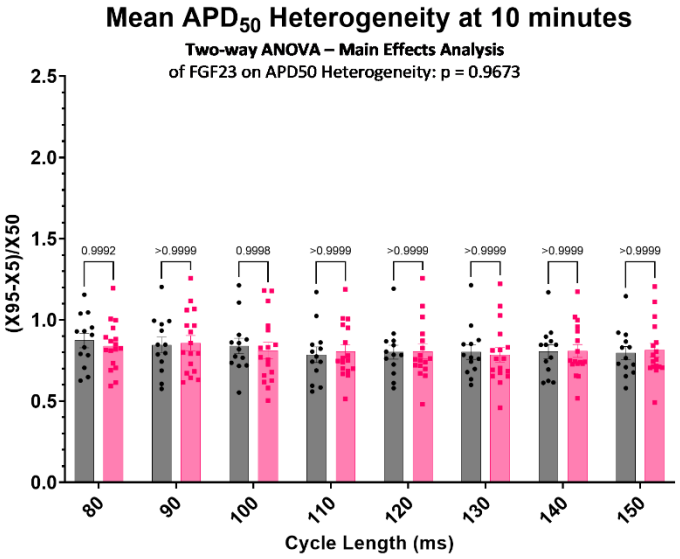
Action potential duration (APD) heterogeneity at **A** – 30% repolarisation; **B** – 50% repolarisation; and **C** – 80% repolarisation. Optical mapping recordings were taken at baseline, 10 & 30 minutes into treatment with 10 ng/mL FGF23 (**pink**) or vehicle control phosphate buffered saline (**grey**), and following a 20-minute washout period. Data presented as mean ± S.E.M. Two-way ANOVA (treatment x APD heterogeneity); P values shown for main effects analysis of FGF23 on APD heterogeneity and Sidak multiple comparison tests (N = 13 – 15 hearts per group).

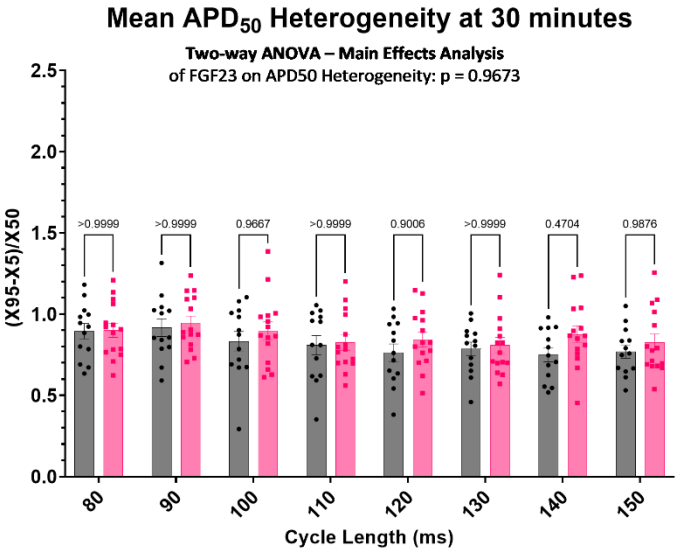
A

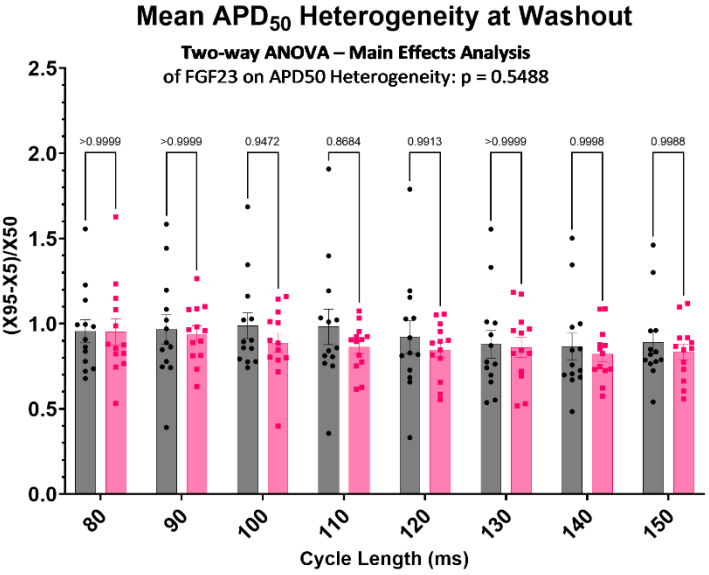


B

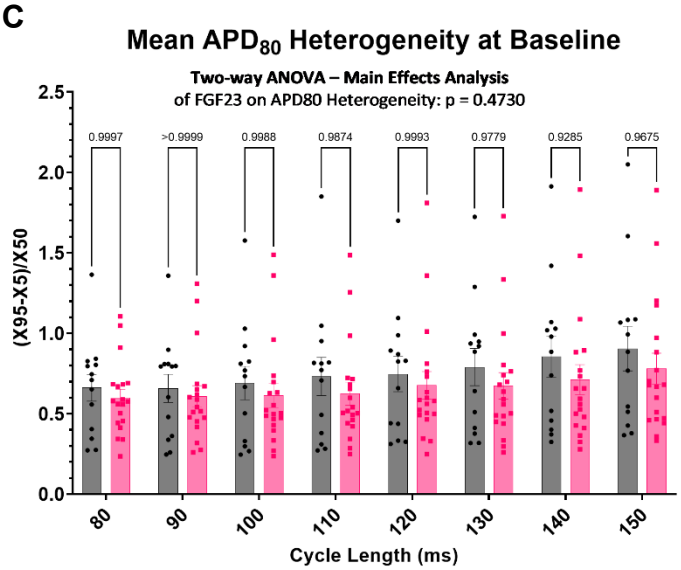

Mean APD50 Heterogeneity at Baseline
Two-way ANOVA – Main Effects Analysis
of FGF23 on APD50 Heterogeneity: p = 0.4499
(X95-X5)/X50
0.9910
0.9222
0.8326
0.9938
0.9843
>0.9999
0.9872
>0.9999
80
90
100
110
120
130
140
150
Cycle Length (ms)

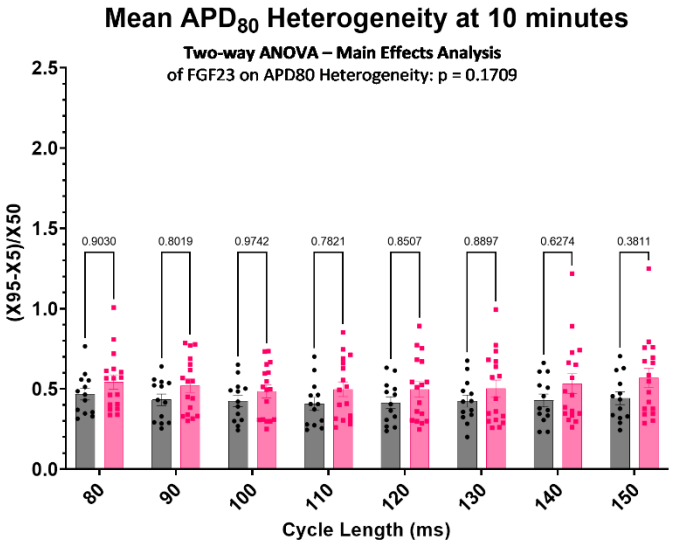

Mean APD50 Heterogeneity at 10 minutes
Two-way ANOVA – Main Effects Analysis
of FGF23 on APD50 Heterogeneity: p = 0.9673
(X95-X5)/X50
0.9992
>0.9999
0.9998
>0.9999
>0.9999
>0.9999
>0.9999
>0.9999
80
90
100
110
120
130
140
150
Cycle Length (ms)

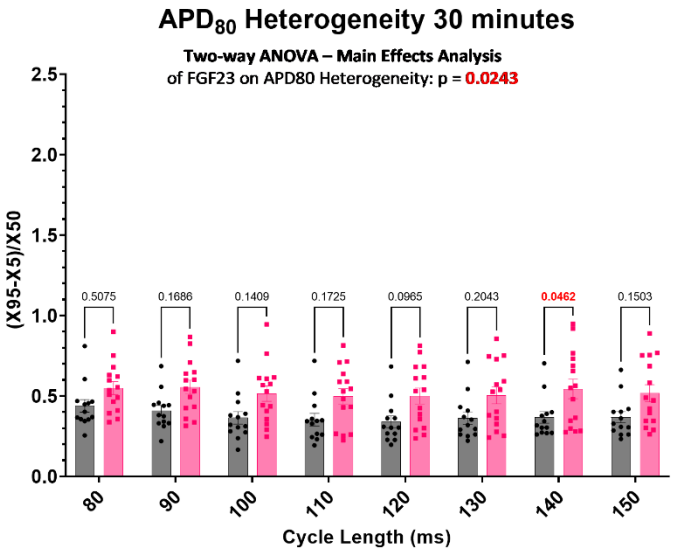

Mean APD50 Heterogeneity at 30 minutes
Two-way ANOVA – Main Effects Analysis
of FGF23 on APD50 Heterogeneity: p = 0.9673
(X95-X5)/X50
>0.9999
>0.9999
0.9667
>0.9999
0.9006
>0.9999
0.4704
0.9876
80
90
100
110
120
130
140
150
Cycle Length (ms)

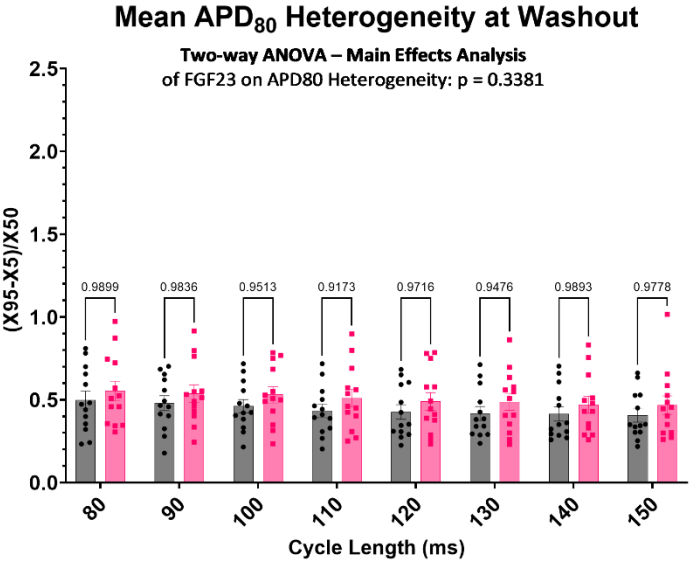

Mean APD50 Heterogeneity at Washout
Two-way ANOVA – Main Effects Analysis
of FGF23 on APD50 Heterogeneity: p = 0.5488
(X95-X5)/X50
>0.9999
>0.9999
0.9472
0.8684
0.9913
>0.9999
0.9998
0.9988
80
90
100
110
120
130
140
150
Cycle Length (ms)

C


Mean APD80 Heterogeneity at Baseline
Two-way ANOVA – Main Effects Analysis
of FGF23 on APD80 Heterogeneity: p = 0.4730
0.9997
>0.9999
0.9988
0.9874
0.9993
0.9779
0.9285
0.9675
(X95-X5)/X50
Cycle Length (ms)


Mean APD80 Heterogeneity at 10 minutes
Two-way ANOVA – Main Effects Analysis
of FGF23 on APD80 Heterogeneity: p = 0.1709
0.9030
0.8019
0.9742
0.7821
0.8507
0.8897
0.6274
0.3811
(X95-X5)/X50
Cycle Length (ms)


APD80 Heterogeneity 30 minutes
Two-way ANOVA – Main Effects Analysis
of FGF23 on APD80 Heterogeneity: p = 0.0243
0.5075
0.1686
0.1409
0.1725
0.0965
0.2043
0.0462
0.1503
(X95-X5)/X50
Cycle Length (ms)

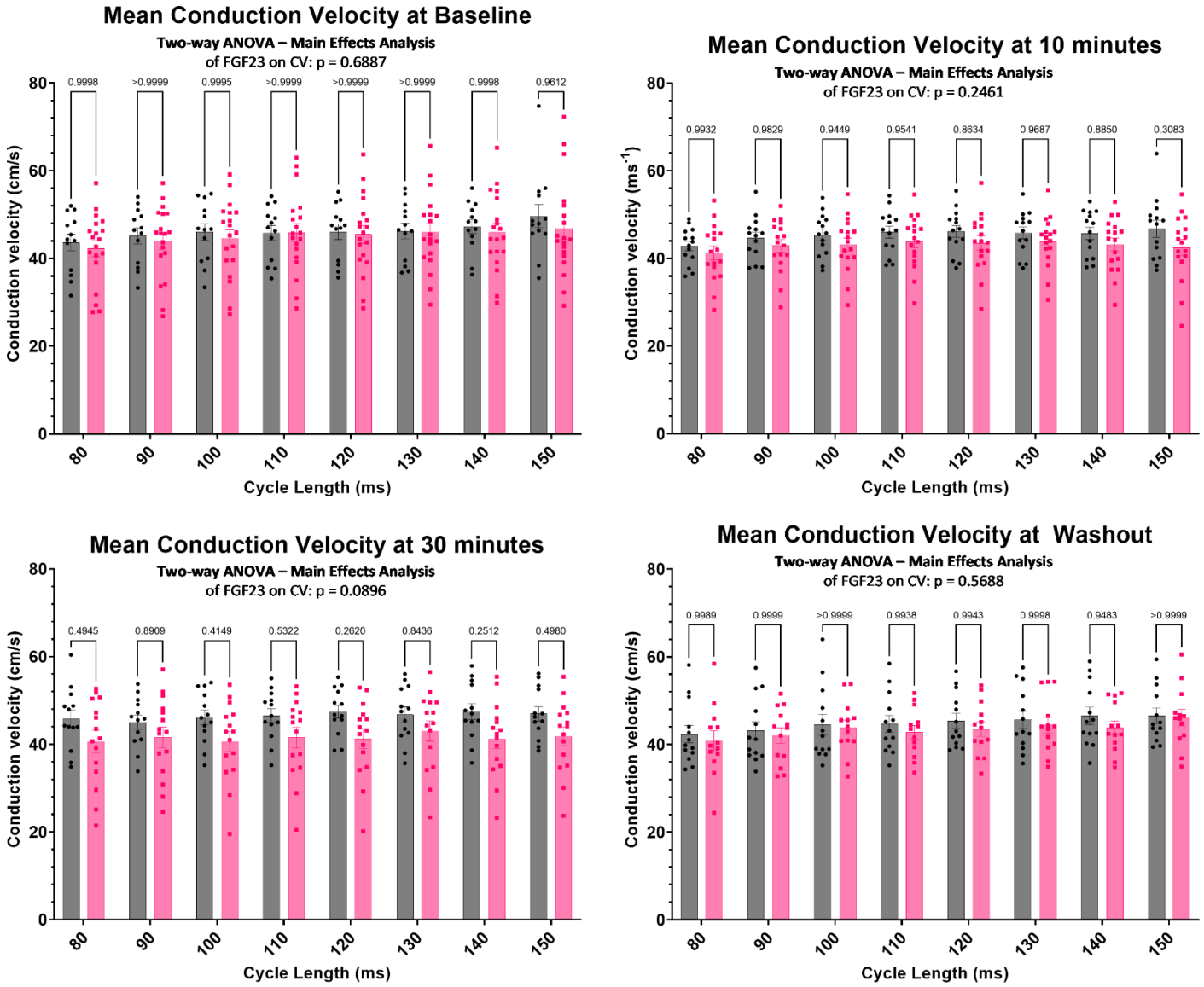

Mean APD80 Heterogeneity at Washout
Two-way ANOVA – Main Effects Analysis
of FGF23 on APD80 Heterogeneity: p = 0.3381
0.9899
0.9836
0.9513
0.9173
0.9716
0.9476
0.9893
0.9778
(X95-X5)/X50
Cycle Length (ms)

5.4.3. Conduction Velocity

Conduction velocity represents the velocity at which a depolarising electrical impulse is conducted through the myocardium. 10 ng/mL FGF23 infusion produced a non-significant reduction in conduction velocity after 30 minutes treatment (mean reduction in conduction velocity 5.08 cm/s [95%CI -0.84 to 11.00], p = 0.0896). No change in conduction velocity between groups was observed at washout (simple main effects p = 0.5688; **Figure 5-5**).

Figure 5-5. Effect of FGF23 on murine left ventricular conduction velocity by optical mapping.

Conduction velocity (CV) was measured from optical mapping recordings taken at baseline, 10 & 30 minutes into treatment with 10 ng/mL FGF23 (**pink**) or vehicle control phosphate buffered saline (**grey**), and following a 20-minute washout period. Data presented as mean ± S.E.M. Two-way ANOVA (treatment x CV) were performed; P values shown for main effects analysis of FGF23 on CV and Sidak multiple comparison tests (N = 13 – 15 hearts per group).

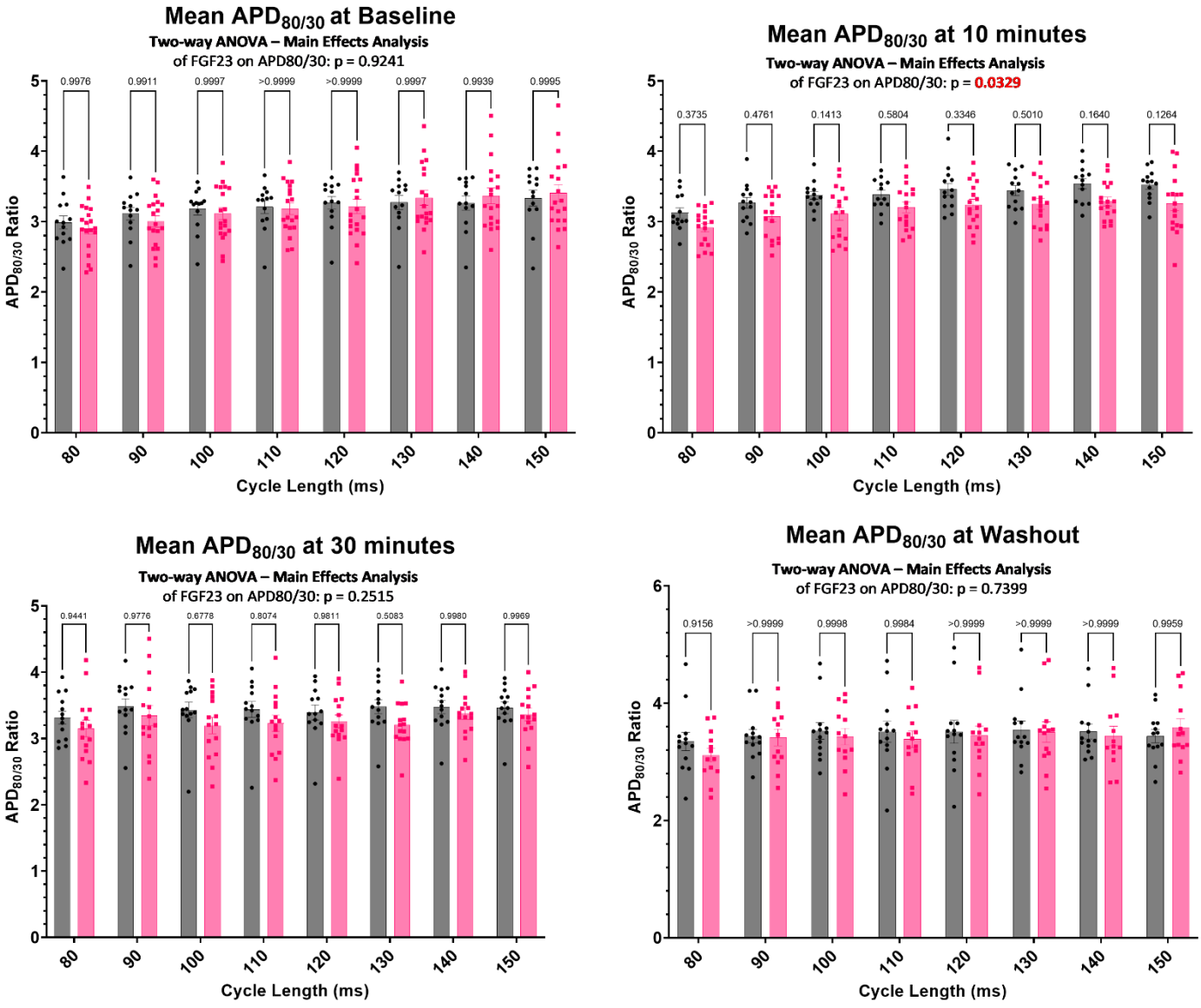


5.4.4. Triangulation

Triangulation is expressed as a ratio of APD_{80} over APD_{30}. Increase in triangulation indicates prolongation of the phase 3 repolarisation time between APD_{80} and APD_{30} and is a risk factor for ventricular arrhythmia [536-538]. Left ventricular triangulation was reduced following 10 minutes treatment with 10 ng/mL FGF23 versus control (mean reduction in $APD_{80/30}$ 0.22 [95%CI 0.02 to 0.42], p = 0.0329, **Figure 5-6**), which is in keeping with earlier results where shortening was seen more prominently at APD_{80} than at APD_{30}. Curiously, triangulation at 30 minutes, where the shortening in APD_{80} was most marked, was unchanged (mean reduction in $APD_{80/30}$ -0.17 [95%CI -0.13 to 0.47], p = 0.2515, **Figure 5-6**).

Figure 5-6. Effect of FGF23 on murine left ventricular action potential triangulation by optical mapping.

Action potential triangulation was defined as a ratio of action potential duration at 80% repolarisation over 30% repolarisation, or APD80/30. Optical mapping recordings were taken at baseline, 10 & 30 minutes into treatment with 10 ng/mL FGF23 (**pink**) or vehicle control phosphate buffered saline (**grey**), and following a 20-minute washout period. Data presented as mean ± S.E.M. Two-way ANOVA (treatment x APD80/30) were performed; P values shown for main effects analysis of FGF23 on APD80/30 and Sidak multiple comparison tests (N = 13 – 15 hearts per group).

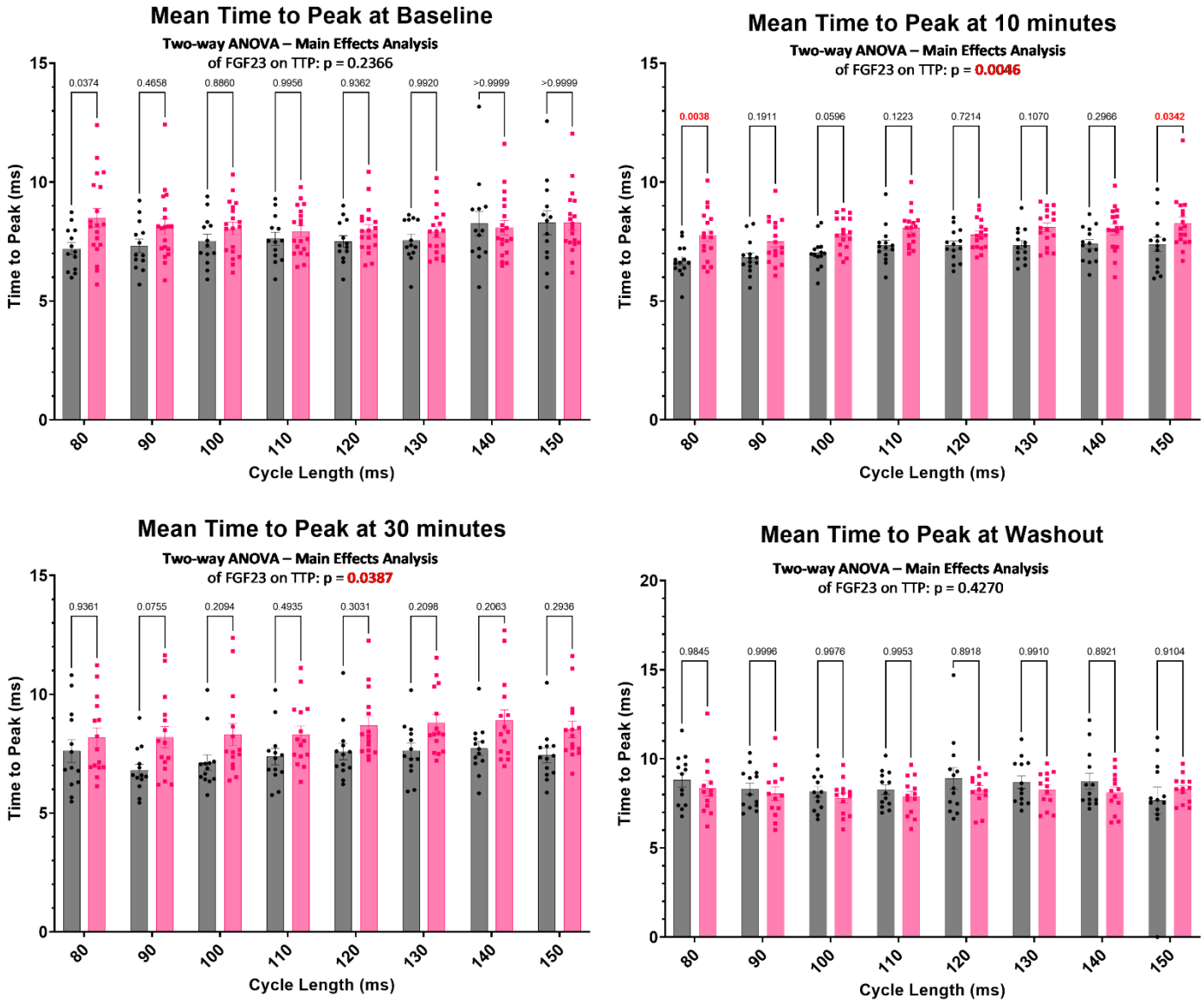


5.4.5. Time to peak of action potential depolarisation

Time to peak (TTP) was determined from the time from 10% rise to 90% from electrical diastole. It represents the speed at which the rapid inward current of Na^+ ions during phase 0 causes peak depolarisation of the membrane. In this study, time to peak depolarisation was lengthened at both 10 minute (mean increase in TTP 0.75 ms [95%CI 0.25 to 1.24], p = 0.0046) and 30 minute (mean increase in TTP 1.08 ms [95%CI 0.06 to 2.10], p = 0.0387) timepoints versus control (**Figure 5-7**). Mean time to peak at baseline and following 20 minute washout in KHB was similar between the FGF23 hearts and those infused with control KHB.

Figure 5-7. Effect of FGF23 on murine left ventricular time to peak of action potential depolarisation by optical mapping.

Time to peak (TTP) was defined as the time from 10% to 90% action potential depolarisation. Optical mapping recordings were taken at baseline, 10 & 30 minutes into treatment with 10 ng/mL FGF23 (**pink**) or vehicle control phosphate buffered saline (**grey**), and following a 20-minute washout period. Data presented as mean ± S.E.M. Two-way ANOVA (treatment x TTP) were performed; P values shown for main effects analysis of FGF23 on TTP and Sidak multiple comparison tests (N = 13 – 15 hearts per group).

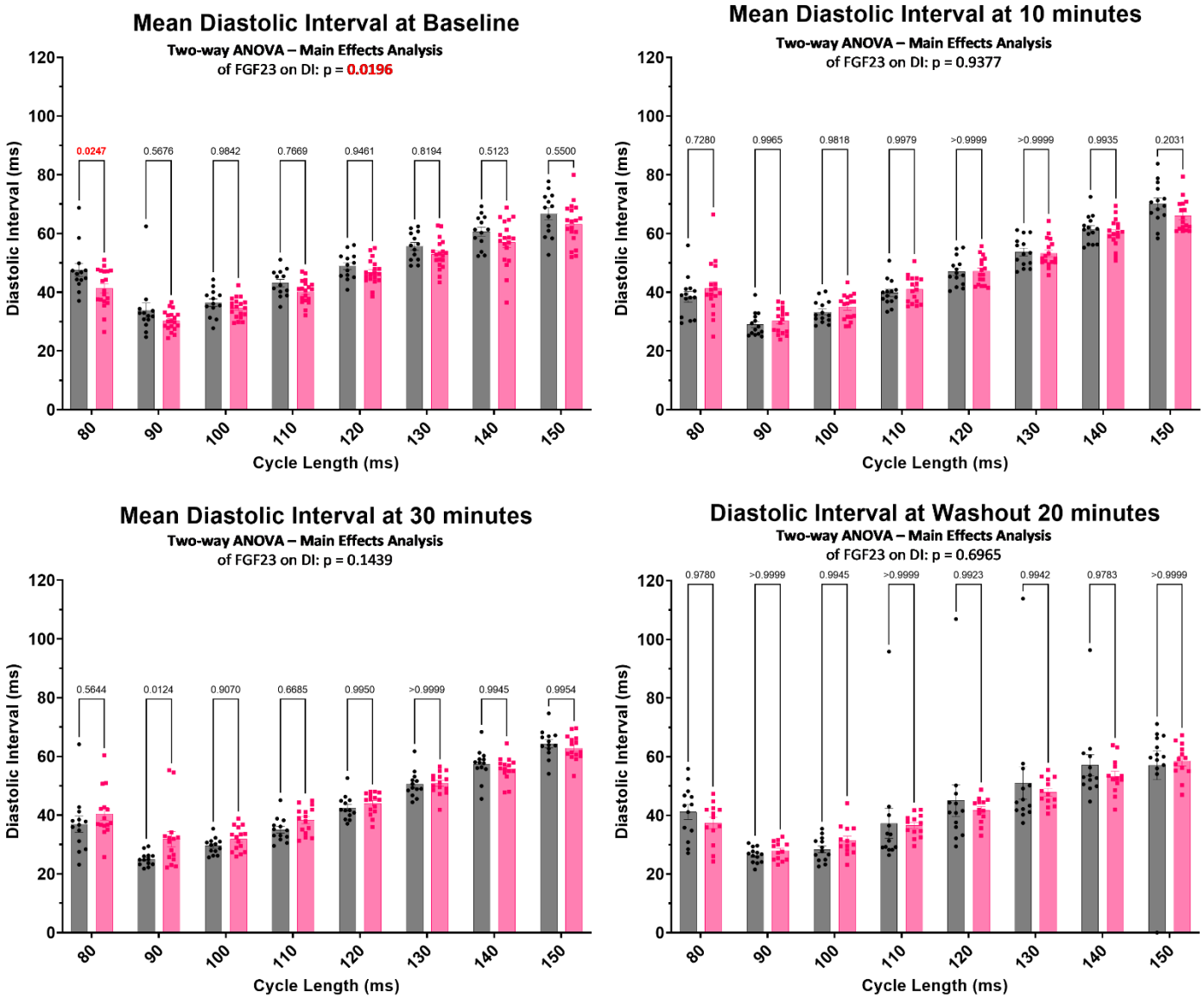


5.4.6. Diastolic interval

Diastolic interval (DI) represents phase 4 of the action potential, and in this study was calculated as the time from APD_{90} to the activation of the following action potential. Diastolic interval was shorter at baseline in the FGF23 treatment group (mean reduction in DI 3.33 ms [95%CI 0.57 to 6.09], p = 0.0196, **Figure 5-8**), with no significant changes seen between it and the control group once FGF23 infusion occurred at 10- (p = 0.9377) and 30-minute (p = 0.1439) timepoints. This remained the case at washout (p = 0.6965).

Figure 5-8. Effect of FGF23 on murine left ventricular diastolic interval by optical mapping.

Diastolic interval (DI) was calculated from action potential duration at 90% repolarisation to the following activation time. Optical mapping recordings were taken at baseline, 10 & 30 minutes into treatment with 10 ng/mL FGF23 (**pink**) or vehicle control phosphate buffered saline (**grey**), and following a 20-minute washout period. Data presented as mean ± S.E.M. Two-way ANOVA (treatment x DI) were performed; P values shown for main effects analysis of FGF23 on DI and Sidak multiple comparison tests (N = 13 – 15 hearts per group).

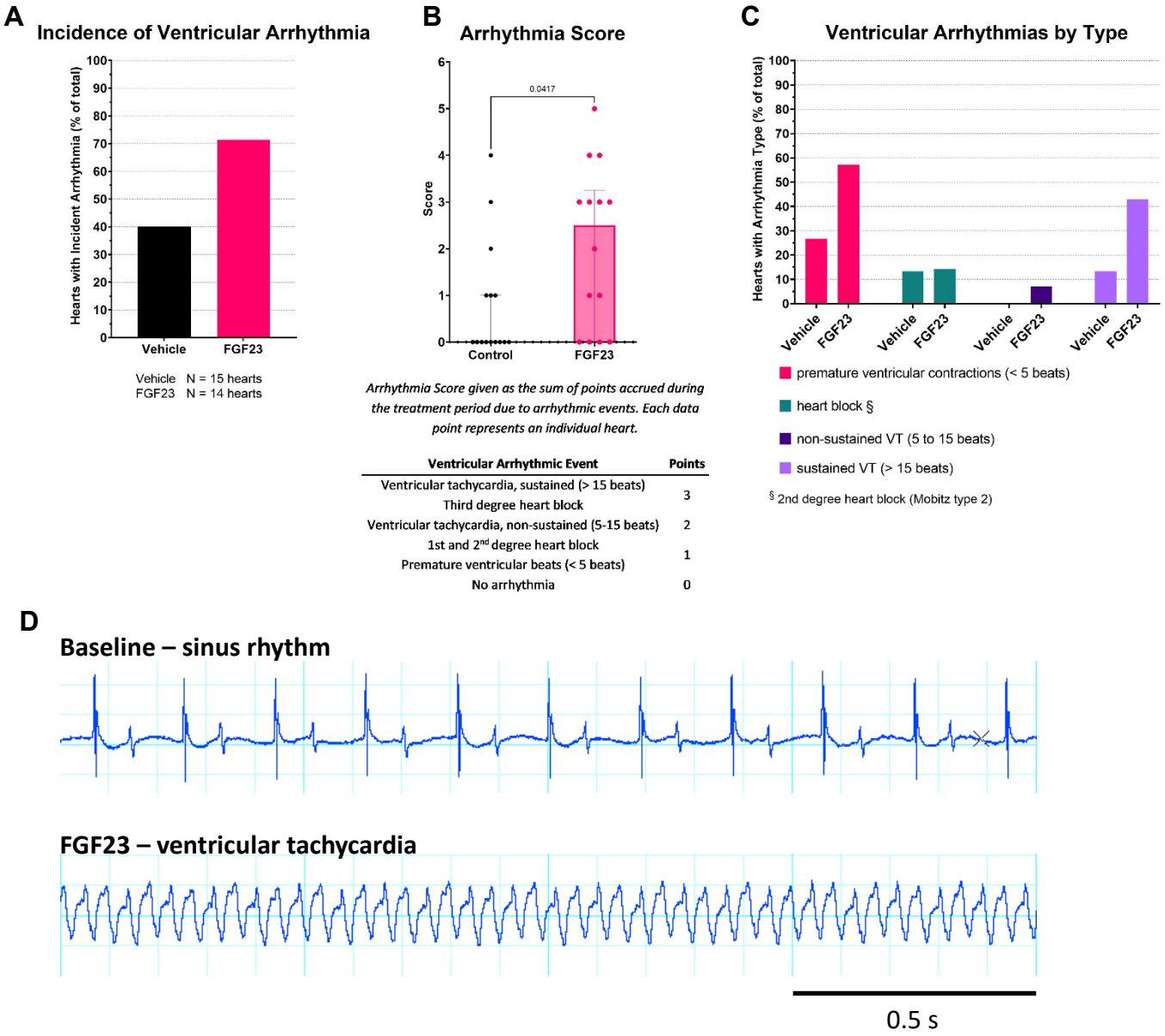


5.4.7. Ventricular arrhythmia burden

Ventricular arrhythmias were observed *ex vivo* in both FGF23-treated and control hearts within the 30-minute treatment period. However, the incidence was greater in the FGF23-treated hearts (10 of 14 hearts) compared to in control hearts (6 of 15 hearts, **Figure 5-9 A**). Median cumulative arrhythmia score was significantly greater in the FGF23 group ($p = 0.0417$, **Figure 5-9 B**), which reflects the higher incidence of significant, life-threatening ventricular arrhythmias (**Figure 5-9 C**). Premature ventricular beats were the most frequently observed arrhythmia (8 of 14 FGF23; 4 of 15 control hearts). Two hearts in both groups sustained conduction block with intermittent non-conducted beats. Whilst 2 of 15 hearts from the control group went into ventricular tachycardia, this was seen in 7 out of 14 hearts following FGF23 treatment.

Figure 5-9. Ventricular arrhythmia burden in *ex vivo* murine hearts in response to acute FGF23 treatment.

Arrhythmia burden was assessed following 30 minutes perfusion with 10 ng/mL fibroblast growth factor 23 (FGF23; N = 14) or vehicle (phosphate buffered saline; N = 15). **A** – Incidence of ventricular arrhythmias. **B** – Arrhythmia score presented as median ± interquartile range; Mann-Whitney U test. **C** – Ventricular arrhythmias by type. **D** – Representative ECG recording at baseline and following FGF23 treatment.



5.5. DISCUSSION

The present study is one of the first to use a Langendorff-perfused whole beating mouse heart to investigate the effects of FGF23 on cardiac electrophysiology, and the first to do so using optical mapping. Acute, 30-minute exposure of mouse hearts to elevated levels of FGF23 (10 ng/mL) resulted in shortening of APD_{50} and APD_{80}; increased APD_{80} heterogeneity; lengthening of time to peak depolarisation; and increased incidence and severity of ventricular arrhythmias. Although not reaching statistical significance, there was a trend towards shortening of APD_{30} and reduction in conduction velocity in the FGF23-treated hearts, which was not seen at baseline or washout timepoints.

5.5.1. FGF23 alters action potential duration and increases arrhythmogenic burden

Only one other study reported on the effect of FGF23 on action potential characteristics. Using isolated rabbit pulmonary vein cardiomyocytes, Huang et al. [524] showed that 4-6 hour treatment with 1 ng/mL FGF23 *in vitro* resulted in significant shortening of action potential duration (APD_{75} and APD_{50}) by patch clamp technique. However, the mechanism was unclear. Pulmonary vein cardiomyocytes had faster spontaneous beating rates following FGF23 treatment which could account for shortening of APD, and the authors hypothesised that the shortening could also be due to a larger NCX reverse-mode current usually observed in phase 1 of the AP. In our study, the shortening in APD was *independent* of beat rate. Huang et al. [524] also reported a FGF23-dependent increase in late Na^+ current ($I_{Na,late}$). This is, under normal physiological conditions, a small inward Na^+ current which follows the much larger $I_{Na,early}$ as

Na^+ channels recover from inactivation and reopen during the plateau (phase 3) of the AP. In pathological conditions such as heart failure[539], $I_{Na,late}$ amplitude is increased resulting in lengthening of APD [540], and is associated with increased arrhythmogenesis through intracellular Na^+ and Ca^{2+} overload [541]. Curiously the increase in $I_{Na,late}$ in their study did not result in lengthening of APD, but the opposite [524]. Crucially, they also observed increased arrhythmogenic burden as found in our study. Pulmonary vein cardiomyocytes had increased amplitude of delayed after depolarisations (DAD) following FGF23 treatment [524], which are transient depolarisations occurring in the diastolic period (phase 4) following an AP. DADs, if suprathreshold, can trigger an AP causing a premature ventricular contraction or re-entrant arrhythmia as observed on our study. Shortening of the APD also reduces the refractory period, facilitating re-entry [542].

Increased incidence of DADs were also reported by Kao et al. [523] where atrial HL-1 cardiomyocytes experienced a higher incidence of DADs after 24-hr treatment with 25 ng/mL FGF23, although APD at 20, 50 and 90% repolarisation was unchanged. Curiously, treatment of these cells with 10 ng/mL FGF23 did not alter DAD incidence. Further evidence of FGF23-associated arrhythmias in *ex vivo* and *in vivo* settings can be found in two later studies. Navarro-Garcia et al. [257] not only found that FGF23 at 100 ng/mL evoked DADs and missed transients during 2 Hz pacing of isolated adult Wistar rat cardiomyocytes, mice also experienced more frequent premature ventricular contractions 10 minutes following a single 40 µg/kg intraperitoneal FGF23 injection. In separate experiments using CD1 mice, Graves et al. [526] reported an increased incidence of premature ventricular beats, bigeminy and ventricular tachycardia in isolated CD1 hearts treated with 9

ng/mL FGF23 for 30 minutes versus control. A prolongation of QTc was observed, corresponding to a lengthening of APD, which is in contrast to our study findings. Although there were similarities in experimental protocol, Graves and colleagues utilised male CD1 mice with a greater mean age – 13-15 weeks versus female 9-15 weeks used in the present study. In clinical studies, women have been found to be at greater risk of atrial fibrillation [543], whilst supraventricular ectopics were more frequent in men [544]. Evidence from prior cellular studies indicate differences between male and female cardiac cellular electrophysiology and Ca^{2+} handling possibly as a result of sex hormones [545], highlighting the need for future studies to utilise cells or animals from both sexes.

5.5.2. FGF23 increases action potential heterogeneity and reduces conduction velocity

In the present study, increased spatial APD_{80} heterogeneity and reduced conduction velocity in the left ventricle was observed as a result of FGF23 treatment. Increased APD heterogeneity and slowing of conduction velocity are risk factors for the formation of rotational re-entrant waves predisposing to tachyarrhythmias and fibrillation [534,546]. For a re-entrant wave to excite the heart prior to the following sinus beat, the tissue must be non-refractory. A decrease in conduction velocity (and refractory period as in APD shortening) shortens the cardiac wavelength, allowing the possibility of multiple excitation waves to re-excite the tissue without a sinus excitation, sustaining a cardiac arrhythmia [546].

The mechanism by which FGF23 affects APD heterogeneity and conduction velocity is unclear, especially given that the CD1 mice used were young and healthy adults, free of structural alterations such as fibrosis or hypertrophy which

may affect intercellular electrical coupling. There are inherent differences in cellular APD dependent on their spatial location within the ventricle [547]. At baseline, APD heterogeneity was most marked at slower cycle lengths, in line with observations by others [547-549]. The difference in APD heterogeneity between the treatment groups was also most marked at slower cycle lengths.

In summary, the data presents evidence that that FGF23 increases left ventricular arrhythmia burden through shortening of action potential duration, increased APD heterogeneity and reduction in conduction velocity. Further development of optical mapping analysis packages will allow the identification, location and analysis of spiral waves and re-entrant arrhythmias. Future work should investigate the effects of FGF23 on atrial arrhythmogenesis using the current beating-heart model given the previously described associations between elevated FGF23 and atrial fibrillation, and investigate whether the addition of soluble Klotho and or a FGF receptor blocker attenuates the pro-arrhythmic phenomena.

CHAPTER 6. EXPLORING MURINE VENTRICULAR CALCIUM IONIC HANDLING FOLLOWING ACUTE FIBROBLAST GROWTH FACTOR 23 TREATMENT

6.1. EXTENT OF PERSONAL CONTRIBUTION

All experiments were conducted by the author of this thesis.

6.2. INTRODUCTION

Work in Chapter 5 demonstrated statistically significant shortening of APD in *ex vivo* Langendorff-perfused whole murine hearts within 30 minutes of acute treatment with 10 ng/mL FGF23 irrespective of pacing cycle length. APD shortening was more marked at 50% and 80% repolarisation, with a non-significant effect at APD_{30}. This suggests that changes in ionic currents in phases 2 and 3 are likely to result in the shortening of APD. As previously discussed, cardiomyocyte calcium handling is a key determinant of the cardiac action potential in phase 2/3 and excitation-contraction coupling. Prior studies have utilised isolated cardiac myocytes or ventricular muscle strip preparations with varying results – studies by Touchberry [254], Kao [523], Huang [524] and Graves [526] found increased $[Ca^{2+}]_i$, whereas Verkaik [525] and Navarro-Garcia [257] showed the opposite following FGF23 treatment.

Leveraging on the experimental protocol of the acute *ex vivo* model established in Chapter 5, I simultaneously loaded the Langendorff-perfused murine heart with a membrane potential and calcium-sensitive fluorescent dye. Mouse hearts were loaded with Rhod-2 AM and RH237 fluorescent dyes, which are sensitive to changes in intracellular calcium and membrane potential, respectively. This allowed concurrent exploration of left ventricular calcium handling dynamics and action potential characteristics using optical mapping. The optical mapping method was otherwise identical to that described in the general methods section and summarised again in the preceding chapter 5 methods.

6.3. RESULTS

The effects of FGF23 on action potential duration, heterogeneity, conduction velocity, time to peak and diastolic interval are first presented, followed by data on calcium transient properties, and finally ventricular arrhythmia burden.

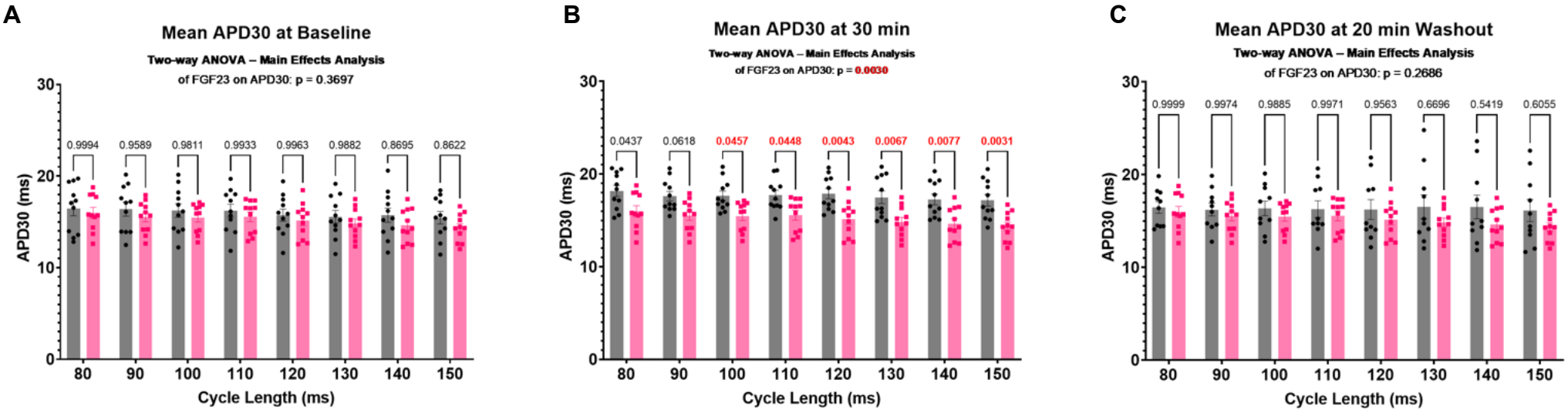
6.3.1. Effect of FGF23 on action potential duration and heterogeneity

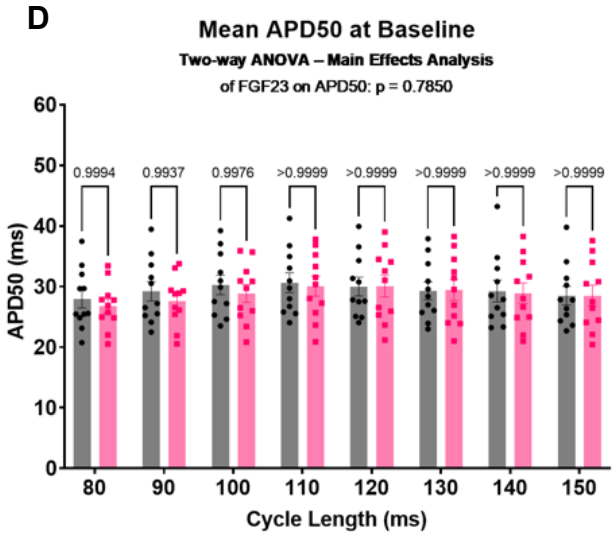
No difference in APD was seen at baseline between the FGF23-treated and control mouse hearts (simple main effects $p > 0.37$, **Figure 6-1 A**, **D** and **G**). Treatment of mouse hearts with 10 ng/mL FGF23 for 30 minutes resulted in shortening of left ventricular action potential duration at 30% (mean reduction in APD_{30}= 2.44 ms [95% CI 0.93 to 3.94], $p = 0.0030$; **Figure 6-1 B**) , 50% (mean reduction in APD_{50} = 5.76 ms [95% CI 1.52 to 10.01], $p = 0.0103$, **Figure 6-1 E**) and 80% repolarisation (mean reduction in APD_{80} = 6.03 ms [95% CI 0.67 to 11.40],$p = 0.0293$, **Figure 6-1 H**). The shortening effect appeared greater at longer pacing cycle lengths, however there were no interactions between cycle length and FGF23 treatment in the ANOVA model (cycle length x treatment $p > 0.3$). The APD-shortening effect was no longer present following a 20-minute washout period (simple main effects $p > 0.24$, **Figure 6-1 C**, **F** and **I**).

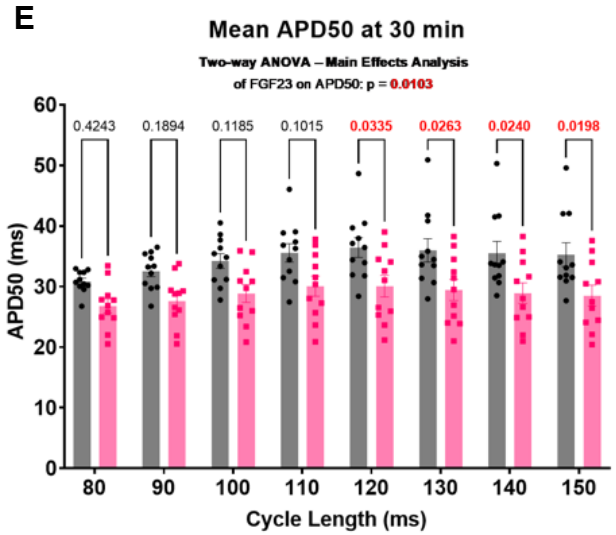
Although FGF23 appeared to cause a mild increase in APD_{50} (mean increase in APD_{50} heterogeneity = 0.18 [95% CI -0.03 to 0.39], $p = 0.0886$) and APD_{80} heterogeneity (mean increase in APD_{80} heterogeneity = 0.06 [95% CI -0.07 to 0.19], $p = 0.3573$), this did not reach statistical significance (**Figure 6-2**).

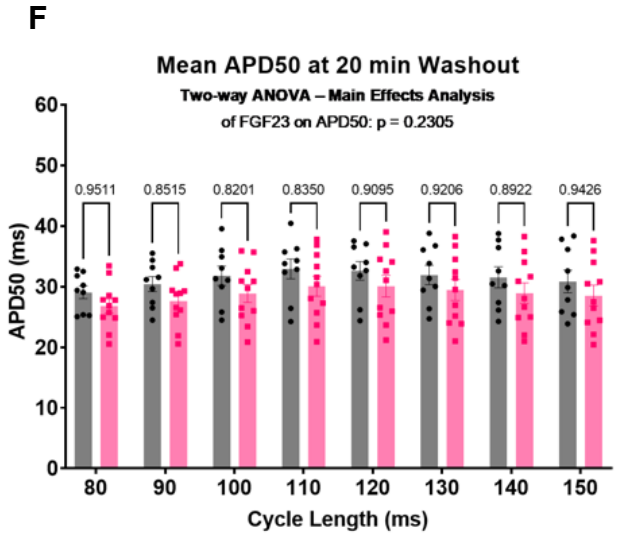
Figure 6-1. Effect of FGF23 on murine left ventricular action potential duration by optical mapping.

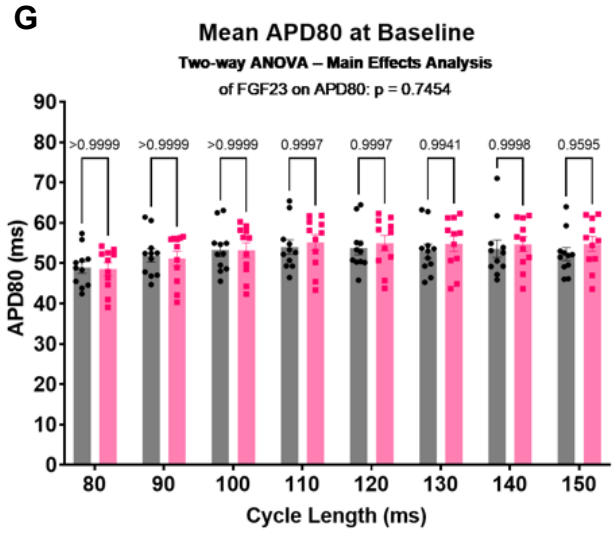
Action potential duration (APD) at **A-C** – 30% repolarisation; **D-F** – 50% repolarisation; and **G-I** – 80% repolarisation. Optical mapping recordings were taken at baseline, 30 minutes into treatment with 10 ng/mL FGF23 (**pink**) or vehicle control phosphate buffered saline (**grey**), and following a 20-minute washout period. Data presented as mean ± S.E.M. Two-way ANOVA (treatment x APD); P values shown for main effects analysis of FGF23 on APD, and Sidak multiple comparison tests (N = 11 hearts per group).

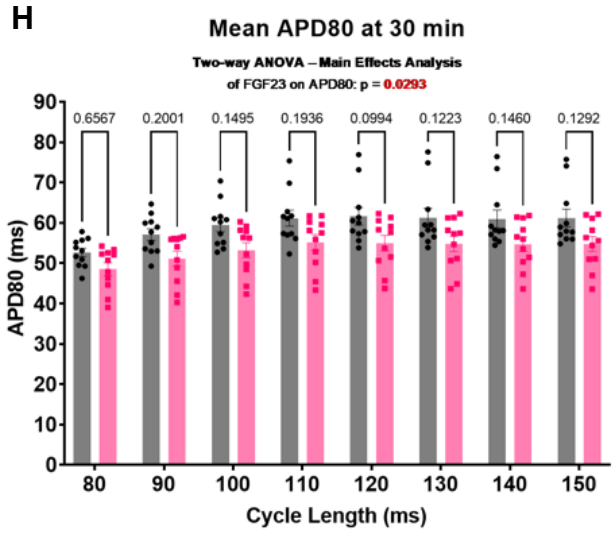



D
Mean APD50 at Baseline
Two-way ANOVA – Main Effects Analysis
of FGF23 on APD50: p = 0.7850
0.9994
0.9937
0.9976
>0.9999
>0.9999
>0.9999
>0.9999
>0.9999
APD50 (ms)
Cycle Length (ms)


E
Mean APD50 at 30 min
Two-way ANOVA – Main Effects Analysis
of FGF23 on APD50: p = 0.0103
0.4243
0.1894
0.1185
0.1015
0.0335
0.0263
0.0240
0.0198
APD50 (ms)
Cycle Length (ms)


F
Mean APD50 at 20 min Washout
Two-way ANOVA – Main Effects Analysis
of FGF23 on APD50: p = 0.2305
0.9511
0.8515
0.8201
0.8350
0.9095
0.9206
0.8922
0.9426
APD50 (ms)
Cycle Length (ms)


G
Mean APD80 at Baseline
Two-way ANOVA – Main Effects Analysis
of FGF23 on APD80: p = 0.7454
>0.9999
>0.9999
>0.9999
0.9997
0.9997
0.9941
0.9998
0.9595
APD80 (ms)
Cycle Length (ms)


H
Mean APD80 at 30 min
Two-way ANOVA – Main Effects Analysis
of FGF23 on APD80: p = 0.0293
0.6567
0.2001
0.1495
0.1936
0.0994
0.1223
0.1460
0.1292
APD80 (ms)
Cycle Length (ms)

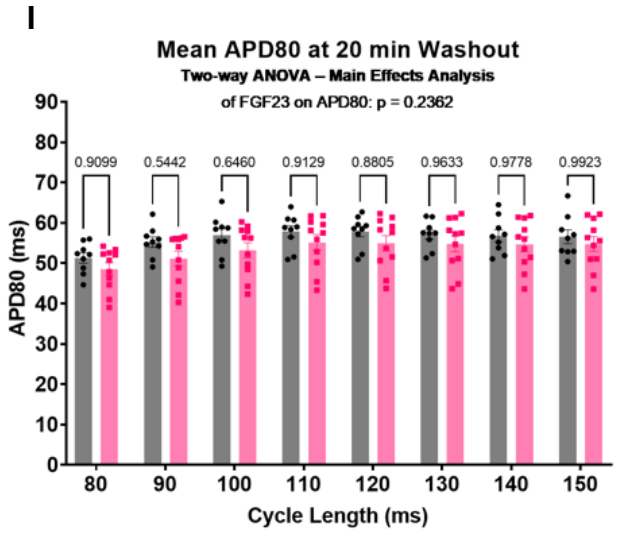
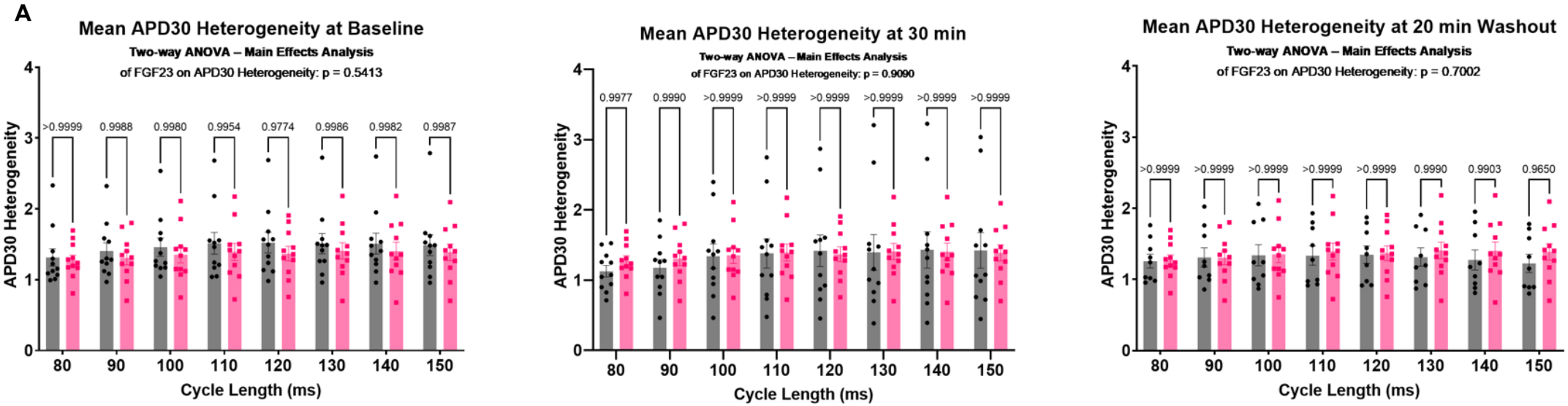
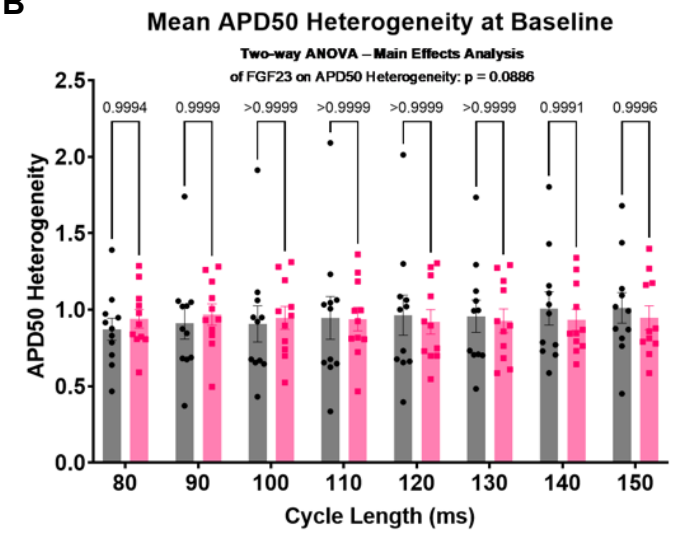

I
Mean APD80 at 20 min Washout
Two-way ANOVA – Main Effects Analysis
of FGF23 on APD80: p = 0.2362
0.9099
0.5442
0.6460
0.9129
0.8805
0.9633
0.9778
0.9923
APD80 (ms)
Cycle Length (ms)

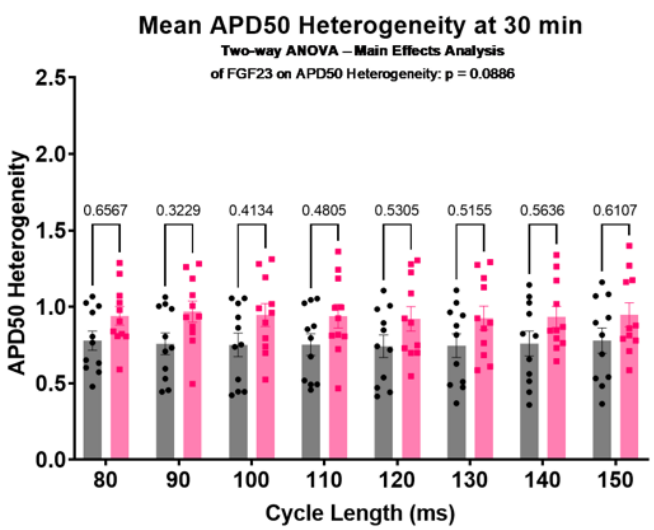
Figure 6-2. Effect of FGF23 on murine left ventricular action potential duration heterogeneity by optical mapping.

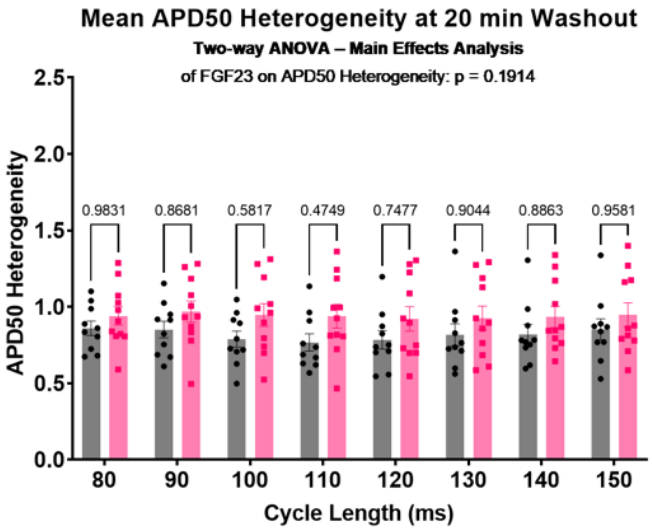
Action potential duration (APD) heterogeneity at **A** – 30% repolarisation; **B** – 50% repolarisation; and **C** – 80% repolarisation. Optical mapping recordings were taken at baseline, 30 minutes into treatment with 10 ng/mL FGF23 (**pink**) or vehicle control phosphate buffered saline (**grey**), and following a 20-minute washout period. Data presented as mean ± S.E.M. Two-way ANOVA (treatment x APD heterogeneity); P values shown for main effects analysis of FGF23 on APD heterogeneity and Sidak multiple comparison tests (N = 11 hearts per group).



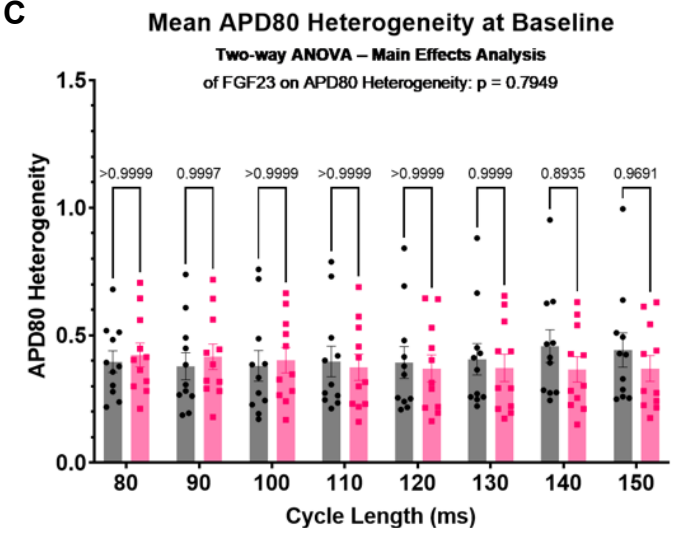
B

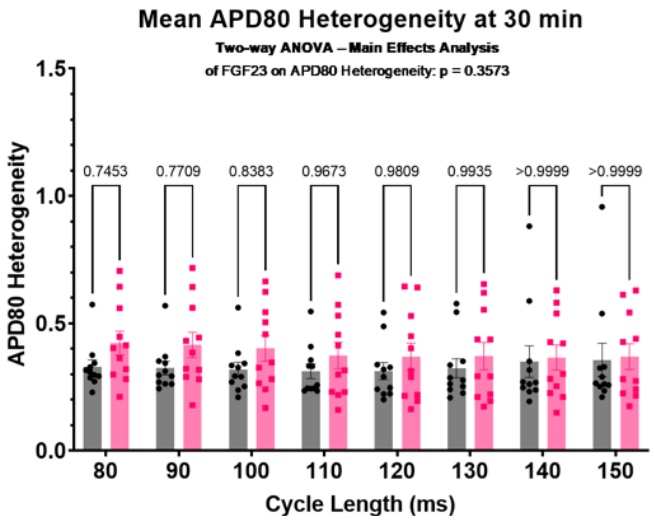

Mean APD50 Heterogeneity at Baseline
Two-way ANOVA – Main Effects Analysis
of FGF23 on APD50 Heterogeneity: p = 0.0886
0.9994
0.9999
>0.9999
>0.9999
>0.9999
>0.9999
0.9991
0.9996
APD50 Heterogeneity
Cycle Length (ms)

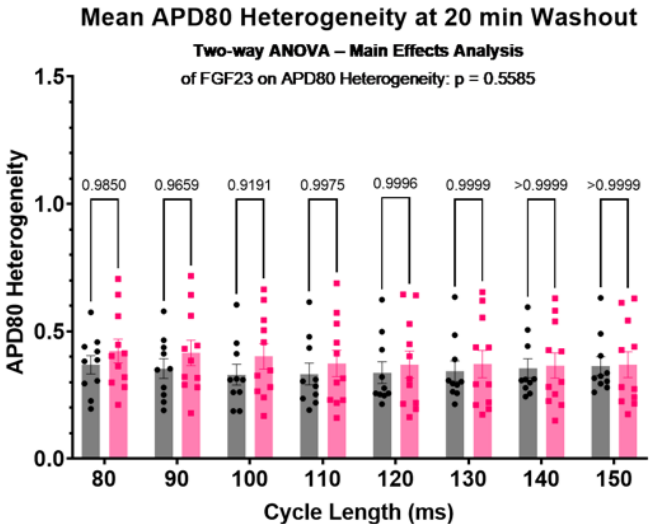

Mean APD50 Heterogeneity at 30 min
Two-way ANOVA – Main Effects Analysis
of FGF23 on APD50 Heterogeneity: p = 0.0886
0.6567
0.3229
0.4134
0.4805
0.5305
0.5155
0.5636
0.6107
APD50 Heterogeneity
Cycle Length (ms)


Mean APD50 Heterogeneity at 20 min Washout
Two-way ANOVA – Main Effects Analysis
of FGF23 on APD50 Heterogeneity: p = 0.1914
0.9831
0.8681
0.5817
0.4749
0.7477
0.9044
0.8863
0.9581
APD50 Heterogeneity
Cycle Length (ms)

C


Mean APD80 Heterogeneity at Baseline
Two-way ANOVA – Main Effects Analysis
of FGF23 on APD80 Heterogeneity: p = 0.7949
>0.9999
0.9997
>0.9999
>0.9999
>0.9999
0.9999
0.8935
0.9691
APD80 Heterogeneity
Cycle Length (ms)


Mean APD80 Heterogeneity at 30 min
Two-way ANOVA – Main Effects Analysis
of FGF23 on APD80 Heterogeneity: p = 0.3573
0.7453
0.7709
0.8383
0.9673
0.9809
0.9935
>0.9999
>0.9999
APD80 Heterogeneity
Cycle Length (ms)

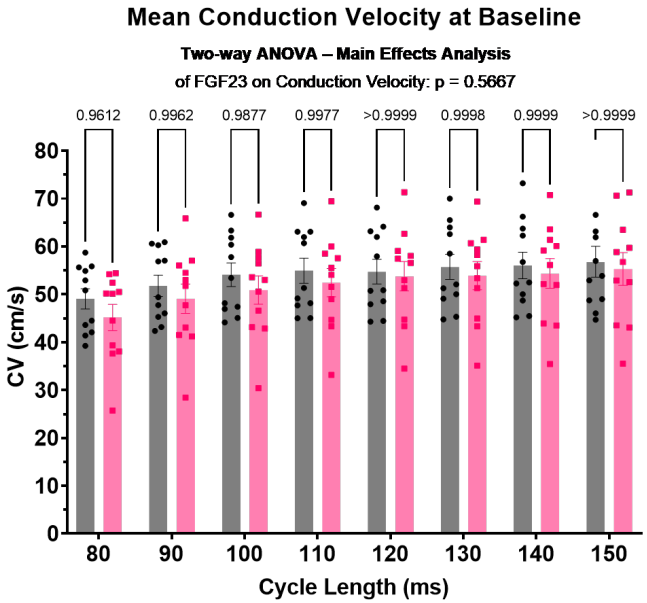

Mean APD80 Heterogeneity at 20 min Washout
Two-way ANOVA – Main Effects Analysis
of FGF23 on APD80 Heterogeneity: p = 0.5585
0.9850
0.9659
0.9191
0.9975
0.9996
0.9999
>0.9999
>0.9999
APD80 Heterogeneity
Cycle Length (ms)

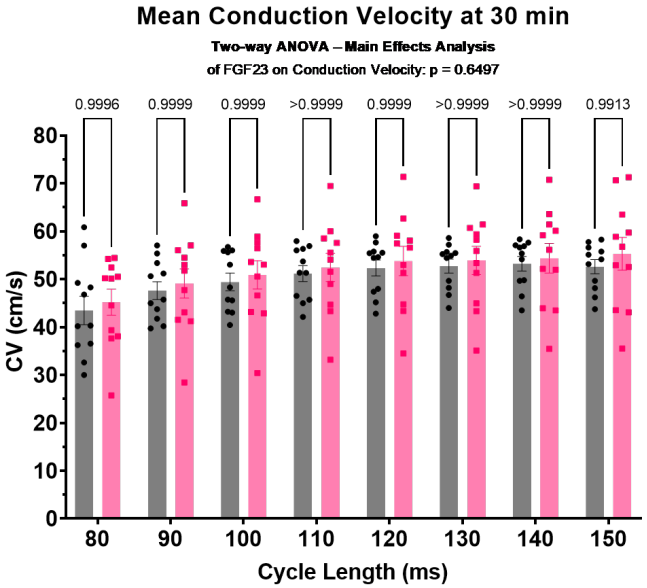
6.3.2. Effect of FGF23 on action potential conduction velocity, time to peak depolarisation and diastolic interval

FGF23 treatment for 30 minutes did not alter action potential conduction velocity (mean reduction in conduction velocity = -1.57 cm/s [95% CI -8.65 to 5.52], p = 0.6497, **Figure 6-3**) or time to peak depolarisation (mean reduction in time to peak = 0.15 ms [95% CI -0.81 to 1.11], p = 0.7490, **Figure 6-4**) versus control hearts. Curiously, action potential diastolic interval appeared to be lengthened by FGF23 treatment (mean increase in diastolic interval at 30 minutes = 4.83 ms [95% CI -0.48 to 10.15], p = 0.0725), an effect which was most significant following 20 minute washout (mean increase in diastolic interval = 5.78 ms [95% CI 0.22 to 11.34], p = 0.0423, **Figure 6-5**).

Figure 6-3. Effect of FGF23 on murine left ventricular conduction velocity by optical mapping.

Conduction velocity (CV) was measured from optical mapping recordings taken at baseline, 10 & 30 minutes into treatment with 10 ng/mL FGF23 (**pink**) or vehicle control phosphate buffered saline (**grey**), and following a 20-minute washout period. Data presented as mean ± S.E.M. Two-way ANOVA (treatment x CV) were performed; P values shown for main effects analysis of FGF23 on CV and Sidak multiple comparison tests (N = 11 hearts per group).





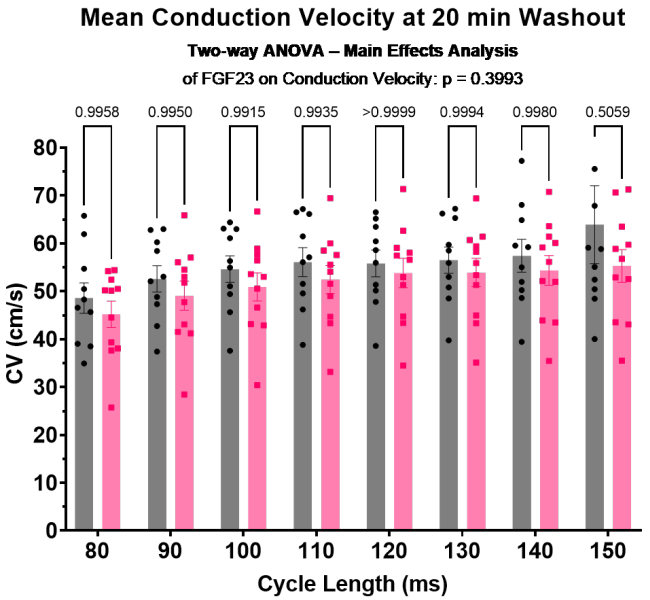
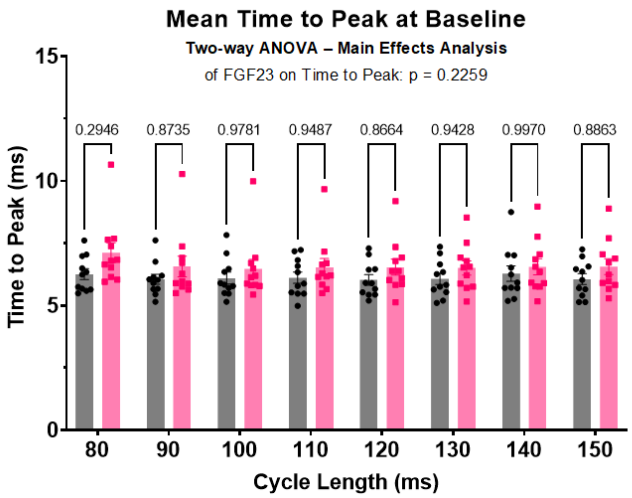
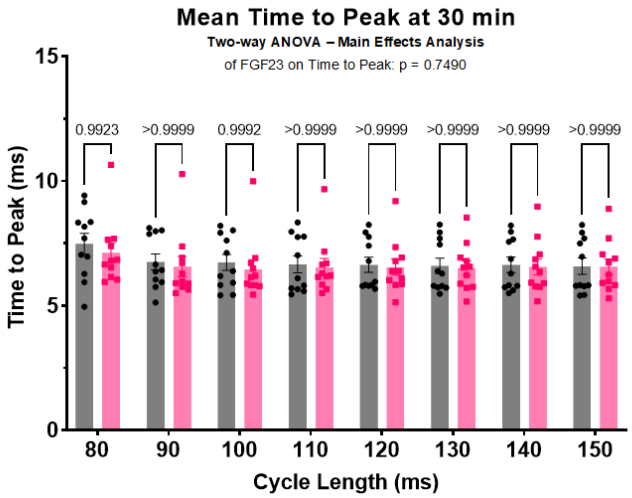


Figure 6-4. Effect of FGF23 on murine left ventricular time to peak of action potential depolarisation by optical mapping.

Time to peak (TTP) was defined as the time from 10% to 90% action potential depolarisation. Optical mapping recordings were taken at baseline, 30 minutes into treatment with 10 ng/mL FGF23 (**pink**) or vehicle control phosphate buffered saline (**grey**), and following a 20-minute washout period. Data presented as mean ± S.E.M. Two-way ANOVA (treatment x TTP) were performed; P values shown for main effects analysis of FGF23 on TTP and Sidak multiple comparison tests (N = 11 hearts per group).





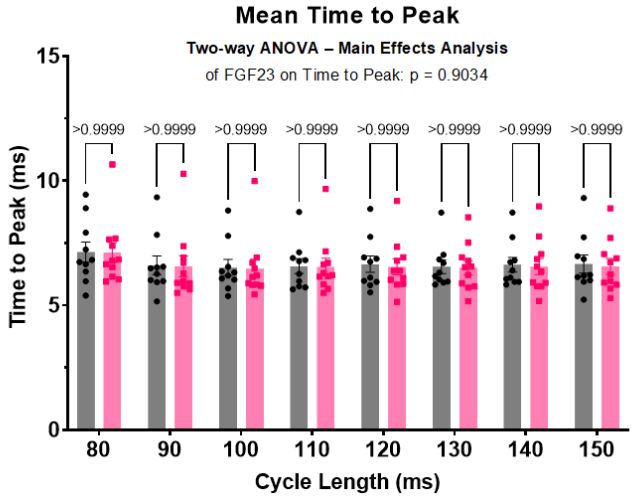
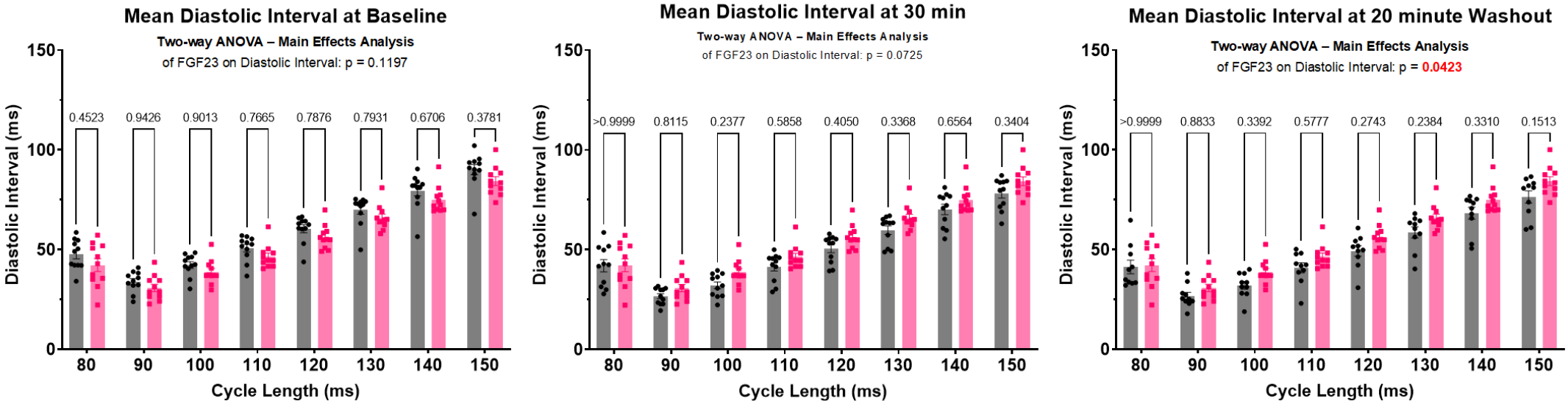


Figure 6-5. Effect of FGF23 on murine left ventricular diastolic interval by optical mapping.

Diastolic interval (DI) was calculated from action potential duration at 90% repolarisation to the following activation time. Optical mapping recordings were taken at baseline, 30 minutes into treatment with 10 ng/mL FGF23 (**pink**) or vehicle control phosphate buffered saline (**grey**), and following a 20-minute washout period. Data presented as mean ± S.E.M. Two-way ANOVA (treatment x DI) were performed; P values shown for main effects analysis of FGF23 on DI and Sidak multiple comparison tests (N = 11 hearts per group).



6.3.3. FGF23 effects on ventricular calcium transient duration and amplitude

The calcium transient begins shortly after membrane depolarisation when Ca^{2+} influx through LTCC triggers rapid release of Ca^{2+} from the SR through RyR2 resulting in a sharp and significant increase in $[Ca^{2+}]_i$. The gradual decay occurs as RyR2 close and $[Ca2+]_i$ is removed by NCX, SERCA2 and mitochondrial Ca^{2+} uniporter, respectively extruding Ca^{2+} from the cell and replenishing SR, mitochondrial Ca^{2+} stores until the next membrane depolarisation by a propagated AP [506]. In this study, calcium transient duration (CaTD) was defined as the time from maximum upstroke velocity to 50% ($CaTD_{50}$) and 80% ($CaTD_{80}$) transient decay.

After 30 minutes treatment, mean CaTD fluorescence amplitude fell by 742 ± 59 a.u. in the control group versus 24 ± 49 a.u. in FGF23 treatment group. However, the difference between means was non-significant (mean change in fluorescence amplitude = 717 a.u., p = 0.6934, **Figure 6-6 A**), suggesting that peak $[Ca^{2+}]_i$ is not altered by FGF23.

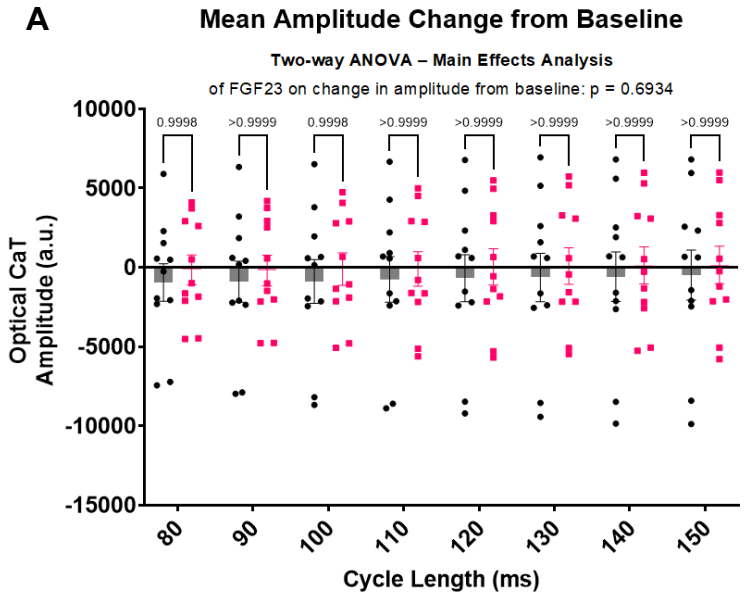
FGF23 treatment for 30 minutes resulted in shortening of $CaTD_{50}$ (mean shortening of $CaTD_{50}$ = 4.50 ms [95% CI 0.39 to 8.62], p = 0.0334) and $CaTD_{80}$ (mean shortening of $CaTD_{80}$ = 4.84 ms [95% CI 1.50 to 8.18], p = 0.0067, **Figure 6-6 B** and **C**). The effect of CaTD shortening persisted into the washout period (mean shortening of $CaTD_{50}$ = 4.77 ms [95% CI 0.22 to 9.31], p = 0.0408; mean shortening of $CaTD_{80}$ = 5.14 ms [95% CI 1.84 to 8.43], p = 0.0041, **Figure 6-6 B** and **C**). Whilst the shortening appeared to be most marked at lower cycle lengths, no interaction between cycle length and FGF23 treatment was found in the two-

way ANOVA models ($p > 0.2$). These findings are consistent with the action potential shortening observed in these hearts and those in Chapter 5, which underwent optical mapping under the same treatment conditions, but were loaded with a different voltage sensitive dye.

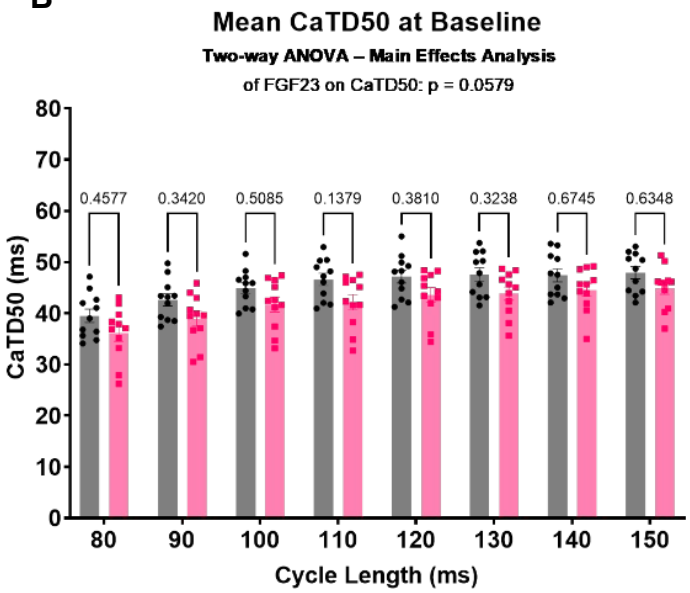
Shortening of CaTD was accompanied by significant increases in CaTD heterogeneity at both 50% (mean increase in CaTD50 heterogeneity = 0.14 [95% CI 0.01 to 0.27], $p = 0.0373$) and 80% decay (mean increase in CaTD80 heterogeneity = 0.12 [95% CI 0.02 to 0.22], $p = 0.0227$, **Figure 6-7 A** and **B**). The increases in heterogeneity remained following the 20-minute washout (mean increase in $CaTD_{50}$ heterogeneity = 0.19 ms [95% CI 0.01 to 0.38], $p = 0.0396$; mean increase in $CaTD_{80}$ heterogeneity = 0.16 ms [95% CI 0.04 to 0.28], $p = 0.0138$, **Figure 6-7 A** and **B**).

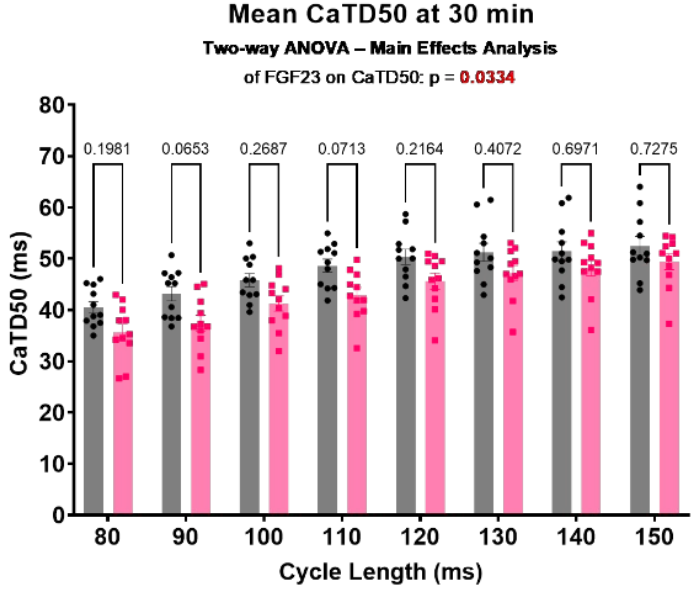
Figure 6-6. Effect of FGF23 on murine left ventricular calcium transient duration and amplitude by optical mapping.

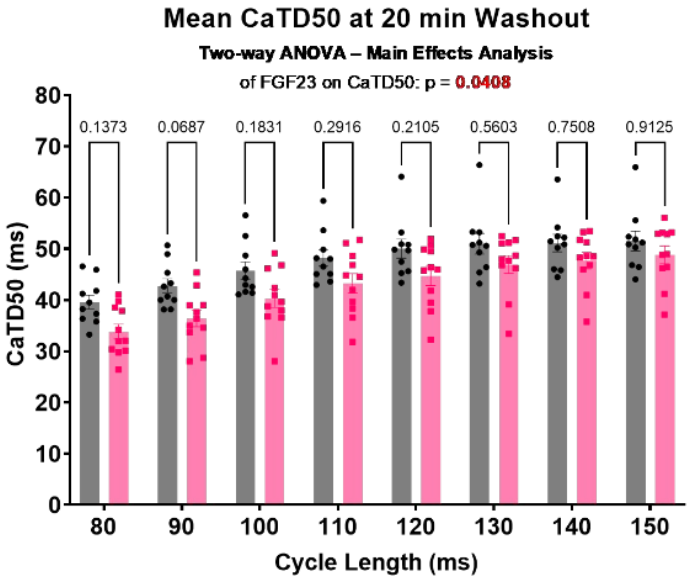
Optical mapping recordings were taken at baseline, 30 minutes into treatment with 10 ng/mL FGF23 (**pink**) or vehicle control phosphate buffered saline (**grey**), and following a 20-minute washout period. **A** – Mean change in raw optical calcium transient fluorescence amplitude at 30 minutes compared to baseline fluorescence amplitude. Calcium transient duration (CaTD) at **B** – 50% decay; and **C** – 80% decay. Data presented as mean ± S.E.M. Two-way ANOVA (treatment x CaTD / change in amplitude) were performed; P values shown for main effects analysis of FGF23 on CaTD / change in amplitude and Sidak multiple comparison tests (N = 11 hearts per group).



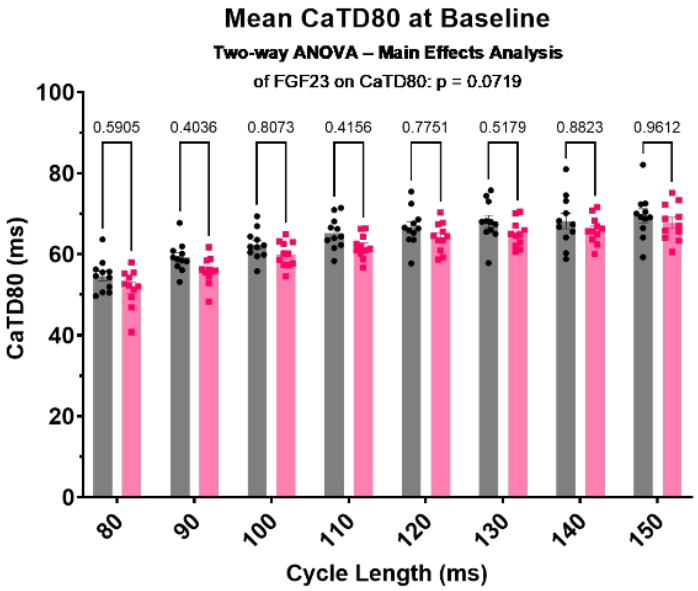
B

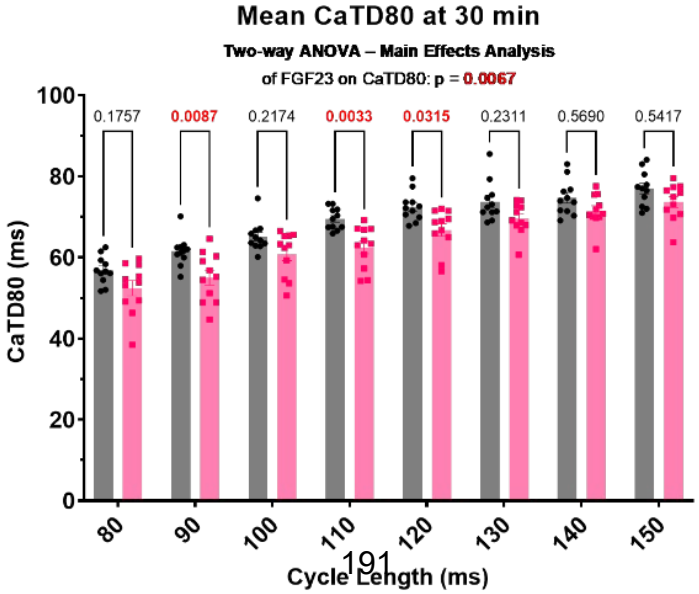

Mean CaTD50 at Baseline
Two-way ANOVA – Main Effects Analysis
of FGF23 on CaTD50: p = 0.0579
0.4577 0.3420 0.5085 0.1379 0.3810 0.3238 0.6745 0.6348
CaTD50 (ms)
Cycle Length (ms)


Mean CaTD50 at 30 min
Two-way ANOVA – Main Effects Analysis
of FGF23 on CaTD50: p = 0.0334
0.1981 0.0653 0.2687 0.0713 0.2164 0.4072 0.6971 0.7275
CaTD50 (ms)
Cycle Length (ms)


Mean CaTD50 at 20 min Washout
Two-way ANOVA – Main Effects Analysis
of FGF23 on CaTD50: p = 0.0408
0.1373 0.0687 0.1831 0.2916 0.2105 0.5603 0.7508 0.9125
CaTD50 (ms)
Cycle Length (ms)

C


Mean CaTD80 at Baseline
Two-way ANOVA – Main Effects Analysis
of FGF23 on CaTD80: p = 0.0719
0.5905 0.4036 0.8073 0.4156 0.7751 0.5179 0.8823 0.9612
CaTD80 (ms)
Cycle Length (ms)


Mean CaTD80 at 30 min
Two-way ANOVA – Main Effects Analysis
of FGF23 on CaTD80: p = 0.0067
0.1757 0.0087 0.2174 0.0033 0.0315 0.2311 0.5690 0.5417
CaTD80 (ms)
Cycle Length (ms)

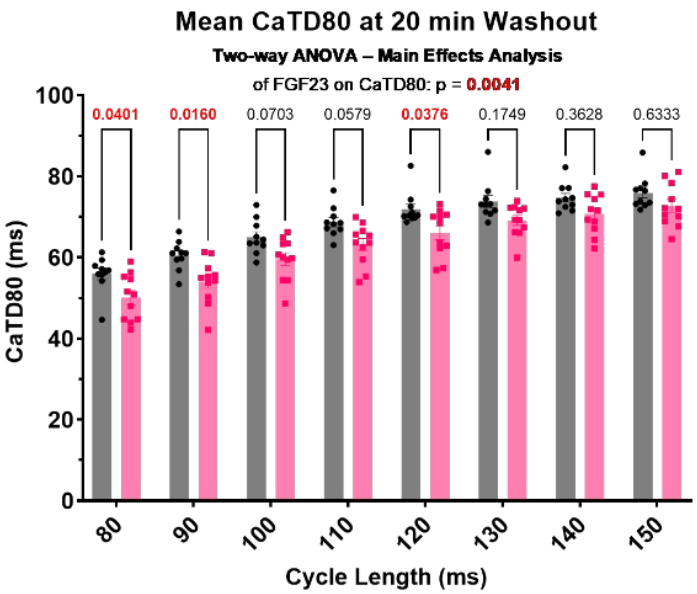
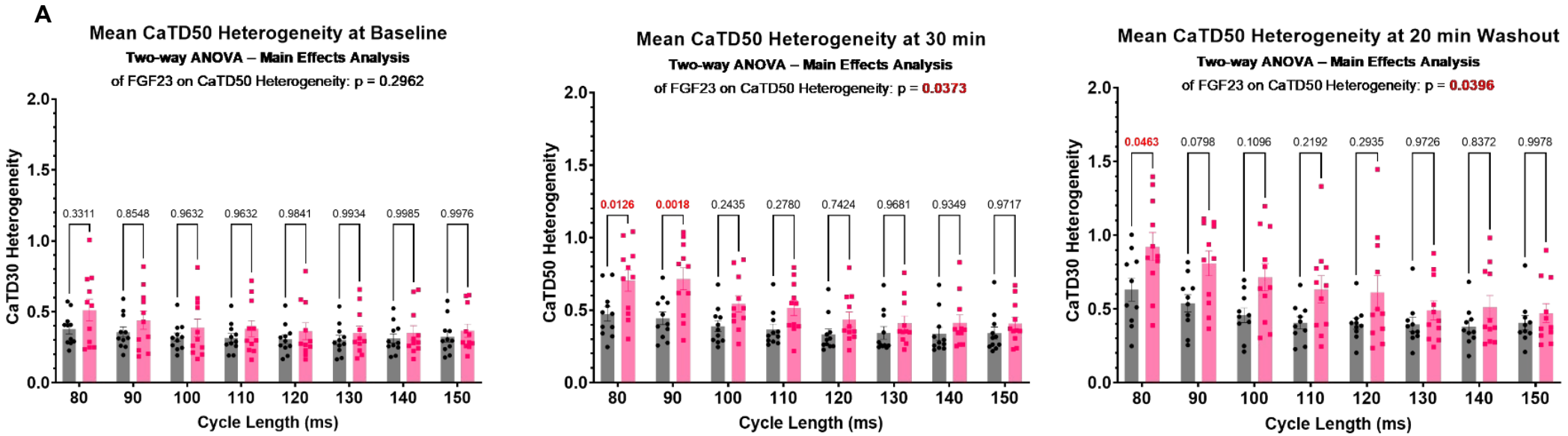
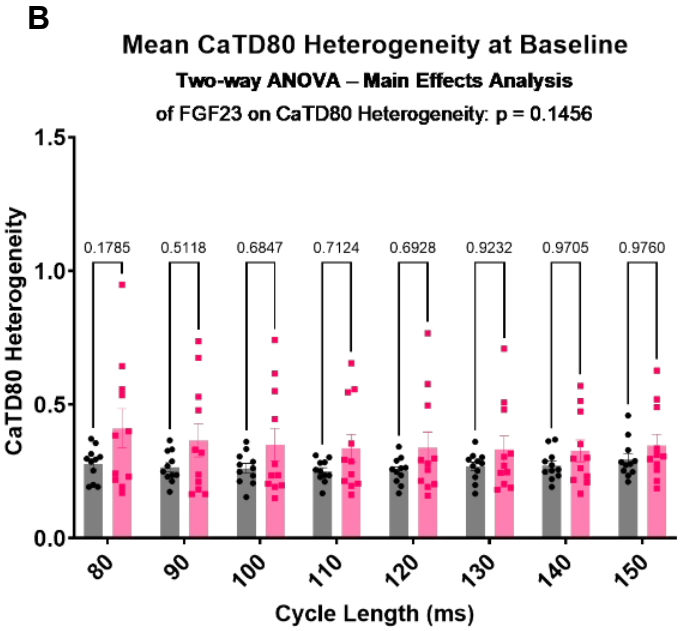

Mean CaTD80 at 20 min Washout
Two-way ANOVA – Main Effects Analysis
of FGF23 on CaTD80: p = 0.0041
0.0401 0.0160 0.0703 0.0579 0.0376 0.1749 0.3628 0.6333
CaTD80 (ms)
Cycle Length (ms)

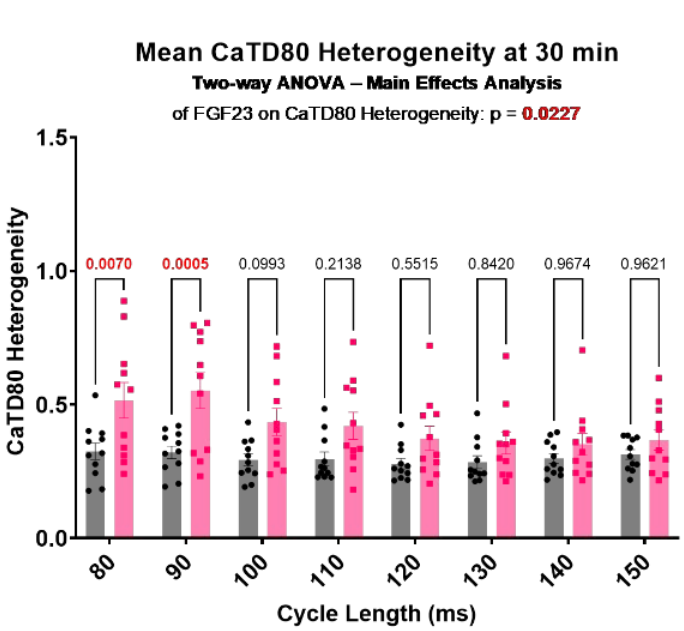
Figure 6-7. Effect of FGF23 on murine left ventricular calcium transient duration heterogeneity by optical mapping.

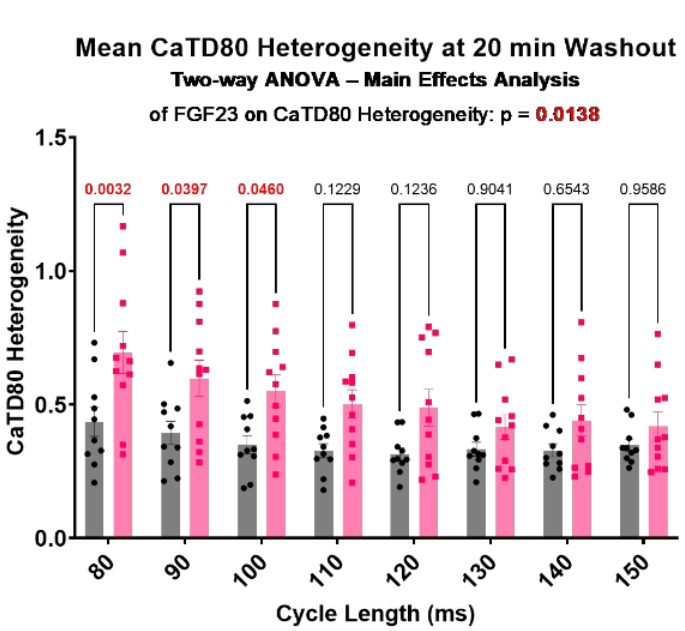
Calcium transient duration (CaTD) heterogeneity at **A** – 50% decay; and **B** – 80% decay. Optical mapping recordings were taken at baseline, 30 minutes into treatment with 10 ng/mL FGF23 (**pink**) or vehicle control phosphate buffered saline (**grey**), and following a 20-minute washout period. Data presented as mean ± S.E.M. Two-way ANOVA (treatment x CaTD heterogeneity) were performed; P values shown for main effects analysis of FGF23 on CaTD heterogeneity and Sidak multiple comparison tests (N = 11 hearts per group).



B


Mean CaTD80 Heterogeneity at Baseline
Two-way ANOVA – Main Effects Analysis
of FGF23 on CaTD80 Heterogeneity: p = 0.1456
CaTD80 Heterogeneity
1.5
1.0
0.5
0.0
0.1785
0.5118
0.6847
0.7124
0.6928
0.9232
0.9705
0.9760
80
90
100
110
120
130
140
150
Cycle Length (ms)


Mean CaTD80 Heterogeneity at 30 min
Two-way ANOVA – Main Effects Analysis
of FGF23 on CaTD80 Heterogeneity: p = 0.0227
CaTD80 Heterogeneity
1.5
1.0
0.5
0.0
0.0070
0.0005
0.0993
0.2138
0.5515
0.8420
0.9674
0.9621
80
90
100
110
120
130
140
150
Cycle Length (ms)


Mean CaTD80 Heterogeneity at 20 min Washout
Two-way ANOVA – Main Effects Analysis
of FGF23 on CaTD80 Heterogeneity: p = 0.0138
CaTD80 Heterogeneity
1.5
1.0
0.5
0.0
0.0032
0.0397
0.0460
0.1229
0.1236
0.9041
0.6543
0.9586
80
90
100
110
120
130
140
150
Cycle Length (ms)

6.3.4. Time to peak of calcium transient and calcium transient decay following FGF23 treatment

To further study the effect of FGF23 on the calcium transient, time to peak and calcium decay were studied. Following 10 ng/mL FGF23 treatment for 30 minutes, the time to peak of the calcium transient remained unchanged versus control (mean change in time to peak = -0.35 ms [95% CI -2.08 to 2.78], p = 0.7646). There were no significant changes at baseline (simple main effects p = 0.7502) or at 20-minute washout (simple main effects p = 0.7496) between groups (**Figure 6-8**). Calcium transient decay expressed as exponential decay constant tau was prolonged by a mean of 7.95 ms (95% CI 0.10 to 15.8, p = 0.0475) following FGF23 treatment, however there was a significant interaction between cycle length and FGF23 treatment (p = 0.0256). Further scrutiny of the multiple comparison tests show that FGF23 treatment has a stronger effect on tau at 90 ms (p = 0.0007) and 100ms (p = 0.2197), whilst there was generally no observed effect at other, longer cycle lengths (p > 0.7, **Figure 6-9**). Tau heterogeneity was unchanged by FGF23 treatment at baseline, 30 minute and 20-minute washout timepoints with respective simple main effects p = 0.1301, 0.2973 and 0.1301 (**Figure 6-10**).

Figure 6-8. Effect of FGF23 on murine left ventricular time to peak of calcium transient by optical mapping.

Time to peak (TTP) was defined as the time from 10% to 90% of the peak of the calcium transient. Optical mapping recordings were taken at baseline, 30 minutes into treatment with 10 ng/mL FGF23 (**pink**) or vehicle control phosphate buffered saline (**grey**), and following a 20-minute washout period. Data presented as mean ± S.E.M. Two-way ANOVA (treatment x TTP) were performed; P values shown for main effects analysis of FGF23 on TTP and Sidak multiple comparison tests (N = 11 hearts per group).

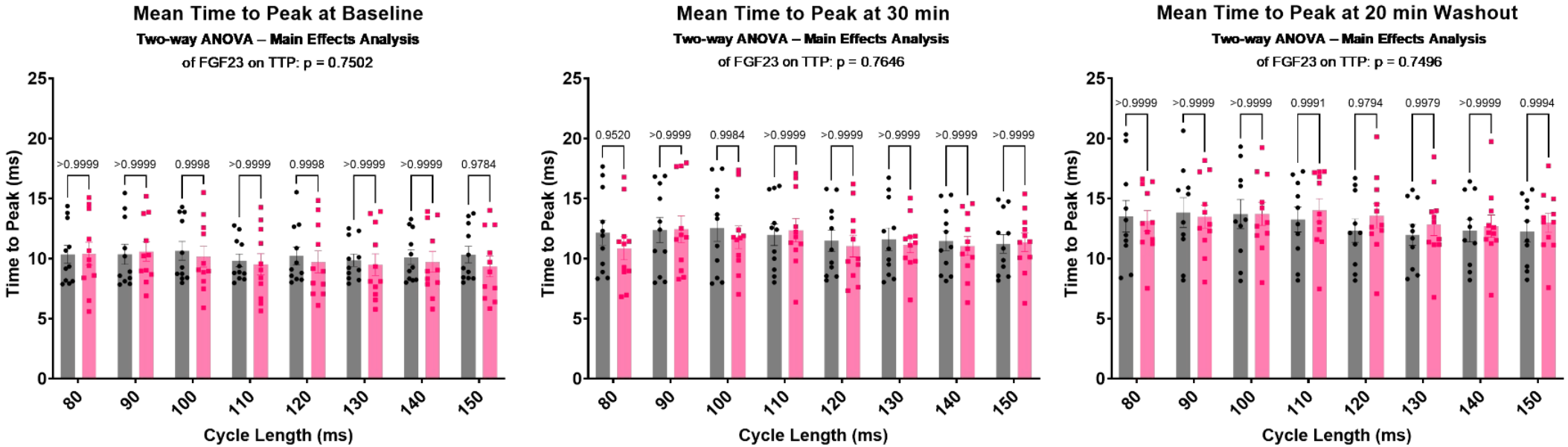


Figure 6-9. Effect of FGF23 on murine left ventricular calcium transient decay coefficient tau by optical mapping.

Tau was obtained from exponential curve fitting between 90% and 30% decay of the calcium transient. Optical mapping recordings were taken at baseline, 30 minutes into treatment with 10 ng/mL FGF23 (**pink**) or vehicle control phosphate buffered saline (**grey**), and following a 20-minute washout period. Data presented as mean ± S.E.M. Two-way ANOVA (treatment x Tau) were performed; P values shown for main effects analysis of FGF23 on Tau and Sidak multiple comparison tests (N = 11 hearts per group).

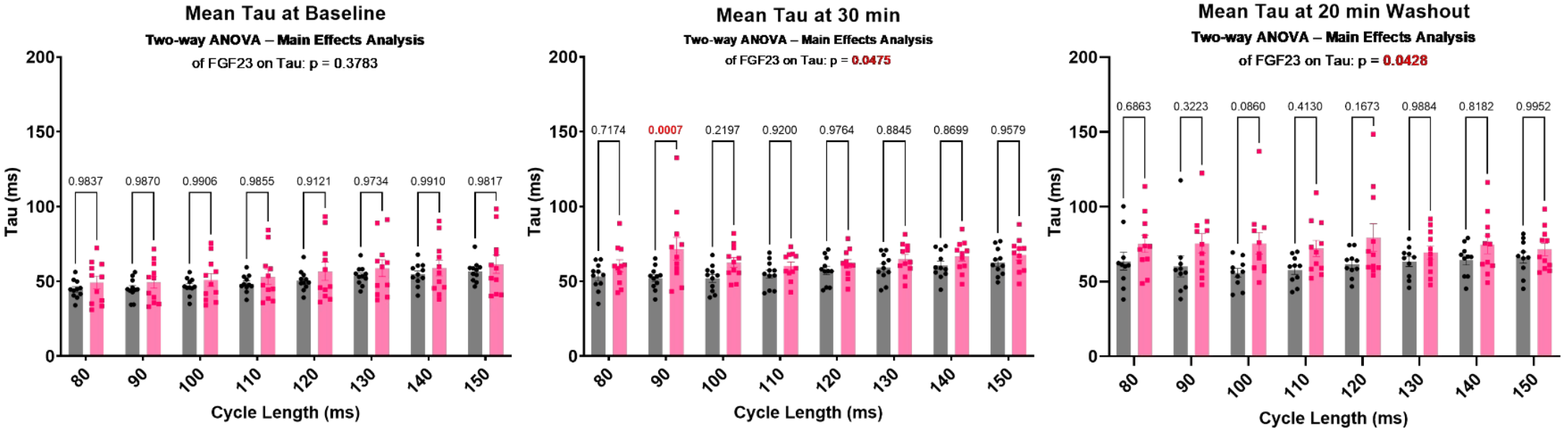
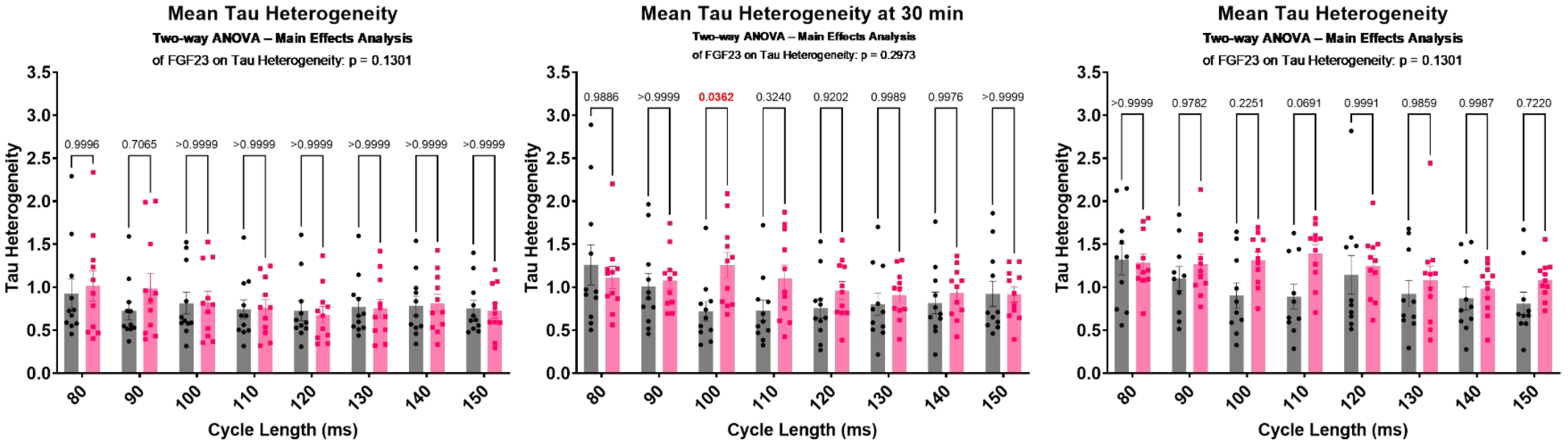


Figure 6-10. Effect of FGF23 on murine left ventricular calcium transient decay heterogeneity by optical mapping.

Tau heterogeneity was obtained from optical mapping recordings were taken at baseline, 30 minutes into treatment with 10 ng/mL FGF23 (**pink**) or vehicle control phosphate buffered saline (**grey**), and following a 20-minute washout period. Data presented as mean ± S.E.M. Two-way ANOVA (treatment x Tau heterogeneity) were performed; P values shown for main effects analysis of FGF23 on Tau heterogeneity and Sidak multiple comparison tests (N = 11 hearts per group).



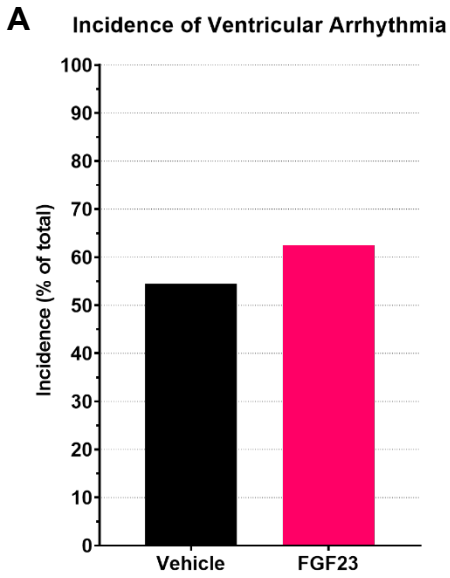
6.3.5. Ventricular arrhythmia burden and effective refractory period

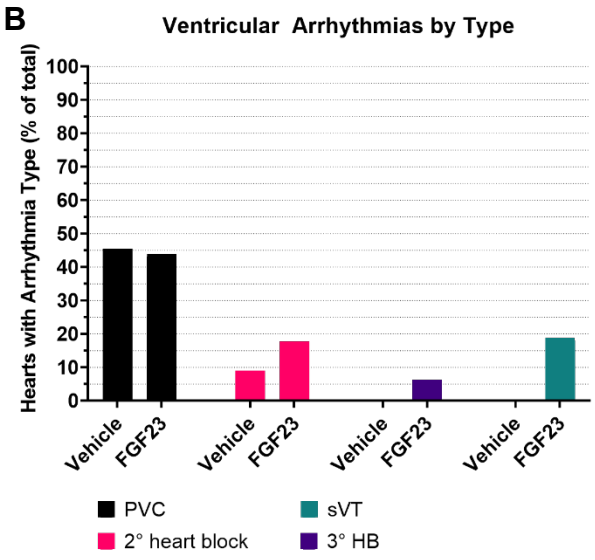
Ventricular arrhythmias were observed in 54% of control (6 of 11) and 62.5% of FGF23-treated (10 of 16) hearts with the 30-minute treatment period (**A**). Whilst the incidence of premature ventricular beats was similar in both groups (46% control vs 43.8% FGF23), FGF23 treated hearts had more instances of 2nd degree heart block (18% vs 9%), 3rd degree heard block (6% vs 0%) and ventricular tachycardia (19% vs 0%) compared to control hearts. Overall arrhythmia score using the same criteria as employed in Chapter 5 showed a high arrhythmia burden in hearts treated with FGF23 (mean score 1.38 ± 0.36 vs control 0.55 ± 0.16) but this did not reach statistical significance ($p = 0.0834$).

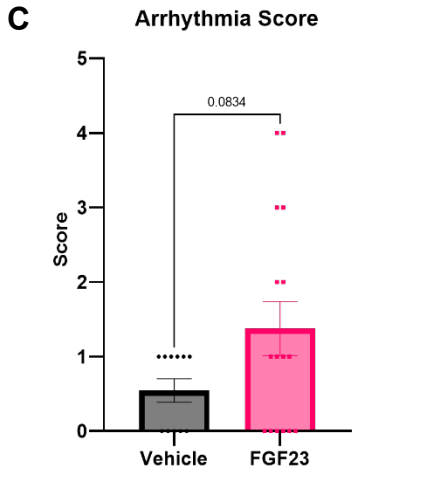
Effective refractory period (ERP) was determined in both treatment groups using a S1-S2 protocol. There were no significant differences between treatment groups at baseline, 30 minute and 20-minute washout timepoints.

Figure 6-11. Ventricular arrhythmia burden and effective refractory period of *ex vivo* murine hearts in response to acute FGF23 treatment.

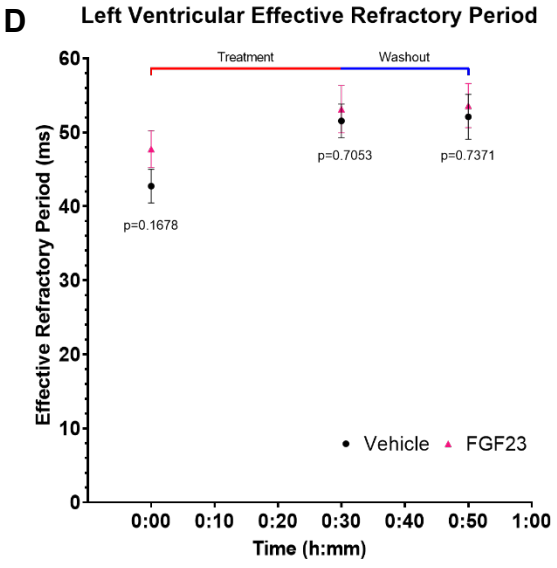
Arrhythmia burden **(A-C)** was assessed following 30 minutes perfusion with 10 ng/mL fibroblast growth factor 23 (FGF23; N = 16) or vehicle (phosphate buffered saline; N = 11). **A** – Incidence of ventricular arrhythmias. **B** – Ventricular arrhythmias by type. **C** – Arrhythmia score presented as median ± interquartile range; Mann-Whitney U test. **D** – Left ventricular effective refractory period at baseline, 30 minutes following infusion of 10 ng/mL FGF23 or vehicle control, and 20-minute washout.







Ventricular Arrhythmic Event	Points
Ventricular tachycardia, sustained (> 15 beats)	3
Third degree heart block	
Ventricular tachycardia, non-sustained (5-15 beats)	2
1st and 2nd degree heart block	1
Premature ventricular beats (< 5 beats)	
No arrhythmia	0



6.4. DISCUSSION

6.4.1. FGF23, ventricular APD shortening and increased arrhythmogenicity

Using a calcium and voltage optical mapping setup, dual fluorescent dye-loaded murine hearts were found to exhibit APD shortening following 30 minute treatment with 10 ng/mL FGF23 compared to vehicle control hearts. The APD shortening was no longer present following a 20-minute washout, mirroring the findings in single fluorescent (voltage) dye-loaded murine hearts in Chapter 5. Other common findings include increased ventricular arrhythmia burden following FGF23 treatment, although to a lesser extent than in the single-loaded experiments. This was due to the marginally greater incidence of premature ventricular contractions in the control dual-loaded hearts compared to the control single loaded hearts (5 of 11 hearts vs 4 of 15 hearts). This may be due to the use of a calcium dye, which can buffer some of the intracellular calcium over the course of the optical experiment and, therefore, negatively impact cellular electrophysiology. Other differences between the two experiments included a smaller, statistically non-significant rise in APD heterogeneity as result of FGF23 treatment than found in the single-loaded hearts, and the lack effect of the treatment on time to peak depolarisation in the dual-loaded hearts.

6.4.2. Differences between single, and dual calcium-voltage loaded experiments

Whilst much effort was made to ensure the single and dual-loaded experimental protocols were as well-matched as possible – e.g. identical murine strain of similar gender and age; anaesthetic, cardiac extraction and Langendorff

perfusion methodology and buffers; cardiac pacing protocols and treatment timepoints – the main sources of variation were the use of a different voltage-sensitive dye (RH237 $\lambda_{ex}/\lambda_{em}$ 528/782 nm) which has a different emission wavelength, but similar peak excitation band to the calcium dye (Rhod-2 AM $\lambda_{ex}/\lambda_{em}$ 530/570-625 nm) allowing simultaneous capture of voltage and calcium fluorescence using a single wavelength light source [550,551]; and the additional ~10 minutes at the beginning of each dual-loaded experiment to allow loading of both dyes, resulting in a later baseline time point (i.e. start of FGF23/vehicle control treatment).

Evidence of this later baseline time point can be seen when comparing the baseline APDs from both experiments. In Langendorff-perfused murine hearts, I have observed a prolongation of APD over the course of the experiment as seen in the time/treatment control hearts: a later experimental start time resulted in longer baseline APDs – mean APD_{50} and APD_{80} at baseline were 29.38 ms and 52.58 ms, respectively, in the dual-loaded experiments; in the single-loaded experiments, mean APD50 and APD80 at baseline were 25.67 ms and 58.00 ms, respectively. At the washout timepoint, 50 minutes after the baseline timepoint, mean APD50 and APD80 were 32.60 ms and 58.84 ms in the dual-loaded hearts, as compared to 31.37 ms and 56.20 ms in the single-loaded hearts. A possible explanation for the prolongation of APD with time is an altered balance or dysfunction of one or more ion channels responsible for APD repolarisation (e.g. reduced NCX and SERCA2a activity resulting in longer calcium transient decay) as a result of gradual tissue ischaemia and necrosis. This is an unavoidable limitation which has been alleviated by several experimental optimisations to

maintain normal electrophysiological function for as long as possible: anaesthetic minimisation and efficient cardiac extraction, flushing the heart with heparinised, ice-cold KHB to reduce thrombosis and metabolic demand; rapid cannulation and perfusion with warmed, oxygenated and pH-adjusted KHB to minimise cold-ischaemic time; use of lowest possible loading doses of fluorescent dyes and solubilising of dyes with the addition of Pluronic F-127 to facilitate loading; minimising excitation LED intensity and 'ON' time to reduce photobleaching.

6.4.3. FGF23 and ventricular calcium handling

In these dual-loaded experiments, ventricular CaTD was shortened following 30 minutes of 10 ng/mL FGF23 treatment versus time/vehicle controls. This suggests that alterations in calcium handling are responsible, at least in part, for the shortening in APD observed. CaTD transient heterogeneity was significantly increased, as was the CaT decay constant *tau*. Navarro-Garcia et al. [257] also reported *in vitro* prolongation of calcium decay in isolated rat cardiomyocytes treated with a much higher concentration of FGF23 (50 and 100 ng/mL). These cells exhibited a longer time to peak calcium transient, reduced calcium transient amplitude, and SR calcium load due to increases in calcium spark frequency. Another *in vitro* study by Verkaik et al. [524] also reported reduced peak systolic calcium, prolonged time to peak and slower decay in mouse ventricular cardiomyocytes isolated from 5/6 nephrectomy mice.

In contrast, several studies reported opposite effects: Touchberry et al. [254] (18 ng/mL FGF23, isolated CD1 mouse cardiomyocytes), Kao et al. [523] (25 ng/mL FGF23, HL-1 mouse atrial cardiomyocytes), Huang et al. (1 ng/mL FGF23, rabbit pulmonary cardiomyocytes), and Graves et al. [526] (9 ng/mL FGF23, CD1

ventricular muscle strips) all reported increased $[Ca^{2+}]_i$ [254,526], CaT amplitude [523], SR calcium content [523] and I_{CaL} [523,524] compared to control. In the *ex vivo* experiments described in this chapter, mean CaT amplitude was not different between the FGF23-treated and vehicle control hearts, implying that FGF23 does not alter peak systolic $[Ca^{2+}]_i$. There was however considerable variation in the calcium signal amplitude in both control and FGF23 treated hearts in part due to variations in dye loading, which can be addressed by using a ratiometric dye such as Indo-1 or Fura-2.

It is challenging to reconcile the variation in experiment findings reported by these authors due to fundamental variations in experimental technique. Varying concentrations of FGF23 and cardiac cells/tissue from different species and cardiac chambers were employed. There were commonalities between studies and these were as follows: 1) all but one study (Verkaik et al. [525]) studied the effects of acute exposure to FGF23, where calcium measurements were taken from tens of minutes to hours following superfusion of treatment solutions with the longest being 24 hours prior to Ca^{2+} imaging [523]; 2) all authors utilised nonratiometric fluorescein dyes to measure Ca^{2+}; 3) cells were isolated from disease-free animals with the exception of Verkaik et al. [525], who utilised CKD animal models; 4) although there was great variation in FGF23 concentrations utilised (1 to 100 ng/mL), the dosing range is comparable to circulating FGF23 levels in CKD [178,552-554]; 5) *in vitro* nature of studies.

Unlike in this current study, no other published studies have studied the effects of FGF23 on cardiac calcium dynamics using an intact, beating whole-heart preparation. This allowed for a more physiological assessment of cardiac

electrophysiology compared to *in vitro*, (single) cellular techniques. Optical mapping also has the added benefit of high spatial *and* temporal resolution across the whole imaged cardiac surface, and simultaneous voltage-calcium optical mapping offers unique insights into the optical AP and CaT in the same heart. Due to a hardware fault, I was unable to synchronise the two cameras used to record the record the AP and CaT separately. As a result, the temporal relationship between the voltage and calcium traces could not be deduced from the optical mapping recordings.

In conclusion, data from the dual-loaded murine hearts show that acute FGF23 treatment induced ventricular APD and CaTD shortening, and increased CaTD spatial heterogeneity, providing a substrate for the increased ventricular arrhythmias observed.

CHAPTER 7. CONSEQUENCES OF CHRONICALLY RAISED FIBROBLAST GROWTH FACTOR 23 ON MURINE CARDIAC MORPHOLOGY AND ELECTROPHYSIOLOGY

7.1. EXTENT OF PERSONAL CONTRIBUTION

Intraperitoneal rmFGF23 injections were performed by staff scientists at the Biomedical Sciences Unit, University of Birmingham. Sophie Broadway-Stringer acquired the in vivo echocardiograms and performed analysis of the images. I performed all other aspects of the presented data.

.

7.2. INTRODUCTION

Following on from the experiments in Chapters 5 and 6, which investigated the effect of acute FGF23 elevations on murine cardiac electrophysiology, we hypothesised that longer periods of elevated FGF23, as found in chronic kidney disease would cause similar, pathological changes in cardiac electrical function, but also result in cardiac remodelling and dysfunction. As previously discussed, elevations in FGF23 have already been associated with increased ventricular remodelling and hypertrophy in humans [555,556] and in murine studies [171,172].

To address this question, a murine model of FGF23 excess was generated (see Chapter 2.7.2.2) by injecting adult, female CD1 mice with once daily 3.12 µg intraperitoneal injections of FGF23 for seven days, such that the daily dose of FGF23 would exceed 80 µg/kg/day. The daily dose was comparable to that used by Faul et al. [171], although in their study, FGF23 was administered by tail vein injection in two daily doses, eight hours apart, for five days.

Venepuncture for plasma FGF23 quantification were performed on day 4 of injections; *in vivo* echocardiography and cardiac isolation for Langendorff-perfused left ventricular optical mapping were conducted on day 8. Mouse hearts were loaded with a voltage-sensitive membrane dye Di-4-ANEPPS utilising an identical optical mapping setup to that described in previous chapters. Whole cardiac mass and mass by cardiac chamber were adjusted for body weight and tibial length. Tissue was retained for immunoblotting.

7.3. RESULTS

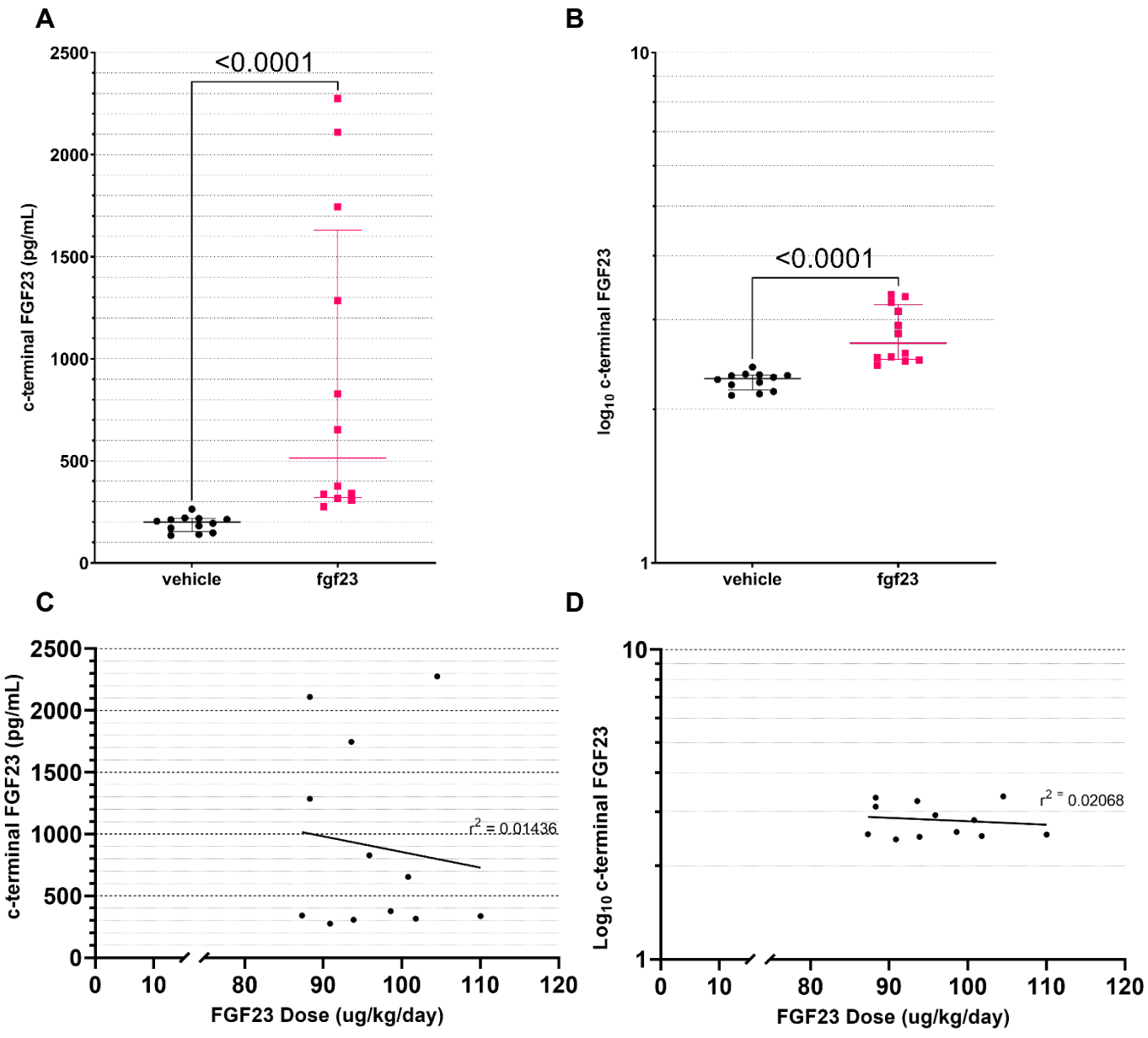
7.3.1. Plasma FGF23 quantification

C-terminal FGF23 was quantified from plasma obtained following day 4 of 7 daily intraperitoneal injections of 3.12 µg FGF23 or vehicle (phosphate buffered saline). Care was taken to allow ~4 hours to have elapsed since the intraperitoneal injection before saphenous vein venepuncture. All mice received above the target 80 µg/kg daily dose. Mean dose delivered was 96 ± 2 µg/kg with a minimum of 87 µg/kg and a maximum of 110 µg/kg.

C-terminal FGF23 levels were non-parametrically distributed in the FGF23-treated animals and were significantly higher than in the vehicle control (median plasma $FGF23_{FGF23}$ = 514 (1310) pg/mL; median plasma $FGF23_{vehicle}$ = 199 (64) pg/mL, $p < 0.0001$, **Figure 7-1 A**). The difference remained after log-normalisation of FGF23 values ($p < 0.0001$, **Figure 7-1 B**). There was no correlation between dose of FGF23 delivered, and c-terminal FGF23 level (r^2 = 0.01436, **Figure 7-1 C**), which did not change with log-normalisation of FGF23 levels (r2 = 0.02068, **Figure 7-1 D**).

Figure 7-1. Plasma c-terminal FGF23 quantification by sandwich ELISA.

CD1 mice underwent 7 daily intraperitoneal injections of vehicle control phosphate buffered saline or 3.12 µg FGF23. Plasma was obtained following the fourth daily intraperitoneal injection (N = 12 per group). **A** – Plasma levels. Median, interquartile range; Mann-Whitney U test. **B** – Log transformed plasma levels. Mean ± S.E.M.; unpaired t-test. **C** – Correlation of daily FGF23 dose (ug/kg) with plasma FGF23 level. **D** – Correlation with log-transformed plasma FGF23 level. Linear regression with r^2 shown.



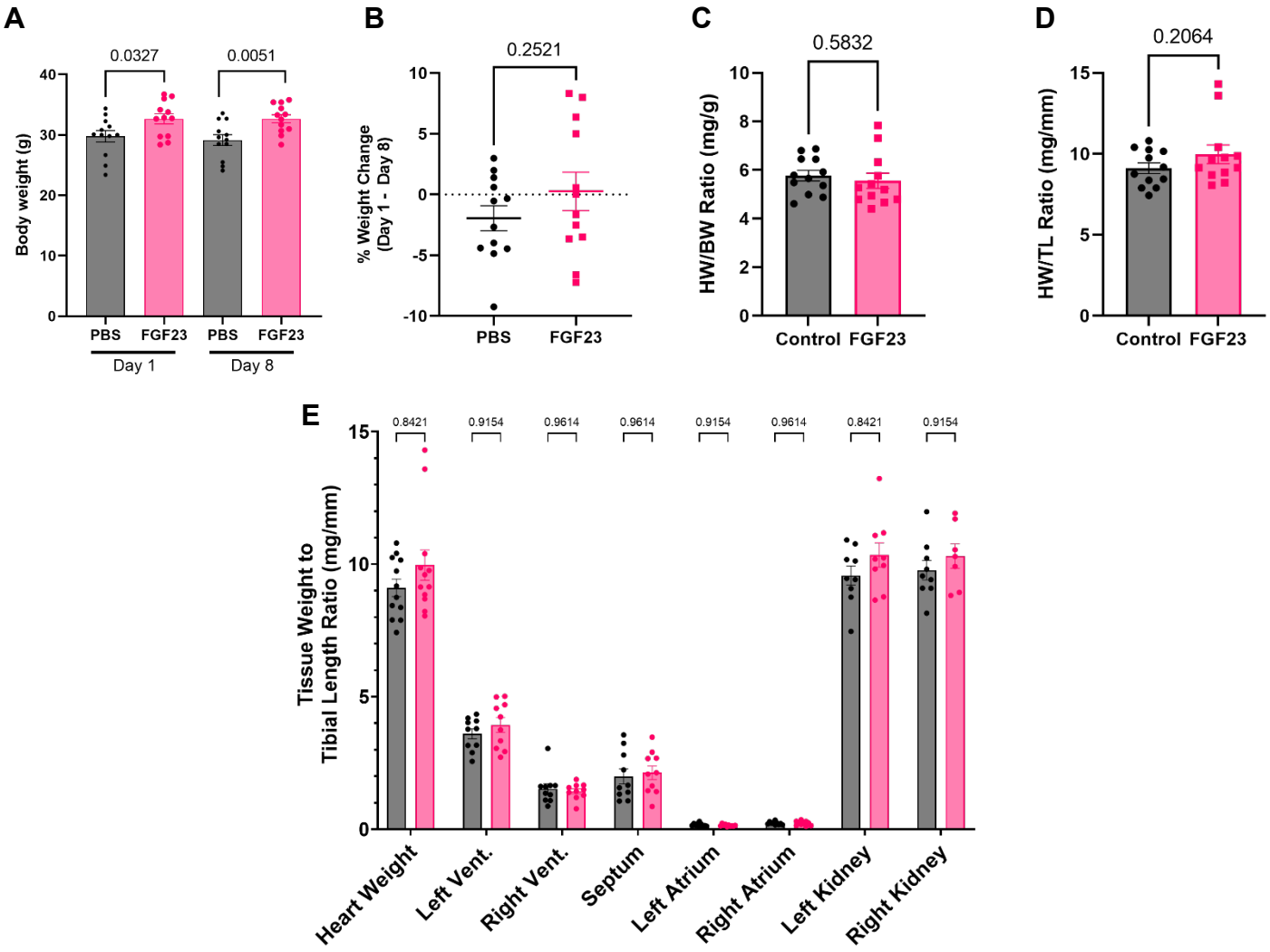
7.3.2. Body and tissue weight

Following 7 days of FGF23 or vehicle intraperitoneal injections, mice underwent terminal anaesthesia and cardiac extraction on day 8. Mice assigned to the vehicle (PBS) group had a lower body mass at day 1 of the protocol (mean difference = 2.9 ± 1.3 g, p = 0.0327, **Figure 7-2 A**) than mice assigned to the FGF23 group). This remained the case at day 8 (mean difference = 3.5 ± 1.1 g, p = 0.0051, **Figure 7-2 A**). Although the vehicle control mice experienced a small reduction in body weight during the 7 day protocol (mean percentage change of -1.96 ± 1.03%), this was not significantly different from the FGF23-treated mice (mean percentage change of 0.26 ± 1.58%, p = 0.2521, **Figure 7-2 B**).

No differences in heart weights were observed between the two groups at day 8 of the protocol when normalised to body weight (p = 0.5832) and tibial length (p = 0.2064, **Figure 7-2 C** & **D**). Cardiac chambers were dissected, individually weighed, and adjusted for tibial length. FGF23 treatment did not alter cardiac chamber weights (p > 0.9, **Figure 7-2 E**).

Figure 7-2. Body and tissue weights.

CD1 mice underwent 7 daily intraperitoneal injections of vehicle control phosphate buffered saline or 3.12 µg FGF23, and underwent terminal anaesthesia on day 8. (N = 12 per group). **A** – CD1 mice were weighed at day 1 and 8 prior to terminal anaesthesia. **B** - Percentage weight change between day 1 and 8. **C** – Heart weight to body weight ratio at day 8. **D** – Heart weight to tibial length ratio at day 8. **E** – Hearts were dissected to separate the individual chambers. Cardiac chamber and kidney weights were adjusted to tibial length. Mean ± S.E.M.; unpaired t-test, N = 12 per group.

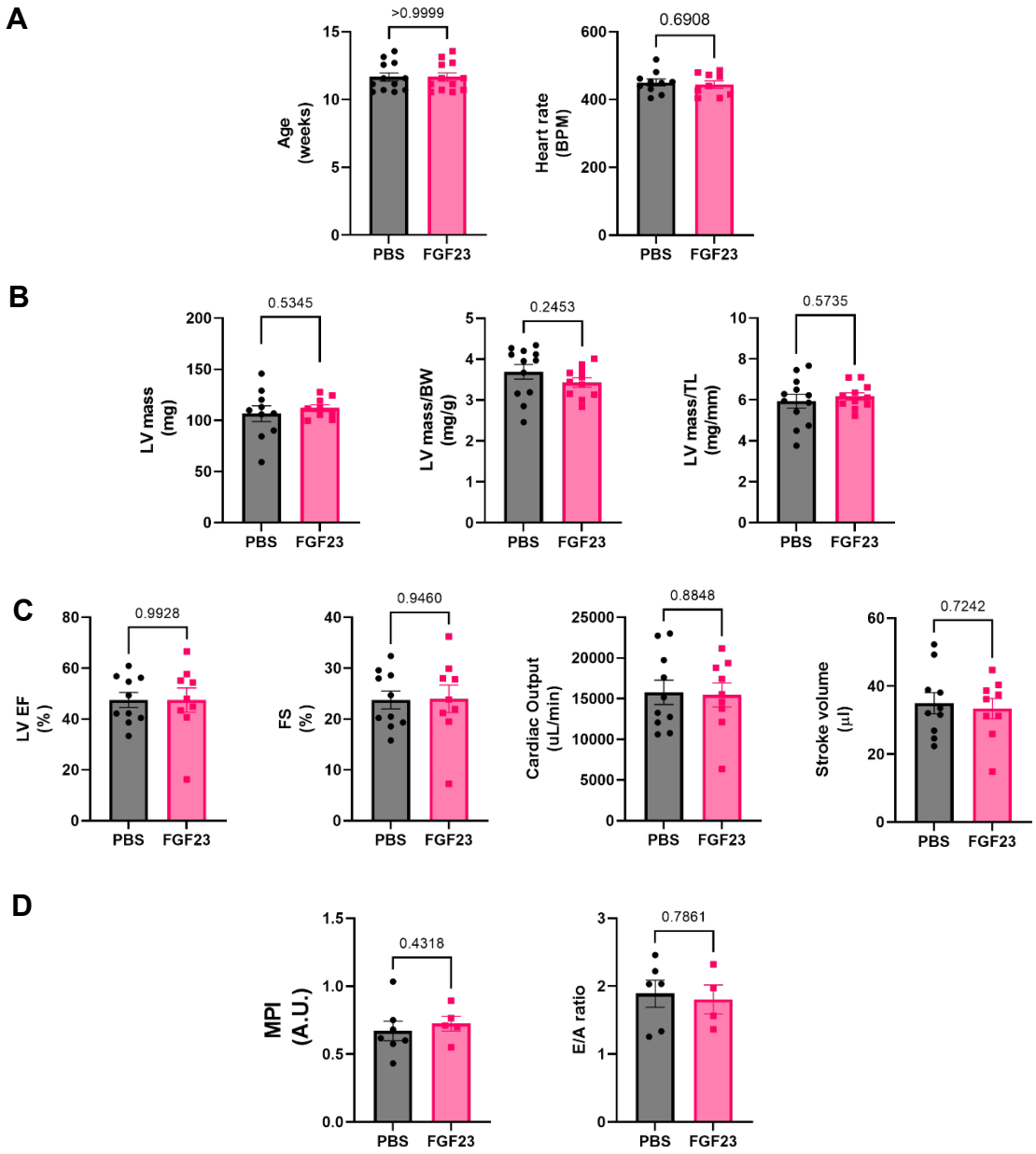


7.3.3. Echocardiogram parameters – LV mass and function

In vivo echocardiograms were performed under 0.5-3% isoflurane anaesthesia (**Figure 7-3**). Echocardiograms were abandoned for mice with anaesthetic complications, labile heart rate or poor views. Mean age of the mice was 11.6 ± 0.3 weeks old. Mean heart rate at time of echocardiogram was 450 ± 10 bpm in control mice versus 444 ± 11 bpm in FGF23 mice ($p = 0.6908$, **Figure 7-3 A**). FGF23 did not alter uncorrected LV mass ($p = 0.5345$), nor was there a difference between groups after correcting for body weight ($p = 0.2453$) and tibial length ($p = 0.5735$, **Figure 7-3 B**). Markers of LV systolic function (**Figure 7-3 C**) were near-identical in both groups with a difference between mean LVEF of just -0.05 ± 5 % (mean $EF_{vehicle} = 44.49$, mean $EF_{FGF23} = 47.44$ $p = 0.9928$). Fractional shortening ($p = 0.9460$), cardiac output ($p = 0.8848$) and stroke volume ($p = 0.7242$) were comparable. Diastolic parameters were only measured in 7 of 12 vehicle control and 5 of 12 FGF23 mice due to limited views. FGF23 treatment did not significantly alter myocardial perfusion index ($p = 0.4318$) or E/A ratio ($p = 7861$) (**Figure 7-3 D**). Taken together, FGF23 treated mice did not exhibit any changes in left ventricular structure or function.

Figure 7-3. In vivo echocardiogram.

CD1 mice underwent 7 daily intraperitoneal injections of vehicle control phosphate buffered saline or 3.12 µg FGF23. In vivo echocardiograms were performed on day 8 under isoflurane anaesthesia. **A** – Mouse age and heart rate; **B** – LV mass measurements; **C** – markers of systolic function; **D** – markers of diastolic function. Mean ± S.E.M.; unpaired t-test, N = 9-12 per treatment group for systolic parameters; N = 5-7 per treatment group for diastolic parameters.



7.3.4. Optical mapping and arrhythmias

The same mice that were subjected to echocardiogram underwent cardiac extraction under terminal anaesthesia on the same day (day 8). Hearts were isolated for Langendorff-perfusion and optical mapping using voltage-sensitive fluorescent dye Di-4-ANEPPS.

FGF23 treatment for 7 days did not change APD at 30, 50 and 80% repolarisation (simple main effects p = 0.9997, 0.7120, 0.7050 respectively), $APD_{30,\ 50,\ 80}$ heterogeneity (simple main effects p = 0.0686, 0.3889, 0.6302, respectively), AP conduction velocity (simple main effects p = 0.2226), time to peak depolarisation (simple main effects p = 0.9544) or diastolic interval (p = 0.8202) versus vehicle control mice (**Figure 7-4**). APD and conduction were not correlated with log-normal plasma FGF23 (**Figure 7-5**).

During the optical mapping experiments, hearts were monitored for ventricular arrhythmias. They were present in 33% (3 of 9) control and 36% (4 of 11) hearts from FGF23-treated mice (**Figure 7-6 A**).

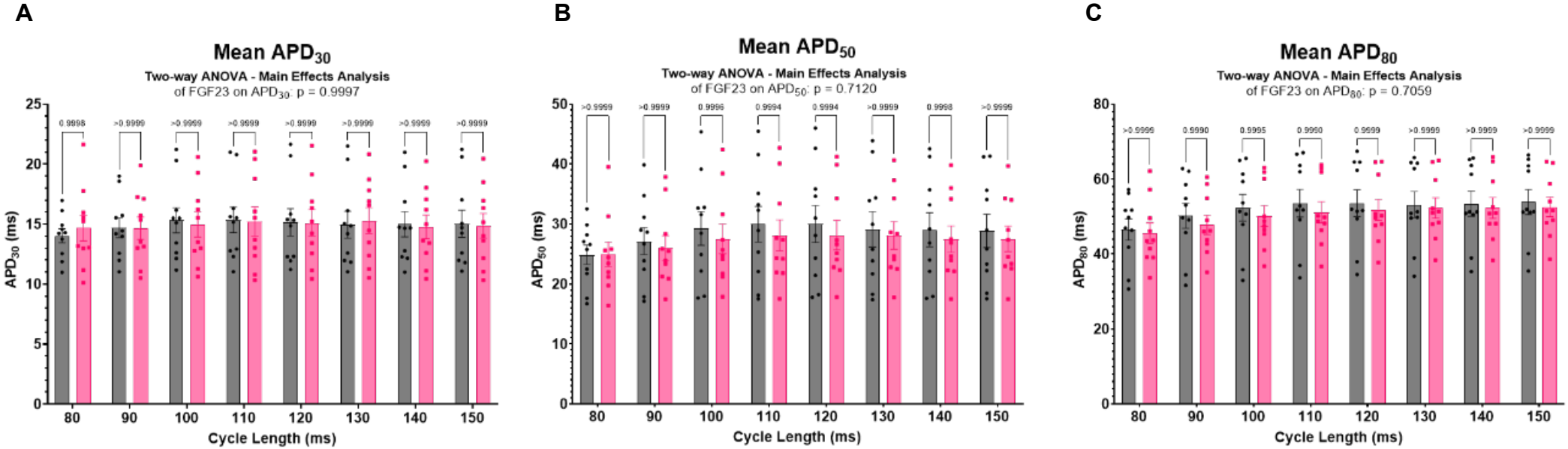
Ventricular arrhythmias were mostly due to sinus arrhythmias and premature ventricular beats, which were more common in hearts from FGF-treated mice: sinus arrhythmias were observed in 18% (2 of 11) hearts and premature ventricular beats in 27% (3 of 11) hearts from FGF23-treated mice; sinus arrhythmias and premature ventricular beats were detected in 11% (1 of 9) hearts from the control mice (**Figure 7-6 B**). There was one instance of non-sustained ventricular tachycardia in the control hearts (out of 9), and one instance of a 2:1 conduction block in the FGF23 hearts (out of 11, **Figure 7-6 B**).

Arrhythmia scores ($p = 0.8774$, **Figure 7-6 C**) and effective refractory periods ($p = 0.3224$, **Figure 7-6 D**), as determined using previously described S1-S2 protocol, were not significantly different between groups.

Overall, longer term exposure of hearts to excess circulating FGF23 resulted in minor increases in the incidence of arrhythmogenic phenomena, without significantly altering action potential characteristics.

Figure 7-4. Left ventricle optical mapping.

CD1 mice underwent 7 daily intraperitoneal injections of vehicle control phosphate buffered saline or 3.12 µg FGF23, and underwent terminal anaesthesia on day 8. Hearts were isolated for optical mapping of left ventricle action potentials.(N = 10 per group). **A-C** – Action potential duration at 30, 50 and 80% repolarisation. **D-F** – Action potential heterogeneity at 30, 50 and 80% repolarisation. **G-I** – Conduction velocity, time to peak depolarisation and diastolic interval. Data presented as mean ± S.E.M. Two-way ANOVA (treatment x parameter); P values shown for main effects analysis of FGF23 on parameter, and Sidak multiple comparison tests (N = 10 per group).



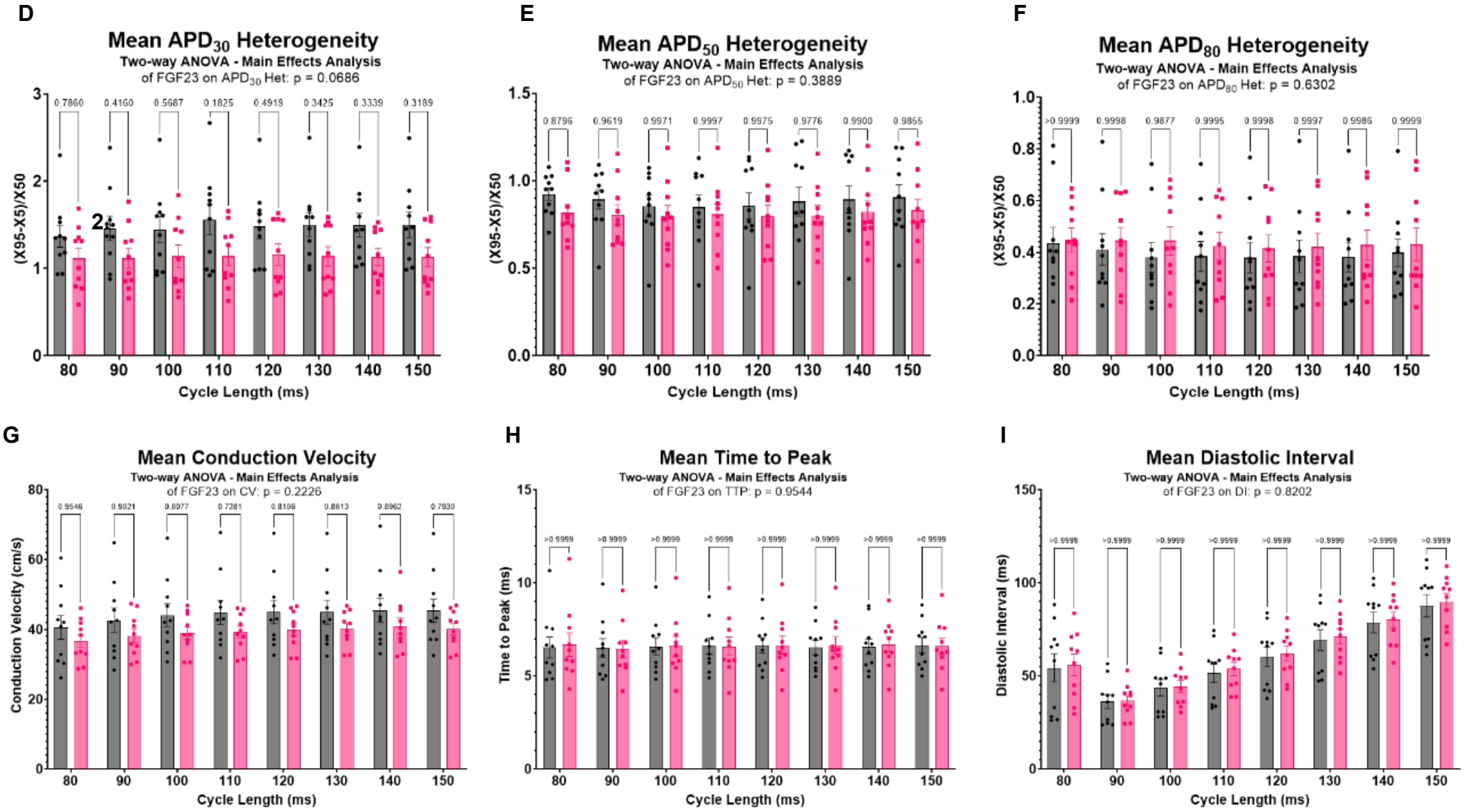

D
Mean APD30 Heterogeneity
Two-way ANOVA - Main Effects Analysis
of FGF23 on APD30 Het: p = 0.0686
(X95-X5)/X50
Cycle Length (ms)
E
Mean APD50 Heterogeneity
Two-way ANOVA - Main Effects Analysis
of FGF23 on APD50 Het: p = 0.3889
(X95-X5)/X50
Cycle Length (ms)
F
Mean APD80 Heterogeneity
Two-way ANOVA - Main Effects Analysis
of FGF23 on APD80 Het: p = 0.6302
(X95-X5)/X50
Cycle Length (ms)
G
Mean Conduction Velocity
Two-way ANOVA - Main Effects Analysis
of FGF23 on CV: p = 0.2226
Conduction Velocity (cm/s)
Cycle Length (ms)
H
Mean Time to Peak
Two-way ANOVA - Main Effects Analysis
of FGF23 on TTP: p = 0.9544
Time to Peak (ms)
Cycle Length (ms)
I
Mean Diastolic Interval
Two-way ANOVA - Main Effects Analysis
of FGF23 on DI: p = 0.8202
Diastolic Interval (ms)
Cycle Length (ms)

Figure 7-5. Correlation of left ventricle electrophysiological parameter with plasma FGF23 level.

Action potential duration at 30%, 50% and 80% repolarisation and conduction velocity were plotted against plasma c-terminal FGF23 levels at three cycle lengths – 80, 110, 150 ms. Linear regression line with 95% confidence interval bands and r^2 shown. N = 20 per cycle length and electrophysiology parameter.

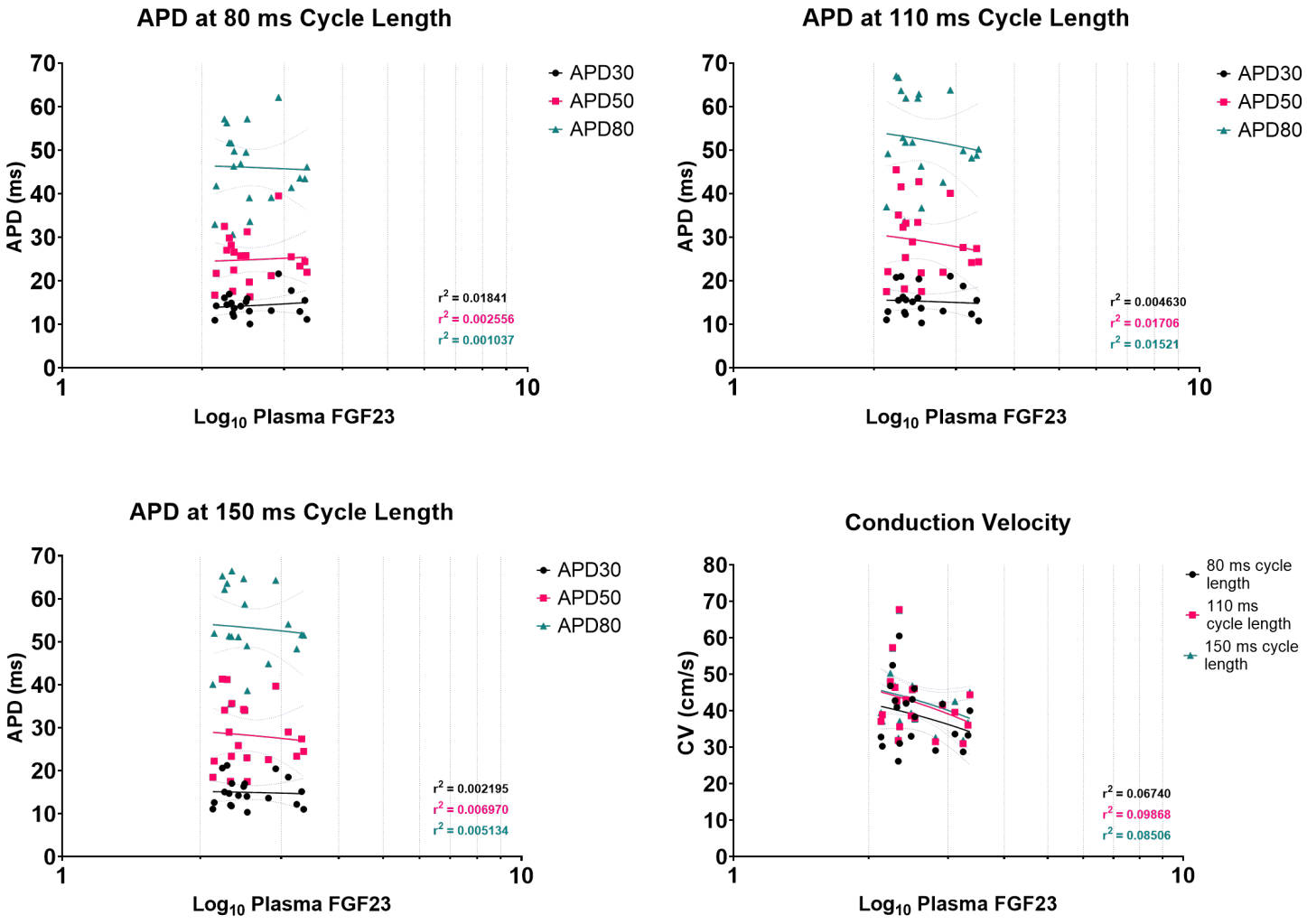
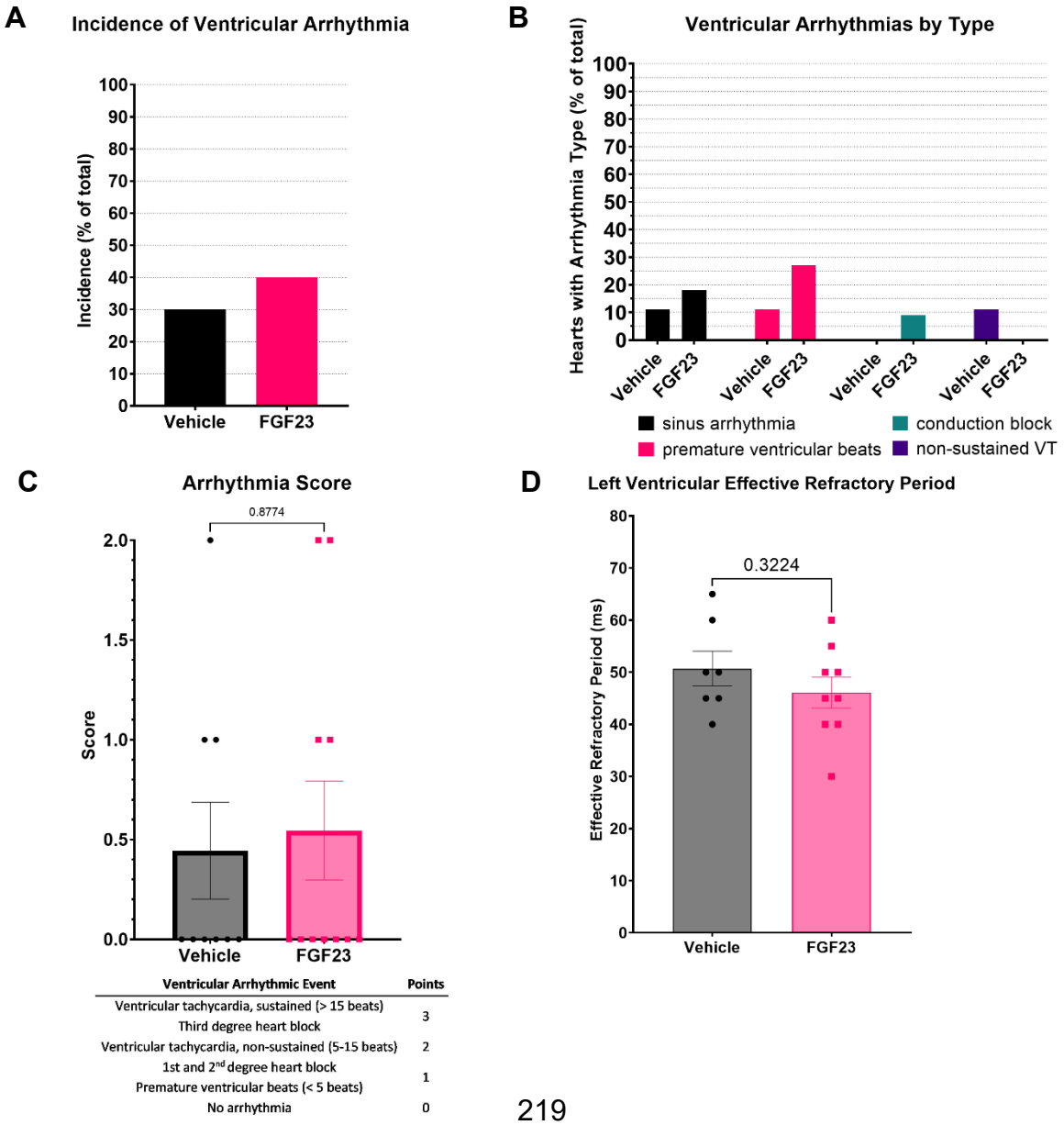


Figure 7-6. Ventricular arrhythmia burden and effective refractory period of *ex vivo* murine hearts in response to chronic systemic FGF23 treatment.

Following 7 daily intraperitoneal of FGF23 or vehicle control phosphate buffered saline, hearts were isolated and Langendorff perfused. Arrhythmia burden **(A-C)** was assessed *ex vivo* during optical mapping. **A** – Incidence of ventricular arrhythmias. **B** – Ventricular arrhythmias by type. **C** – Arrhythmia score presented as median ± interquartile range; Mann-Whitney U test (N = 9 control; N = 11 FGF23). **D** – Left ventricular effective refractory period presented as mean ± S.E.M.; unpaired t-test (N = 7 control; N = 9 FGF23).

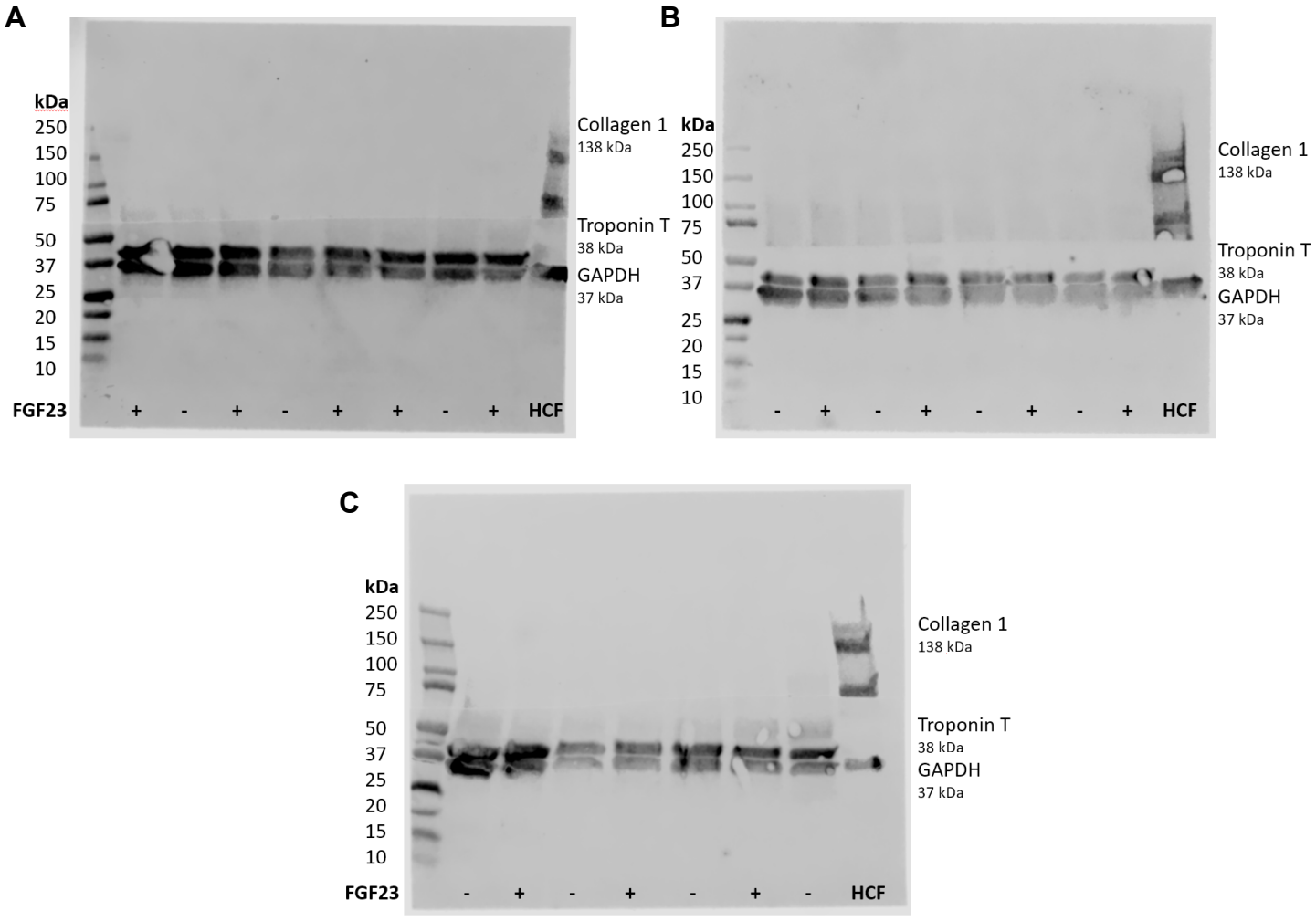


7.3.5. Immunoblotting of cardiac lysates

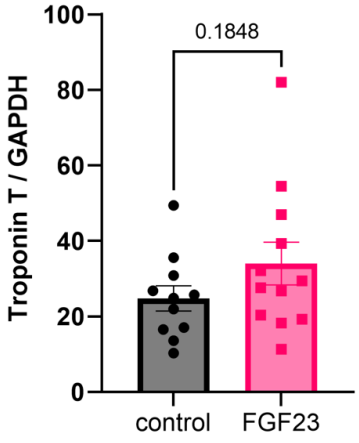
Left ventricular lysates obtained from mice following 7 days treatment with intraperitoneal FGF23 were subjected to western blotting. 50 µg of protein was loaded into each lane, with a human cardiac myofibroblast lysate used as positive control. Neither collagen 1 (**Figure 7-7**), nor collagen 3 (**Figure 7-8**) were present in the left ventricular lysates, irrespective of whether the hearts had been exposed to FGF23. Both collagens were clearly present in the positive control samples. Collagen 1 and 3 may not have been adequately solubilised by the extraction technique and buffer. Alternative methods of assessing collagen 1 and 3 expression and excretion is required, e.g. RT-PCR, histology or hydroxyl-proline assay. Troponin T was used as a loading control and was present in ventricles from both control and FGF23-treated mice with no significant difference between groups ($p = 0.1848$, **Figure 7-7 D**). There was no correlation between Troponin T expression and plasma FGF23 level (**Figure 7-7 E**). Heat shock protein 27 (Hsp27) is a potential biomarker for cardiovascular disease in haemodialysis patients and is inversely associated with cardiovascular mortality and sudden cardiac death in patients requiring haemodialysis [557]. It was not reliably expressed in the ventricular lysates from both treatment groups (**Figure 7-8**).

Figure 7-7. Western blot of collagen 1 and troponin T in murine left ventricular lysates.

Following 7 days of treatment with intraperitoneal FGF23 (N = 12) or vehicle control phosphate buffered saline (N = 11), murine hearts were isolated. Left ventricular tissue lysates (50ug per lane) were subjected to infrared fluorescence immunoblotting. A human cardiac myofibroblast (HCF) lysate was used as control. GAPDH was used as a loading control across all samples. **A-C** – Raw western blots. **D** – Troponin T expression as a ratio to GAPDH. **E** – Correlation between Troponin T expression and log-normal plasma FGF23 concentration. Data presented as mean ± S.E.M.; unpaired t-test. Collagen 1 expression was unquantifiable.



D


0.1848
100
80
60
40
20
0
Troponin T / GAPDH
control
FGF23

E

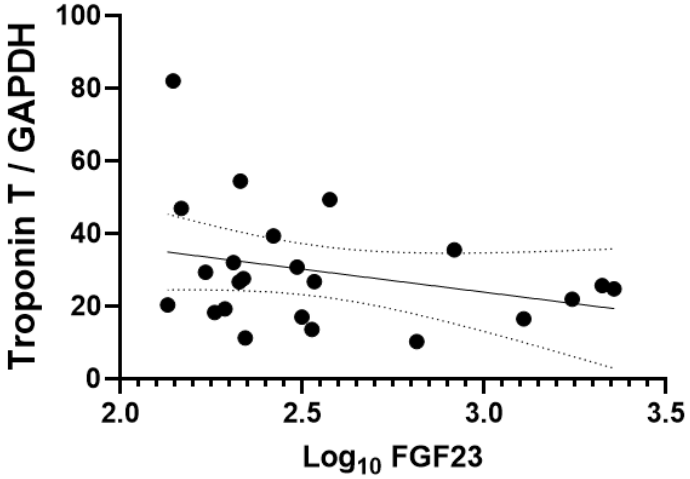
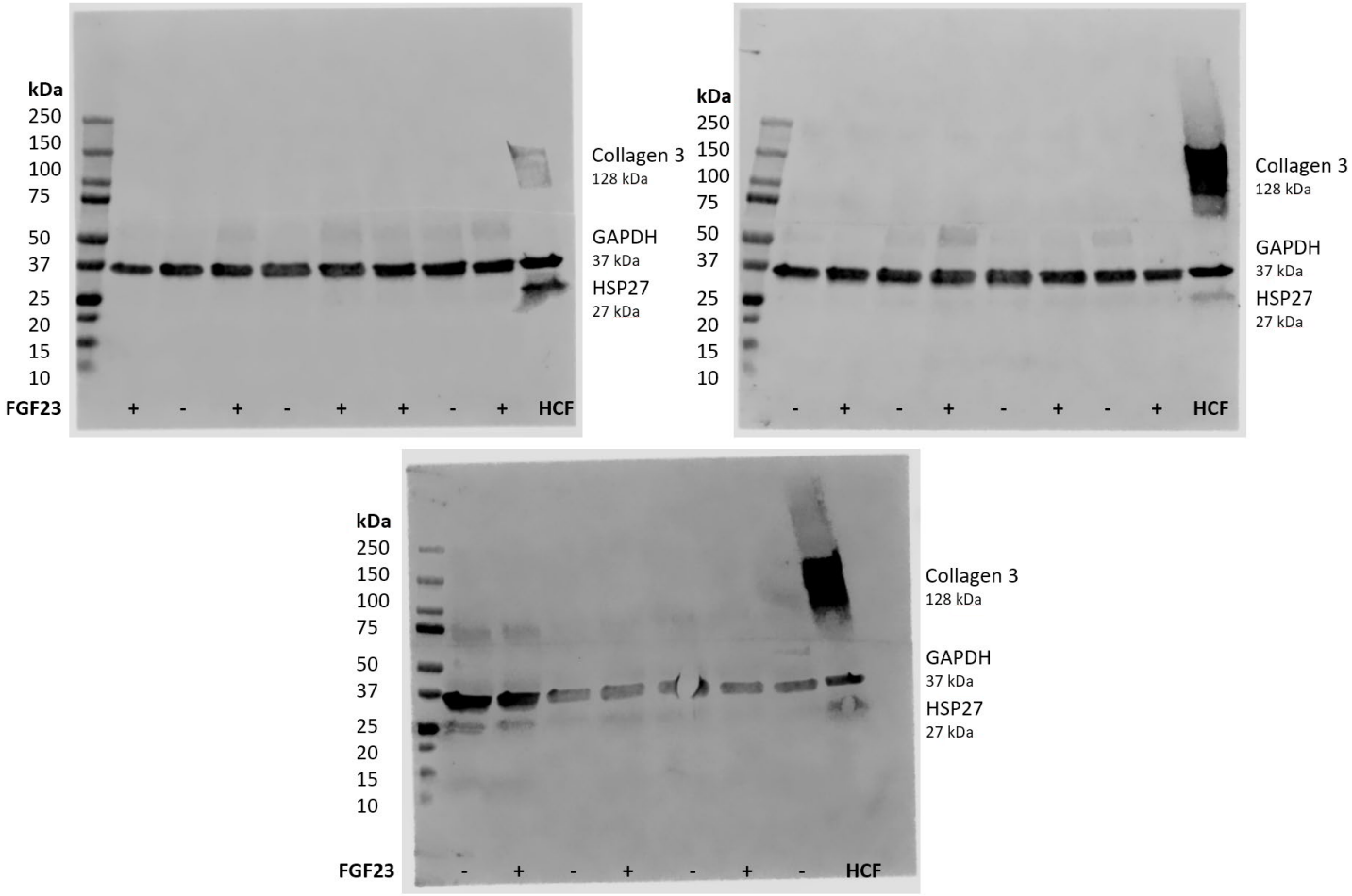

100
80
60
40
20
0
Troponin T / GAPDH
2.0
2.5
3.0
3.5
Log10 FGF23

Figure 7-8. Western blot of collagen 3 and heat shock protein 27 (HSP27) in murine left ventricular lysates.

Following 7 days of treatment with intraperitoneal FGF23 (N = 12) or vehicle control phosphate buffered saline (N = 11), murine hearts were isolated. Left ventricular tissue was subjected to infrared fluorescence immunoblotting . A human cardiac myofibroblast (HCF) lysate was used as control. GAPDH was used as a loading control across all samples. Quantification of band intensity was not performed due to lack of expression of both collagen 3 and HSP27 in the murine ventricular lysates.



7.4. DISCUSSION

In this study, the longer-term, 7-day effects of *in vivo* FGF23 excess on the murine heart morphology and function were investigated. FGF23 did not alter left ventricular action potential characteristics measured by optical mapping. Whilst there is no published data on the longer-term effects of FGF23 on the cardiac action potential, these results contrast with the acute effects on APD (shortening), which have previously been discussed in Chapters 5 and 6 of this thesis. Further evidence of *in vitro* shortening of APD following acute FGF23 treatment was reported by Huang et al. [524], who treated rabbit pulmonary vein cardiomyocytes for 4-6 hours. Although not to the same extent as found in the acute FGF23 experiments reported in Chapters 5 and 6, the hearts from mice which had received 7 days of intraperitoneal FGF23 injections exhibited increased incidence of sinus arrhythmia and extra-systolic beats. There were fewer instances of severe ventricular tachyarrhythmias.

A potential explanation for the milder phenotype observed in the chronic FGF23 experiments is the presence of soluble αKlotho, which was absent in the acute model. The biological relevance of αKlotho in terms of FGF23 signalling has been previous reviewed in Chapter 1.4. and will be briefly summarised here. αKlotho is a key co-receptor which enables efficient binding of FGF23 to FGFR1 [159]. Its expression is significantly reduced in CKD [177]. It was previously thought that its differential expression within the human body determines the tissue specificity of FGF23. For example, the heart and its constituent cells do not express αKlotho [152]. However, recent work by Faul, Grabner and colleagues showed that FGF23 can act in an αKlotho-independent, FGFR4 signalling pathway to cause

pathological hypertrophic changes to the heart [171,172,174]. Furthermore, the addition of recombinant αKlotho to αKlotho-deficient CKD mice attenuated cardiac hypertrophy and fibrosis [213,237,391,395], and prevented FGF23-induced, FGFR-dependent calcium dysfunction in isolated rat cardiomyocytes [257]. It is, therefore, conceivable that absence of soluble and transmembrane αKlotho induces pro-hypertrophic and pro-arrhythmic FGF23 signalling pathways, whilst the presence, or addition of circulating αKlotho in αKlotho-deficient states can rescue this phenotype by re-directing the FGF23 signalling towards more physiological pathways as seen in healthy states (e.g. regulation of mineral bone health).

In the acute model, murine hearts, which do not express αKlotho, were exposed to FGF23, resulting in significant pro-arrhythmic perturbations in action potential and calcium transient characteristics. In comparison, the chronic *in vivo* model was conducted in healthy, young adult mice, which would have had preserved renal function and therefore normal circulating αKlotho, although these were not measured in the present study. The presence of soluble, circulating αKlotho may have been protective. It was not possible to acquire soluble αKlotho in time for the experiments described in this thesis. Future work will investigate the potential of pre-treatment with αKlotho to protect the heart from acute and chronic FGF23 elevations.

There were no changes in cardiac, and specifically, ventricular morphology and function on post-mortem cardiac chamber weights or *in vivo* echocardiography following 7 days of FGF23 intraperitoneal injections. Other groups have previously reported the prohypertrophic effects of FGF23 in preclinical settings.

These include increased cross-sectional myocyte surface area *in vitro* using neonatal rat ventricular myocytes [171,174], neonatal mouse ventricular myocytes [172], HL-1 atrial cardiomyocytes [254]; cardiac hypertrophy *in vivo* by a single direct intramyocardial FGF23 injection into the left ventricular free wall with assessment by cardiac weight, echocardiogram and histology 7-14 days later [171]; and following 5 days of high-dose intravenous FGF23 injections [171]. Increases in hypertrophic gene expression of atrial natriuretic peptide (ANP), BNP, β-myosin heavy chain (MHC) have also been reported following exogenous FGF23 [171,254].

A reason for the discrepancy between the results of this study and those described above is the FGF23 dosing used, rather than the exposure time, which was initially thought to be the case. Prior *in vitro* studies have employed higher FGF23 concentrations – the lowest being 0.9 ng/mL [254], going up to 100 ng/mL [171,172,174] with dose-dependent effects. In the acute FGF23 experiments (Chapters 5 and 6), murine hearts were continuously perfused with 10 ng/mL FGF23 for 30 minutes, resulting in significant pathological findings. In the chronic *in vivo* FGF23 experiments, mice received seven daily intraperitoneal injections of 3.12 µg FGF23 achieving a mean dose of 96 µg/kg (target was > 80 µg/kg) and a median plasma FGF23 level of 514 pg/mL. Faul and colleagues [171] found that the same 80 µg/kg dosing given *intravenously* for 5 days resulted in a higher mean serum FGF23 level of 800 RU/mL in mice. In separate models of FGF23 excess (Klotho-deficient / Klotho-heterozygous mice), they reported mean serum FGF23 levels upwards of 1000 and 5000 RU/mL, which was associated with dose-dependent hypertrophy and increased β-MHC, ANP and BNP mRNA.

Intraperitoneal administration is a widely used means of administering drugs in animal studies, however it is plausible that the drug is administered into the abdominal fat, intestines, other solid organs, or subcutaneous tissues rather than into the intended peritoneal cavity, resulting in lower circulating drug levels. Verkaik and colleagues [525] also employed the intraperitoneal route and, in spite of a higher dose (160 μg/kg/day for 7 days), reported no change in ventricular morphology and molecular markers of hypertrophy (e.g. ANP, α-MHC, β-MHC) in mice. Although the authors did not quantify circulating FGF23 levels, the findings were mirrored by separate experiments in 5/6 nephrectomy mice with mean plasma FGF23 levels of 720 pg/mL, which did not have any evidence of cardiac hypertrophy. Interestingly, cardiomyocytes isolated from both intraperitoneal FGF23 and 5/6 nephrectomy mouse models were found to have disturbed calcium handling, as described in Chapter 6, without affecting contractile function. Whilst assessment of arrhythmia was not included in their experimental design, it raises the possibility for FGF23 to cause electrical remodelling of the heart prior to the development of structural remodelling, hypertrophy, and fibrosis. This may account for the mild increase in incidence of arrhythmias observed in the FGF23-treated mice in this present study.

Taken together, moderate increases in FGF23 over a seven-day period may not be sufficient to induce pathological structural remodelling. However, the increased incidence of cardiac arrhythmias suggests the presence of an underlying disturbance in cardiac ionic handling. A further study utilising higher doses of FGF23 *and* further characterisation of ex vivo ventricular calcium handling dynamics by optical mapping is warranted.

CHAPTER 8. CONCLUSIONS

8.1. THESIS OUTCOMES

The major aim of this thesis was to explore the role of FGF23 in the pathogenesis of CKD-associated cardiomyopathy. On a background of literature linking chronic kidney disease and elevated FGF23 levels to cardiac fibrosis, hypertrophy and electromechanical dysfunction, the aims of this thesis were to examine the potential for reversal of activated human cardiac myofibroblasts to a more quiescent phenotype, and also to determine whether FGF23 plays a direct role in the human cardiac fibroblast activation. In addition, I set out to investigate the effect of acute FGF23 elevations on murine ventricular electrophysiology, and longer-term exposure on ventricular morphology and function.

The main outcomes of this thesis are as follows:

- Chronic activation of primary human ventricular cardiac fibroblasts and hiPSC-derived cardiac fibroblasts led to terminal differentiation into myofibroblasts *in vitro*. Neither culture on softer substrates, mimicking the effects of reducing extracellular matrix stiffness and diastolic dysfunction, nor TGF-β inhibition reversed the myofibroblast phenotype. Myofibroblasts exhibited diminished responses to further activating stimuli from TGF-β and reduced proliferative capacity. Long-term activation of hiPSC-derived cardiac fibroblasts led to an irreversible myofibroblast phenotype characterised by loss of fibrous α-SMA expression. These *in vitro* data suggest that cardiac fibrosis resulting from chronic, terminal activation and differentiation of myofibroblasts fibroblasts under diseased conditions

such as CKD may not be reversible through de-activation of fibroblasts. Moreover, antifibrotic agents aimed at reversal of fibrotic tissue may not be sufficient in rescuing the myofibroblast phenotype by restoration of extracellular matrix compliance alone (Chapter 3).

- Primary human ventricular cardiac fibroblasts expressed all four fibroblast growth factor receptors, with FGFR1 being most highly expressed. FGF23/FGFR co-receptor αKlotho was not expressed. Culture of fibroblasts across a range of soft and stiff culture plates did not affect FGFR expression or cardiac fibroblast activation state, and neither did treatment with FGF23 at concentrations equivalent to but not exceeding circulating levels found in patients with kidney failure with replacement therapy. Experiments utilising hiPSC-derived cardiac fibroblasts recapitulated the lack of effect of FGF23 on FGFR expression and cardiac fibroblast activation. These experiments, although conducted in the absence of αKlotho, indicate that FGF23 at levels seen in CKD may not play a direct role in the activation of human cardiac fibroblasts *in vitro* (Chapter 4).
- Acute exposure of *ex vivo* Langendorff-perfused mouse hearts to high concentration FGF23 shortened left ventricle action potential duration and calcium transient duration, reducing the wavelength of the cardiac impulse, and increasing the incidence of premature ventricular beats and re-entrant arrhythmias. This was consistent across two separate optical mapping experiments utilising different membrane voltage-sensitive fluorescent dyes, with the second experiment conducted as part of a dual

voltage-calcium dye loaded preparation. These findings may explain in part the increased arrhythmia burden observed in patients with advanced kidney disease (Chapter 5 and 6).

- Moderate levels of circulating FGF23 excess for seven days did not cause *in vivo* alterations in murine cardiac morphology or mechanical function. *Ex vivo* left ventricular action potential characteristics were unchanged, however, an increase in ventricular arrhythmias was observed compared to vehicle control mice, raising the possibility of underlying cardiac ionic perturbations (e.g. calcium, potassium or sodium), which require further study (Chapter 7).

8.2. GENERAL LIMITATIONS

8.2.1. Cellular studies

8.2.1.1. Limitations of single cell-type studies and cellular isolation

Whilst two human fibroblast cell lines were specifically chosen, going beyond previously published studies using murine cells, there are fundamental limitations to single cell-type *in vitro* studies. In the heart, fibroblasts relate to other cell types such cardiomyocytes through a variety of bioelectromechanical mechanisms including, but not limited to, paracrine signalling (e.g. TGF-β, angiotensin II); electrical and ionic coupling via membrane nanotubes and gap junctions; and extracellular matrix interactions [78,558]. These are lacking in the current study. Primary human cardiac fibroblasts are also subject to the inevitable mechanical, chemical, and hypoxic stress from trituration, enzymatic digestion of the extracellular matrix and tissue ischaemia during the cell isolation procedure. The

exact cell isolation protocols were not available as the cells were procured from a commercial source.

8.2.1.2. Mechano-electrically static culture conditions

The impact of extracellular matrix stiffness on fibroblast phenotype and activation status was mimicked using polyacrylamide hydrogel culture substrates with varying tensile strength. However, cells grown in a 2D monolayer under static culture conditions do not experience the dynamic and pulsatile mechanoelectric forces *in vivo*. For example, cardiac tissue has an inherent, passive stiffness or tension, which is defined by contributions from the extracellular matrix such as collagen, cytoskeletal, and sarcomeric structures such as microtubules and titin [559]. During diastole, cardiac muscle undergoes relaxation and expansion of cardiac chambers to accommodate incoming blood. The rate of relaxation depends on factors including passive tension of the muscle and cardiomyocyte cytosolic calcium removal and re-uptake. As preload increases, stretching of the cardiac muscle wall occurs, increasing sarcomere length and passive tension further, generating more force (active tension) during systole as cardiac muscle contracts to expel blood into the circulatory system [560]. Three-dimensional cardiac models, such as hiPSC-derived multicellular beating engineered heart tissues and organoids, address some of these limitations by more closely resembling the structure, function and cellular maturity of human myocardium [561,562].

8.2.1.3. αKlotho

As already discussed in the previous chapters, the absence of circulating αKlotho at healthy, physiological, or reduced levels as seen in CKD limits the translatability of the *in vitro*, and *ex vivo* studies.

8.2.1.4. Western blots

Due to time constraints and challenges with antibody optimisation, fibroblast growth factor receptor protein expression was not quantified. Furthermore, collagen 1 and collagen 3 protein expression was measured in fibroblast lysates. As these proteins are excreted, future studies should include quantification of extracellular matrix proteins within the cell culture media, including other abundant extracellular matrix proteins e.g. fibronectin.

8.2.2. Murine studies

8.2.2.1. Murine versus human cardiac physiology

The data presented in Chapters 5, 6 and 7 were obtained using a mouse model. As already discussed in Chapter 5.2.2, there are fundamental differences between murine cardiac electrophysiology and that of in the human heart with distinct ionic currents and action potential morphology. In addition, the resting mouse heart beat rate is seven to 10 times faster than in humans, again, impacting on ECG morphology [563]. Therefore, the findings should be interpreted with caution as they may not directly translate into humans. Whilst larger mammals such as guinea pigs and rabbits more closely resemble human physiology, mice were selected due to the desire to align closely with the 3Rs

principles – replacement, reduction, and refinement, whilst still sharing physiological and genetic similarities with humans.

8.2.2.2. Cardiac isolation and tissue ischaemia

Animal procedures, specifically cardiac isolation under terminal anaesthesia, cannulation of the murine hearts and Langendorff perfusion, were conducted only after extensive training and satisfactory sign-off from expert trainers and operators in animal handling and procedures, and within the confines of the Home Office personal and project license. Each mouse heart was exposed to cold ischaemic time – typically 2 to 4 minutes, defined from the moment of aortic transection and cardiac extraction to aortic cannulation and retrograde Langendorff perfusion with oxygenated, body temperature KHB. In addition to carrying out the isolation as quickly as possible, mice were administered an intraperitoneal injection of heparin prior to surgery; hearts were immediately placed into ice-cold, heparinised KHB and cannulated *ex vivo* before rapidly transferring onto the Langendorff apparatus to limit the ischaemia-reperfusion injury and intravascular thrombosis. Despite this, some tissue ischaemia is unavoidable, in part due to crystalloid solutions being inferior carriers of oxygen compared to blood. This may account for the presence of minor arrhythmic phenomena in the hearts from healthy, control mice.

8.2.2.3. Duration of exposure and circulating concentration of FGF23 in the chronic murine model

As discussed in Chapter 7, the circulating FGF23 concentration achieved by daily intraperitoneal injections at a dose of ~90 µg/kg was moderate, roughly equivalent to levels seen in humans with stage 4 CKD [564]. Prior studies, including

data presented within this thesis, have demonstrated clear physiological effects using higher concentrations of FGF23 comparable to, or exceeding, levels observed in patients with stage 5 CKD or those requiring dialysis. Given the relatively short exposure period in this study (7 days), compared to the natural history and definition of CKD (> 3 months), a longer study with higher circulating FGF23 concentrations is needed to replicate the long-term cardiac sequalae of FGF23 excess in CKD.

8.2.3. Optical mapping limitations

8.2.3.1. Blebbistatin

The mechanical uncoupler blebbistatin was used across all optical mapping experiments in this thesis. It prevents cardiac muscle contraction through inhibition of myosin II activity and minimises motion artifacts during optical mapping. However, it has been reported to cause action potential changes such as APD prolongation and reduced ventricular fibrillation inducibility in optical mapping experiments when compared to contracting hearts without blebbistatin [565,566]. It is poorly soluble in water at high concentrations and prone to precipitation, which can deposit in small arterioles and capillaries causing tissue ischaemia. Blue/ultraviolet light sensitivity results deactivation of blebbistatin, generation of reactive oxygen species and cellular damage [567]. In order to overcome these limitations, several optimisations were made to the optical mapping setup: the minimum amount of blebbistatin to achieve excitation-contraction uncoupling was utilised; a KHB inflow 0.22 μm pre-filter was used to capture any precipitation or undissolved solids; optical mapping was conducted in a dark room; and a 530±20 nm bandpass excitation LED filter minimised

blue/ultraviolet light-induced blebbistatin inactivation and free radical production [568].

8.2.3.2. Limited depth of penetration

The spectral characteristics of the fluorescent dyes used requires excitation by green light. These wavelengths are absorbed by blood and tissue, which limits the optical mapping to the epicardial layers [527]. As previously discussed, there is inherent spatial heterogeneity in cardiac cellular composition [569] and electrophysiology [570,571] across different areas of the heart and in different layers of the ventricular wall, predisposing to arrhythmogenesis in diseased states [571-573]. It is not possible to extrapolate the electrophysiological changes found in this thesis to the myocardial and endocardial layers.

8.3. FUTURE WORK

8.3.1. In vitro experiments

Prior studies have utilised hearts destined for transplantation, but discarded due to patient-donor mismatch, or other factors. Experiments utilising freshly isolated human cardiac fibroblasts from such hearts would provide a better starting point for experimentation. Plasticity of the myofibroblast phenotype can be examined at various timepoints after isolation as a result of pro-fibrotic stimuli. Co-culture with other resident cells of the heart, whether in direct contact with each other, or separated by a permeable membrane in the same media, will yield more physiologically relevant data and allow better understanding of the crosstalk between cell types. Although technically demanding, the previously discussed engineered heart tissues, in combination with electrical and mechanical stimuli,

would provide a better platform for experimentation, although the general reliance on hiPSC-derived cells calls into question their structural and functional maturity [574].

Key to future experiments is the addition of αKlotho to the cell culture media as a pre-treatment at physiologically relevant concentrations. In αKlotho-deficient disease models such as CKD, the potential of αKlotho as a therapeutic agent can be investigated. Other potential therapeutic agents such as calcineurin and FGFR4 antagonists may inhibit known FGF23-associated pathological signalling pathways.

8.3.2. Optical mapping experiments and analysis

The changes to action potential characteristics and increased incidence of arrhythmias call for further characterisation of mechanisms underpinning these changes.

8.3.2.1. Phase mapping

Shortening of APD facilitates wavelength for re-entry. A recent publication by Li et al. [575] provided a standardised framework for quantifying fibrillation dynamics using phase mapping. Using the suggested analysis framework, optical mapping data can be used to identify spiral waves (also known as rotational drivers) rotating around a phase singularity. Localisation, quantification, and assessment of the stability of such phase singularities may provide insights into the underlying fibrillatory mechanism.

8.3.2.2. Further characterisation of cardiac ionic handling

To further understand the pathophysiology of CaTD shortening observed following FGF23 treatment, expression, and phosphorylation status of key cardiomyocyte calcium handling proteins LTCC, CaMKII, RyR2, NCX, SERCA2a, PLB can be assessed by western blotting.

Ratiometric calcium-sensitive fluorescent dyes Indo-1 and Fura-2 have been used to image $[Ca^{2+}]_i$ in cardiac tissue and minimise the effects of unequal dye loading and photobleaching . However, there are several potential issues, in part due to requiring excitation wavelengths in the ultraviolet spectrum. Penetration depth of the excitation light is reduced due to increased absorption of excitation photons. Blebbistatin may be inactivated by the ultraviolet illumination resulting in failure to suppress contractile motion during longer recording, although this study showed that epicardial ultraviolet illumination did not restore contractions in rat hearts perfused with 10 μM blebbistatin [576]. In addition, Fura 2 has a high affinity (low dissociation constant K_d) for Ca^{2+}, which may interfere with and prolong CaTD measurements [577].

The effects of FGF23 on the handling of other ions within the cardiomyocyte is relatively unknown. To this date, there have been no published reports of optical mapping of cardiac sodium and potassium. Ratiometric dyes SBFI and PBFI have been used *in vitro*, but as they have excitation wavelengths in the ultraviolet spectrum, compatibility with blebbistatin may be problematic, in addition to the already discussed poor tissue penetration. Single cell patch clamp remains the gold-standard for assessing cellular sodium and potassium handling.

Finally, the use of red-shifted, near-infrared voltage-sensitive dyes such as Di-4-ANBDQPQ or Di-4-ANBDQBS allow deeper penetration depth and blood-perfused *in vivo* optical mapping due to the light being less strongly absorbed by blood and tissue [578].

8.3.2.3. High circulating concentration, chronic FGF23 excess model

In view of the results and limitations discussed, a longer-term, higher-dose FGF23 murine model is warranted. There are two specific methods by which this can be achieved.

Firstly, high circulating FGF23 levels can be achieved through intravenous tail vein administration, bypassing the need for absorption through the peritoneal membrane, and reducing the risk of injection into unintended tissues [171]. The use of a tail vein catheter may allow longer-term studies, although these may be complicated by infections, vessel trauma and catheter displacement. Alternatively, implantable osmotic minipumps can deliver a continuous infusion of FGF23 reducing handling stress and repeated injections/venepuncture. However, the stability and therefore biological activity of recombinant FGF23 after extended periods at 37 °C are unknown. Daily monitoring of murine urinary phosphate excretion in metabolic cages may be a simple and non-invasive method of assessing *in vivo* FGF23 activity.

Secondly, prior studies have utilised murine models of CKD such as 5/6 nephrectomy [383,525], hypertension-induced e.g. spontaneously hypertensive rats [579], DOCA salt/AngII [580,581], Col4a3-knockout [582,583] and adenine-induced nephropathy [401,584,585]. The 5/6 nephrectomy approach, although widely used, is

not favoured due to postoperative complications and animal mortality. Hypertensive CKD models recapitulate the heart failure with preserved ejection phenotype and are associated with proteinuria. However, dissecting the effect of the hypertension itself from other drivers of the cardiovascular disease is challenging. Col4a3-knockouts produce a severe CKD phenotype characterised by LV systolic dysfunction, increased transcription of hypertrophic genes and high levels of circulating FGF23 (intact FGF23 5400 to 7799 pg/mL) [582,583]. Dietary adenine induces renal tubulointerstitial fibrosis, cardiac remodelling and vascular calcification [586]. Recent studies have also reported high levels of circulating FGF23 (20,000 to 37,000 pg/mL) [401,584]. The use of the adenine-induced nephropathy model in a FGFR4-knockout mouse may dissect the role of FGF23 in the pathogenesis of cardiovascular disease without affecting its regulation of phosphate homeostasis. Long-term administration of a FGFR4 blocker or recombinant αKlotho supplementation may be viable, but costly.

In summary, future work will likely combine the complexity of a multicellular engineered heart tissue preparation or a carefully chosen CKD animal model, with state-of-the-art experimental methods such as optical mapping to further interrogate the role of FGF23 in the pathogenesis of CKD-associated cardiomyopathy. These models will also allow the application of existing, experimental and novel molecular inhibitors in both prevention and treatment of CKD-associated cardiomyopathy.

References

1. Law, J.P., Pickup, L., Pavlovic, D., Townend, J.N. & Ferro, C.J. Hypertension and cardiomyopathy associated with chronic kidney disease: epidemiology, pathogenesis and treatment considerations. *J Hum Hypertens* 37, 1-19 (2023).
2. Law, J.P.*, et al.* Clinical Potential of Targeting Fibroblast Growth Factor-23 and alphaKlotho in the Treatment of Uremic Cardiomyopathy. *J Am Heart Assoc* 9, e016041 (2020).
3. National Kidney, F. K/DOQI clinical practice guidelines for chronic kidney disease: evaluation, classification, and stratification. *Am J Kidney Dis* 39, S1-266 (2002).
4. Levey, A.S.*, et al.* The definition, classification, and prognosis of chronic kidney disease: a KDIGO Controversies Conference report. *Kidney international* 80, 17-28 (2011).
5. Improving Global Outcomes CKD Work Group. KDIGO 2012 clinical practice guideline for the evaluation and management of chronic kidney disease. *Kidney Int Suppl* 3, 1-150 (2013).
6. Stevens, L.A., Coresh, J., Greene, T. & Levey, A.S. Assessing kidney function--measured and estimated glomerular filtration rate. *N Engl J Med* 354, 2473-2483 (2006).
7. Levey, A.S.*, et al.* A more accurate method to estimate glomerular filtration rate from serum creatinine: a new prediction equation. Modification of Diet in Renal Disease Study Group. *Ann Intern Med* 130, 461-470 (1999).
8. Myers, G.L.*, et al.* Recommendations for improving serum creatinine measurement: a report from the Laboratory Working Group of the National Kidney Disease Education Program. *Clin Chem* 52, 5-18 (2006).
9. Levey, A.S.*, et al.* A new equation to estimate glomerular filtration rate. *Ann Intern Med* 150, 604-612 (2009).
10. Matsushita, K.*, et al.* Comparison of risk prediction using the CKD-EPI equation and the MDRD study equation for estimated glomerular filtration

rate. *JAMA : the journal of the American Medical Association* 307, 1941-1951 (2012).

11. Drueke, T., Le Pailleur, C., Zingraff, J. & Jungers, P. Uremic cardiomyopathy and pericarditis. *Adv Nephrol Necker Hosp* 9, 33-70 (1980).
12. Hung, J., Harris, P.J., Uren, R.F., Tiller, D.J. & Kelly, D.T. Uremic cardiomyopathy--effect of hemodialysis on left ventricular function in end-stage renal failure. *N Engl J Med* 302, 547-551 (1980).
13. Mall, G., Huther, W., Schneider, J., Lundin, P. & Ritz, E. Diffuse intermyocardiocytic fibrosis in uraemic patients. *Nephrol Dial Transplant* 5, 39-44 (1990).
14. Aoki, J.*, et al.* Clinical and pathologic characteristics of dilated cardiomyopathy in hemodialysis patients. *Kidney international* 67, 333-340 (2005).
15. Hayer, M.K.*, et al.* Diffuse Myocardial Interstitial Fibrosis and Dysfunction in Early Chronic Kidney Disease. *Am J Cardiol* 121, 656-660 (2018).
16. Rutherford, E.*, et al.* Defining myocardial tissue abnormalities in end-stage renal failure with cardiac magnetic resonance imaging using native T1 mapping. *Kidney international* 90, 845-852 (2016).
17. Graham-Brown, M.P.*, et al.* Novel cardiac nuclear magnetic resonance method for noninvasive assessment of myocardial fibrosis in hemodialysis patients. *Kidney international* 90, 835-844 (2016).
18. Edwards, N.C.*, et al.* Diffuse interstitial fibrosis and myocardial dysfunction in early chronic kidney disease. *Am J Cardiol* 115, 1311-1317 (2015).
19. Mark, P.B.*, et al.* Redefinition of uremic cardiomyopathy by contrast-enhanced cardiac magnetic resonance imaging. *Kidney international* 69, 1839-1845 (2006).
20. Chen, L.*, et al.* Sodium Fluoride (NaF) Induces Inflammatory Responses Via Activating MAPKs/NF-kappaB Signaling Pathway and Reducing Anti-inflammatory Cytokine Expression in the Mouse Liver. *Biol Trace Elem Res* 189, 157-171 (2019).

21. Foley, R.N.*, et al.* Clinical and echocardiographic disease in patients starting end-stage renal disease therapy. *Kidney international* 47, 186-192 (1995).
22. Parfrey, P.S.*, et al.* The clinical course of left ventricular hypertrophy in dialysis patients. *Nephron* 55, 114-120 (1990).
23. Edwards, N.C.*, et al.* Defining the natural history of uremic cardiomyopathy in chronic kidney disease: the role of cardiovascular magnetic resonance. *JACC. Cardiovascular imaging* 7, 703-714 (2014).
24. Wang, X. & Shapiro, J.I. Evolving concepts in the pathogenesis of uraemic cardiomyopathy. *Nat Rev Nephrol* 15, 159-175 (2019).
25. Drueke, T., Le Pailleur, C., Sigal-Saglier, M. & Zingraff, J. Angiocardiographic and haemodynamic studies in chronic haemodialysis patients with cardiomegaly. *Proc Eur Dial Transplant Assoc* 16, 244-251 (1979).
26. Drueke, T.*, et al.* Congestive cardiomyopathy in uraemic patients on long term haemodialysis. *Br Med J* 1, 350-353 (1977).
27. London, G.M., Marchais, S.J., Guerin, A.P. & Metivier, F. Contributive factors to cardiovascular hypertrophy in renal failure. *Am J Hypertens* 2, 261S-263S (1989).
28. Go, A.S., Chertow, G.M., Fan, D., McCulloch, C.E. & Hsu, C.Y. Chronic kidney disease and the risks of death, cardiovascular events, and hospitalization. *N Engl J Med* 351, 1296-1305 (2004).
29. Bright, R. Reports of medical cases, selected with a view of illustrating the symptoms and cure of diseases by a reference to morbid anatomy. (London, 1927).
30. Wilks, S. Guy's Hospital Report. Vol. 11 (London, 1853).
31. Traube, L. Ueber den Zusammenhang von Herz-und Nieren-krankheiten. (Berlin, 1956).
32. Cameron, J.S. & Hicks, J. High blood pressure and the kidney: the forgotten contribution of William Senhouse Kirkes. *Kidney international* 57, 724-734 (2000).

33. Park, M.*, et al.* Associations between kidney function and subclinical cardiac abnormalities in CKD. *J Am Soc Nephrol* 23, 1725-1734 (2012).
34. Levin, A., Singer, J., Thompson, C.R., Ross, H. & Lewis, M. Prevalent left ventricular hypertrophy in the predialysis population: identifying opportunities for intervention. *Am J Kidney Dis* 27, 347-354 (1996).
35. Paoletti, E., Bellino, D., Cassottana, P., Rolla, D. & Cannella, G. Left ventricular hypertrophy in nondiabetic predialysis CKD. *Am J Kidney Dis* 46, 320-327 (2005).
36. London, G.M.*, et al.* Alterations of left ventricular hypertrophy in and survival of patients receiving hemodialysis: follow-up of an interventional study. *J Am Soc Nephrol* 12, 2759-2767 (2001).
37. Parfrey, P.S.*, et al.* Outcome and risk factors for left ventricular disorders in chronic uraemia. *Nephrol Dial Transplant* 11, 1277-1285 (1996).
38. Levy, D., Garrison, R.J., Savage, D.D., Kannel, W.B. & Castelli, W.P. Prognostic implications of echocardiographically determined left ventricular mass in the Framingham Heart Study. *N Engl J Med* 322, 1561-1566 (1990).
39. Shlipak, M.G.*, et al.* Cardiovascular mortality risk in chronic kidney disease: comparison of traditional and novel risk factors. *JAMA : the journal of the American Medical Association* 293, 1737-1745 (2005).
40. Haider, A.W., Larson, M.G., Benjamin, E.J. & Levy, D. Increased left ventricular mass and hypertrophy are associated with increased risk for sudden death. *J Am Coll Cardiol* 32, 1454-1459 (1998).
41. Verdecchia, P.*, et al.* Atrial fibrillation in hypertension: predictors and outcome. *Hypertension* 41, 218-223 (2003).
42. Erkuner, O.*, et al.* Effect of Systemic Hypertension With Versus Without Left Ventricular Hypertrophy on the Progression of Atrial Fibrillation (from the Euro Heart Survey). *Am J Cardiol* 122, 578-583 (2018).
43. Zoccali, C.*, et al.* Left ventricular mass monitoring in the follow-up of dialysis patients: prognostic value of left ventricular hypertrophy progression. *Kidney international* 65, 1492-1498 (2004).

44. Shenasa, M., Shenasa, H. & El-Sherif, N. Left ventricular hypertrophy and arrhythmogenesis. *Card Electrophysiol Clin* 7, 207-220 (2015).
45. Chatterjee, S.*, et al.* Meta-analysis of left ventricular hypertrophy and sustained arrhythmias. *Am J Cardiol* 114, 1049-1052 (2014).
46. Hennersdorf, M.G., Schueller, P.O., Steiner, S. & Strauer, B.E. Prevalence of paroxysmal atrial fibrillation depending on the regression of left ventricular hypertrophy in arterial hypertension. *Hypertens Res* 30, 535-540 (2007).
47. Schillaci, G.*, et al.* Continuous relation between left ventricular mass and cardiovascular risk in essential hypertension. *Hypertension* 35, 580-586 (2000).
48. Devereux, R.B.*, et al.* Prognostic significance of left ventricular mass change during treatment of hypertension. *JAMA : the journal of the American Medical Association* 292, 2350-2356 (2004).
49. Simpson, H.J.*, et al.* Left ventricular hypertrophy: reduction of blood pressure already in the normal range further regresses left ventricular mass. *Heart* 96, 148-152 (2010).
50. Hammond, I.W.*, et al.* The prevalence and correlates of echocardiographic left ventricular hypertrophy among employed patients with uncomplicated hypertension. *J Am Coll Cardiol* 7, 639-650 (1986).
51. Wolf, W.C., Yoshida, H., Agata, J., Chao, L. & Chao, J. Human tissue kallikrein gene delivery attenuates hypertension, renal injury, and cardiac remodeling in chronic renal failure. *Kidney international* 58, 730-739 (2000).
52. McMahon, A.C., Greenwald, S.E., Dodd, S.M., Hurst, M.J. & Raine, A.E. Prolonged calcium transients and myocardial remodelling in early experimental uraemia. *Nephrol Dial Transplant* 17, 759-764 (2002).
53. Suzuki, H., Nakamoto, H., Okada, H., Sugahara, S. & Kanno, Y. A selective angiotensin receptor antagonist, Valsartan, produced regression of left ventricular hypertrophy associated with a reduction of arterial stiffness. *Adv Perit Dial* 19, 59-66 (2003).

54. Tai, D.J., *et al.* Cardiovascular effects of angiotensin converting enzyme inhibition or angiotensin receptor blockade in hemodialysis: a meta-analysis. *Clin J Am Soc Nephrol* 5, 623-630 (2010).
55. Hammer, F., *et al.* A randomized controlled trial of the effect of spironolactone on left ventricular mass in hemodialysis patients. *Kidney international* 95, 983-991 (2019).
56. Zile, M.R., Baicu, C.F. & Gaasch, W.H. Diastolic heart failure--abnormalities in active relaxation and passive stiffness of the left ventricle. *N Engl J Med* 350, 1953-1959 (2004).
57. Otsuka, T., Suzuki, M., Yoshikawa, H. & Sugi, K. Left ventricular diastolic dysfunction in the early stage of chronic kidney disease. *J Cardiol* 54, 199-204 (2009).
58. de Bie, M.K., *et al.* Left ventricular diastolic dysfunction in dialysis patients assessed by novel speckle tracking strain rate analysis: prevalence and determinants. *Int J Nephrol* 2012, 963504 (2012).
59. Farshid, A., Pathak, R., Shadbolt, B., Arnolda, L. & Talaulikar, G. Diastolic function is a strong predictor of mortality in patients with chronic kidney disease. *BMC Nephrol* 14, 280 (2013).
60. Pabst, S., *et al.* Pulmonary hypertension in patients with chronic kidney disease on dialysis and without dialysis: results of the PEPPER-study. *PLoS One* 7, e35310 (2012).
61. Moreo, A., *et al.* Influence of myocardial fibrosis on left ventricular diastolic function: noninvasive assessment by cardiac magnetic resonance and echo. *Circ Cardiovasc Imaging* 2, 437-443 (2009).
62. Wanner, C., Amann, K. & Shoji, T. The heart and vascular system in dialysis. *Lancet* 388, 276-284 (2016).
63. Pecoits-Filho, R., Bucharles, S. & Barberato, S.H. Diastolic heart failure in dialysis patients: mechanisms, diagnostic approach, and treatment. *Seminars in dialysis* 25, 35-41 (2012).
64. Nagueh, S.F., *et al.* Recommendations for the Evaluation of Left Ventricular Diastolic Function by Echocardiography: An Update from the American Society of Echocardiography and the European Association of

Cardiovascular Imaging. *Eur Heart J Cardiovasc Imaging* 17, 1321-1360 (2016).

65. McDonagh, T.A.*, et al.* 2021 ESC Guidelines for the diagnosis and treatment of acute and chronic heart failure. *Eur Heart J* 42, 3599-3726 (2021).
66. Rakhit, D.J.*, et al.* Prognostic role of subclinical left ventricular abnormalities and impact of transplantation in chronic kidney disease. *American heart journal* 153, 656-664 (2007).
67. Edwards, N.C., Ferro, C.J., Townend, J.N. & Steeds, R.P. Aortic distensibility and arterial-ventricular coupling in early chronic kidney disease: a pattern resembling heart failure with preserved ejection fraction. *Heart* 94, 1038-1043 (2008).
68. Hensen, L.C.R.*, et al.* Prevalence of left ventricular systolic dysfunction in pre-dialysis and dialysis patients with preserved left ventricular ejection fraction. *Eur J Heart Fail* 20, 560-568 (2018).
69. Stack, A.G. & Bloembergen, W.E. A cross-sectional study of the prevalence and clinical correlates of congestive heart failure among incident US dialysis patients. *Am J Kidney Dis* 38, 992-1000 (2001).
70. Collins, A.J. Impact of congestive heart failure and other cardiac diseases on patient outcomes. *Kidney Int Suppl*, S3-7 (2002).
71. Jassal, S.V., Trpeski, L., Zhu, N., Fenton, S. & Hemmelgarn, B. Changes in survival among elderly patients initiating dialysis from 1990 to 1999. *CMAJ* 177, 1033-1038 (2007).
72. Sood, M.M., Pauly, R.P., Rigatto, C. & Komenda, P. Left ventricular dysfunction in the haemodialysis population. *NDT Plus* 1, 199-205 (2008).
73. Drazner, M.H.*, et al.* Increased left ventricular mass is a risk factor for the development of a depressed left ventricular ejection fraction within five years: the Cardiovascular Health Study. *J Am Coll Cardiol* 43, 2207-2215 (2004).
74. Milani, R.V., Drazner, M.H., Lavie, C.J., Morin, D.P. & Ventura, H.O. Progression from concentric left ventricular hypertrophy and normal

ejection fraction to left ventricular dysfunction. *Am J Cardiol* 108, 992-996 (2011).

75. Krishnamoorthy, A.*, et al.* Progression from normal to reduced left ventricular ejection fraction in patients with concentric left ventricular hypertrophy after long-term follow-up. *Am J Cardiol* 108, 997-1001 (2011).
76. Yancy, C.W.*, et al.* 2013 ACCF/AHA guideline for the management of heart failure: a report of the American College of Cardiology Foundation/American Heart Association Task Force on Practice Guidelines. *J Am Coll Cardiol* 62, e147-239 (2013).
77. Zannad, F. & Rossignol, P. Cardiorenal Syndrome Revisited. *Circulation* 138, 929-944 (2018).
78. Hall, C., Gehmlich, K., Denning, C. & Pavlovic, D. Complex Relationship Between Cardiac Fibroblasts and Cardiomyocytes in Health and Disease. *J Am Heart Assoc* 10, e019338 (2021).
79. Pickup, L.C., Law, J.P., Townend, J.N. & Ferro, C.J. Sudden cardiac death in chronic renal disease: aetiology and risk reduction strategies. *Nephrol Dial Transplant* 36, 1386-1388 (2021).
80. Brown, P.F., Miller, C., Di Marco, A. & Schmitt, M. Towards cardiac MRI based risk stratification in idiopathic dilated cardiomyopathy. *Heart* 105, 270-275 (2019).
81. Amann, K., Breitbach, M., Ritz, E. & Mall, G. Myocyte/capillary mismatch in the heart of uremic patients. *J Am Soc Nephrol* 9, 1018-1022 (1998).
82. Cecchi, F.*, et al.* Coronary microvascular dysfunction and prognosis in hypertrophic cardiomyopathy. *N Engl J Med* 349, 1027-1035 (2003).
83. Nelson, M.D., Wei, J. & Bairey Merz, C.N. Coronary microvascular dysfunction and heart failure with preserved ejection fraction as female-pattern cardiovascular disease: the chicken or the egg? *Eur Heart J* 39, 850-852 (2018).
84. Radhakrishnan, A.*, et al.* Coronary microvascular dysfunction: a key step in the development of uraemic cardiomyopathy? *Heart* 105, 1302-1309 (2019).

85. Murthy, V.L.*, et al.* Coronary vascular dysfunction and prognosis in patients with chronic kidney disease. *JACC. Cardiovascular imaging* 5, 1025-1034 (2012).
86. Shah, N.R.*, et al.* Prognostic Value of Coronary Flow Reserve in Patients with Dialysis-Dependent ESRD. *J Am Soc Nephrol* 27, 1823-1829 (2016).
87. Cooper, L.T.*, et al.* The role of endomyocardial biopsy in the management of cardiovascular disease: a scientific statement from the American Heart Association, the American College of Cardiology, and the European Society of Cardiology. *Circulation* 116, 2216-2233 (2007).
88. Becker, A.E., Heijmans, C.D. & Essed, C.E. Chronic non-ischaemic congestive heart disease and endomyocardial biopsies. Worth the extra? *Eur Heart J* 12, 218-223 (1991).
89. Simonetti, O.P.*, et al.* An improved MR imaging technique for the visualization of myocardial infarction. *Radiology* 218, 215-223 (2001).
90. McCrohon, J.A.*, et al.* Differentiation of heart failure related to dilated cardiomyopathy and coronary artery disease using gadolinium-enhanced cardiovascular magnetic resonance. *Circulation* 108, 54-59 (2003).
91. Moon, J.C.*, et al.* The histologic basis of late gadolinium enhancement cardiovascular magnetic resonance in hypertrophic cardiomyopathy. *J Am Coll Cardiol* 43, 2260-2264 (2004).
92. Bull, S.*, et al.* Human non-contrast T1 values and correlation with histology in diffuse fibrosis. *Heart* 99, 932-937 (2013).
93. Hayer, M.*, et al.* PROGRESSION OF MYOCARADIAL FIBROSIS IN CHRONIC KIDNEY DISEASE. *Nephrol Dial Transplant* 34, i35-i36 (2019).
94. Mominadam, S.*, et al.* Interdialytic blood pressure obtained by ambulatory blood pressure measurement and left ventricular structure in hypertensive hemodialysis patients. *Hemodial Int* 12, 322-327 (2008).
95. Braunwald, E. *Heart disease Third edition*, (WB Saunders Co, United States, 1988).
96. Ritz, E. Left ventricular hypertrophy in renal disease: beyond preload and afterload. *Kidney international* 75, 771-773 (2009).

97. Gross, M.L. & Ritz, E. Hypertrophy and fibrosis in the cardiomyopathy of uremia--beyond coronary heart disease. *Seminars in dialysis* 21, 308-318 (2008).
98. Ritz, E. & Wanner, C. The challenge of sudden death in dialysis patients. *Clin J Am Soc Nephrol* 3, 920-929 (2008).
99. Harris, D. *Lange Mohrman and Heller's Cardiovascular Physiology*, (2023).
100. Komuro, I.*, et al.* Stretching cardiac myocytes stimulates protooncogene expression. *J Biol Chem* 265, 3595-3598 (1990).
101. Sadoshima, J., Jahn, L., Takahashi, T., Kulik, T.J. & Izumo, S. Molecular characterization of the stretch-induced adaptation of cultured cardiac cells. An in vitro model of load-induced cardiac hypertrophy. *J Biol Chem* 267, 10551-10560 (1992).
102. Komuro, I., Kurabayashi, M., Takaku, F. & Yazaki, Y. Expression of cellular oncogenes in the myocardium during the developmental stage and pressure-overloaded hypertrophy of the rat heart. *Circ Res* 62, 1075-1079 (1988).
103. Rockman, H.A.*, et al.* Segregation of atrial-specific and inducible expression of an atrial natriuretic factor transgene in an in vivo murine model of cardiac hypertrophy. *Proc Natl Acad Sci U S A* 88, 8277-8281 (1991).
104. Fiorillo, C.*, et al.* Cardiac volume overload rapidly induces oxidative stress-mediated myocyte apoptosis and hypertrophy. *Biochim Biophys Acta* 1741, 173-182 (2005).
105. Boguslavskyi, A.*, et al.* Cardiac hypertrophy in mice expressing unphosphorylatable phospholemman. *Cardiovasc Res* 104, 72-82 (2014).
106. Bastug-Ozel, Z.*, et al.* Heart failure leads to altered beta2-adrenoceptor/cyclic adenosine monophosphate dynamics in the sarcolemmal phospholemman/Na,K ATPase microdomain. *Cardiovasc Res* 115, 546-555 (2019).
107. He, S.*, et al.* A dataset of dual calcium and voltage optical mapping in healthy and hypertrophied murine hearts. *Sci Data* 8, 314 (2021).

108. Briet, M.*, et al.* Arterial stiffness and enlargement in mild-to-moderate chronic kidney disease. *Kidney international* 69, 350-357 (2006).
109. Ferreira, J.P., Girerd, N., Pannier, B., Rossignol, P. & London, G.M. High Pulse-Wave Velocity Defines a Very High Cardiovascular Risk Cohort of Dialysis Patients under Age 60. *Am J Nephrol* 45, 72-81 (2017).
110. Sarafidis, P.A.*, et al.* Ambulatory Pulse Wave Velocity Is a Stronger Predictor of Cardiovascular Events and All-Cause Mortality Than Office and Ambulatory Blood Pressure in Hemodialysis Patients. *Hypertension* 70, 148-157 (2017).
111. Briet, M., Boutouyrie, P., Laurent, S. & London, G.M. Arterial stiffness and pulse pressure in CKD and ESRD. *Kidney international* 82, 388-400 (2012).
112. Pannier, B., Guerin, A.P., Marchais, S.J., Safar, M.E. & London, G.M. Stiffness of capacitive and conduit arteries: prognostic significance for end-stage renal disease patients. *Hypertension* 45, 592-596 (2005).
113. Pickup, L., Radhakrishnan, A., Townend, J.N. & Ferro, C.J. Arterial stiffness in chronic kidney disease: a modifiable cardiovascular risk factor? *Curr Opin Nephrol Hypertens* 28, 527-536 (2019).
114. Mourad, J.J.*, et al.* Increased stiffness of radial artery wall material in end-stage renal disease. *Hypertension* 30, 1425-1430 (1997).
115. Cecelja, M. & Chowienczyk, P. Dissociation of aortic pulse wave velocity with risk factors for cardiovascular disease other than hypertension: a systematic review. *Hypertension* 54, 1328-1336 (2009).
116. McEniery, C.M.*, et al.* The impact of cardiovascular risk factors on aortic stiffness and wave reflections depends on age: the Anglo-Cardiff Collaborative Trial (ACCT III). *Hypertension* 56, 591-597 (2010).
117. Stewart, A.D., Jiang, B., Millasseau, S.C., Ritter, J.M. & Chowienczyk, P.J. Acute reduction of blood pressure by nitroglycerin does not normalize large artery stiffness in essential hypertension. *Hypertension* 48, 404-410 (2006).
118. Zheng, X.*, et al.* Arterial Stiffness as a Predictor of Clinical Hypertension. *J Clin Hypertens (Greenwich)* 17, 582-591 (2015).

119. Liao, D.*, et al.* Arterial stiffness and the development of hypertension. The ARIC study. *Hypertension* 34, 201-206 (1999).
120. Dernellis, J. & Panaretou, M. Aortic stiffness is an independent predictor of progression to hypertension in nonhypertensive subjects. *Hypertension* 45, 426-431 (2005).
121. Salaymeh, K.J. & Banerjee, A. Evaluation of arterial stiffness in children with Williams syndrome: Does it play a role in evolving hypertension? *American heart journal* 142, 549-555 (2001).
122. Blacher, J.*, et al.* Impact of aortic stiffness on survival in end-stage renal disease. *Circulation* 99, 2434-2439 (1999).
123. Guerin, A.P.*, et al.* Impact of aortic stiffness attenuation on survival of patients in end-stage renal failure. *Circulation* 103, 987-992 (2001).
124. Chue, C.D., Townend, J.N., Steeds, R.P. & Ferro, C.J. Arterial stiffness in chronic kidney disease: causes and consequences. *Heart* 96, 817-823 (2010).
125. Belz, G.G. Elastic properties and Windkessel function of the human aorta. *Cardiovasc Drugs Ther* 9, 73-83 (1995).
126. Zoccali, C.*, et al.* Chronic Fluid Overload and Mortality in ESRD. *J Am Soc Nephrol* 28, 2491-2497 (2017).
127. Hur, E.*, et al.* Effect of fluid management guided by bioimpedance spectroscopy on cardiovascular parameters in hemodialysis patients: a randomized controlled trial. *Am J Kidney Dis* 61, 957-965 (2013).
128. Hung, S.C.*, et al.* Volume overload correlates with cardiovascular risk factors in patients with chronic kidney disease. *Kidney international* 85, 703-709 (2014).
129. Martin, L.C.*, et al.* Association between hypervolemia and ventricular hypertrophy in hemodialysis patients. *Am J Hypertens* 17, 1163-1169 (2004).
130. Di Lullo, L., Floccari, F. & Polito, P. Right ventricular diastolic function in dialysis patients could be affected by vascular access. *Nephron Clin Pract* 118, c257-261 (2011).

131. Di Lullo, L., Gorini, A., Russo, D., Santoboni, A. & Ronco, C. Left Ventricular Hypertrophy in Chronic Kidney Disease Patients: From Pathophysiology to Treatment. *Cardiorenal Med* 5, 254-266 (2015).
132. Metivier, F., Marchais, S.J., Guerin, A.P., Pannier, B. & London, G.M. Pathophysiology of anaemia: focus on the heart and blood vessels. *Nephrol Dial Transplant* 15 Suppl 3, 14-18 (2000).
133. Beard, J.L., Tobin, B.W. & Smith, S.M. Effects of iron repletion and correction of anemia on norepinephrine turnover and thyroid metabolism in iron deficiency. *Proc Soc Exp Biol Med* 193, 306-312 (1990).
134. Muller, R.*, et al.* Changes in the alpha adrenergic system and increase in blood pressure with recombinant human erythropoietin (rHuEpo) therapy for renal anemia. *Clin Invest Med* 14, 614-622 (1991).
135. London, G.M.*, et al.* Vascular changes in hemodialysis patients in response to recombinant human erythropoietin. *Kidney international* 36, 878-882 (1989).
136. Cannella, G.*, et al.* Reversal of left ventricular hypertrophy following recombinant human erythropoietin treatment of anaemic dialysed uraemic patients. *Nephrol Dial Transplant* 6, 31-37 (1991).
137. Pascual, J.*, et al.* Regression of left ventricular hypertrophy after partial correction of anemia with erythropoietin in patients on hemodialysis: a prospective study. *Clin Nephrol* 35, 280-287 (1991).
138. Fellner, S.K., Lang, R.M., Neumann, A., Korcarz, C. & Borow, K.M. Cardiovascular consequences of correction of the anemia of renal failure with erythropoietin. *Kidney international* 44, 1309-1315 (1993).
139. Heidenreich, S., Rahn, K.H. & Zidek, W. Direct vasopressor effect of recombinant human erythropoietin on renal resistance vessels. *Kidney international* 39, 259-265 (1991).
140. Vaziri, N.D.*, et al.* Role of nitric oxide resistance in erythropoietin-induced hypertension in rats with chronic renal failure. *Am J Physiol* 271, E113-122 (1996).

141. Wada, Y.*, et al.* Erythropoietin impairs endothelium-dependent vasorelaxation through cyclooxygenase-dependent mechanisms in humans. *Am J Hypertens* 12, 980-987 (1999).
142. Dhingra, R.K., Young, E.W., Hulbert-Shearon, T.E., Leavey, S.F. & Port, F.K. Type of vascular access and mortality in U.S. hemodialysis patients. *Kidney international* 60, 1443-1451 (2001).
143. Pastan, S., Soucie, J.M. & McClellan, W.M. Vascular access and increased risk of death among hemodialysis patients. *Kidney international* 62, 620-626 (2002).
144. Xue, J.L., Dahl, D., Ebben, J.P. & Collins, A.J. The association of initial hemodialysis access type with mortality outcomes in elderly Medicare ESRD patients. *Am J Kidney Dis* 42, 1013-1019 (2003).
145. Reddy, Y.N.V.*, et al.* Long-term cardiovascular changes following creation of arteriovenous fistula in patients with end stage renal disease. *Eur Heart J* 38, 1913-1923 (2017).
146. van Duijnhoven, E.C., Cheriex, E.C., Tordoir, J.H., Kooman, J.P. & van Hooff, J.P. Effect of closure of the arteriovenous fistula on left ventricular dimensions in renal transplant patients. *Nephrol Dial Transplant* 16, 368-372 (2001).
147. Unger, P., Velez-Roa, S., Wissing, K.M., Hoang, A.D. & van de Borne, P. Regression of left ventricular hypertrophy after arteriovenous fistula closure in renal transplant recipients: a long-term follow-up. *Am J Transplant* 4, 2038-2044 (2004).
148. Scholz, S.S.*, et al.* Effects of Arteriovenous Fistula on Blood Pressure in Patients With End-Stage Renal Disease: A Systematic Meta-Analysis. *J Am Heart Assoc* 8, e011183 (2019).
149. Chue, C.D.*, et al.* Serum phosphate is associated with left ventricular mass in patients with chronic kidney disease: a cardiac magnetic resonance study. *Heart* 98, 219-224 (2012).
150. Pavlovic, D. Endogenous cardiotonic steroids and cardiovascular disease, where to next? *Cell Calcium* 86, 102156 (2020).

151. Ito, M.*, et al.* Vitamin D and phosphate regulate fibroblast growth factor-23 in K-562 cells. *Am J Physiol Endocrinol Metab* 288, E1101-1109 (2005).
152. Richter, B. & Faul, C. FGF23 Actions on Target Tissues-With and Without Klotho. *Front Endocrinol (Lausanne)* 9, 189 (2018).
153. Ornitz, D.M. & Itoh, N. Fibroblast growth factors. *Genome Biol* 2, REVIEWS3005 (2001).
154. Eswarakumar, V.P., Lax, I. & Schlessinger, J. Cellular signaling by fibroblast growth factor receptors. *Cytokine Growth Factor Rev* 16, 139-149 (2005).
155. Ben-Dov, I.Z.*, et al.* The parathyroid is a target organ for FGF23 in rats. *J Clin Invest* 117, 4003-4008 (2007).
156. Krajisnik, T.*, et al.* Fibroblast growth factor-23 regulates parathyroid hormone and 1alpha-hydroxylase expression in cultured bovine parathyroid cells. *J Endocrinol* 195, 125-131 (2007).
157. Gattineni, J.*, et al.* FGF23 decreases renal NaPi-2a and NaPi-2c expression and induces hypophosphatemia in vivo predominantly via FGF receptor 1. *Am J Physiol Renal Physiol* 297, F282-291 (2009).
158. Olauson, H.*, et al.* Parathyroid-specific deletion of Klotho unravels a novel calcineurin-dependent FGF23 signaling pathway that regulates PTH secretion. *PLoS Genet* 9, e1003975 (2013).
159. Chen, G.*, et al.* alpha-Klotho is a non-enzymatic molecular scaffold for FGF23 hormone signalling. *Nature* 553, 461-466 (2018).
160. Kuro-o, M.*, et al.* Mutation of the mouse klotho gene leads to a syndrome resembling ageing. *Nature* 390, 45-51 (1997).
161. Kato, Y.*, et al.* Establishment of the anti-Klotho monoclonal antibodies and detection of Klotho protein in kidneys. *Biochem Biophys Res Commun* 267, 597-602 (2000).
162. Lim, K.*, et al.* alpha-Klotho Expression in Human Tissues. *J Clin Endocrinol Metab* 100, E1308-1318 (2015).
163. Chen, C.D., Podvin, S., Gillespie, E., Leeman, S.E. & Abraham, C.R. Insulin stimulates the cleavage and release of the extracellular domain of

Klotho by ADAM10 and ADAM17. *Proc Natl Acad Sci U S A* 104, 19796-19801 (2007).

164. Bloch, L.*, et al.* Klotho is a substrate for alpha-, beta- and gamma-secretase. *FEBS Lett* 583, 3221-3224 (2009).
165. Chen, C.D.*, et al.* Identification of cleavage sites leading to the shed form of the anti-aging protein klotho. *Biochemistry* 53, 5579-5587 (2014).
166. Hu, M.C.*, et al.* Renal Production, Uptake, and Handling of Circulating alphaKlotho. *J Am Soc Nephrol* 27, 79-90 (2016).
167. Urakawa, I.*, et al.* Klotho converts canonical FGF receptor into a specific receptor for FGF23. *Nature* 444, 770-774 (2006).
168. Kurosu, H.*, et al.* Regulation of fibroblast growth factor-23 signaling by klotho. *J Biol Chem* 281, 6120-6123 (2006).
169. Hum, J.M.*, et al.* Chronic Hyperphosphatemia and Vascular Calcification Are Reduced by Stable Delivery of Soluble Klotho. *J Am Soc Nephrol* 28, 1162-1174 (2017).
170. Liu, X.*, et al.* Differential Regulatory Role of Soluble Klothos on Cardiac Fibrogenesis in Hypertension. *Am J Hypertens* 29, 1140-1147 (2016).
171. Faul, C.*, et al.* FGF23 induces left ventricular hypertrophy. *J Clin Invest* 121, 4393-4408 (2011).
172. Grabner, A.*, et al.* Activation of Cardiac Fibroblast Growth Factor Receptor 4 Causes Left Ventricular Hypertrophy. *Cell Metab* 22, 1020-1032 (2015).
173. Singh, S.*, et al.* Fibroblast growth factor 23 directly targets hepatocytes to promote inflammation in chronic kidney disease. *Kidney international* 90, 985-996 (2016).
174. Grabner, A.*, et al.* FGF23/FGFR4-mediated left ventricular hypertrophy is reversible. *Sci Rep* 7, 1993 (2017).
175. Samak, M.*, et al.* Cardiac Hypertrophy: An Introduction to Molecular and Cellular Basis. *Med Sci Monit Basic Res* 22, 75-79 (2016).
176. Molkentin, J.D. Calcineurin-NFAT signaling regulates the cardiac hypertrophic response in coordination with the MAPKs. *Cardiovasc Res* 63, 467-475 (2004).

177. Isakova, T.*, et al.* Fibroblast growth factor 23 is elevated before parathyroid hormone and phosphate in chronic kidney disease. *Kidney international* 79, 1370-1378 (2011).
178. Gutierrez, O.M.*, et al.* Fibroblast growth factor 23 and mortality among patients undergoing hemodialysis. *N Engl J Med* 359, 584-592 (2008).
179. Shimada, T.*, et al.* Circulating fibroblast growth factor 23 in patients with end-stage renal disease treated by peritoneal dialysis is intact and biologically active. *J Clin Endocrinol Metab* 95, 578-585 (2010).
180. Kestenbaum, B.*, et al.* Fibroblast growth factor-23 and cardiovascular disease in the general population: the Multi-Ethnic Study of Atherosclerosis. *Circ Heart Fail* 7, 409-417 (2014).
181. Lutsey, P.L.*, et al.* Fibroblast growth factor-23 and incident coronary heart disease, heart failure, and cardiovascular mortality: the Atherosclerosis Risk in Communities study. *J Am Heart Assoc* 3, e000936 (2014).
182. Scialla, J.J.*, et al.* Fibroblast growth factor-23 and cardiovascular events in CKD. *J Am Soc Nephrol* 25, 349-360 (2014).
183. Seiler, S.*, et al.* Associations of FGF-23 and sKlotho with cardiovascular outcomes among patients with CKD stages 2-4. *Clin J Am Soc Nephrol* 9, 1049-1058 (2014).
184. Moe, S.M.*, et al.* Cinacalcet, Fibroblast Growth Factor-23, and Cardiovascular Disease in Hemodialysis: The Evaluation of Cinacalcet HCl Therapy to Lower Cardiovascular Events (EVOLVE) Trial. *Circulation* 132, 27-39 (2015).
185. Marthi, A.*, et al.* Fibroblast Growth Factor-23 and Risks of Cardiovascular and Noncardiovascular Diseases: A Meta-Analysis. *J Am Soc Nephrol* 29, 2015-2027 (2018).
186. Mathew, J.S.*, et al.* Fibroblast growth factor-23 and incident atrial fibrillation: the Multi-Ethnic Study of Atherosclerosis (MESA) and the Cardiovascular Health Study (CHS). *Circulation* 130, 298-307 (2014).
187. Mehta, R.*, et al.* Association of Fibroblast Growth Factor 23 With Atrial Fibrillation in Chronic Kidney Disease, From the Chronic Renal Insufficiency Cohort Study. *JAMA Cardiol* 1, 548-556 (2016).

188. Mizia-Stec, K.*, et al.* Lower soluble Klotho and higher fibroblast growth factor 23 serum levels are associated with episodes of atrial fibrillation. *Cytokine* 111, 106-111 (2018).
189. Dong, Q.*, et al.* FGF23 regulates atrial fibrosis in atrial fibrillation by mediating the STAT3 and SMAD3 pathways. *J Cell Physiol* 234, 19502-19510 (2019).
190. Chua, W.*, et al.* Data-driven discovery and validation of circulating blood-based biomarkers associated with prevalent atrial fibrillation. *Eur Heart J* 40, 1268-1276 (2019).
191. Arnlov, J.*, et al.* Higher fibroblast growth factor-23 increases the risk of all-cause and cardiovascular mortality in the community. *Kidney international* 83, 160-166 (2013).
192. Westerberg, P.A.*, et al.* Fibroblast growth factor 23, mineral metabolism and mortality among elderly men (Swedish MrOs). *BMC Nephrol* 14, 85 (2013).
193. Brandenburg, V.M.*, et al.* Fibroblast growth factor 23 (FGF23) and mortality: the Ludwigshafen Risk and Cardiovascular Health Study. *Atherosclerosis* 237, 53-59 (2014).
194. Masson, S.*, et al.* The fibroblast growth factor-23 and Vitamin D emerge as nontraditional risk factors and may affect cardiovascular risk. *J Intern Med* 277, 318-330 (2015).
195. Souma, N.*, et al.* Fibroblast Growth Factor 23 and Cause-Specific Mortality in the General Population: The Northern Manhattan Study. *J Clin Endocrinol Metab* 101, 3779-3786 (2016).
196. Bergmark, B.A.*, et al.* Association of Fibroblast Growth Factor 23 With Recurrent Cardiovascular Events in Patients After an Acute Coronary Syndrome: A Secondary Analysis of a Randomized Clinical Trial. *JAMA Cardiol* 3, 473-480 (2018).
197. Chua, W.*, et al.* Development and external validation of predictive models for prevalent and recurrent atrial fibrillation: a protocol for the analysis of the CATCH ME combined dataset. *BMC Cardiovasc Disord* 19, 120 (2019).

198. Smith, E.R. The use of fibroblast growth factor 23 testing in patients with kidney disease. *Clin J Am Soc Nephrol* 9, 1283-1303 (2014).
199. Olauson, H., Mencke, R., Hillebrands, J.L. & Larsson, T.E. Tissue expression and source of circulating alphaKlotho. *Bone* 100, 19-35 (2017).
200. Forster, R.E.*, et al.* Vitamin D receptor controls expression of the anti-aging klotho gene in mouse and human renal cells. *Biochem Biophys Res Commun* 414, 557-562 (2011).
201. Tsujikawa, H., Kurotaki, Y., Fujimori, T., Fukuda, K. & Nabeshima, Y. Klotho, a gene related to a syndrome resembling human premature aging, functions in a negative regulatory circuit of vitamin D endocrine system. *Mol Endocrinol* 17, 2393-2403 (2003).
202. Fernandez-Fernandez, B.*, et al.* Albumin downregulates Klotho in tubular cells. *Nephrol Dial Transplant* 33, 1712-1722 (2018).
203. Moreno, J.A.*, et al.* The inflammatory cytokines TWEAK and TNFalpha reduce renal klotho expression through NFkappaB. *J Am Soc Nephrol* 22, 1315-1325 (2011).
204. de Borst, M.H., Vervloet, M.G., ter Wee, P.M. & Navis, G. Cross talk between the renin-angiotensin-aldosterone system and vitamin D-FGF-23-klotho in chronic kidney disease. *J Am Soc Nephrol* 22, 1603-1609 (2011).
205. Tang, R.*, et al.* Fosinopril and losartan regulate klotho gene and nicotinamide adenine dinucleotide phosphate oxidase expression in kidneys of spontaneously hypertensive rats. *Kidney Blood Press Res* 34, 350-357 (2011).
206. Marsell, R.*, et al.* Gene expression analysis of kidneys from transgenic mice expressing fibroblast growth factor-23. *Nephrol Dial Transplant* 23, 827-833 (2008).
207. Pavik, I.*, et al.* Secreted Klotho and FGF23 in chronic kidney disease Stage 1 to 5: a sequence suggested from a cross-sectional study. *Nephrol Dial Transplant* 28, 352-359 (2013).
208. Lu, X. & Hu, M.C. Klotho/FGF23 Axis in Chronic Kidney Disease and Cardiovascular Disease. *Kidney Dis (Basel)* 3, 15-23 (2017).

209. Kawaguchi, H.*, et al.* Independent impairment of osteoblast and osteoclast differentiation in klotho mouse exhibiting low-turnover osteopenia. *J Clin Invest* 104, 229-237 (1999).
210. Suga, T.*, et al.* Disruption of the klotho gene causes pulmonary emphysema in mice. Defect in maintenance of pulmonary integrity during postnatal life. *Am J Respir Cell Mol Biol* 22, 26-33 (2000).
211. Hu, M.C.*, et al.* Klotho and phosphate are modulators of pathologic uremic cardiac remodeling. *J Am Soc Nephrol* 26, 1290-1302 (2015).
212. Chen, K.*, et al.* Klotho Deficiency Causes Heart Aging via Impairing the Nrf2-GR Pathway. *Circ Res* 128, 492-507 (2021).
213. Xie, J., Yoon, J., An, S.W., Kuro-o, M. & Huang, C.L. Soluble Klotho Protects against Uremic Cardiomyopathy Independently of Fibroblast Growth Factor 23 and Phosphate. *J Am Soc Nephrol* 26, 1150-1160 (2015).
214. Drew, D.A.*, et al.* Soluble Klotho and Incident Hypertension. *Clin J Am Soc Nephrol* 16, 1502-1511 (2021).
215. Otani-Takei, N.*, et al.* Association between Serum Soluble Klotho Levels and Mortality in Chronic Hemodialysis Patients. *Int J Endocrinol* 2015, 406269 (2015).
216. Marcais, C.*, et al.* Circulating Klotho Associates With Cardiovascular Morbidity and Mortality During Hemodialysis. *J Clin Endocrinol Metab* 102, 3154-3161 (2017).
217. Memmos, E.*, et al.* Low plasma Klotho is associated with with cardiovascular events in hemodialysis independently of major risk factors, FGF23, arterial stiffness and intima-medial-thickness. *Nephrol Dial Transplant* 34, i38 (2019).
218. Gao, S., Xu, J., Zhang, S. & Jin, J. Meta-Analysis of the Association between Fibroblast Growth Factor 23 and Mortality and Cardiovascular Events in Hemodialysis Patients. *Blood Purif* 47 Suppl 1, 24-30 (2019).
219. Zhou, X., Chen, K., Lei, H. & Sun, Z. Klotho gene deficiency causes salt-sensitive hypertension via monocyte chemotactic protein-1/CC chemokine receptor 2-mediated inflammation. *J Am Soc Nephrol* 26, 121-132 (2015).

220. Citterio, L.*, et al.* Klotho Gene in Human Salt-Sensitive Hypertension. *Clin J Am Soc Nephrol* 15, 375-383 (2020).
221. Wang, Y., Kuro-o, M. & Sun, Z. Klotho gene delivery suppresses Nox2 expression and attenuates oxidative stress in rat aortic smooth muscle cells via the cAMP-PKA pathway. *Aging Cell* 11, 410-417 (2012).
222. Saito, Y.*, et al.* In vivo klotho gene delivery protects against endothelial dysfunction in multiple risk factor syndrome. *Biochem Biophys Res Commun* 276, 767-772 (2000).
223. Wang, Y. & Sun, Z. Klotho gene delivery prevents the progression of spontaneous hypertension and renal damage. *Hypertension* 54, 810-817 (2009).
224. Andrukhova, O.*, et al.* FGF23 regulates renal sodium handling and blood pressure. *EMBO Mol Med* 6, 744-759 (2014).
225. Han, X.*, et al.* Cardiovascular Effects of Renal Distal Tubule Deletion of the FGF Receptor 1 Gene. *J Am Soc Nephrol* 29, 69-80 (2018).
226. Di Marco, G.S.*, et al.* Cardioprotective effect of calcineurin inhibition in an animal model of renal disease. *Eur Heart J* 32, 1935-1945 (2011).
227. Leifheit-Nestler, M.*, et al.* Induction of cardiac FGF23/FGFR4 expression is associated with left ventricular hypertrophy in patients with chronic kidney disease. *Nephrol Dial Transplant* 31, 1088-1099 (2016).
228. Leifheit-Nestler, M.*, et al.* Vitamin D treatment attenuates cardiac FGF23/FGFR4 signaling and hypertrophy in uremic rats. *Nephrol Dial Transplant* 32, 1493-1503 (2017).
229. Dai, B.*, et al.* A comparative transcriptome analysis identifying FGF23 regulated genes in the kidney of a mouse CKD model. *PLoS One* 7, e44161 (2012).
230. Trask, A.J.*, et al.* Inhibition of angiotensin-converting enzyme 2 exacerbates cardiac hypertrophy and fibrosis in Ren-2 hypertensive rats. *Am J Hypertens* 23, 687-693 (2010).
231. Crackower, M.A.*, et al.* Angiotensin-converting enzyme 2 is an essential regulator of heart function. *Nature* 417, 822-828 (2002).

232. Santos, R.A. & Ferreira, A.J. Angiotensin-(1-7) and the renin-angiotensin system. *Curr Opin Nephrol Hypertens* 16, 122-128 (2007).
233. Zhang, B.*, et al.* Up-regulation of FGF23 release by aldosterone. *Biochem Biophys Res Commun* 470, 384-390 (2016).
234. Bockmann, I.*, et al.* FGF23-Mediated Activation of Local RAAS Promotes Cardiac Hypertrophy and Fibrosis. *Int J Mol Sci* 20, 4634 (2019).
235. Xie, J.*, et al.* Cardioprotection by Klotho through downregulation of TRPC6 channels in the mouse heart. *Nat Commun* 3, 1238 (2012).
236. Grabner, A. & Faul, C. The role of fibroblast growth factor 23 and Klotho in uremic cardiomyopathy. *Curr Opin Nephrol Hypertens* 25, 314-324 (2016).
237. Yang, K.*, et al.* Klotho Protects Against Indoxyl Sulphate-Induced Myocardial Hypertrophy. *J Am Soc Nephrol* 26, 2434-2446 (2015).
238. Slavic, S.*, et al.* Genetic Ablation of Fgf23 or Klotho Does not Modulate Experimental Heart Hypertrophy Induced by Pressure Overload. *Sci Rep* 7, 11298 (2017).
239. Leifheit-Nestler, M.*, et al.* Fo083chronic Fgf23 Overload Fails to Induce Cardiac Dysfunctions. *Nephrology Dialysis Transplantation* 34, i37 (2019).
240. Souders, C.A., Bowers, S.L. & Baudino, T.A. Cardiac fibroblast: the renaissance cell. *Circ Res* 105, 1164-1176 (2009).
241. Fan, D., Takawale, A., Lee, J. & Kassiri, Z. Cardiac fibroblasts, fibrosis and extracellular matrix remodeling in heart disease. *Fibrogenesis Tissue Repair* 5, 15 (2012).
242. de Bakker, J.M.*, et al.* Fractionated electrograms in dilated cardiomyopathy: origin and relation to abnormal conduction. *J Am Coll Cardiol* 27, 1071-1078 (1996).
243. Weber, K.T. Fibrosis and hypertensive heart disease. *Curr Opin Cardiol* 15, 264-272 (2000).
244. Espira, L. & Czubryt, M.P. Emerging concepts in cardiac matrix biology. *Can J Physiol Pharmacol* 87, 996-1008 (2009).
245. Chaturvedi, R.R.*, et al.* Passive stiffness of myocardium from congenital heart disease and implications for diastole. *Circulation* 121, 979-988 (2010).

246. Hao, H.*, et al.* FGF23 promotes myocardial fibrosis in mice through activation of beta-catenin. *Oncotarget* 7, 64649-64664 (2016).
247. Leifheit-Nestler, M. & Haffner, D. Paracrine Effects of FGF23 on the Heart. *Front Endocrinol (Lausanne)* 9, 278 (2018).
248. Faul, C. Cardiac actions of fibroblast growth factor 23. *Bone* 100, 69-79 (2017).
249. Roberts, P.R. & Green, D. Arrhythmias in chronic kidney disease. *Heart* 97, 766-773 (2011).
250. Boriani, G.*, et al.* Chronic kidney disease in patients with cardiac rhythm disturbances or implantable electrical devices: clinical significance and implications for decision making-a position paper of the European Heart Rhythm Association endorsed by the Heart Rhythm Society and the Asia Pacific Heart Rhythm Society. *Europace* 17, 1169-1196 (2015).
251. Kalra, P.A., Green, D. & Poulikakos, D. Arrhythmia in hemodialysis patients and its relation to sudden death. *Kidney international* 93, 781-783 (2018).
252. Turakhia, M.P., Schiller, N.B. & Whooley, M.A. Prognostic significance of increased left ventricular mass index to mortality and sudden death in patients with stable coronary heart disease (from the Heart and Soul Study). *Am J Cardiol* 102, 1131-1135 (2008).
253. Takeshita, K.*, et al.* Sinoatrial node dysfunction and early unexpected death of mice with a defect of klotho gene expression. *Circulation* 109, 1776-1782 (2004).
254. Touchberry, C.D.*, et al.* FGF23 is a novel regulator of intracellular calcium and cardiac contractility in addition to cardiac hypertrophy. *Am J Physiol Endocrinol Metab* 304, E863-873 (2013).
255. Hsueh, C.H.*, et al.* Pathogenesis of arrhythmias in a model of CKD. *J Am Soc Nephrol* 25, 2812-2821 (2014).
256. Glukhov, A.V.*, et al.* Calsequestrin 2 deletion causes sinoatrial node dysfunction and atrial arrhythmias associated with altered sarcoplasmic reticulum calcium cycling and degenerative fibrosis within the mouse atrial pacemaker complex1. *Eur Heart J* 36, 686-697 (2015).

257. Navarro-Garcia, J.A.*, et al.* Fibroblast growth factor-23 promotes rhythm alterations and contractile dysfunction in adult ventricular cardiomyocytes. *Nephrol Dial Transplant* 34, 1864-1875 (2019).
258. Mehta, R.*, et al.* Fibroblast Growth Factor 23 and Anemia in the Chronic Renal Insufficiency Cohort Study. *Clin J Am Soc Nephrol* 12, 1795-1803 (2017).
259. Chua, W.*, et al.* Quantification of fibroblast growth factor 23 and N-terminal pro-B-type natriuretic peptide to identify patients with atrial fibrillation using a high-throughput platform: A validation study. *PLoS Med* 18, e1003405 (2021).
260. Ter Maaten, J.M.*, et al.* Fibroblast growth factor 23 is related to profiles indicating volume overload, poor therapy optimization and prognosis in patients with new-onset and worsening heart failure. *Int J Cardiol* 253, 84-90 (2018).
261. Panwar, B.*, et al.* Fibroblast growth factor 23 and risk of incident stroke in community-living adults. *Stroke* 46, 322-328 (2015).
262. Seiler, S.*, et al.* The phosphatonin fibroblast growth factor 23 links calcium-phosphate metabolism with left-ventricular dysfunction and atrial fibrillation. *Eur Heart J* 32, 2688-2696 (2011).
263. Dong, Q.B.*, et al.* [Relationship between FGF23/FGFR4 expression in atrial tissue and atrial fibrosis in patients with atrial fibrillation]. *Zhonghua Yi Xue Za Zhi* 98, 1003-1007 (2018).
264. Kearney, P.M.*, et al.* Global burden of hypertension: analysis of worldwide data. *Lancet* 365, 217-223 (2005).
265. Bromfield, S. & Muntner, P. High blood pressure: the leading global burden of disease risk factor and the need for worldwide prevention programs. *Curr Hypertens Rep* 15, 134-136 (2013).
266. Muntner, P.*, et al.* Hypertension awareness, treatment, and control in adults with CKD: results from the Chronic Renal Insufficiency Cohort (CRIC) Study. *Am J Kidney Dis* 55, 441-451 (2010).

267. Kestenbaum, B.*, et al.* Differences in kidney function and incident hypertension: the multi-ethnic study of atherosclerosis. *Ann Intern Med* 148, 501-508 (2008).
268. Bidani, A.K. & Griffin, K.A. Pathophysiology of hypertensive renal damage: implications for therapy. *Hypertension* 44, 595-601 (2004).
269. Brantsma, A.H., Bakker, S.J., de Zeeuw, D., de Jong, P.E. & Gansevoort, R.T. Urinary albumin excretion as a predictor of the development of hypertension in the general population. *J Am Soc Nephrol* 17, 331-335 (2006).
270. Group, S.R.*, et al.* A Randomized Trial of Intensive versus Standard Blood-Pressure Control. *N Engl J Med* 373, 2103-2116 (2015).
271. Clinical management of primary hypertension in adults (NICE guideline 127). National Institute for Health and Clinical Excellence. (2011).
272. Weber, M.A.*, et al.* Clinical practice guidelines for the management of hypertension in the community: a statement by the American Society of Hypertension and the International Society of Hypertension. *J Clin Hypertens (Greenwich)* 16, 14-26 (2014).
273. James, P.A.*, et al.* 2014 evidence-based guideline for the management of high blood pressure in adults: report from the panel members appointed to the Eighth Joint National Committee (JNC 8). *JAMA : the journal of the American Medical Association* 311, 507-520 (2014).
274. Board, J.B.S. Joint British Societies' consensus recommendations for the prevention of cardiovascular disease (JBS3). *Heart* 100 Suppl 2, ii1-ii67 (2014).
275. Mancia, G.*, et al.* 2013 ESH/ESC Guidelines for the management of arterial hypertension: the Task Force for the management of arterial hypertension of the European Society of Hypertension (ESH) and of the European Society of Cardiology (ESC). *J Hypertens* 31, 1281-1357 (2013).
276. Cheung, A.K.*, et al.* Executive summary of the KDIGO 2021 Clinical Practice Guideline for the Management of Blood Pressure in Chronic Kidney Disease. *Kidney international* 99, 559-569 (2021).

277. Levy, D., Salomon, M., D'Agostino, R.B., Belanger, A.J. & Kannel, W.B. Prognostic implications of baseline electrocardiographic features and their serial changes in subjects with left ventricular hypertrophy. *Circulation* 90, 1786-1793 (1994).
278. Mathew, J.*, et al.* Reduction of cardiovascular risk by regression of electrocardiographic markers of left ventricular hypertrophy by the angiotensin-converting enzyme inhibitor ramipril. *Circulation* 104, 1615-1621 (2001).
279. Prineas, R.J., Rautaharju, P.M., Grandits, G., Crow, R. & Group, M.R. Independent risk for cardiovascular disease predicted by modified continuous score electrocardiographic criteria for 6-year incidence and regression of left ventricular hypertrophy among clinically disease free men: 16-year follow-up for the multiple risk factor intervention trial. *J Electrocardiol* 34, 91-101 (2001).
280. Dahlof, B.*, et al.* Cardiovascular morbidity and mortality in the Losartan Intervention For Endpoint reduction in hypertension study (LIFE): a randomised trial against atenolol. *Lancet* 359, 995-1003 (2002).
281. Soliman, E.Z.*, et al.* Effect of Intensive Blood Pressure Lowering on Left Ventricular Hypertrophy in Patients With Hypertension: SPRINT (Systolic Blood Pressure Intervention Trial). *Circulation* 136, 440-450 (2017).
282. Yildiz, M.*, et al.* Left ventricular hypertrophy and hypertension. *Prog Cardiovasc Dis* 63, 10-21 (2020).
283. Devereux, R.B.*, et al.* Effects of once-daily angiotensin-converting enzyme inhibition and calcium channel blockade-based antihypertensive treatment regimens on left ventricular hypertrophy and diastolic filling in hypertension: the prospective randomized enalapril study evaluating regression of ventricular enlargement (preserve) trial. *Circulation* 104, 1248-1254 (2001).
284. Pitt, B.*, et al.* Effects of eplerenone, enalapril, and eplerenone/enalapril in patients with essential hypertension and left ventricular hypertrophy: the 4E-left ventricular hypertrophy study. *Circulation* 108, 1831-1838 (2003).

285. Investigators, A.E.S. & Group, A.C. Effects of perindopril-indapamide on left ventricular diastolic function and mass in patients with type 2 diabetes: the ADVANCE Echocardiography Substudy. *J Hypertens* 29, 1439-1447 (2011).
286. Klingbeil, A.U., Schneider, M., Martus, P., Messerli, F.H. & Schmieder, R.E. A meta-analysis of the effects of treatment on left ventricular mass in essential hypertension. *Am J Med* 115, 41-46 (2003).
287. Fagard, R.H., Celis, H., Thijs, L. & Wouters, S. Regression of left ventricular mass by antihypertensive treatment: a meta-analysis of randomized comparative studies. *Hypertension* 54, 1084-1091 (2009).
288. de Simone, G.*, et al.* Lack of reduction of left ventricular mass in treated hypertension: the strong heart study. *J Am Heart Assoc* 2, e000144 (2013).
289. Lonnebakken, M.T.*, et al.* Left Ventricular Hypertrophy Regression During Antihypertensive Treatment in an Outpatient Clinic (the Campania Salute Network). *J Am Heart Assoc* 6(2017).
290. Kanno, Y.*, et al.* Angiotensin receptor antagonist regresses left ventricular hypertrophy associated with diabetic nephropathy in dialysis patients. *J Cardiovasc Pharmacol* 43, 380-386 (2004).
291. Mitsuhashi, H.*, et al.* Effect of losartan on ambulatory short-term blood pressure variability and cardiovascular remodeling in hypertensive patients on hemodialysis. *Atherosclerosis* 207, 186-190 (2009).
292. Suzuki, H.*, et al.* Selection of the dose of angiotensin converting enzyme inhibitor for patients with diabetic nephropathy depends on the presence or absence of left ventricular hypertrophy. *Hypertens Res* 25, 865-873 (2002).
293. Robson, R.*, et al.* Effects of simvastatin and enalapril on serum lipoprotein concentrations and left ventricular mass in patients on dialysis. The Perfect Study Collaborative Group. *J Nephrol* 10, 33-40 (1997).
294. Matsumoto, N.*, et al.* Effects of imidapril on left ventricular mass in chronic hemodialysis patients. *Hypertens Res* 29, 253-260 (2006).
295. Yu, W.C., Lin, Y.P., Lin, I.F., Chuang, S.Y. & Chen, C.H. Effect of ramipril on left ventricular mass in normotensive hemodialysis patients. *Am J Kidney Dis* 47, 478-484 (2006).

296. London, G.M.*, et al.* Cardiac hypertrophy, aortic compliance, peripheral resistance, and wave reflection in end-stage renal disease. Comparative effects of ACE inhibition and calcium channel blockade. *Circulation* 90, 2786-2796 (1994).
297. Shibasaki, Y.*, et al.* Angiotensin II type 1 receptor antagonist, losartan, causes regression of left ventricular hypertrophy in end-stage renal disease. *Nephron* 90, 256-261 (2002).
298. Yilmaz, R.*, et al.* Impact of amlodipine or ramipril treatment on left ventricular mass and carotid intima-media thickness in nondiabetic hemodialysis patients. *Ren Fail* 32, 903-912 (2010).
299. Zeltner, R., Poliak, R., Stiasny, B., Schmieder, R.E. & Schulze, B.D. Renal and cardiac effects of antihypertensive treatment with ramipril vs metoprolol in autosomal dominant polycystic kidney disease. *Nephrol Dial Transplant* 23, 573-579 (2008).
300. Agarwal, R., Sinha, A.D., Pappas, M.K., Abraham, T.N. & Tegegne, G.G. Hypertension in hemodialysis patients treated with atenolol or lisinopril: a randomized controlled trial. *Nephrol Dial Transplant* 29, 672-681 (2014).
301. Kang, H.*, et al.* Effects of sacubitril/valsartan in patients with heart failure and chronic kidney disease: A meta-analysis. *Eur J Pharmacol* 884, 173444 (2020).
302. Solomon, S.D.*, et al.* Angiotensin-Neprilysin Inhibition in Heart Failure with Preserved Ejection Fraction. *N Engl J Med* 381, 1609-1620 (2019).
303. Pieske, B.*, et al.* Effect of Sacubitril/Valsartan vs Standard Medical Therapies on Plasma NT-proBNP Concentration and Submaximal Exercise Capacity in Patients With Heart Failure and Preserved Ejection Fraction: The PARALLAX Randomized Clinical Trial. *JAMA : the journal of the American Medical Association* 326, 1919-1929 (2021).
304. Sarafidis, P.*, et al.* SGLT-2 inhibitors and GLP-1 receptor agonists for nephroprotection and cardioprotection in patients with diabetes mellitus and chronic kidney disease. A consensus statement by the EURECA-m and the DIABESITY working groups of the ERA-EDTA. *Nephrol Dial Transplant* 34, 208-230 (2019).

305. Sarafidis, P.*, et al.* Sodium--glucose co-transporter-2 inhibitors for patients with diabetic and nondiabetic chronic kidney disease: a new era has already begun. *J Hypertens* 39, 1090-1097 (2021).
306. Zelniker, T.A.*, et al.* SGLT2 inhibitors for primary and secondary prevention of cardiovascular and renal outcomes in type 2 diabetes: a systematic review and meta-analysis of cardiovascular outcome trials. *Lancet* 393, 31-39 (2019).
307. Herrington, W.G.*, et al.* The potential for improving cardio-renal outcomes by sodium-glucose co-transporter-2 inhibition in people with chronic kidney disease: a rationale for the EMPA-KIDNEY study. *Clin Kidney J* 11, 749-761 (2018).
308. Heerspink, H.J.L.*, et al.* Dapagliflozin in Patients with Chronic Kidney Disease. *N Engl J Med* 383, 1436-1446 (2020).
309. Brown, A.*, et al.* Dapagliflozin Improves Left Ventricular Myocardial Longitudinal Function in Patients With Type 2 Diabetes. *JACC. Cardiovascular imaging* 14, 503-504 (2021).
310. Suzuki, G.*, et al.* Effects of long-term monotherapy with eplerenone, a novel aldosterone blocker, on progression of left ventricular dysfunction and remodeling in dogs with heart failure. *Circulation* 106, 2967-2972 (2002).
311. Fraccarollo, D.*, et al.* Additive improvement of left ventricular remodeling and neurohormonal activation by aldosterone receptor blockade with eplerenone and ACE inhibition in rats with myocardial infarction. *J Am Coll Cardiol* 42, 1666-1673 (2003).
312. Wang, D.*, et al.* Role of a selective aldosterone blocker in mice with chronic heart failure. *J Card Fail* 10, 67-73 (2004).
313. Ortiz, A.*, et al.* Mineralocorticoid receptor antagonists for nephroprotection and cardioprotection in patients with diabetes mellitus and chronic kidney disease. *Nephrol Dial Transplant* 38, 10-25 (2023).
314. Edwards, N.C., Steeds, R.P., Stewart, P.M., Ferro, C.J. & Townend, J.N. Effect of spironolactone on left ventricular mass and aortic stiffness in

early-stage chronic kidney disease: a randomized controlled trial. *J Am Coll Cardiol* 54, 505-512 (2009).

315. Edwards, N.C.*, et al.* Effects of Spironolactone and Chlorthalidone on Cardiovascular Structure and Function in Chronic Kidney Disease: A Randomized, Open-Label Trial. *Clin J Am Soc Nephrol* 16, 1491-1501 (2021).
316. Pitt, B.*, et al.* Cardiovascular Events with Finerenone in Kidney Disease and Type 2 Diabetes. *N Engl J Med* 385, 2252-2263 (2021).
317. Bakris, G.L., Agarwal, R., Filippatos, G. & Group, F.-D.S. Finerenone and Chronic Kidney Disease Outcomes in Type 2 Diabetes. Reply. *N Engl J Med* 384, e42 (2021).
318. Agarwal, R.*, et al.* Cardiovascular and kidney outcomes with finerenone in patients with type 2 diabetes and chronic kidney disease: the FIDELITY pooled analysis. *Eur Heart J* 43, 474-484 (2022).
319. Ettehad, D.*, et al.* Blood pressure lowering for prevention of cardiovascular disease and death: a systematic review and meta-analysis. *Lancet* 387, 957-967 (2016).
320. Williams, B.*, et al.* 2018 ESC/ESH Guidelines for the management of arterial hypertension. *Eur Heart J* 39, 3021-3104 (2018).
321. Ly, J. & Chan, C.T. Impact of augmenting dialysis frequency and duration on cardiovascular function. *ASAIO J* 52, e11-14 (2006).
322. Fagugli, R.M.*, et al.* Effects of short daily hemodialysis and extended standard hemodialysis on blood pressure and cardiac hypertrophy: a comparative study. *J Nephrol* 19, 77-83 (2006).
323. Weinreich, T., De los Rios, T., Gauly, A. & Passlick-Deetjen, J. Effects of an increase in time vs. frequency on cardiovascular parameters in chronic hemodialysis patients. *Clin Nephrol* 66, 433-439 (2006).
324. Susantitaphong, P., Koulouridis, I., Balk, E.M., Madias, N.E. & Jaber, B.L. Effect of frequent or extended hemodialysis on cardiovascular parameters: a meta-analysis. *Am J Kidney Dis* 59, 689-699 (2012).
325. Powell, J.R.*, et al.* Ten years experience of in-center thrice weekly long overnight hemodialysis. *Clin J Am Soc Nephrol* 4, 1097-1101 (2009).

326. Chan, C.T., Floras, J.S., Miller, J.A., Richardson, R.M. & Pierratos, A. Regression of left ventricular hypertrophy after conversion to nocturnal hemodialysis. *Kidney international* 61, 2235-2239 (2002).
327. Wong, B.*, et al.* In-Center Nocturnal Hemodialysis Versus Conventional Hemodialysis: A Systematic Review of the Evidence. *Am J Kidney Dis* 70, 218-234 (2017).
328. Odudu, A., Eldehni, M.T., McCann, G.P. & McIntyre, C.W. Randomized Controlled Trial of Individualized Dialysate Cooling for Cardiac Protection in Hemodialysis Patients. *Clin J Am Soc Nephrol* 10, 1408-1417 (2015).
329. Mathew, A.*, et al.* Mortality and Hospitalizations in Intensive Dialysis: A Systematic Review and Meta-Analysis. *Can J Kidney Health Dis* 5, 2054358117749531 (2018).
330. Kraus, M.A.*, et al.* Intensive Hemodialysis and Potential Risks With Increasing Treatment. *Am J Kidney Dis* 68, S51-S58 (2016).
331. Al Rahbi, F. & Al Salmi, I. Commercial Kidney Transplantation: Attitude, Knowledge, Perception, and Experience of Recipients. *Kidney Int Rep* 2, 626-633 (2017).
332. Neale, J. & Smith, A.C. Cardiovascular risk factors following renal transplant. *World J Transplant* 5, 183-195 (2015).
333. Devine, P.A., Courtney, A.E. & Maxwell, A.P. Cardiovascular risk in renal transplant recipients. *J Nephrol* 32, 389-399 (2019).
334. Alhaj, E.*, et al.* Uremic cardiomyopathy: an underdiagnosed disease. *Congest Heart Fail* 19, E40-45 (2013).
335. Patel, H., Madanieh, R., Kosmas, C.E., Vatti, S.K. & Vittorio, T.J. Reversible Cardiomyopathies. *Clin Med Insights Cardiol* 9, 7-14 (2015).
336. Kaesler, N., Babler, A., Floege, J. & Kramann, R. Cardiac Remodeling in Chronic Kidney Disease. *Toxins (Basel)* 12(2020).
337. Hawwa, N., Schreiber, M.J., Jr. & Tang, W.H. Pharmacologic management of chronic reno-cardiac syndrome. *Curr Heart Fail Rep* 10, 54-62 (2013).
338. Lekawanvijit, S.*, et al.* Does indoxyl sulfate, a uraemic toxin, have direct effects on cardiac fibroblasts and myocytes? *Eur Heart J* 31, 1771-1779 (2010).

339. Pickup, L.C.*, et al.* Changes in left ventricular structure and function associated with renal transplantation: a systematic review and meta-analysis. *ESC Heart Fail* 8, 2045-2057 (2021).
340. Stewart, G.A.*, et al.* Echocardiography overestimates left ventricular mass in hemodialysis patients relative to magnetic resonance imaging. *Kidney international* 56, 2248-2253 (1999).
341. Contti, M.M.*, et al.* Kidney transplantation is associated with reduced myocardial fibrosis. A cardiovascular magnetic resonance study with native T1 mapping. *J Cardiovasc Magn Reson* 21, 21 (2019).
342. Hayer, M.K.*, et al.* Early effects of kidney transplantation on the heart - A cardiac magnetic resonance multi-parametric study. *Int J Cardiol* 293, 272-277 (2019).
343. Ferrari, S.L., Bonjour, J.P. & Rizzoli, R. Fibroblast growth factor-23 relationship to dietary phosphate and renal phosphate handling in healthy young men. *J Clin Endocrinol Metab* 90, 1519-1524 (2005).
344. Burnett, S.M.*, et al.* Regulation of C-terminal and intact FGF-23 by dietary phosphate in men and women. *Journal of bone and mineral research : the official journal of the American Society for Bone and Mineral Research* 21, 1187-1196 (2006).
345. Scanni, R., vonRotz, M., Jehle, S., Hulter, H.N. & Krapf, R. The human response to acute enteral and parenteral phosphate loads. *J Am Soc Nephrol* 25, 2730-2739 (2014).
346. Antoniucci, D.M., Yamashita, T. & Portale, A.A. Dietary phosphorus regulates serum fibroblast growth factor-23 concentrations in healthy men. *J Clin Endocrinol Metab* 91, 3144-3149 (2006).
347. Moe, S.M.*, et al.* Vegetarian compared with meat dietary protein source and phosphorus homeostasis in chronic kidney disease. *Clin J Am Soc Nephrol* 6, 257-264 (2011).
348. Di Iorio, B.*, et al.* Acute effects of very-low-protein diet on FGF23 levels: a randomized study. *Clin J Am Soc Nephrol* 7, 581-587 (2012).

349. Sigrist, M., *et al.* Responsiveness of FGF-23 and mineral metabolism to altered dietary phosphate intake in chronic kidney disease (CKD): results of a randomized trial. *Nephrol Dial Transplant* 28, 161-169 (2013).
350. Rodriguez-Ortiz, M.E., *et al.* Inflammation both increases and causes resistance to FGF23 in normal and uremic rats. *Clin Sci (Lond)* 134, 15-32 (2020).
351. Oliveira, R.B., *et al.* Early control of PTH and FGF23 in normophosphatemic CKD patients: a new target in CKD-MBD therapy? *Clin J Am Soc Nephrol* 5, 286-291 (2010).
352. Block, G.A., *et al.* Effects of phosphate binders in moderate CKD. *J Am Soc Nephrol* 23, 1407-1415 (2012).
353. Chue, C.D., *et al.* Cardiovascular effects of sevelamer in stage 3 CKD. *J Am Soc Nephrol* 24, 842-852 (2013).
354. Rodelo-Haad, C., *et al.* Phosphate control in reducing FGF23 levels in hemodialysis patients. *PLoS One* 13, e0201537 (2018).
355. Sprague, S.M., *et al.* Long-term efficacy and safety of sucroferric oxyhydroxide in African American dialysis patients. *Hemodial Int* 22, 480-491 (2018).
356. Shimada, T., *et al.* Vitamin D receptor-independent FGF23 actions in regulating phosphate and vitamin D metabolism. *Am J Physiol Renal Physiol* 289, F1088-1095 (2005).
357. Rodriguez-Ortiz, M.E., *et al.* Calcium deficiency reduces circulating levels of FGF23. *J Am Soc Nephrol* 23, 1190-1197 (2012).
358. Shahbazian, H., *et al.* Oral nicotinamide reduces serum phosphorus, increases HDL, and induces thrombocytopenia in hemodialysis patients: a double-blind randomized clinical trial. *Nefrologia* 31, 58-65 (2011).
359. Labonte, E.D., *et al.* Gastrointestinal Inhibition of Sodium-Hydrogen Exchanger 3 Reduces Phosphorus Absorption and Protects against Vascular Calcification in CKD. *J Am Soc Nephrol* 26, 1138-1149 (2015).
360. Block, G.A., *et al.* The effects of tenapanor on serum fibroblast growth factor 23 in patients receiving hemodialysis with hyperphosphatemia. *Nephrol Dial Transplant* 34, 339-346 (2019).

361. Block, G.A., Rosenbaum, D.P., Yan, A. & Chertow, G.M. Efficacy and Safety of Tenapanor in Patients with Hyperphosphatemia Receiving Maintenance Hemodialysis: A Randomized Phase 3 Trial. *J Am Soc Nephrol* 30, 641-652 (2019).
362. Ix, J.H.*, et al.* Effects of Nicotinamide and Lanthanum Carbonate on Serum Phosphate and Fibroblast Growth Factor-23 in CKD: The COMBINE Trial. *J Am Soc Nephrol* 30, 1096-1108 (2019).
363. Marks, J.*, et al.* Intestinal phosphate absorption in a model of chronic renal failure. *Kidney international* 72, 166-173 (2007).
364. Sabbagh, Y.*, et al.* Intestinal npt2b plays a major role in phosphate absorption and homeostasis. *J Am Soc Nephrol* 20, 2348-2358 (2009).
365. Giral, H.*, et al.* Regulation of rat intestinal Na-dependent phosphate transporters by dietary phosphate. *Am J Physiol Renal Physiol* 297, F1466-1475 (2009).
366. Lau, W.L.*, et al.* Vitamin D receptor agonists increase klotho and osteopontin while decreasing aortic calcification in mice with chronic kidney disease fed a high phosphate diet. *Kidney international* 82, 1261-1270 (2012).
367. Ritter, C.S., Zhang, S., Delmez, J., Finch, J.L. & Slatopolsky, E. Differential expression and regulation of Klotho by paricalcitol in the kidney, parathyroid, and aorta of uremic rats. *Kidney international* 87, 1141-1152 (2015).
368. Teng, M.*, et al.* Activated injectable vitamin D and hemodialysis survival: a historical cohort study. *J Am Soc Nephrol* 16, 1115-1125 (2005).
369. Shoben, A.B., Rudser, K.D., de Boer, I.H., Young, B. & Kestenbaum, B. Association of oral calcitriol with improved survival in nondialyzed CKD. *J Am Soc Nephrol* 19, 1613-1619 (2008).
370. Thadhani, R.*, et al.* Vitamin D therapy and cardiac structure and function in patients with chronic kidney disease: the PRIMO randomized controlled trial. *JAMA : the journal of the American Medical Association* 307, 674-684 (2012).

371. Wetmore, J.B., Liu, S., Krebill, R., Menard, R. & Quarles, L.D. Effects of cinacalcet and concurrent low-dose vitamin D on FGF23 levels in ESRD. *Clin J Am Soc Nephrol* 5, 110-116 (2010).
372. Koizumi, M., Komaba, H., Nakanishi, S., Fujimori, A. & Fukagawa, M. Cinacalcet treatment and serum FGF23 levels in haemodialysis patients with secondary hyperparathyroidism. *Nephrol Dial Transplant* 27, 784-790 (2012).
373. Kim, H.J.*, et al.* Cinacalcet lowering of serum fibroblast growth factor-23 concentration may be independent from serum Ca, P, PTH and dose of active vitamin D in peritoneal dialysis patients: a randomized controlled study. *BMC Nephrol* 14, 112 (2013).
374. Sprague, S.M.*, et al.* Effect of Cinacalcet and Vitamin D Analogs on Fibroblast Growth Factor-23 during the Treatment of Secondary Hyperparathyroidism. *Clin J Am Soc Nephrol* 10, 1021-1030 (2015).
375. Block, G.A.*, et al.* Effect of Etelcalcetide vs Placebo on Serum Parathyroid Hormone in Patients Receiving Hemodialysis With Secondary Hyperparathyroidism: Two Randomized Clinical Trials. *JAMA : the journal of the American Medical Association* 317, 146-155 (2017).
376. Ogata, H., Ritz, E., Odoni, G., Amann, K. & Orth, S.R. Beneficial effects of calcimimetics on progression of renal failure and cardiovascular risk factors. *J Am Soc Nephrol* 14, 959-967 (2003).
377. Odenwald, T.*, et al.* Acute blood pressure effects and chronic hypotensive action of calcimimetics in uremic rats. *J Am Soc Nephrol* 17, 655-662 (2006).
378. Eddington, H.*, et al.* A randomised controlled trial to examine the effects of cinacalcet on bone and cardiovascular parameters in haemodialysis patients with advanced secondary hyperparathyroidism. *BMC Nephrol* 22, 106 (2021).
379. Charytan, C.*, et al.* Cinacalcet hydrochloride is an effective treatment for secondary hyperparathyroidism in patients with CKD not receiving dialysis. *Am J Kidney Dis* 46, 58-67 (2005).

380. Chonchol, M.*, et al.* A randomized, double-blind, placebo-controlled study to assess the efficacy and safety of cinacalcet HCl in participants with CKD not receiving dialysis. *Am J Kidney Dis* 53, 197-207 (2009).
381. Bergwitz, C. & Juppner, H. Phosphate sensing. *Adv Chronic Kidney Dis* 18, 132-144 (2011).
382. Bon, N.*, et al.* Phosphate-dependent FGF23 secretion is modulated by PiT2/Slc20a2. *Mol Metab* 11, 197-204 (2018).
383. Shalhoub, V.*, et al.* FGF23 neutralization improves chronic kidney disease-associated hyperparathyroidism yet increases mortality. *J Clin Invest* 122, 2543-2553 (2012).
384. Hasegawa, H.*, et al.* Direct evidence for a causative role of FGF23 in the abnormal renal phosphate handling and vitamin D metabolism in rats with early-stage chronic kidney disease. *Kidney international* 78, 975-980 (2010).
385. Perwad, F. & Portale, A.A. Burosumab Therapy for X-Linked Hypophosphatemia and Therapeutic Implications for CKD. *Clin J Am Soc Nephrol* 14, 1097-1099 (2019).
386. Di Marco, G.S.*, et al.* Treatment of established left ventricular hypertrophy with fibroblast growth factor receptor blockade in an animal model of CKD. *Nephrol Dial Transplant* 29, 2028-2035 (2014).
387. Yanochko, G.M.*, et al.* Pan-FGFR inhibition leads to blockade of FGF23 signaling, soft tissue mineralization, and cardiovascular dysfunction. *Toxicol Sci* 135, 451-464 (2013).
388. Katoh, M. Therapeutics Targeting FGF Signaling Network in Human Diseases. *Trends Pharmacol Sci* 37, 1081-1096 (2016).
389. Doi, S.*, et al.* Klotho inhibits transforming growth factor-beta1 (TGF-beta1) signaling and suppresses renal fibrosis and cancer metastasis in mice. *J Biol Chem* 286, 8655-8665 (2011).
390. Shi, M.*, et al.* alphaKlotho Mitigates Progression of AKI to CKD through Activation of Autophagy. *J Am Soc Nephrol* 27, 2331-2345 (2016).

391. Hu, M.C., *et al.* Recombinant alpha-Klotho may be prophylactic and therapeutic for acute to chronic kidney disease progression and uremic cardiomyopathy. *Kidney international* 91, 1104-1114 (2017).
392. Kuro, O.M. The Klotho proteins in health and disease. *Nat Rev Nephrol* 15, 27-44 (2019).
393. Guo, Y., *et al.* Klotho protects the heart from hyperglycemia-induced injury by inactivating ROS and NF-kappaB-mediated inflammation both in vitro and in vivo. *Biochim Biophys Acta Mol Basis Dis* 1864, 238-251 (2018).
394. Ding, J., *et al.* Klotho inhibits angiotensin II-induced cardiac hypertrophy, fibrosis, and dysfunction in mice through suppression of transforming growth factor-beta1 signaling pathway. *Eur J Pharmacol* 859, 172549 (2019).
395. Suassuna, P.G.A., *et al.* alphaKlotho attenuates cardiac hypertrophy and increases myocardial fibroblast growth factor 21 expression in uremic rats. *Exp Biol Med (Maywood)* 245, 66-78 (2020).
396. King, G.D., *et al.* Identification of novel small molecules that elevate Klotho expression. *Biochem J* 441, 453-461 (2012).
397. Zhang, H., *et al.* Generation of Quiescent Cardiac Fibroblasts From Human Induced Pluripotent Stem Cells for In Vitro Modeling of Cardiac Fibrosis. *Circ Res* 125, 552-566 (2019).
398. MacKenna, D., Summerour, S.R. & Villarreal, F.J. Role of mechanical factors in modulating cardiac fibroblast function and extracellular matrix synthesis. *Cardiovasc Res* 46, 257-263 (2000).
399. Bagchi, R.A., Lin, J., Wang, R. & Czubryt, M.P. Regulation of fibronectin gene expression in cardiac fibroblasts by scleraxis. *Cell Tissue Res* 366, 381-391 (2016).
400. Czaya, B., *et al.* Hyperphosphatemia increases inflammation to exacerbate anemia and skeletal muscle wasting independently of FGF23-FGFR4 signaling. *Elife* 11(2022).
401. Clinkenbeard, E.L., *et al.* Increased FGF23 protects against detrimental cardio-renal consequences during elevated blood phosphate in CKD. *JCI Insight* 4(2019).

402. Moench, I.*, et al.* High FGF23 Levels Failed to Predict Cardiac Hypertrophy in Animal Models of Hyperphosphatemia and Chronic Renal Failure. *J Endocr Soc* 5, bvab066 (2021).
403. Kaludjerovic, J.*, et al.* Klotho expression in long bones regulates FGF23 production during renal failure. *FASEB J* 31, 2050-2064 (2017).
404. Taylor, A.*, et al.* FGFR4 does not contribute to progression of chronic kidney disease. *Sci Rep* 9, 14023 (2019).
405. Kagi, L.*, et al.* Regulation of vitamin D metabolizing enzymes in murine renal and extrarenal tissues by dietary phosphate, FGF23, and 1,25(OH)2D3. *PLoS One* 13, e0195427 (2018).
406. O'Shea, C.*, et al.* ElectroMap: High-throughput open-source software for analysis and mapping of cardiac electrophysiology. *Sci Rep* 9, 1389 (2019).
407. O'Shea, C.*, et al.* High-Throughput Analysis of Optical Mapping Data Using ElectroMap. *J Vis Exp* (2019).
408. Liu, T.*, et al.* Current Understanding of the Pathophysiology of Myocardial Fibrosis and Its Quantitative Assessment in Heart Failure. *Front Physiol* 8, 238 (2017).
409. Gulati, A.*, et al.* Association of fibrosis with mortality and sudden cardiac death in patients with nonischemic dilated cardiomyopathy. *JAMA* 309, 896-908 (2013).
410. Garg, P.*, et al.* Left ventricular fibrosis and hypertrophy are associated with mortality in heart failure with preserved ejection fraction. *Sci Rep* 11, 617 (2021).
411. Ibanez, B.*, et al.* 2017 ESC Guidelines for the management of acute myocardial infarction in patients presenting with ST-segment elevation: The Task Force for the management of acute myocardial infarction in patients presenting with ST-segment elevation of the European Society of Cardiology (ESC). *Eur Heart J* 39, 119-177 (2018).
412. Wu, T.J.*, et al.* Characteristics of wave fronts during ventricular fibrillation in human hearts with dilated cardiomyopathy: role of increased fibrosis in the generation of reentry. *J Am Coll Cardiol* 32, 187-196 (1998).

413. Yancy, C.W.*, et al.* 2013 ACCF/AHA guideline for the management of heart failure: executive summary: a report of the American College of Cardiology Foundation/American Heart Association Task Force on practice guidelines. *Circulation* 128, 1810-1852 (2013).
414. Yancy, C.W.*, et al.* 2017 ACC/AHA/HFSA Focused Update of the 2013 ACCF/AHA Guideline for the Management of Heart Failure: A Report of the American College of Cardiology/American Heart Association Task Force on Clinical Practice Guidelines and the Heart Failure Society of America. *Circulation* 136, e137-e161 (2017).
415. Wynn, T.A. & Ramalingam, T.R. Mechanisms of fibrosis: therapeutic translation for fibrotic disease. *Nat Med* 18, 1028-1040 (2012).
416. Tucker, N.R.*, et al.* Transcriptional and Cellular Diversity of the Human Heart. *Circulation* 142, 466-482 (2020).
417. Litvinukova, M.*, et al.* Cells of the adult human heart. *Nature* 588, 466-472 (2020).
418. Zhang, P., Su, J. & Mende, U. Cross talk between cardiac myocytes and fibroblasts: from multiscale investigative approaches to mechanisms and functional consequences. *Am J Physiol Heart Circ Physiol* 303, H1385-1396 (2012).
419. Segura, A.M., Frazier, O.H. & Buja, L.M. Fibrosis and heart failure. *Heart Fail Rev* 19, 173-185 (2014).
420. Creemers, E.E. & Pinto, Y.M. Molecular mechanisms that control interstitial fibrosis in the pressure-overloaded heart. *Cardiovasc Res* 89, 265-272 (2011).
421. Tallquist, M.D. & Molkentin, J.D. Redefining the identity of cardiac fibroblasts. *Nat Rev Cardiol* 14, 484-491 (2017).
422. Travers, J.G., Kamal, F.A., Robbins, J., Yutzey, K.E. & Blaxall, B.C. Cardiac Fibrosis: The Fibroblast Awakens. *Circ Res* 118, 1021-1040 (2016).
423. Wynn, T.A. Cellular and molecular mechanisms of fibrosis. *J Pathol* 214, 199-210 (2008).

424. Li, J.*, et al.* beta-Arrestins regulate human cardiac fibroblast transformation and collagen synthesis in adverse ventricular remodeling. *J Mol Cell Cardiol* 76, 73-83 (2014).
425. Ackers-Johnson, M.*, et al.* A Simplified, Langendorff-Free Method for Concomitant Isolation of Viable Cardiac Myocytes and Nonmyocytes From the Adult Mouse Heart. *Circ Res* 119, 909-920 (2016).
426. Hecker, L., Jagirdar, R., Jin, T. & Thannickal, V.J. Reversible differentiation of myofibroblasts by MyoD. *Exp Cell Res* 317, 1914-1921 (2011).
427. Cartledge, J.E.*, et al.* Functional crosstalk between cardiac fibroblasts and adult cardiomyocytes by soluble mediators. *Cardiovasc Res* 105, 260-270 (2015).
428. Nakajima, H.*, et al.* Atrial but not ventricular fibrosis in mice expressing a mutant transforming growth factor-beta(1) transgene in the heart. *Circ Res* 86, 571-579 (2000).
429. Nagaraju, C.K.*, et al.* Myofibroblast Phenotype and Reversibility of Fibrosis in Patients With End-Stage Heart Failure. *J Am Coll Cardiol* 73, 2267-2282 (2019).
430. Kuwahara, F.*, et al.* Transforming growth factor-beta function blocking prevents myocardial fibrosis and diastolic dysfunction in pressure-overloaded rats. *Circulation* 106, 130-135 (2002).
431. Wang, H., Haeger, S.M., Kloxin, A.M., Leinwand, L.A. & Anseth, K.S. Redirecting valvular myofibroblasts into dormant fibroblasts through light-mediated reduction in substrate modulus. *PLoS One* 7, e39969 (2012).
432. Nguyen, D.T., Nagarajan, N. & Zorlutuna, P. Effect of Substrate Stiffness on Mechanical Coupling and Force Propagation at the Infarct Boundary. *Biophys J* 115, 1966-1980 (2018).
433. Borbely, A.*, et al.* Cardiomyocyte stiffness in diastolic heart failure. *Circulation* 111, 774-781 (2005).
434. Ceccato, T.L.*, et al.* Defining the Cardiac Fibroblast Secretome in a Fibrotic Microenvironment. *J Am Heart Assoc* 9, e017025 (2020).

435. Herum, K.M., Choppe, J., Kumar, A., Engler, A.J. & McCulloch, A.D. Mechanical regulation of cardiac fibroblast profibrotic phenotypes. *Mol Biol Cell* 28, 1871-1882 (2017).
436. Landry, N.M., Rattan, S.G. & Dixon, I.M.C. An Improved Method of Maintaining Primary Murine Cardiac Fibroblasts in Two-Dimensional Cell Culture. *Sci Rep* 9, 12889 (2019).
437. Santiago, J.J.*, et al.* Cardiac fibroblast to myofibroblast differentiation in vivo and in vitro: expression of focal adhesion components in neonatal and adult rat ventricular myofibroblasts. *Dev Dyn* 239, 1573-1584 (2010).
438. Khalil, H.*, et al.* Fibroblast-specific TGF-beta-Smad2/3 signaling underlies cardiac fibrosis. *J Clin Invest* 127, 3770-3783 (2017).
439. Zeigler, A.C., Richardson, W.J., Holmes, J.W. & Saucerman, J.J. A computational model of cardiac fibroblast signaling predicts context-dependent drivers of myofibroblast differentiation. *J Mol Cell Cardiol* 94, 72-81 (2016).
440. Landry, N.M., Rattan, S.G. & Dixon, I.M.C. An Improved Method of Maintaining Primary Murine Cardiac Fibroblasts in Two-Dimensional Cell Culture. *Scientific Reports* 9, 12889 (2019).
441. Sweeney, M., Corden, B. & Cook, S.A. Targeting cardiac fibrosis in heart failure with preserved ejection fraction: mirage or miracle? *EMBO Mol Med* 12, e10865 (2020).
442. Neumann, S.*, et al.* Aldosterone and d-Glucose Stimulate the Proliferation of Human Cardiac Myofibroblasts In Vitro. *Hypertension* 39, 756-760 (2002).
443. Stockand, J.D. & Meszaros, J.G. Aldosterone stimulates proliferation of cardiac fibroblasts by activating Ki-RasA and MAPK1/2 signaling. *American Journal of Physiology-Heart and Circulatory Physiology* 284, H176-H184 (2003).
444. Olson, E.R., Naugle, J.E., Zhang, X., Bomser, J.A. & Meszaros, J.G. Inhibition of cardiac fibroblast proliferation and myofibroblast differentiation by resveratrol. *American Journal of Physiology-Heart and Circulatory Physiology* 288, H1131-H1138 (2005).

445. Ongstad, E. & Kohl, P. Fibroblast-myocyte coupling in the heart: Potential relevance for therapeutic interventions. *Journal of molecular and cellular cardiology* 91, 238-246 (2016).
446. Kohl, P. & Gourdie, R.G. Fibroblast-myocyte electrotonic coupling: does it occur in native cardiac tissue? *Journal of molecular and cellular cardiology* 70, 37-46 (2014).
447. Kazbanov, I.V., ten Tusscher, K.H. & Panfilov, A.V. Effects of Heterogeneous Diffuse Fibrosis on Arrhythmia Dynamics and Mechanism. *Sci Rep* 6, 20835 (2016).
448. Li, R.K.*, et al.* Overexpression of transforming growth factor-beta1 and insulin-like growth factor-I in patients with idiopathic hypertrophic cardiomyopathy. *Circulation* 96, 874-881 (1997).
449. Almendral, J.L., Shick, V., Rosendorff, C. & Atlas, S.A. Association between transforming growth factor-beta(1) and left ventricular mass and diameter in hypertensive patients. *J Am Soc Hypertens* 4, 135-141 (2010).
450. Hein, S.*, et al.* Progression from compensated hypertrophy to failure in the pressure-overloaded human heart: structural deterioration and compensatory mechanisms. *Circulation* 107, 984-991 (2003).
451. Meng, X.M., Nikolic-Paterson, D.J. & Lan, H.Y. TGF-beta: the master regulator of fibrosis. *Nat Rev Nephrol* 12, 325-338 (2016).
452. Molkentin, J.D.*, et al.* Fibroblast-Specific Genetic Manipulation of p38 Mitogen-Activated Protein Kinase In Vivo Reveals Its Central Regulatory Role in Fibrosis. *Circulation* 136, 549-561 (2017).
453. Tocris-Bioscience. SD208 Certificate of Analysis. (2021).
454. Teekakirikul, P.*, et al.* Cardiac fibrosis in mice with hypertrophic cardiomyopathy is mediated by non-myocyte proliferation and requires Tgf-beta. *J Clin Invest* 120, 3520-3529 (2010).
455. Derangeon, M.*, et al.* Transforming growth factor beta receptor inhibition prevents ventricular fibrosis in a mouse model of progressive cardiac conduction disease. *Cardiovasc Res* 113, 464-474 (2017).

456. Mitra, M.S.*, et al.* A Potent Pan-TGFbeta Neutralizing Monoclonal Antibody Elicits Cardiovascular Toxicity in Mice and Cynomolgus Monkeys. *Toxicol Sci* 175, 24-34 (2020).
457. Anderton, M.J.*, et al.* Induction of heart valve lesions by small-molecule ALK5 inhibitors. *Toxicol Pathol* 39, 916-924 (2011).
458. Kelly M Credill, A.J.S. Nonclinical Safety Evaluation of a Transforming Growth Factor β Receptor I Kinase Inhibitor in Fischer 344 Rats and Beagle Dogs. *Journal of Clinical Toxicology* 04(2014).
459. Kovacs, R.J.*, et al.* Cardiac Safety of TGF-beta Receptor I Kinase Inhibitor LY2157299 Monohydrate in Cancer Patients in a First-in-Human Dose Study. *Cardiovasc Toxicol* 15, 309-323 (2015).
460. Santini, V.*, et al.* Phase II Study of the ALK5 Inhibitor Galunisertib in Very Low-, Low-, and Intermediate-Risk Myelodysplastic Syndromes. *Clin Cancer Res* 25, 6976-6985 (2019).
461. Evans, R.A., Tian, Y.C., Steadman, R. & Phillips, A.O. TGF-beta1-mediated fibroblast-myofibroblast terminal differentiation-the role of Smad proteins. *Exp Cell Res* 282, 90-100 (2003).
462. Penke, L.R. & Peters-Golden, M. Molecular determinants of mesenchymal cell activation in fibroproliferative diseases. *Cell Mol Life Sci* 76, 4179-4201 (2019).
463. Molenaar, B.*, et al.* Single-cell transcriptomics following ischemic injury identifies a role for B2M in cardiac repair. *Commun Biol* 4, 146 (2021).
464. Ruiz-Villalba, A.*, et al.* Single-Cell RNA Sequencing Analysis Reveals a Crucial Role for CTHRC1 (Collagen Triple Helix Repeat Containing 1) Cardiac Fibroblasts After Myocardial Infarction. *Circulation* 142, 1831-1847 (2020).
465. Phan, S.H. The myofibroblast in pulmonary fibrosis. *Chest* 122, 286S-289S (2002).
466. Hinz, B. Matrix mechanics and regulation of the fibroblast phenotype. *Periodontol 2000* 63, 14-28 (2013).
467. Bhana, B.*, et al.* Influence of substrate stiffness on the phenotype of heart cells. *Biotechnol Bioeng* 105, 1148-1160 (2010).

468. Fomovsky, G.M. & Holmes, J.W. Evolution of scar structure, mechanics, and ventricular function after myocardial infarction in the rat. *Am J Physiol Heart Circ Physiol* 298, H221-228 (2010).
469. Vasquez, C.*, et al.* Enhanced fibroblast-myocyte interactions in response to cardiac injury. *Circ Res* 107, 1011-1020 (2010).
470. Wang, J., Chen, H., Seth, A. & McCulloch, C.A. Mechanical force regulation of myofibroblast differentiation in cardiac fibroblasts. *Am J Physiol Heart Circ Physiol* 285, H1871-1881 (2003).
471. Petrov, V.V., Fagard, R.H. & Lijnen, P.J. Stimulation of Collagen Production by Transforming Growth Factor-β₁ During Differentiation of Cardiac Fibroblasts to Myofibroblasts. *Hypertension* 39, 258-263 (2002).
472. Cho, N., Razipour, S.E. & McCain, M.L. Featured Article: TGF-beta1 dominates extracellular matrix rigidity for inducing differentiation of human cardiac fibroblasts to myofibroblasts. *Exp Biol Med (Maywood)* 243, 601-612 (2018).
473. Kollmannsberger, P., Bidan, C.M., Dunlop, J.W.C., Fratzl, P. & Vogel, V. Tensile forces drive a reversible fibroblast-to-myofibroblast transition during tissue growth in engineered clefts. *Sci Adv* 4, eaao4881 (2018).
474. de Jager, D.J.*, et al.* Cardiovascular and noncardiovascular mortality among patients starting dialysis. *JAMA : the journal of the American Medical Association* 302, 1782-1789 (2009).
475. Thompson, S.*, et al.* Cause of Death in Patients with Reduced Kidney Function. *J Am Soc Nephrol* 26, 2504-2511 (2015).
476. Camelliti, P., Borg, T.K. & Kohl, P. Structural and functional characterisation of cardiac fibroblasts. *Cardiovasc Res* 65, 40-51 (2005).
477. Leifheit-Nestler, M.*, et al.* Fibroblast growth factor 23 is induced by an activated renin-angiotensin-aldosterone system in cardiac myocytes and promotes the pro-fibrotic crosstalk between cardiac myocytes and fibroblasts. *Nephrol Dial Transplant* (2018).
478. van den Borne, S.W.*, et al.* Myocardial remodeling after infarction: the role of myofibroblasts. *Nat Rev Cardiol* 7, 30-37 (2010).

479. Akamatsu, T.*, et al.* Direct isolation of myofibroblasts and fibroblasts from bleomycin-injured lungs reveals their functional similarities and differences. *Fibrogenesis Tissue Repair* 6, 15 (2013).
480. Roy, C.*, et al.* Fibroblast growth factor 23: a biomarker of fibrosis and prognosis in heart failure with preserved ejection fraction. *ESC Heart Fail* (2020).
481. Milovanova, L.Y.*, et al.* Elevated Fibroblast Growth Factor 23 and Decreased Klotho Levels Are Associated With Diastolic Dysfunction in CKD G4-5D Patients. *Kidney Int Rep* 5, 1118 (2020).
482. Han, X., Cai, C., Xiao, Z. & Quarles, L.D. FGF23 induced left ventricular hypertrophy mediated by FGFR4 signaling in the myocardium is attenuated by soluble Klotho in mice. *J Mol Cell Cardiol* 138, 66-74 (2020).
483. Chen, X. & Thibeault, S.L. Response of fibroblasts to transforming growth factor-beta1 on two-dimensional and in three-dimensional hyaluronan hydrogels. *Tissue Eng Part A* 18, 2528-2538 (2012).
484. Asano, S.*, et al.* Matrix stiffness regulates migration of human lung fibroblasts. *Physiol Rep* 5(2017).
485. Chen, A.A., Khetani, S.R., Lee, S., Bhatia, S.N. & Van Vliet, K.J. Modulation of hepatocyte phenotype in vitro via chemomechanical tuning of polyelectrolyte multilayers. *Biomaterials* 30, 1113-1120 (2009).
486. Liguori, T.T.A., Liguori, G.R., Moreira, L.F.P. & Harmsen, M.C. Fibroblast growth factor-2, but not the adipose tissue-derived stromal cells secretome, inhibits TGF-β1-induced differentiation of human cardiac fibroblasts into myofibroblasts. *Scientific Reports* 8, 16633 (2018).
487. Chen, P.Y., Qin, L., Li, G., Tellides, G. & Simons, M. Fibroblast growth factor (FGF) signaling regulates transforming growth factor beta (TGFbeta)-dependent smooth muscle cell phenotype modulation. *Sci Rep* 6, 33407 (2016).
488. Correia, A.C., Moonen, J.R., Brinker, M.G. & Krenning, G. FGF2 inhibits endothelial-mesenchymal transition through microRNA-20a-mediated repression of canonical TGF-beta signaling. *J Cell Sci* 129, 569-579 (2016).

489. Ito, T., Sawada, R., Fujiwara, Y., Seyama, Y. & Tsuchiya, T. FGF-2 suppresses cellular senescence of human mesenchymal stem cells by down-regulation of TGF-beta2. *Biochem Biophys Res Commun* 359, 108-114 (2007).
490. Ichise, T., Yoshida, N. & Ichise, H. FGF2-induced Ras-MAPK signalling maintains lymphatic endothelial cell identity by upregulating endothelial-cell-specific gene expression and suppressing TGFbeta signalling through Smad2. *J Cell Sci* 127, 845-857 (2014).
491. Wolf, M. Update on fibroblast growth factor 23 in chronic kidney disease. *Kidney international* 82, 737-747 (2012).
492. Park, D.S. & Fishman, G.I. The cardiac conduction system. *Circulation* 123, 904-915 (2011).
493. Boriani, G. & Raatikainen, M.J.P. Anatomy and physiology of the atrioventricular node. in *ESC CardioMed* (eds. Boriani, G., Camm, A.J., Lüscher, T.F., Maurer, G. & Serruys, P.W.) 1957-1958 (Oxford University Press, 2018).
494. Ho, Y., Matsuyama, T.-a. & Ishibashi-Ueda, H. Normal conduction system, coronary arteries, and coronary veins. in *ESC CardioMed* (eds. Ho, Y., Camm, A.J., Lüscher, T.F., Maurer, G. & Serruys, P.W.) 69-72 (Oxford University Press, 2018).
495. Nerbonne, J.M., Nichols, C.G., Schwarz, T.L. & Escande, D. Genetic manipulation of cardiac K(+) channel function in mice: what have we learned, and where do we go from here? *Circ Res* 89, 944-956 (2001).
496. Guo, W., Xu, H., London, B. & Nerbonne, J.M. Molecular basis of transient outward K+ current diversity in mouse ventricular myocytes. *J Physiol* 521 Pt 3, 587-599 (1999).
497. Nerbonne, J.M. Molecular basis of functional voltage-gated K+ channel diversity in the mammalian myocardium. *J Physiol* 525 Pt 2, 285-298 (2000).
498. Balasubramaniam, R., Grace, A.A., Saumarez, R.C., Vandenberg, J.I. & Huang, C.L. Electrogram prolongation and nifedipine-suppressible

ventricular arrhythmias in mice following targeted disruption of KCNE1. *J Physiol* 552, 535-546 (2003).

499. Danik, S.*, et al.* Correlation of repolarization of ventricular monophasic action potential with ECG in the murine heart. *Am J Physiol Heart Circ Physiol* 283, H372-381 (2002).
500. Land, S. (2013).
501. Joukar, S. A comparative review on heart ion channels, action potentials and electrocardiogram in rodents and human: extrapolation of experimental insights to clinic. *Lab Anim Res* 37, 25 (2021).
502. Hall, J.E. *Guyton and Hall Textbook of Medical Physiology (13th Edition)*, (Beijing da xue yi xue chu ban she, 2019).
503. Eisner, D.A., Caldwell, J.L., Kistamas, K. & Trafford, A.W. Calcium and Excitation-Contraction Coupling in the Heart. *Circ Res* 121, 181-195 (2017).
504. Lehman, W., Craig, R. & Vibert, P. Ca(2+)-induced tropomyosin movement in Limulus thin filaments revealed by three-dimensional reconstruction. *Nature* 368, 65-67 (1994).
505. Spudich, J.A. The myosin swinging cross-bridge model. *Nat Rev Mol Cell Biol* 2, 387-392 (2001).
506. Bers, D.M. Cardiac excitation-contraction coupling. *Nature* 415, 198-205 (2002).
507. MacLennan, D.H. & Kranias, E.G. Phospholamban: a crucial regulator of cardiac contractility. *Nat Rev Mol Cell Biol* 4, 566-577 (2003).
508. Mattiazzi, A. & Kranias, E.G. The role of CaMKII regulation of phospholamban activity in heart disease. *Front Pharmacol* 5, 5 (2014).
509. Witcher, D.R., Kovacs, R.J., Schulman, H., Cefali, D.C. & Jones, L.R. Unique phosphorylation site on the cardiac ryanodine receptor regulates calcium channel activity. *J Biol Chem* 266, 11144-11152 (1991).
510. Rodriguez, P., Bhogal, M.S. & Colyer, J. Stoichiometric phosphorylation of cardiac ryanodine receptor on serine 2809 by calmodulin-dependent kinase II and protein kinase A. *J Biol Chem* 278, 38593-38600 (2003).

511. Ai, X., Curran, J.W., Shannon, T.R., Bers, D.M. & Pogwizd, S.M. Ca2+/calmodulin-dependent protein kinase modulates cardiac ryanodine receptor phosphorylation and sarcoplasmic reticulum Ca2+ leak in heart failure. *Circ Res* 97, 1314-1322 (2005).
512. Wehrens, X.H., Lehnart, S.E., Reiken, S.R. & Marks, A.R. Ca2+/calmodulin-dependent protein kinase II phosphorylation regulates the cardiac ryanodine receptor. *Circ Res* 94, e61-70 (2004).
513. Marx, S.O.*, et al.* PKA phosphorylation dissociates FKBP12.6 from the calcium release channel (ryanodine receptor): defective regulation in failing hearts. *Cell* 101, 365-376 (2000).
514. Studer, R.*, et al.* Gene expression of the cardiac Na(+)-Ca2+ exchanger in end-stage human heart failure. *Circ Res* 75, 443-453 (1994).
515. Hobai, I.A. & O'Rourke, B. Decreased sarcoplasmic reticulum calcium content is responsible for defective excitation-contraction coupling in canine heart failure. *Circulation* 103, 1577-1584 (2001).
516. Richter, B., Haller, J., Haffner, D. & Leifheit-Nestler, M. Klotho modulates FGF23-mediated NO synthesis and oxidative stress in human coronary artery endothelial cells. *Pflugers Arch* 468, 1621-1635 (2016).
517. Zima, A.V. & Blatter, L.A. Redox regulation of cardiac calcium channels and transporters. *Cardiovasc Res* 71, 310-321 (2006).
518. Schaper, J.*, et al.* Impairment of the myocardial ultrastructure and changes of the cytoskeleton in dilated cardiomyopathy. *Circulation* 83, 504-514 (1991).
519. Gomez, A.M., Guatimosim, S., Dilly, K.W., Vassort, G. & Lederer, W.J. Heart failure after myocardial infarction: altered excitation-contraction coupling. *Circulation* 104, 688-693 (2001).
520. van Oort, R.J.*, et al.* Ryanodine receptor phosphorylation by calcium/calmodulin-dependent protein kinase II promotes life-threatening ventricular arrhythmias in mice with heart failure. *Circulation* 122, 2669-2679 (2010).
521. Piacentino, V., 3rd*, et al.* Cellular basis of abnormal calcium transients of failing human ventricular myocytes. *Circ Res* 92, 651-658 (2003).

522. Miyamura, M.*, et al.* Circulating Fibroblast Growth Factor 23 Has a U-Shaped Association With Atrial Fibrillation Prevalence. *Circ J* 79, 1742-1748 (2015).
523. Kao, Y.H.*, et al.* FGF-23 dysregulates calcium homeostasis and electrophysiological properties in HL-1 atrial cells. *Eur J Clin Invest* 44, 795-801 (2014).
524. Huang, S.Y.*, et al.* Fibroblast growth factor 23 dysregulates late sodium current and calcium homeostasis with enhanced arrhythmogenesis in pulmonary vein cardiomyocytes. *Oncotarget* 7, 69231-69242 (2016).
525. Verkaik, M.*, et al.* High Fibroblast Growth Factor 23 concentrations in experimental renal failure impair calcium handling in cardiomyocytes. *Physiol Rep* 6, e13591 (2018).
526. Graves, J.M.*, et al.* Fibroblast growth factor 23 (FGF23) induces ventricular arrhythmias and prolongs QTc interval in mice in an FGF receptor 4-dependent manner. *Am J Physiol Heart Circ Physiol* 320, H2283-H2294 (2021).
527. O'Shea, C.*, et al.* Cardiac optical mapping - State-of-the-art and future challenges. *Int J Biochem Cell Biol* 126, 105804 (2020).
528. Elharrar, V. & Surawicz, B. Cycle length effect on restitution of action potential duration in dog cardiac fibers. *Am J Physiol* 244, H782-792 (1983).
529. Schram, G., Pourrier, M., Melnyk, P. & Nattel, S. Differential distribution of cardiac ion channel expression as a basis for regional specialization in electrical function. *Circ Res* 90, 939-950 (2002).
530. Gaborit, N.*, et al.* Regional and tissue specific transcript signatures of ion channel genes in the non-diseased human heart. *J Physiol* 582, 675-693 (2007).
531. Drouin, E., Charpentier, F., Gauthier, C., Laurent, K. & Le Marec, H. Electrophysiologic characteristics of cells spanning the left ventricular wall of human heart: evidence for presence of M cells. *J Am Coll Cardiol* 26, 185-192 (1995).

532. Sicouri, S. & Antzelevitch, C. A subpopulation of cells with unique electrophysiological properties in the deep subepicardium of the canine ventricle. The M cell. *Circ Res* 68, 1729-1741 (1991).
533. Lachaud, Q.*, et al.* Electrophysiological heterogeneity in large populations of rabbit ventricular cardiomyocytes. *Cardiovasc Res* 118, 3112-3125 (2022).
534. Avula, U.M.R.*, et al.* Heterogeneity of the action potential duration is required for sustained atrial fibrillation. *JCI Insight* 5(2019).
535. Varela, M., Colman, M.A., Hancox, J.C. & Aslanidi, O.V. Atrial Heterogeneity Generates Re-entrant Substrate during Atrial Fibrillation and Anti-arrhythmic Drug Action: Mechanistic Insights from Canine Atrial Models. *PLoS Comput Biol* 12, e1005245 (2016).
536. Hondeghem, L.M., Carlsson, L. & Duker, G. Instability and triangulation of the action potential predict serious proarrhythmia, but action potential duration prolongation is antiarrhythmic. *Circulation* 103, 2004-2013 (2001).
537. Hondeghem, L.M., Dujardin, K. & De Clerck, F. Phase 2 prolongation, in the absence of instability and triangulation, antagonizes class III proarrhythmia. *Cardiovasc Res* 50, 345-353 (2001).
538. Osadchii, O.E. Electrocardiographic marker of the cardiac action potential triangulation induced by antiarrhythmic drugs in perfused guinea-pig heart. *Exp Physiol* 107, 864-878 (2022).
539. Pourrier, M., Williams, S., McAfee, D., Belardinelli, L. & Fedida, D. CrossTalk proposal: The late sodium current is an important player in the development of diastolic heart failure (heart failure with a preserved ejection fraction). *J Physiol* 592, 411-414 (2014).
540. Undrovinas, A.I., Maltsev, V.A. & Sabbah, H.N. Repolarization abnormalities in cardiomyocytes of dogs with chronic heart failure: role of sustained inward current. *Cell Mol Life Sci* 55, 494-505 (1999).
541. Kistamas, K., Hezso, T., Horvath, B. & Nanasi, P.P. Late sodium current and calcium homeostasis in arrhythmogenesis. *Channels (Austin)* 15, 1-19 (2021).

542. Ravens, U. & Cerbai, E. Role of potassium currents in cardiac arrhythmias. *Europace* 10, 1133-1137 (2008).
543. Siddiqi, H.K.*, et al.* Sex Differences in Atrial Fibrillation Risk: The VITAL Rhythm Study. *JAMA Cardiol* 7, 1027-1035 (2022).
544. Manolio, T.A.*, et al.* Cardiac arrhythmias on 24-h ambulatory electrocardiography in older women and men: the Cardiovascular Health Study. *J Am Coll Cardiol* 23, 916-925 (1994).
545. Linde, C.*, et al.* Sex differences in cardiac arrhythmia: a consensus document of the European Heart Rhythm Association, endorsed by the Heart Rhythm Society and Asia Pacific Heart Rhythm Society. *Europace* 20, 1565-1565ao (2018).
546. Han, B., Trew, M.L. & Zgierski-Johnston, C.M. Cardiac Conduction Velocity, Remodeling and Arrhythmogenesis. *Cells* 10(2021).
547. Bishop, M.J., Vigmond, E.J. & Plank, G. The functional role of electrophysiological heterogeneity in the rabbit ventricle during rapid pacing and arrhythmias. *Am J Physiol Heart Circ Physiol* 304, H1240-1252 (2013).
548. Glukhov, A.V.*, et al.* Transmural dispersion of repolarization in failing and nonfailing human ventricle. *Circ Res* 106, 981-991 (2010).
549. Yan, G.X., Shimizu, W. & Antzelevitch, C. Characteristics and distribution of M cells in arterially perfused canine left ventricular wedge preparations. *Circulation* 98, 1921-1927 (1998).
550. Salama, G. & Hwang, S.M. Simultaneous optical mapping of intracellular free calcium and action potentials from Langendorff perfused hearts. *Curr Protoc Cytom* Chapter 12, Unit 12 17 (2009).
551. Choi, B.R. & Salama, G. Simultaneous maps of optical action potentials and calcium transients in guinea-pig hearts: mechanisms underlying concordant alternans. *J Physiol* 529 Pt 1, 171-188 (2000).
552. Weber, T.J., Liu, S., Indridason, O.S. & Quarles, L.D. Serum FGF23 levels in normal and disordered phosphorus homeostasis. *Journal of bone and mineral research : the official journal of the American Society for Bone and Mineral Research* 18, 1227-1234 (2003).

553. Larsson, T., Nisbeth, U., Ljunggren, O., Juppner, H. & Jonsson, K.B. Circulating concentration of FGF-23 increases as renal function declines in patients with chronic kidney disease, but does not change in response to variation in phosphate intake in healthy volunteers. *Kidney international* 64, 2272-2279 (2003).
554. Nakanishi, S.*, et al.* Serum fibroblast growth factor-23 levels predict the future refractory hyperparathyroidism in dialysis patients. *Kidney international* 67, 1171-1178 (2005).
555. Gutierrez, O.M.*, et al.* Fibroblast growth factor 23 and left ventricular hypertrophy in chronic kidney disease. *Circulation* 119, 2545-2552 (2009).
556. Mirza, M.A., Larsson, A., Melhus, H., Lind, L. & Larsson, T.E. Serum intact FGF23 associate with left ventricular mass, hypertrophy and geometry in an elderly population. *Atherosclerosis* 207, 546-551 (2009).
557. Jaroszynski, A.*, et al.* Serum heat shock protein 27 levels predict cardiac mortality in hemodialysis patients. *BMC Nephrol* 19, 359 (2018).
558. Pellman, J., Zhang, J. & Sheikh, F. Myocyte-fibroblast communication in cardiac fibrosis and arrhythmias: Mechanisms and model systems. *J Mol Cell Cardiol* 94, 22-31 (2016).
559. Granzier, H.L. & Labeit, S. The giant protein titin: a major player in myocardial mechanics, signaling, and disease. *Circ Res* 94, 284-295 (2004).
560. Knight, W.E.*, et al.* Ex vivo Methods for Measuring Cardiac Muscle Mechanical Properties. *Front Physiol* 11, 616996 (2020).
561. Campostrini, G., Windt, L.M., van Meer, B.J., Bellin, M. & Mummery, C.L. Cardiac Tissues From Stem Cells: New Routes to Maturation and Cardiac Regeneration. *Circ Res* 128, 775-801 (2021).
562. Ergir, E.*, et al.* Generation and maturation of human iPSC-derived 3D organotypic cardiac microtissues in long-term culture. *Sci Rep* 12, 17409 (2022).
563. Kaese, S. & Verheule, S. Cardiac electrophysiology in mice: a matter of size. *Front Physiol* 3, 345 (2012).

564. Wolf, M. Forging forward with 10 burning questions on FGF23 in kidney disease. *J Am Soc Nephrol* 21, 1427-1435 (2010).
565. Brack, K.E., Narang, R., Winter, J. & Ng, G.A. The mechanical uncoupler blebbistatin is associated with significant electrophysiological effects in the isolated rabbit heart. *Exp Physiol* 98, 1009-1027 (2013).
566. Kappadan, V.*, et al.* High-Resolution Optical Measurement of Cardiac Restitution, Contraction, and Fibrillation Dynamics in Beating vs. Blebbistatin-Uncoupled Isolated Rabbit Hearts. *Front Physiol* 11, 464 (2020).
567. Varkuti, B.H.*, et al.* A highly soluble, non-phototoxic, non-fluorescent blebbistatin derivative. *Sci Rep* 6, 26141 (2016).
568. Sakamoto, T., Limouze, J., Combs, C.A., Straight, A.F. & Sellers, J.R. Blebbistatin, a myosin II inhibitor, is photoinactivated by blue light. *Biochemistry* 44, 584-588 (2005).
569. Chen, L.*, et al.* Multifaceted Spatial and Functional Zonation of Cardiac Cells in Adult Human Heart. *Circulation* 145, 315-318 (2022).
570. Watanabe, T., Delbridge, L.M., Bustamante, J.O. & McDonald, T.F. Heterogeneity of the action potential in isolated rat ventricular myocytes and tissue. *Circ Res* 52, 280-290 (1983).
571. Li, G.R., Feng, J., Yue, L. & Carrier, M. Transmural heterogeneity of action potentials and Ito1 in myocytes isolated from the human right ventricle. *Am J Physiol* 275, H369-377 (1998).
572. Akar, F.G. & Rosenbaum, D.S. Transmural electrophysiological heterogeneities underlying arrhythmogenesis in heart failure. *Circ Res* 93, 638-645 (2003).
573. Stankovicova, T., Szilard, M., De Scheerder, I. & Sipido, K.R. M cells and transmural heterogeneity of action potential configuration in myocytes from the left ventricular wall of the pig heart. *Cardiovasc Res* 45, 952-960 (2000).
574. Tani, H. & Tohyama, S. Human Engineered Heart Tissue Models for Disease Modeling and Drug Discovery. *Front Cell Dev Biol* 10, 855763 (2022).

575. Li, X.*, et al.* Standardised Framework for Quantitative Analysis of Fibrillation Dynamics. *Sci Rep* 9, 16671 (2019).
576. Swift, L.M.*, et al.* Properties of blebbistatin for cardiac optical mapping and other imaging applications. *Pflugers Arch* 464, 503-512 (2012).
577. Jaimes, R., 3rd*, et al.* A technical review of optical mapping of intracellular calcium within myocardial tissue. *Am J Physiol Heart Circ Physiol* 310, H1388-1401 (2016).
578. Lee, P.*, et al.* In vivo ratiometric optical mapping enables high-resolution cardiac electrophysiology in pig models. *Cardiovasc Res* 115, 1659-1671 (2019).
579. Ofstad, J. & Iversen, B.M. Glomerular and tubular damage in normotensive and hypertensive rats. *Am J Physiol Renal Physiol* 288, F665-672 (2005).
580. Kirchhoff, F.*, et al.* Rapid development of severe end-organ damage in C57BL/6 mice by combining DOCA salt and angiotensin II. *Kidney international* 73, 643-650 (2008).
581. Saito, T.*, et al.* Fibroblast Growth Factor 23 Exacerbates Cardiac Fibrosis in Deoxycorticosterone Acetate-Salt Mice With Hypertension. *Lab Invest* 103, 100003 (2023).
582. Stubbs, J.R.*, et al.* Longitudinal evaluation of FGF23 changes and mineral metabolism abnormalities in a mouse model of chronic kidney disease. *Journal of bone and mineral research : the official journal of the American Society for Bone and Mineral Research* 27, 38-46 (2012).
583. Francis, C.*, et al.* Ferric citrate reduces fibroblast growth factor 23 levels and improves renal and cardiac function in a mouse model of chronic kidney disease. *Kidney international* 96, 1346-1358 (2019).
584. Matthias, J.*, et al.* Extra-Large Galpha Protein (XLalphas) Deficiency Causes Severe Adenine-Induced Renal Injury with Massive FGF23 Elevation. *Endocrinology* 161(2020).
585. Yokozawa, T., Zheng, P.D., Oura, H. & Koizumi, F. Animal model of adenine-induced chronic renal failure in rats. *Nephron* 44, 230-234 (1986).

586. Diwan, V., Mistry, A., Gobe, G. & Brown, L. Adenine-induced chronic kidney and cardiovascular damage in rats. *J Pharmacol Toxicol Methods* 68, 197-207 (2013).